

# Towards implementing new isotopes for environmental research: Redetermination of the $^{32}\text{Si}$ half-life

Présentée le 30 septembre 2022

Faculté des sciences de base  
Laboratoire de physique des réacteurs et de comportement des systèmes  
Programme doctoral en chimie et génie chimique

pour l'obtention du grade de Docteur ès Sciences

par

**Mario Aaron VEICHT**

Acceptée sur proposition du jury

Prof. K. Sivula, président du jury  
Prof. A. Pautz, Dr D. Schumann, directeurs de thèse  
Prof. G. W. Severin, rapporteur  
Prof. S. M. Qaim, rapporteur  
Prof. K. V. Agrawal, rapporteur





## ■ Acknowledgement

---

First, a big thank you to **Dr Dorothea Schumann** (Group leader: Isotope and Target Chemistry), my line manager and thesis Co-Directrice, but also the mastermind behind the SINCHRON-Project. Undoubtedly, you have been a key person regarding my PhD since you provided valuable personal and priceless scientific support. Besides, you always had an open ear, and while entering your office with problems, I usually left with a solution or at least many ideas to tackle those. Therefore, I express my sincere gratitude to you, as I could not have asked for a better PI to perform my PhD. Similarly, I want to acknowledge the tremendous support that I received throughout my PhD from my thesis Director, **Prof. Andreas Pautz**, who also happens to be the Division Head of Nuclear Energy and Safety at PSI. Since the very beginning, you have always been interested in my scientific work. Despite your busy schedule, you always found time to meet regularly with me to update you concerning the project's status. Here, special thanks to **Prof. Robert Eichler** (Head of the Laboratory of Radiochemistry (LRC)). You are a very inspiring person, and many thanks for all the support and advices given during my time at the LRC.

Besides, it is also my pleasure to say thank you to my **PhD Committee**. First, many thanks **Prof. Varoon Kumar** (EPFL Valais, Switzerland). Thank you for joining my committee during my Candidacy Exam in the first year of PhD. It has been challenging yet a pleasure to answer the critical questions and provide a thoroughly revised timeline of my PhD studies. Furthermore, I am grateful that with **Prof. Gregory Severin** (Michigan State University, U.S.A.), and **Prof. Syed Qaim** (Forschungszentrum Jülich, Germany), I have two experts from the field of Radiochemistry in my PhD Committee that have shown great interest in my work, and I looked forward to presenting my work from the past four years. Special thanks belong to **Prof. Kevin Sivula** (EPFL). Thank you for being both the President during my Candidacy Exam and my PhD Oral Defense. Thank you for providing such good conditions to grow personally and scientifically, thank you for taking me as your assistant, and thank you for always having time for any query that I had. It has been a great pleasure for me! The lab support from **Frédéric Gummy** was also very much appreciated. Providing the updated software for the photovoltaic system did make the difference, Fred! Moving further to the academic experience at EPFL/UNIL. First, I am very grateful to have met **Dr MER Anne-Sophie Chauvin**. Initially, it has been challenging for me with my French, but your attitude towards teaching encouraged me to take that spirit further in the laboratories. Your involvement in teaching the general and analytical chemistry at UNIL is exceptional! Moreover, many thanks for suggesting me for the SCGC's EPFL Teaching Excellence Award, which has been a big honor for me. These excellent teaching conditions are also linked to the work and help of **Dr Julien Andres**, whose contribution I very much appreciate and acknowledge, too. Despite running so many TPs per weekday, it has always been a pleasure when you came by my TP Lab to have a little chat. Thanks a lot for the excellent organization! On this subject, many thanks to the responsible Technicians **Laetitia Pannetier** and **Claude Nuessler** for their assistance, too! Thanks to **Dr Natalia Gasilova**, who performed with me a one-day ICP-MS training at EPFL Valais. Thank you for sharing your expertise also afterwards, thus, always assisting me via email! This was a great help. Also, I acknowledge the support from **Anne Lene Odegaard**. You guided me through the initial process of getting started and helped me find my way at EDCH. You've always given me quick answers to my – sometimes – comprehensive questions.

Moving on to my place to be: PSI. Many thanks to **Dr Stephan Heinitz**! You gave me the introduction to the LRC, and you shared much valuable information before leaving for Belgium. Besides the fascinating tours in the PSI facilities, the beauty of swimming in the Aare during the lunch break also remained a very nice memory!

Many thanks, of course, to **Dr Ionut Mihalcea**. We spent countless hours together in the lab, to materialize the idea of SINCHRON into a final product: the  $^{32}\text{Si}$  fraction. Moreover, we had many interesting discussions about virtually any topic. It was a great pleasure to spend the four years and eventually write and publish three papers together. All the best for your future! Many thanks to **Dr Ivan Kajan**, with whom I completed the first project, and, thus, many thanks for the tremendous support and countless discussions concerning gamma-measurements and related uncertainties. On this subject, thanks to **Dr Rugard Dressler**. Your knowledge regarding measurement techniques and uncertainties has helped me in many ways. To my colleagues working at OIPA: Many thanks to **Dr Zeynep Talip** (Radionuclide Development Group, RDG) for sharing your expertise in developing radiochemical separation procedures. Moreover, you've been directly involved in the project's success by taking care ordering the new ICP-OES, which significantly improved the analytical quality of the work, especially regarding silicon analysis. Further, many thanks to **Dr Pascal Grundler** (RDG). You always helped me with material and shared details about lab equipment. Besides, thanks for helping with the LN2 detector fillings, including troubleshootings! On this subject, thanks to **Colin** (RDG). You developed a great understanding of responsibilities early, and I wish you the best of luck in your career! Finally, thanks a lot, **Chiara** (RDG), for organizing the LRC seminar with me and for nice discussions throughout my PhD. Including establishing new traditions: Cheers! Then, many thanks to the wizard of OIPA, when it comes to technical questions, **Muhamet Djelili**. You helped me a lot and provided me with not less than always a solution in no time. Your efforts are greatly appreciated! Regarding my lab work, I greatly appreciate the work performed by the former master's students **Shaohuang** (now: PhD Student, SFU Canada) and especially **Jennifer** (now: PhD Student at LRC, ETH Zurich). Furthermore, only with the help of **Dr Djordje Cvjetinovic** (now: PostDoc at LRC) was it possible to process all the vanadium discs according to the schedule and provide the necessary stock of  $^{32}\text{Si}$  on time. If it wouldn't be without contamination: a big "Thank you!" to our Radioprotection for excellent support and interesting discussions! I wish you, **Tobias, Thomas, Andreas, Marcel, and Yannick** all the best for the future! Special thanks to **Prof. Patrick Steinegger**. During my time, he became both the appointed Group Leader of the Heavy Element Group (LRC) and Tenure Track Assistant Professor of Radiochemistry (D-CHAB, ETH Zurich). Thanks, Patrick, for your continuous support and, besides, for sharing your passion for the beauty of LaTeX and vector programs. I wish you loads of success in your future career! Moving onwards, I'd like to thank my office mates, especially the "old generation fellows", with whom I had a great time in the beginning, and it was great to be able to see you graduating and celebrating your success altogether. Therefore, thank you, **Ivan D, Mu, Erik, Paul I, Yves, Benjamin**. I very much enjoyed the time with you guys! Special thanks to **Nadine**, who always helped whenever it was needed. Many thanks to the "new generation fellows" of OFLB/101 and LRC (**Paul D, Ivan Z, Lu, and Noemi**), who encouraged me a lot during the writing period: I wish you all the best for your future! My big gratitude to the further LRC Members, **Dr Emilio Maugeri, Dr Jörg Neuhausen, Angela Blattmann, Alexander Vögele** (for taking care of many of my queries), and **Dominik Hermann** (for building MODUS and providing us with coffee!).

Also, I have been lucky to benefit from working with many more collaborators involved in the SINCHRON-Project. Many thanks, **Dr Claude Bailat, Dr Youcef Nedjadi** (that I could spend six weeks at IRA), **Dr Stefan Röllin** (for inviting me twice to the Spiez Laboratory and measuring the  $^{32}\text{Si}$ ), **Dr Ole Naehle, Dr Karsten Kossert** (for inviting us to PTB and having in-depth discussions), **Dr Christof Vockenhuber, Matthias Schlomberg** (for AMS measurements, and pleasant visits at your facility), **Dr Peter Sprung** (for showing me the principles (and troubles) of MC-ICP-MS), **Dr Jean-Christophe David** (for the theoretical cross-section calculations with INCL/ABLA, in-depth explanations, and co-authoring the first paper), and **Prof. Rolf Michel** and **Dr Erik Strub** (for providing V samples and the necessary data to finish the V(p,x)-projects).

Last but not least, I thank the former Postdocs from PTB, **Dr Nataša Lalović** and **Dr Dmytro Symochko** (sharing many information and ideas). Also, many thanks to **Dr Teresa Durán** (explanations on the decay measurements), pursuing her research at IRA and working on the prospective decay measurements of  $^{32}\text{Si}$ . Moreover, A special thanks to many more people involved in my PhD: **Dr Steffen Happel** (R&D Director, TrisKem), **Dr Nick van der Meulen** (Groupleader: Radionuclide Development), **Roger Geissmann** (Groupleader: Radionuclide – Production and Maintenance), **Hans Leu** (PSI Hot Laboratory), **Dr Ben Russel** (Science Area Leader, NPL), **Carmen Heim** and **Sandra Matthews** (Vistor Centre psi forum). It has been a great time at PSI. Many thanks!

Finally, these last lines belong to my friends and my family. Special thanks and words of appreciation go to my cherished "PhD"-friends, **Jiri, Jeremy, Josh** and **Tobi S!** Thank you so much for your support! My sincere gratitude to you, **Samer**, and I thank you for your personal and academic guidance throughout the past years. Besides, special thanks to my Bodensee and Heidelberg people. **Julian, Tobi R, Marco, Oli**, and **Andreas, Matti, Simon, Tobi F** and **Johannes!** I'm very lucky and happy to have you! And most of my gratitude goes to my family: **Mama** and **Ralf**, my two lovely brothers, **Jan** and **Ben**, with **Marie** and **Gaia!** And, thank you, to my **Patrycja**, for endless support and help throughout this time.

*Thank you! Vielen Dank! Dziękuję bardzo! Merci beaucoup! Grazie mille!*

■ **Funding** from the **SNSF** for the **SINCHRON**-project (N° 177229) is greatly appreciated.

---

*“If you can’t explain it to a six year old, you don’t understand it yourself.” - Albert Einstein*



# ■ Abstract

---

Radiometric dating is a well-established contemporary technique that has proved a versatile tool for absolute age determinations: A famous example is mentioned here, referring to the precise age determination of the Iceman (also known as Ötzi), which was achieved using the radiocarbon dating (carbon-14,  $^{14}\text{C}$ ) method. Generally, for radiometric dating, the half-life ( $T_{1/2}$ ) is a critical aspect, which must be known with high precision. Interestingly, a significant dating gap currently exists between chronologies based on  $^{210}\text{Pb}$  ( $T_{1/2} \approx 22$  years) and  $^{14}\text{C}$  ( $T_{1/2} \approx 5700$  years). Therefore, a chronometer for the time frame of about 100 to 1000 years is missing. However, a dating tool covering this time range is vital for several applications, inter alia, for assessing the anthropogenic impact in regard to climate variations on Earth. Here, the cosmogenic nuclide,  $^{32}\text{Si}$ , could potentially fill this dating gap. But an issue arises due to the imprecisely determined  $T_{1/2}$  of  $^{32}\text{Si}$ . Currently recommended values demonstrate potential biases, while reported values show a wide scattering with significant uncertainties. Consequently, an often-cited value for the  $^{32}\text{Si}$  half-life is referenced to the NuDat3.0-database stating an averaged value of  $\approx 153$  years, however, with high uncertainty. As a result, this hinders its application as a geochronometer since relative precise time information cannot be provided.

Hence, the aim of the SNSF-funded SINCHRON ( $^{32}\text{Si}$ : a new chronometer) project, and therefore the primary goal of this thesis, concerns the re-determination of the  $^{32}\text{Si}$  half-life. Previous half-life determinations were limited by the use of samples with very low activities, e.g., related to the use of natural  $^{32}\text{Si}$  sources. To overcome the issue with the small amounts,  $^{32}\text{Si}$  was artificially produced at the Paul Scherrer Institut (PSI). Therefore, metallic vanadium discs were irradiated for almost two years (between 2011 and 2012) with 590 MeV-protons. Dedicated irradiation positions in the Swiss Spallation Neutron Source (SINQ) target were selected, as this irradiation was part of the SINQ Target Irradiation Program (STIP-6 program). Subsequently, a pioneering wet chemical separation system was developed to allow for the selective removal of  $^{32}\text{Si}$  from the proton-irradiated vanadium matrix. Here, a combination of ion-exchange, chelating, and extraction chromatography resins was applied. As a result, 20 mL of an ultra-pure  $^{32}\text{Si}$  solution could be produced, fulfilling the desired parameters related to the half-life re-determination.

Within the framework of this thesis, the determination of the half-life via the direct method was applied; i.e., both the determination of the number of atoms ( $N$ ), in combination with the activity ( $A$ ), are required. Within the SINCHRON-collaboration, several independent measurements were performed between various multinational metrological institutes. Based on the different requirements, the  $^{32}\text{Si}$  solution was manufactured accordingly: (I) the solution's activity concentration was confirmed to be  $>100$  kBq/g, (II) the hexafluorosilicate anion ( $\text{SiF}_6^{2-}$ ) is a chemically very stable Si species, (III) ultra-traces of  $^{32}\text{S}$  were successfully removed which was especially necessary for ICP-MS measurements. Besides, (IV) solid AMS samples ( $^{32}\text{SiO}_2$ ,  $\text{K}_2^{32}\text{SiF}_6$ ) could be prepared from the stock solution, too. After successfully processing around 40 proton-irradiated vanadium discs, PSI now owns an unique worldwide amount ( $\approx 20$  MBq) of  $^{32}\text{Si}$ , which allows providing samples with a high  $^{32}\text{Si}$  activity. Due to the efforts undertaken at PSI, we are getting close to settling the  $^{32}\text{Si}$  half-life and thus close to providing a new, recommended value with low uncertainty ( $<5\%$ ). Within the scope of this work, a preliminary  $T_{1/2}$  for  $^{32}\text{Si}$  of  $125 \pm 5$  ( $1\sigma$ ) years has been determined.

Additionally, we studied vanadium as a target material. Due to the particle interactions during the irradiation process, many more interesting, rare, and exotic isotopes are produced (mainly via spallation) as by-products. Their applications are numerous but mainly needed for medical purposes ( $^{44}\text{Ti}$ ) or astrophysical research ( $^{41}\text{Ca}$  and  $^{26}\text{Al}$ ).

Consequently, we herein present further nuclear data; namely, the production cross-sections of  $^{44}\text{Ti}$ ,  $^{41}\text{Ca}$ , and  $^{26}\text{Al}$  for proton-irradiated vanadium. For the latter two nuclides, the presented data also represent the very first experimental determination of the cross-section for vanadium as a target. Seven proton-irradiated vanadium discs of different origins were used for these experiments since detailed information on the irradiation conditions was available for these samples. In this context, two independent gamma spectrometric measurement systems were used for the activity determination of  $^{44}\text{Ti}$ , and no prior chemical separation of  $^{44}\text{Ti}$  from the matrix was required. Contrarily,  $^{41}\text{Ca}$  and  $^{26}\text{Al}$  were successfully separated using a selective and robust chromatographic wet chemical separation scheme which was developed and applied. As a result, a recovery yield for each isotope of  $>99\%$  was achieved. The activity of these nuclides could then be determined using accelerator mass spectrometry (AMS), whereby the solutions were chemically treated beforehand in order to obtain solid  $^{41}\text{CaF}_2$  or  $^{26}\text{Al}_2\text{O}_3$  samples receive.

Ultimately, this thesis provides extensive studies which suggest that proton-irradiated vanadium is considered a valuable source for numerous, rare, and exotic radionuclides. Among the rarest of these,  $^{32}\text{Si}$  is particularly noteworthy, since its separation and purification from the radioactive matrix will allow the half-life to be redetermined; more than 70 years after the nuclide was first discovered. Among the rarest of these, the separation and purification of  $^{32}\text{Si}$  from the radioactive matrix is particularly noteworthy, as this allows for the determination of its half-life – over 70 years later since its first discovery. Consequently, the SINCHRON-collaboration seeks to foster radiosilicon as a future tool for nuclear dating. In this context, and given the unique worldwide amount of  $^{32}\text{Si}$ , a future task will also cover the production of reference standards for AMS to enable the determination of  $^{32}\text{Si}$  in environmental samples and thus being able to eventually use  $^{32}\text{Si}$  for absolute age determinations.

### Keywords:

$^{32}\text{Si}$  • radiochemical separations • ion-exchange chromatography • extraction chromatography • half-life re-determination • nuclear production cross-sections • exotic radionuclides • artificial production • spallation

## ■ Résumé

---

La datation radiométrique est une technique contemporaine bien établie qui s'est avérée être un outil polyvalent pour la détermination de l'âge absolu : Un exemple célèbre est mentionné ici, faisant référence à la détermination précise de l'âge de l'homme des glaces (également connu sous le nom d'Ötzi), qui a été réalisée en utilisant la méthode de datation au radiocarbone (carbone 14,  $^{14}\text{C}$ ). En général, pour la datation radiométrique, la demi-vie ( $T_{1/2}$ ) est un aspect critique, qui doit être connu avec une grande précision. Il est intéressant de noter qu'il existe actuellement un écart de datation significatif entre les chronologies basées sur le  $^{210}\text{Pb}$  ( $T_{1/2} \approx 22$  ans) et le  $^{14}\text{C}$  ( $T_{1/2} \approx 5700$  ans). Il manque donc un chronomètre pour la période allant de 100 à 1000 ans environ. Or, un outil de datation couvrant cette gamme de temps est vital pour plusieurs applications, entre autres pour évaluer l'impact anthropique en ce qui concerne les variations climatiques sur la Terre. Le nucléide cosmogénique, le  $^{32}\text{Si}$ , pourrait potentiellement combler ce manque de datation. Mais un problème se pose en raison de l'imprécision du  $T_{1/2}$  du  $^{32}\text{Si}$ . Les valeurs actuellement recommandées présentent des biais potentiels, tandis que les valeurs rapportées montrent une grande dispersion avec des incertitudes significatives. Par conséquent, une valeur souvent citée pour la demi-vie du  $^{32}\text{Si}$  est référencée dans la base de données NuDat3.0 et indique une valeur moyenne de  $\approx 153$  ans, avec toutefois une grande incertitude. Par conséquent, cela entrave son application en tant que géochronomètre puisque des informations temporelles relativement précises ne peuvent être fournies.

Ainsi, l'objectif du projet SINCHRON ( $^{32}\text{Si}$ : a new chronometer) financé par le FNS, et donc l'objectif principal de cette thèse, concerne la redétermination de la demi-vie du  $^{32}\text{Si}$ . Les déterminations précédentes de la demi-vie étaient limitées par l'utilisation d'échantillons avec des activités très faibles, par exemple, liées à l'utilisation de sources naturelles de  $^{32}\text{Si}$ . Pour surmonter le problème des faibles quantités, le  $^{32}\text{Si}$  a été produit artificiellement à l'Institut Paul Scherrer (PSI). Ainsi, des disques de vanadium métallique ont été irradiés pendant presque deux ans (entre 2011 et 2012) avec des protons de 590 MeV. Des positions d'irradiation dédiées dans la cible de la source de neutrons de spallation suisse (SINQ) ont été sélectionnées, car cette irradiation faisait partie du programme d'irradiation de la cible SINQ (angl. STIP-6-Program). Par la suite, un système pionnier de séparation chimique par voie liquide a été développé pour permettre l'élimination sélective du  $^{32}\text{Si}$  de la matrice de vanadium irradiée aux protons. Ici, une combinaison de résines de chromatographie d'échange d'ions, de chélation et d'extraction a été appliquée. En conséquence, 20 mL d'une solution de  $^{32}\text{Si}$  ultra-pure ont pu être produits, remplissant les paramètres souhaités liés à la redétermination de la demi-vie.

Dans le cadre de cette thèse, la détermination de la demi-vie par la méthode directe a été appliquée, c'est-à-dire que la détermination du nombre d'atomes ( $N$ ), en combinaison avec l'activité ( $A$ ), est nécessaire. Dans le cadre de la collaboration SINCHRON, plusieurs mesures indépendantes ont été effectuées entre divers instituts métrologiques multinationaux. Sur la base des différentes exigences, la solution de  $^{32}\text{Si}$  a été fabriquée en conséquence : (I) la concentration d'activité de la solution a été confirmée à  $>100$  kBq/g, (II) l'anion hexafluorosilicate ( $\text{SiF}_6^{2-}$ ) est une espèce de Si chimiquement très stable, (III) les ultra-traces de  $^{32}\text{S}$  ont été éliminées avec succès, ce qui était particulièrement nécessaire pour les mesures ICP-MS. En outre, (IV) des échantillons AMS solides ( $^{32}\text{SiO}_2$ ,  $\text{K}_2^{32}\text{SiF}_6$ ) ont également pu être préparés à partir de la solution mère. Après avoir traité avec succès une quarantaine de disques de vanadium irradiés par des protons, le PSI possède maintenant une quantité unique au monde ( $\approx 20$  MBq) de  $^{32}\text{Si}$ , ce qui permet de fournir des échantillons avec une activité  $^{32}\text{Si}$  élevée. Grâce aux efforts entrepris au PSI, nous sommes sur le point de régler la demi-vie du  $^{32}\text{Si}$  et donc de fournir une nouvelle valeur recommandée avec une faible incertitude ( $< 5\%$ ). Dans le cadre de ce travail, une valeur préliminaire de  $T_{1/2}$  pour le  $^{32}\text{Si}$  de  $125 \pm 5$  ( $1\sigma$ ) ans a été déterminée.

En outre, nous avons étudié le vanadium comme matériau cible. En raison des interactions entre les particules pendant le processus d'irradiation, de nombreux isotopes intéressants, rares et exotiques sont produits (principalement par spallation) comme sous-produits. Leurs applications sont nombreuses mais principalement nécessaires à des fins médicales ( $^{44}\text{Ti}$ ) ou pour la recherche astrophysique ( $^{41}\text{Ca}$  et  $^{26}\text{Al}$ ). Par conséquent, nous présentons ici d'autres données nucléaires, à savoir les sections efficaces de production du  $^{44}\text{Ti}$ , du  $^{41}\text{Ca}$  et du  $^{26}\text{Al}$  pour le vanadium irradié par des protons. Pour ces deux derniers nucléides, les données présentées représentent également la toute première détermination expérimentale de la section efficace pour le vanadium comme cible. Sept disques de vanadium irradiés aux protons de différentes origines ont été utilisés pour ces expériences car des informations détaillées sur les conditions d'irradiation étaient disponibles pour ces échantillons. Dans ce contexte, deux systèmes indépendants de mesure par spectrométrie gamma ont été utilisés pour la détermination de l'activité du  $^{44}\text{Ti}$ , et aucune séparation chimique préalable du  $^{44}\text{Ti}$  de la matrice n'a été nécessaire. Par contre, le  $^{41}\text{Ca}$  et le  $^{26}\text{Al}$  ont été séparés avec succès en utilisant un schéma de séparation chimique liquide sélectif et robuste qui a été développé et appliqué. En conséquence, un rendement de récupération pour chaque isotope de  $>99\%$  a été atteint. L'activité de ces nucléides a ensuite pu être déterminée par spectrométrie de masse par accélérateur (AMS), les solutions ayant été préalablement traitées chimiquement afin d'obtenir des échantillons solides de  $^{41}\text{CaF}_2$  ou de  $^{26}\text{Al}_2\text{O}_3$  reçus.

En définitive, cette thèse fournit des études approfondies qui suggèrent que le vanadium irradié par des protons est considéré comme une source précieuse pour de nombreux radionucléides rares et exotiques. Parmi les plus rares d'entre eux, le  $^{32}\text{Si}$  est particulièrement remarquable, puisque sa séparation et sa purification de la matrice radioactive permettront de redéterminer sa demi-vie, plus de 70 ans après la première découverte de ce nucléide. Parmi les plus rares, la séparation et la purification du  $^{32}\text{Si}$  de la matrice radioactive est particulièrement remarquable, car elle permet de déterminer à nouveau sa demi-vie – plus de 70 ans après sa première découverte. Par conséquent, la collaboration SINCHRON vise à promouvoir le radiosilicium comme futur outil de datation nucléaire. Dans ce contexte, et étant donné la quantité unique de  $^{32}\text{Si}$  dans le monde, une tâche future couvrira également la production d'étalons de référence pour l'AMS afin de permettre la détermination du  $^{32}\text{Si}$  dans les échantillons environnementaux et ainsi pouvoir éventuellement utiliser le  $^{32}\text{Si}$  pour la détermination de l'âge absolu.

### Mots-clés:

$^{32}\text{Si}$  • séparations radiochimiques • chromatographie d'échange d'ions • chromatographie d'extraction • redétermination de la demi-vie • production cross-sections • radionucléides exotiques • production artificielle • spallation

# ■ Zusammenfassung

---

Die radiometrische Datierung ist eine etablierte moderne Technik, die sich als vielseitiges Instrument für absolute Altersbestimmungen erwiesen hat: Als berühmtes Beispiel sei hier die präzise Altersbestimmung des Mannes aus dem Eis (auch bekannt als Ötzi) genannt, die mithilfe der Radiokohlenstoffdatierung (Kohlenstoff-14,  $^{14}\text{C}$ ) durchgeführt wurde. Im Allgemeinen ist bei der radiometrischen Datierung die Halbwertszeit ( $T_{1/2}$ ) ein entscheidender Aspekt, der mit hoher Präzision bekannt sein muss. Interessanterweise, besteht gegenwärtig eine erhebliche Datierungslücke zwischen den Chronologien auf der Grundlage von  $^{210}\text{Pb}$  ( $T_{1/2} \approx 22$  Jahre) und  $^{14}\text{C}$  ( $T_{1/2} \approx 5700$  Jahre). Es fehlt also ein Chronometer für den Zeitrahmen von etwa 100 bis 1000 Jahren. Ein Datierungsinstrument, das diesen Zeitbereich abdeckt, ist jedoch für verschiedene Anwendungen unerlässlich, unter anderem für die Bewertung der anthropogenen Auswirkungen in Bezug auf Klimaschwankungen auf der Erde. Hierbei könnte das kosmogene Nuklid  $^{32}\text{Si}$  diese Datierungslücke möglicherweise schließen. Ein Problem ergibt sich jedoch durch die ungenaue Bestimmung der  $T_{1/2}$  von  $^{32}\text{Si}$ . Die derzeit empfohlenen Werte weisen potenzielle Abweichungen auf, wobei die ermittelten Werte eine breite Streuung mit erheblichen Unsicherheiten aufzeigen. Folglich wird bei einer häufig zitierten Halbwertszeit auf die NuDat3.0-Datenbank verwiesen, die einen gemittelten Wert von  $\approx 153$  Jahren nennt, jedoch verbunden mit einer hohen Unsicherheit. Dies hat wiederum zur Folge, dass dies die Anwendung als Geochronometer verhindert, da keine präzisen relativen Zeitangaben gemacht werden können.

Das Ziel des vom SNF finanzierten Projekts SINCHRON ( $^{32}\text{Si}$ : a new chronometer), und damit auch das Hauptziel dieser Dissertation, ist deshalb die Neubestimmung der  $^{32}\text{Si}$ -Halbwertszeit. Vorangegangene Halbwertszeitbestimmungen waren durch die Verwendung von Proben mit geringen Aktivitäten eingeschränkt, z.B. bedingt durch die Verwendung natürlicher  $^{32}\text{Si}$ -Quellen. Um das Problem der geringen Mengen zu lösen, wurde  $^{32}\text{Si}$  am Paul Scherrer Institut (PSI) künstlich hergestellt. Hierfür wurden metallische Vanadium-Scheiben fast zwei Jahre (zwischen 2011 und 2012) mit 590 MeV-Protonen bestrahlt. Es wurden spezielle Bestrahlungspositionen in der Schweizer Spallations-Neutronenquelle (SINQ) ausgewählt, da diese Bestrahlung Teil des SINQ-Target-Bestrahlungsprogramms (engl. STIP-6-Program) war. Anschließend wurde ein neuartiges nasschemisches Trennsystem entwickelt, das die selektive Abtrennung von  $^{32}\text{Si}$  aus der mit Protonen bestrahlten Vanadium-Matrix ermöglicht. Dabei wurde eine Kombination von Ionenaustauscher-, Chelatbildner- und Extraktions-Chromatographieharzen eingesetzt. Als Ergebnis konnten 20 mL einer hochreinen  $^{32}\text{Si}$ -Lösung hergestellt werden, die die gewünschten Parameter für die Halbwertszeitbestimmung erfüllt.

Im Rahmen dieser Arbeit wurde die Bestimmung der Halbwertszeit über die direkte Methode angewandt, d.h. es ist sowohl die Bestimmung der Anzahl der Atome (N), als auch der Aktivität (A) nötig. Im Rahmen der SINCHRON-Kollaboration wurden mehrere unabhängige Messungen zwischen verschiedenen multinationalen metrologischen Instituten durchgeführt. Basierend auf den unterschiedlichen Anforderungen wurde die  $^{32}\text{Si}$ -Lösung entsprechend hergestellt: (I) die Aktivitätskonzentration der Lösung wurde mit  $>100$  kBq/g bestätigt, (II) das Hexafluorosilikat-Anion ( $\text{SiF}_6^{2-}$ ) ist eine chemisch sehr stabile Si-Spezies, (III) Ultra-Spuren von  $^{32}\text{S}$  wurden erfolgreich entfernt, was insbesondere für ICP-MS-Messungen notwendig war. Ausserdem konnten auch (IV) feste AMS-Proben ( $^{32}\text{SiO}_2$ ,  $\text{K}_2^{32}\text{SiF}_6$ ) aus der Stammlösung hergestellt werden. Nach der erfolgreichen Bearbeitung von rund 40 protonenbestrahlten Vanadiumscheiben verfügt das PSI nun über eine weltweit einmalige Menge ( $\approx 20$  MBq) an  $^{32}\text{Si}$ , die es erlaubt, Proben mit einer hohen  $^{32}\text{Si}$ -Aktivität bereitzustellen. Dank der am PSI unternommenen Anstrengungen stehen wir kurz davor, die Halbwertszeit von  $^{32}\text{Si}$  zu bestimmen und damit einen neuen, empfohlenen Wert mit geringer Unsicherheit ( $<5\%$ ) zu ermitteln. Im Rahmen dieser Arbeit ist zunächst eine vorläufige  $T_{1/2}$  für  $^{32}\text{Si}$  von  $125 \pm 5$  ( $1\sigma$ ) Jahren bestimmt worden.

Zusätzlich haben wir auch Vanadium als Target-(dt. Ziel-) Material untersucht. Aufgrund der Teilchenwechselwirkungen während des Bestrahlungsprozesses entstehen als Nebenprodukte (überwiegend durch Spallation) viele weitere interessante, seltene und exotische Isotope. Ihre Anwendungen sind zahlreich, sie werden aber hauptsächlich für medizinische Zwecke ( $^{44}\text{Ti}$ ) oder für die astrophysikalische Forschung ( $^{41}\text{Ca}$  und  $^{26}\text{Al}$ ) benötigt. Daher präsentieren wir hier weitere nukleare Daten, nämlich die Produktionsquerschnitte von  $^{44}\text{Ti}$ ,  $^{41}\text{Ca}$  und  $^{26}\text{Al}$  für mit Protonen bestrahltes Vanadium. Für die beiden letztgenannten Nuklide stellen die vorgestellten Daten auch die allererste experimentelle Bestimmung des Wirkungsquerschnitts in Hinblick auf Vanadium als Target dar.

Für diese Experimente wurden sieben mit Protonen bestrahlte Vanadiumscheiben unterschiedlicher Herkunft verwendet, da für diese Proben detaillierte Angaben zu den Bestrahlungsbedingungen vorlagen. In diesem Zusammenhang wurden für die Aktivitätsbestimmung von  $^{44}\text{Ti}$  zwei unabhängige gammaspektrometrische Messsysteme verwendet, wobei keine vorherige chemische Abtrennung von  $^{44}\text{Ti}$  aus der Matrix erforderlich war. Im Gegensatz dazu wurden  $^{41}\text{Ca}$  und  $^{26}\text{Al}$  erfolgreich abgetrennt, indem ein selektives und robustes chromatographisches nasschemisches Trennverfahren entwickelt und angewendet wurde. Als Ergebnis wurde eine Ausbeute von  $>99\%$  für jedes Isotop erreicht. Anschliessend konnte die Aktivität dieser Nuklide mittels Beschleuniger-Massenspektrometrie (AMS) bestimmt werden, wobei die Lösungen zuvor chemisch behandelt wurden, um feste  $^{41}\text{CaF}_2$ - bzw.  $^{26}\text{Al}_2\text{O}_3$ -Proben zu erhalten.

Letztlich liefert diese Arbeit umfangreiche Untersuchungen, die zeigen, dass protonenbestrahltes Vanadium als wertvolle Quelle für zahlreiche, seltene und exotische Radionuklide gilt. Unter den seltenen Radionukliden ist die Abtrennung und Reinigung von  $^{32}\text{Si}$  aus der radioaktiven Matrix besonders erwähnenswert, da dies die Bestimmung seiner Halbwertszeit ermöglicht - über 70 Jahre nach seiner ersten Entdeckung. Damit will die SINCHRON-Kollaboration das Radiosilizium als künftiges Instrument für die nukleare Datierung fördern. In diesem Zusammenhang und in Anbetracht der einzigartigen Menge an  $^{32}\text{Si}$  in der Welt wird eine künftige Aufgabe auch darin bestehen, Referenzstandards für AMS herzustellen, um die Bestimmung von  $^{32}\text{Si}$  in Umweltproben zu ermöglichen und so schließlich  $^{32}\text{Si}$  für absolute Altersbestimmungen verwenden zu können.

Abschliessend wurden mit dieser Dissertation umfangreiche Studien vorgelegt, die zeigen, dass mit Protonen bestrahltes Vanadium eine wertvolle Quelle für zahlreiche seltene und exotische Radionuklide darstellt. Unter den Seltenen von diesen ist  $^{32}\text{Si}$  besonders hervorzuheben, da die Abtrennung und Aufreinigung aus der radioaktiven Matrix die Neubestimmung der Halbwertszeit ermöglichen wird; mehr als 70 Jahre nach der ersten Entdeckung des Nuklids. Mit dieser Neubestimmung der Halbwertszeit von  $^{32}\text{Si}$  will die SINCHRON-Kollaboration Radiosilizium als künftiges Instrument für die nukleare Datierung etablieren. In diesem Zusammenhang und in Anbetracht der weltweit einzigartigen Menge an  $^{32}\text{Si}$  wird eine zukünftige Aufgabe auch die Herstellung von Referenzstandards für AMS umfassen, um die Bestimmung von  $^{32}\text{Si}$  in Umweltproben zu ermöglichen und so schließlich  $^{32}\text{Si}$  zur absoluten Altersbestimmung verwenden zu können.

### Schlüsselwörter:

$^{32}\text{Si}$  • Radiochemische Trennungen • Ionenaustauschchromatographie • Extraktions-Chromatographie • Neubestimmung der Halbwertszeit • Nukleare Produktionsquerschnitte • Exotische Radionuklide • Künstliche Herstellung • Spallation





# Table of Contents

## Acknowledgement

Abstract	I
Résumé	III
Zusammenfassung	V
List of Figures	XI
List of Tables	XIX
List of Abbreviations	XXVI

<b>1 Introduction</b>	<b>1</b>
1.1 Environmental Research:	
The need for a new, suitable geochronometer . . . . .	1
1.1.1 Argon-39 ( $^{39}\text{Ar}$ ) . . . . .	4
1.1.2 Silicon-32 ( $^{32}\text{Si}$ ) . . . . .	6
1.1.3 SINCHRON: $^{32}\text{Si}$ - a new chronometer . . . . .	8
1.2 Target material and isotope production:	
The artificial source of $^{32}\text{Si}$ . . . . .	9
1.2.1 Isolation of $^{32}\text{Si}$ from irradiated materials . . . . .	12
1.2.2 Determination of cross-sections:	
The interest in exotic nuclides such as $^{44}\text{Ti}$ , $^{41}\text{Ca}$ and $^{26}\text{Al}$ . . . . .	13
1.3 Goal of the thesis . . . . .	15
<b>2 Theoretical Background</b>	<b>16</b>
2.1 Chemical separations . . . . .	16
2.1.1 Separations using ion-exchange chromatography . . . . .	16
2.1.1.1 Specialized ion-exchange resins: Chelating resins . . . . .	19
2.1.2 Separations using extraction chromatography . . . . .	20
2.2 General theory of column chromatography . . . . .	22
2.2.1 Retention . . . . .	22
2.2.2 Selectivity . . . . .	23
2.2.3 Resolution . . . . .	23
2.2.4 Capacity . . . . .	23
2.2.5 Physical stability . . . . .	24
2.2.6 Chemical stability . . . . .	24
2.3 Measurement methods . . . . .	26
2.3.1 Independent measurements . . . . .	26
2.3.1.1 The direct method . . . . .	27
2.3.1.2 The decay method . . . . .	27

2.4	Instrumental analysis . . . . .	29
2.4.1	Inductively coupled plasma optical emission spectroscopy . . . . .	29
2.4.2	Gamma-ray spectrometry . . . . .	31
2.4.3	Liquid scintillation counting . . . . .	32
2.4.3.1	Chemical quenching . . . . .	33
2.4.3.2	Color quenching . . . . .	33
2.4.3.3	CIEMAT/NIST efficiency tracing . . . . .	34
2.4.4	Validation . . . . .	35
2.4.4.1	Limit of Blank (LoB), Limit of Detection (LoD), and Limit of Quantification (LoQ) . . . . .	35
2.4.4.2	Robustness . . . . .	35
2.4.4.3	Selectivity . . . . .	36
2.4.4.4	Assessment of uncertainties . . . . .	36
2.5	Nuclear spallation . . . . .	39
2.5.1	Nuclear reaction cross-section(s) . . . . .	40
2.5.2	Determination of the activity in irradiated specimen . . . . .	41
2.5.3	Simplification of the calculation of reaction cross-section(s) . . . . .	42
2.5.3.1	Cross-Sections: $^{nat}\text{V}(\text{p}, \text{x})^{44}\text{Ti}$ , $^{nat}\text{V}(\text{p}, \text{x})^{41}\text{Ca}$ , and $^{nat}\text{V}(\text{p}, \text{x})^{26}\text{Al}$ . . . . .	42
2.5.3.2	Theoretical cross-section calculations . . . . .	43
<b>3</b>	<b>Experimental Studies</b>	<b>44</b>
3.1	Instrumental Analysis . . . . .	44
3.1.1	Gamma-ray spectrometry ( $\gamma$ -spectrometry) measurements . . . . .	44
3.1.2	Liquid scintillation counting (LSC) measurements . . . . .	44
3.1.3	Hyphenated inductively coupled plasma (ICP-) techniques . . . . .	45
3.1.3.1	Optical emission spectrometry (OES) . . . . .	45
3.1.3.2	Mass spectrometry (MS) . . . . .	46
3.2	Materials and experimental methods . . . . .	47
3.2.1	Part 1 of 3: Characterisation of the target material . . . . .	47
3.2.1.1	Inactive V discs and the preparation for ICP-MS measurements . . . . .	47
3.2.1.2	Determination of aluminium, iron, and trace elements . . . . .	49
3.2.1.3	Determination of the $^{nat}\text{Si}$ content with ICP-MS . . . . .	49
3.2.1.4	Determination of the $^{nat}\text{Si}$ content with ICP-OES . . . . .	50
3.2.2	Part 2 of 3: Development of radiochemical separation procedures . . . . .	51
3.2.2.1	Preparation for distillation experiments . . . . .	51
3.2.2.2	Preparation for column chromatography experiments . . . . .	52
3.2.2.3	Cation-exchange chromatography: Dowex <sup>®</sup> 50WX8-200 . . . . .	52
3.2.2.4	Purification of the $^{32}\text{Si}$ fractions: Removal of trace impurities . . . . .	53
3.2.2.5	LN <sup>®</sup> resin series: Purification step I . . . . .	54
3.2.2.6	Monophos <sup>®</sup> resin: Purification step II . . . . .	54
3.2.2.7	Evaporation to dryness: Removal of $^3\text{H}$ and $^{39,42}\text{Ar}$ . . . . .	55

3.2.2.8	Anion-exchange chromatography: Dowex® 1X8 200-400 . . . . .	56
3.2.2.8.(I)	K <sub>d</sub> studies . . . . .	56
3.2.2.8.(II)	Ultra-trace removal of sulfur . . . . .	56
3.2.2.8.(III)	Characterisation of the final product: <sup>32</sup> Si in 0.5M HCl .	57
3.2.2.9	Sample preparation for AMS: <sup>32</sup> SiO <sub>2</sub> and K <sub>2</sub> <sup>32</sup> SiF <sub>6</sub> . . . . .	58
3.2.2.9.(I)	<sup>32</sup> SiO <sub>2</sub> samples . . . . .	59
3.2.2.9.(II)	K <sub>2</sub> <sup>32</sup> SiF <sub>6</sub> samples . . . . .	60
3.2.3	Part 3 of 3: Preparation for determining cross-sections . . . . .	62
3.2.3.1	Irradiated vanadium discs and their characterisation . . . . .	62
3.2.3.2	Determination of the <sup>44</sup> Ti activity with γ-spectrometry . . . . .	63
3.2.3.2.(I)	Preparation for LEGe measurements: 2 mL Reference .	64
3.2.3.2.(II)	Preparation for HPGe measurements: 5 mL Reference .	65
3.2.3.3	Development of a separation procedure for <sup>41</sup> Ca and <sup>26</sup> Al . . . . .	66
3.2.3.3.(I)	Change of matrix and separation of carrier-added <sup>32</sup> Si .	66
3.2.3.3.(II)	<sup>41</sup> Ca separation using DGA (normal) . . . . .	67
3.2.3.3.(III)	<sup>26</sup> Al separation using Dowex® 50WX8-200 . . . . .	67
3.2.3.4	Sample preparation for AMS: <sup>41</sup> CaF <sub>2</sub> and <sup>26</sup> Al <sub>2</sub> O <sub>3</sub> . . . . .	68
3.2.3.4.(I)	Preparation of <sup>41</sup> CaF <sub>2</sub> AMS-samples . . . . .	68
3.2.3.4.(II)	Preparation of <sup>26</sup> Al <sub>2</sub> O <sub>3</sub> AMS-samples . . . . .	68
<b>4</b>	<b>Results and Discussion</b>	<b>69</b>
<b>Part 1 of 4</b>		<b>69</b>
4.1	Characterisation of the target material . . . . .	69
4.1.1	Task I: Determination of impurities . . . . .	69
4.1.2	Task II: Determination of the Si content . . . . .	73
<b>Part 2 of 4</b>		<b>76</b>
4.2	Radiochemical separation: V targets from STIP-6 . . . . .	76
4.2.1	Silicon tetrafluoride: Distillation of the volatile Si species . . . . .	76
4.2.2	Column Chromatography: Exchange, extraction, and chelating . . . . .	78
4.2.2.1	Separation from the bulk vanadium matrix: Cation-exchange chromatography: Dowex® 50WX8-200 . . . . .	78
4.2.2.2	Purification of the <sup>32</sup> Si-fractions: LN® resin series . . . . .	86
4.2.2.3	Purification of the <sup>32</sup> Si-fractions: Monophos® resin . . . . .	88
4.2.2.4	Removal of volatile species: Evaporation to dryness . . . . .	89
4.2.2.4.(I)	L-AscA as a reducing agent . . . . .	89
4.2.2.4.(II)	Hydrazine as a reducing agent . . . . .	90
4.2.2.5	Preparation of the final <sup>32</sup> Si solutions: Anion-exchange chromatography: Dowex® 1X8 . . . . .	92
4.2.2.5.(I)	“Pre-Concentration” of several individual <sup>32</sup> Si fractions . .	92

4.2.2.5.(II) Removal of the isobaric interference $^{32}\text{S}$ . . . . .	93
4.2.2.6 Characterisation of the final product: $^{32}\text{Si}$ in 0.5M HCl . . . . .	97
4.2.3 Summary: Radiochemical separation of $^{32}\text{Si}$ . . . . .	100
<b>Part 3 of 4</b> . . . . .	103
4.3 Determination of the cross-section: $^{\text{nat}}\text{V}(\text{p}, \text{x})$ . . . . .	103
4.3.1 $^{\text{nat}}\text{V}(\text{p}, \text{x})^{44}\text{Ti}$ . . . . .	103
4.3.2 $^{\text{nat}}\text{V}(\text{p}, \text{x})^{41}\text{Ca}$ and $^{\text{nat}}\text{V}(\text{p}, \text{x})^{26}\text{Al}$ : Radiochemical separation procedures . . .	106
4.3.2.1 Change of matrix and separation of carrier-added $^{32}\text{Si}$ from $^{41}\text{Ca}$ , $^{26}\text{Al}$ , and $^{\text{nat}}\text{V}$ . . . . .	106
4.3.2.2 Calcium-41 separation with DGA (normal) . . . . .	107
4.3.2.3 Aluminium-26 separation using Dowex <sup>®</sup> 50WX8-200 . . . . .	108
4.3.3 Summary: Radiochemical separation of carrier-added $^{32}\text{Si}$ , $^{41}\text{Ca}$ , and $^{26}\text{Al}$ . . .	109
4.3.4 Sample preparation for AMS: $^{41}\text{CaF}_2$ and $^{26}\text{Al}_2\text{O}_3$ . . . . .	110
4.3.5 Determination of the excitation function: $^{\text{nat}}\text{V}(\text{p}, \text{x})^{41}\text{Ca}$ and $^{\text{nat}}\text{V}(\text{p}, \text{x})^{26}\text{Al}$ .	111
<b>Part 4 of 4</b> . . . . .	113
4.4 Half-Life determination of $^{32}\text{Si}$ . . . . .	113
4.4.1 Determination of the activity (concentration): Standardization using LSC . .	113
4.4.2 Determination of the number of atoms: ICP-MS and AMS measurements . .	117
4.4.3 Combining the number of atoms and the activity (concentration) . . . . .	119
4.4.4 Following the decay of $^{32}\text{Si}$ . . . . .	120
<b>5 Conclusion and Outlook</b>	<b>122</b>
<b>6 Appendices</b>	<b>126</b>
6.1 Liquid scintillation counting (LSC) . . . . .	126
6.2 Uncertainties . . . . .	129
6.3 Silicon distillation apparatus . . . . .	133
<b>7 Bibliography</b>	<b>135</b>
<b>List of Publications</b>	<b>147</b>
<b>Curriculum Vitae</b>	<b>148</b>



# List of Figures

Fig. 1.1	Visible dating gap (red bars) between 100 to 1'000 years, whereby well-established chronometers are indicated by green bars. The bars represent the time range over which the nuclides can be used, as of their half-lives. Taken from Veicht et al. [22]. . . . .	2
Fig. 1.2	The illustration is inspired by Orrell et al. [61] and shows the natural production, the involved transport mechanisms, and accumulation of $^{32}\text{Si}$ . Apart from the enrichment in streams, ponds, or the sea, $^{32}\text{Si}$ is eventually accumulated in (1) sediments and near-surface silicon deposits or in (2) where it is transported by biological, $\text{SiO}_2$ -bearing organisms (Diatoms and Radiolaria), and are finally solidified in the sediments. . . .	6
Fig. 1.3	Compilation of $^{32}\text{Si}$ half-life determinations. Three measurements are excluded (marked with red) and haven't been used in the averaging procedure since they rely on $^{32}\text{Si}$ accumulation rates (ice and sediments), which are not known well [73]. . . . .	7
Fig. 1.4	Sequence of the different steps, starting from the irradiation, moving to the "Cool Down"-Phase, and the ultimate start of the SINCHRON-project, which began with $\gamma$ -spectroscopic measurements of the vanadium discs. . . . .	10
Fig. 1.5	Detailed decay schemes [94] of the relatively long-lived parent nuclide $^{44}\text{Ti}$ and its daughter $^{44g}\text{Sc}$ . . . . .	13
Fig. 1.6	$^{45}\text{Sc}(\text{p},2\text{n})^{44}\text{Ti}$ production path. . . . .	14
Fig. 2.1	The matrix of synthetic ion-exchange resin is composed of (b) polystyrene chains formed from (a) styrene. The matrix (c) of the resin is composed of polystyrene chains cross-linked with divinylbenzene. Adding functional groups to this matrix. The structure of a strong cation-exchange resin containing sulfonic acid functional groups is depicted in panel (d). Picture modified after Schönbachler & Fehr [121], and text adopted accordingly. . . . .	17
Fig. 2.2	Active component of $\text{LN}^{\text{®}}$ , namely the Di(2-ethylhexyl)orthophosphoric acid, and the active component of the DGA resin extractant with $\text{R} = \text{C}_8 ((\text{CH}_2)_7\text{CH}_3)$ . . . . .	21
Fig. 2.3	Part of the "Karlsruhe Nuclide Chart" (10 <sup>th</sup> edition; [138]), in which the isobar ( $A = \text{const.} = 32$ ) is highlighted; $^{32}\text{Si}$ is of special interest. . . .	26
Fig. 2.4	When an electron returns from a higher energy level (e.g., Energy Level	

	3) to a lower energy level (e.g., Energy Level 1), light of a specific wavelength is emitted. The wavelength of the emitted light determines the type of atom or ion (i.e., which element it is) and is related to the energy levels in which the electron is moving (modified after [149]). . . .	29
Fig. 2.5	Schematic of the ICP-OES principle as applied to an Agilent 5110 (modified after [149]). . . . .	30
Fig. 2.6	Insulator: At room temperature, the valence band is separated from the conduction band by over $\approx 10$ eV. Thermal excitation cannot promote electrons from the valence band up to the conduction band. Metal: The valence band and the conduction band overlap, so that free electrons are always present and can easily move from atom to atom, creating a current. . . . .	31
Fig. 2.7	Schematic principle of a photomultiplier tube (adopted after [117]). . . .	32
Fig. 2.8	Scheme of a nuclear reaction cascade (intra-nuclear cascade) in a target, induced by a high-energetic proton (1 GeV). Also shown the subsequent reactions, related to the inter-nuclear cascade. Figure was adopted from [160] and modified accordingly. . . . .	39
Fig. 3.1	Schematic view of the experimental setup used for the evaporation of L-AscA samples. . . . .	55
Fig. 3.2	Overview of the irradiation locations and conditions. Also, initial seven irradiated vanadium discs are shown, with their different appearance, which is likely caused by partial oxidation. Photos are taken from [175], [176], and [177], respectively. . . . .	62
Fig. 3.3	Overview of the sample preparation and the measurements by means of $\gamma$ -spectrometry. All involved steps were mass-controlled using a high-precision scale (XS225 DualRange, Mettler Toledo, Switzerland). . . .	64
Fig. 4.1	Results for the $^{27}\text{Al}$ content from the ICP-MS measurements. A comparison is shown for the different samples (1, 3, 5) and at different dilutions; x 20 and x 200, respectively. . . . .	70
Fig. 4.2	Results for the $^{56}\text{Fe}$ content from the ICP-MS measurements. A comparison is shown for the different samples (1, 3, 5) and at different dilutions; x 20 and x 200, respectively. . . . .	70
Fig. 4.3	Relative recovery yields for the 10 ppb $^{89}\text{Y}$ from the samples (1, 3, 5). The average is indicated by the solid line, uncertainties by the grey dashed line ( $\pm 5\%$ ). . . . .	71

Fig. 4.4	Semi-quantitative determination of the elements detected in the vanadium disc, using the TQ-O. The measurements are reported as an average for samples 1, 3, and 5. Note that the Si-content was already added, too, but will be discussed in detail in the next section. . . . .	72
Fig. 4.5	Results of the determination of the silicon content in the vanadium discs without Helium KED mode. The determined results are reported as the average of the samples 1, 3, and 5. . . . .	74
Fig. 4.6	Results of the determination of the silicon content in the vanadium discs with Helium KED mode. The determined results are reported as the average of the samples 1, 3, and 5. . . . .	74
Fig. 4.7	(a) Silicon yield (25 ppm series) determined in a series of distillation experiments. The yields from the 1 <sup>st</sup> run have been usually lower than from the 2 <sup>nd</sup> run, indicating a built-up of silicon in the system. (b) Generally, with a mean yield between 19 to 25%, the recovery rate was considered too low. . . . .	77
Fig. 4.8	(a) Silicon yield (50 ppm series) determined in a series of distillation experiments. Here, a slight trend is visible, also indicating a built-up of silicon, and generally, the apparent recovery rate from the 1 <sup>st</sup> run is also lower than for the 2 <sup>nd</sup> run. (b) Again, the recovery rate was considered too low, with a mean yield between 19 to 23%. Moreover, an apparent concentration dependence questioned the use with solutions, as no silicon carrier was usually added. . . . .	77
Fig. 4.9	Samples from the development phase were prepared on January 28, 2020, and the picture was taken on March 23, 2022. While the green color occurs usually quite rapidly (within a week) and indicates a mixture of $V^{+IV}$ and $V^{+V}$ , the solutions treated with hydrazine apparently remain stable for even time frames of >2 years, since they maintain their intense, blue color, which is in aqueous solution typical for $V^{+IV}$ . . . . .	80
Fig. 4.10	Gamma spectrum (recorded for 4.5h) confirms the typical impurities after the first separation step. However, using cation-exchange chromatography, vanadium can be quantitatively separated, leading only to trace impurities of other radionuclides which are summarized by Table 4.8. . . . .	80
Fig. 4.11	Calcium intensities as a function of volume during the first separation step. The «dash-dot»-line represents the averaged intensities of the three blanks, including a confidence band with $k=3$ ( $3\sigma$ ): $65 \pm 24$ (a.u.). . . .	82

Fig. 4.12	Nickel intensities as a function of volume during the first separation step. The «dash-dot»-line represents the averaged intensities of the three blanks, including a confidence band with $k=3$ ( $3\sigma$ ): $12 \pm 5$ (a.u.). . . . .	83
Fig. 4.13	Iron intensities as a function of volume during the first separation step. The «dash-dot»-line represents the averaged intensities of the three blanks, including a confidence band with $k=3$ ( $3\sigma$ ): $60 \pm 52$ (a.u.). . . . .	83
Fig. 4.14	Vanadium intensities as a function of volume during the first separation step. The «dash-dot»-line represents the averaged intensities of the three blanks, including a confidence band with $k=3$ ( $3\sigma$ ): $57 \pm 12$ (a.u.). . . . .	84
Fig. 4.15	Example of silicon's elution profile during the separation with the Dowex <sup>®</sup> 50WX8-200 resin (220 mm bed height, $\varnothing = 10$ mm, PMMA column). . . . .	84
Fig. 4.16	(a) Example of the bulk separation, allowing to separate silicon from the majority of the target material. Here, $V^{+IV}$ is visibly retained on the cation-exchange resin. Besides, also other cations (e.g., impurities, spallation-products) are retained on the strongly acidic cation-exchange resin, which is expected due to high (typically $> 10^2$ ) distribution coefficients. At the end of this procedure, a colorless eluate is obtained that contains silicon. (b) After the separation of Si, all remaining cations (except Sc) are eluted using 3M $HNO_3$ , while the collected 50 mL fraction is stored until further use. . . . .	85
Fig. 4.17	Silicon's elution profile during the separation with the LN <sup>®</sup> resin (35 mm bed height, $\varnothing = 9$ mm, ISOLUTE PE column). . . . .	86
Fig. 4.18	Example of $\gamma$ -ray spectra ( $\approx 1$ hr) of a $^{32}Si$ fraction after processing with Dowex <sup>®</sup> 50WX8-200 resin (orange) and the subsequent purification using the LN <sup>®</sup> resin (gray). Contaminants which were to be removed are highlighted in red. . . . .	87
Fig. 4.19	Example of $\gamma$ -ray spectra ( $\approx 1$ hr) of a $^{32}Si$ fraction after processing through Dowex <sup>®</sup> 50WX8-200 resin (orange) and the subsequent purification using the LN <sup>®</sup> resin (gray). Contaminants which were to be removed are highlighted in red. . . . .	87
Fig. 4.20	Silicon's elution profile during the separation with the Monophos <sup>®</sup> resin (30 mm bed height, $\varnothing = 9$ mm, ISOLUTE PE column). . . . .	88
Fig. 4.21	Example of $\gamma$ -ray spectra ( $\approx 1$ hr) of a $^{32}Si$ fraction after purification through LN <sup>®</sup> (grey) and the subsequent purification using the Monophos <sup>®</sup> resin (blue). Nuclide of interest is highlighted in red. . . . .	89

Fig. 4.22	( <b>Left</b> ) Determined activity of tritium using LSC as a function of repeated evaporations (Fraction No.). The values are reported as sum (in kBq) for each individual recovered fraction. Initially, $\approx 800$ MBq $^3\text{H}$ were present in a single $^{32}\text{Si}$ fraction (obtained from processing one irradiated V-Disc). ( <b>Right</b> ) Residue in the PTFE-one-neck flask, after a typical evaporation step using the RotaVap. The residue was somewhat tacky and could never be evaporated to complete dryness. . . . .	90
Fig. 4.23	Spectral comparison between an initial solution $^{32}\text{Si}$ solution (Sample 5; before evaporation), the actual sample (1:100 diluted), and a blank (Sample 6; cocktail). Spectra were recorded using a Tri-Carb <sup>®</sup> 2250CA (PSI) and analyzed by Dr Nataša Lalović (former postdoctoral research at PTB). . . . .	91
Fig. 4.24	Detail of the spectral comparison between an initial solution $^{32}\text{Si}$ solution (Sample 5; before evaporation), the actual sample (1:100 diluted), and a blank (Sample 6; scintillation cocktail). Spectra were recorded using a Tri-Carb <sup>®</sup> 2250CA (PSI) and analyzed by Dr Nataša Lalović (former postdoctoral research at PTB). . . . .	91
Fig. 4.25	( <b>a</b> ) Distribution coefficient as a function of HF concentration for silicon, and ( <b>b</b> ) distribution coefficient as a function of HCl concentration. The red ribbon highlights the chosen experimental conditions. . . . .	93
Fig. 4.26	( <b>a</b> ) Distribution coefficient as a function of HF concentration for titanium, and ( <b>b</b> ) distribution coefficient as a function of HCl concentration. The red ribbon highlights the chosen experimental conditions. . . . .	93
Fig. 4.27	( <b>a</b> ) Exemplary elution profile to study the behavior of S, V, and Si, respectively, under varying HCl concentrations. Sulfur, together with silicon, is retained by the anion-exchange resin, while vanadium is partially retained. ( <b>b</b> ) Exemplary elution profile to highlight the quantitative removal of sulfur. Silicon was in none of the sulfur samples detected, and thus the quantitative recovery ( $98\text{-}100\% \pm 3\%$ ) of Si was constantly observed in the final fraction. . . . .	94
Fig. 4.28	( <b>a</b> ) Elution behavior of calcium on the anion-exchange resin during the “Load” ( $= 0.1\text{M HF}$ ), shown for a small-scale experiment, mimicking the load of e.g., five $^{32}\text{Si}$ fractions. ( <b>b</b> ) Monitoring the sum of the calcium concentration, reaching in total about 90% recovery rate. . . . .	95
Fig. 4.29	( <b>a</b> ) Screening for calcium in the three sulfur wash fractions, and in the final $^{32}\text{Si}$ fraction. ( <b>b</b> ) After another 125 mL of solution, calcium was	

	quantitatively recovered, reaching a total of $503 \text{ } \mu\text{g} \pm 25 \text{ } \mu\text{g}$ . . . . .	96
Fig. 4.30	Spectral comparison of 95 h $\gamma$ -ray measurements, obtained using an HPGe detector. Both spectra show only the presence of typical background nuclides. As an example, some $\gamma$ -emissions from $^{214}\text{Pb}$ , $^{214}\text{Bi}$ , and $^{40}\text{K}$ are shown, including the “511”-keV line. . . . .	97
Fig. 4.31	Comparison of two LSC spectra, immediately after the separation (After Dowex <sup>®</sup> 1X8 separation) and 92 days later, to allow in-growth of the daughter, $^{32}\text{P}$ ( $T_{1/2} = 14.268 \text{ d}$ ). . . . .	98
Fig. 4.32	Example of $A(^{32}\text{Si}) = 1 \text{ kBq}$ , which shows the activity increase after separation due to the in-growth of the daughter nuclide. Ideally, $A(^{32}\text{Si}) = A(^{32}\text{P})$ is reached after $\approx 172$ days. . . . .	99
Fig. 4.33	Overview of the relative weight losses of the $^{32}\text{Si}$ master solution, traced for a period of around five months. . . . .	100
Fig. 4.34	Stepwise separation of nca $^{32}\text{Si}$ from proton-irradiated vanadium matrix. The “SINCHRON-Separation” scheme has been carefully developed to provide a robust and reliable scheme that allowed to prepare $>40$ purified $^{32}\text{Si}$ fractions. As a result, the Laboratory of Radiochemistry (LRC) at PSI has a unique worldwide amount of $A(^{32}\text{Si}) 22 \pm 2 \text{ MBq}$ at its disposal. . . . .	102
Fig. 4.35	Experimental excitation function to produce $^{44}\text{Ti}$ from proton-induced reactions. A comparison between the two data sets is shown. . . . .	104
Fig. 4.36	Further comparison of the excitation function for the $^{44}\text{Ti}$ production with additional data in the low-energy range (data taken from [197]) as well as theoretical calculations. . . . .	104
Fig. 4.37	Example of an elution profile: during the Load, Si is unretained and thus gathered within 230 mL. Afterwards, Ca, Al, and V are eluted from the column with 50 mL (230 mL to 280 mL) 3M $\text{HNO}_3$ . . . . .	106
Fig. 4.38	(a) Example of an elution profile: during the Load, Ca is retained, while Al and V are unretained. Eventually, Ca is eluted with 30 mL 3M $\text{HCl}$ (70 mL to 100 mL)(b) Confirmation of the yield of Ca recovery which was on average $>99\%$ . . . . .	107
Fig. 4.39	(a) Example of an elution profile, showing the successful separation of Al from the bulk vanadium matrix using gradual elution and (b) yield of Al recovery was on average $>99\%$ . . . . .	108
Fig. 4.40	Stepwise separation of carrier-added $^{32}\text{Si}$ , $^{41}\text{Ca}$ , and $^{26}\text{Al}$ from proton-	

irradiated vanadium discs. The “DOGADO-Separation” scheme has been carefully developed to provide a quantitative recovery, with virtually no losses during the separation. Consequently, we obtained pure samples, which were further chemically processed, to obtain solid AMS samples. . . . 109

Fig. 4.41	(a) Comparison between the calculated and experimentally obtained excitation function for the $^{\text{nat}}\text{V}(\text{p}, \text{x})^{41}\text{Ca}$ reaction and (b) detail of the low-energy region. . . . .	111
Fig. 4.42	(a) Comparison between the calculated and experimentally obtained excitation function for the $^{\text{nat}}\text{V}(\text{p}, \text{x})^{26}\text{Al}$ reaction and (b) detail of the low-energy region. . . . .	111
Fig. 4.43	(a) Tracing the activity concentration as a function of time, for different sample matrices to study their long-term behavior. (b) Detail of the first ten days of measurement. . . . .	114
Fig. 4.44	(a) Overview of the time-dependent change of the quench indicating parameter (tSIE), and (b) highlighting the first ten days of measurement, which do not show a significant change in the tSIE and confirm the sample’s stability. . . . .	115
Fig. 4.45	Overview of the arithmetic mean for the different matrices. The mean is based on fifteen independent measurements, whereby the results for $\text{H}_2\text{O}$ and 0.5M HCl are emphasized. . . . .	116
Fig. 4.46	Qualitative example of an ICP-MS measurement with the Element XR <sup>TM</sup> at SL. Two peaks, showing at the lower mass (31.9716) the $^{32}\text{S}$ signal and at the higher mass (31.9737) the $^{32}\text{Si}$ signal, respectively. The integration width (=20%) is highlighted in blue. Please note, the graph is a 1:1 reproduction of the software’s output. . . . .	117
Fig. 4.47	Example of the spatial distribution between $^{32}\text{S}$ and $^{32}\text{Si}$ , showing the successful separation of the two isotopes (taken from [213]). . . . .	118
Fig. 4.48	Results from AMS-S1 (14.40 kBq $^{32}\text{Si}$ solution). The figure was kindly provided for use by M. Schlomberg (ETHZ, LIP). . . . .	118
Fig. 4.49	Plastic scintillator vials illuminated by UV light to stimulate the emission of scintillation light (taken from [214]). . . . .	120
Fig. 4.50	Plastic scintillator geometries to be used for the decay measurements performed at IRA. The $^{32}\text{Si}$ deposition is indicated. The layout and the measures were kindly provided by Dr Teresa Durán (IRA, Switzerland). . . . .	121

Fig. 5.1	Method of distributing aliquots of the "Master Solution" for independent measurements, while PSI ensures careful storage (tracing temperature and tracing mass of the solution). . . . .	123
Fig. 5.2	Compilation of $^{32}\text{Si}$ half-life determinations focused on the direct methods (format date: DD-MM-'YY). Two references for the mean are shown (from Fifield et al. [12], and from the NuDat 3.0 database, which is based on the careful compilation provided by Quellet & Singh [73]). . .	124
Fig. 6.1	Device-specific (a) $^{14}\text{C}$ and (b) $^3\text{H}$ efficiency determinations, used for monitoring the performance metrics of the Tri-Carb <sup>®</sup> 2250CA. . . . .	126
Fig. 6.2	Sequence of the in-house determination of the $^{32}\text{Si}$ activity concentration, using the data thankfully provided by Dr Youcef Nedjadi (Scientist, IRA). . . . .	127
Fig. 6.3	Device-specific $^3\text{H}$ efficiency curve for the Tri-Carb <sup>®</sup> 2250CA. . . . .	128
Fig. 6.4	Technical drawing of MODUS (Mini silicOn Distillation apparatus), thankfully provided by Dominik Herrmann (Technical Assistant, LRC). . . . .	133
Fig. 6.5	Technical drawing of the MODUS' closure, thankfully provided by Dominik Herrmann (Technical Assistant, LRC). . . . .	134





# List of Tables

Table 1.1	Overview of commonly used elements and element pairs to determine absolute ages. . . . .	1
Table 1.2	Overview of suitable nuclides, based on their matching half-lives (range: 100 to 500 y), arranged in order of increasing half-lives. However, none of them are naturally occurring, thus must be produced exclusively artificially. Data taken from [14]. . . . .	2
Table 1.3	Summary of the primary, natural production paths, and their global atmospheric average intake. . . . .	3
Table 1.4	Overview of important contributions regarding Argon Trap Trace Analysis. . . . .	5
Table 1.5	Overview of two examples where carefully performed redeterminations yielded quite different values for the half-life. . . . .	5
Table 1.6	$^{32}\text{Si}$ activity that was involved in the experiments, which can be summed up to $\approx 3.4$ kBq. . . . .	7
Table 1.7	Summary of the foreseen measurement methods and the involved institutions to determine the $^{32}\text{Si}$ 's half-life. . . . .	8
Table 1.8	Calculated activities of the main reaction products of SINQ Target 8, Rod 2. The initial calculations were based on 384 g metallic vanadium, whereas this overview has been adjusted to a processed amount of 63 g (= 150 V-discs). . . . .	11
Table 2.1	Basic classification of ion-exchangers. . . . .	17
Table 2.2	Values of apparent dissociation constants of characteristic ionogenic groups of ion-exchangers ( $pK = -\log_{10}(K)$ ), and are R being the ion-exchanger's polymer backbone (= Resin). . . . .	18
Table 2.3	Typical (major) uncertainties for the experimental procedures. Note that in some cases, the uncertainty is much larger e.g., low activities ( $\gamma$ -spectrometry) or low analyte concentrations (ICP-MS, and -OES). The typical uncertainty are the values assumed for in-house analyses only and do not account for measurements performed elsewhere (e.g., LSC at PTB or IRA). . . . .	38
Table 3.1	Commonly used wavelengths for the analysis of the elements using ICP-OES. Care was taken to avoid interferences during the measurements,	

	stemming from similar emission lines. . . . .	46
Table 3.2	Overview of the discs used for the ICP-MS analyses. . . . .	48
Table 3.3	Sample preparation for the ICP-MS measurements: With calibration curves. . . . .	49
Table 3.4	Sample preparation for the ICP-MS measurements: With TotalQuant <sup>TM</sup> . . . . .	49
Table 3.5	Summary of the sample preparation for the ICP-MS measurements (for <sup>nat</sup> Si). . . . .	49
Table 3.6	Final composition of the representative sample matrix used for the distillation experiments. . . . .	51
Table 3.7	Overview of the <sup>32</sup> Si fractions that were used to produce a <sup>32</sup> Si master solution. . . . .	57
Table 3.8	Sequence of the experimental procedure to produce the prospective <sup>32</sup> Si master solution. . . . .	58
Table 3.9	Overview of the stock solutions used for the preparation of individual sample sets for the AMS measurements at ETH Zurich (Laboratory for Ion Beam Physics, LIP). . . . .	59
Table 3.10	Overview of the first batch of (test) samples (AMS Series SiO <sub>2</sub> (S-I)), based on the <sup>32</sup> Si stock solution with an activity concentration of 14.4 kBq/g for <sup>32</sup> Si. The scheme "D-" refers to the dilution's step number. . . . .	60
Table 3.11	Overview of the second batch of samples (AMS Series SiO <sub>2</sub> (S-II)) based on the <sup>32</sup> Si stock solution with an activity concentration of 108.9 kBq/g for <sup>32</sup> Si. The scheme "D-" refers to the dilution's step number. . . . .	60
Table 3.12	Overview of the third batch of samples (AMS Series K <sub>2</sub> SiF <sub>6</sub> (K-I)) based on the <sup>32</sup> Si stock solution with an activity concentration of 108.9 kBq/g for <sup>32</sup> Si. The scheme "D-" refers to dilution's step number, and K indicates the potassium. . . . .	61
Table 3.13	Overview, characterising the analyzed vanadium specimen. The mass was determined based on measurements, but the mass differences were suspected to, e.g., partial oxidation of the metal (Fig. 3.2). In order to be consisted with the previous work [178], an averaged disc mass of 132 ± 1.32 mg was considered. . . . .	63
Table 3.14	Overview of the different reference sources used for the activity determination respecting different sample geometries. . . . .	65

Table 4.1	Comparison of the $^{27}\text{Al}$ and $^{56}\text{Fe}$ results for the two different measurement techniques. . . . .	71
Table 4.2	Determined metal content (EPFL) in the inactive vanadium discs compared with the certified maximum content of the supplier (SUPL), Goodfellow (Cambridge Ltd., England). . . . .	72
Table 4.3	Summary of possible polyatomic interferences, taken from [142]. . . . .	73
Table 4.4	Overall uncertainties are considered 20% (w/o HKM), and 10% (w/ HKM). Note, that the value for $^{30}\text{Si}$ (x200 dilution) has been excluded from the calculations (see discussion in the text). . . . .	75
Table 4.5	Overview of the ICP-OES results to determine the $^{28,29,30}\text{Si}$ content. Here, samples with and without an additional Si-Spike were used, and different vanadium discs were used (but from the same batch). . . . .	75
Table 4.6	Values for the distribution coefficients taken from [118] for vanadium(IV, V) in the system: $\text{AG}^{\text{®}} 50\text{W-X8} - \text{HCl} - \text{H}_2\text{O}$ . . . . .	78
Table 4.7	Values for the distribution coefficients taken from [118] for vanadium(IV, V) in the system: $\text{AG}^{\text{®}} 50\text{W-X8} - \text{HNO}_3 - \text{H}_2\text{O}$ . . . . .	78
Table 4.8	Overview of the nuclides typically present in the $^{32}\text{Si}$ fraction after the separation from the bulk vanadium matrix. . . . .	81
Table 4.9	Values for the distribution coefficients taken from [118] for calcium, nickel and iron in the system: $\text{AG}^{\text{®}} 50\text{W-X8} - \text{HCl} - \text{H}_2\text{O}$ . . . . .	81
Table 4.10	Values for the distribution coefficients taken from [118] for calcium, nickel and iron in the system: $\text{AG}^{\text{®}} 50\text{W-X8} - \text{HNO}_3 - \text{H}_2\text{O}$ . . . . .	81
Table 4.11	Overview of the Ca recovery rates (in $\mu\text{g}$ ) for the different fractions. . . . .	96
Table 4.12	Overview of the nuclides typically present in the $^{32}\text{Si}$ fraction after the separation from the bulk vanadium matrix. . . . .	97
Table 4.13	Results from the LSC measurements, determined at different time intervals. . . . .	98
Table 4.14	Overview of the measured activities of $^{44}\text{Ti}$ from proton irradiated vanadium discs. . . . .	103
Table 4.15	Measured production cross section of $^{44}\text{Ti}$ . . . . .	103
Table 4.16	Overview of the three fractions obtained per each fully processed vanadium disc. . . . .	109

Table 4.17	Overview of the recovery yields for the AMS samples. . . . .	110
Table 4.18	Overview of the measured production cross-section of the $^{\text{nat}}\text{V}(\text{p}, \text{x})^{41}\text{Ca}$ reaction for the different vanadium specimens, including experiment-specific details. . . . .	112
Table 4.19	Overview of the measured production cross-section of the $^{\text{nat}}\text{V}(\text{p}, \text{x})^{26}\text{Al}$ reaction for the different vanadium specimens, including experiment-specific details. . . . .	112
Table 4.20	Overview of the determined tSIE for the different matrices using the Tri-Carb <sup>®</sup> 2250CA. . . . .	115
Table 4.21	Determined number of atoms of $^{32}\text{Si}$ . The data was kindly provided by Dr Stefan Rölli (Scientist, Spiez Laboratory, Switzerland). . . . .	119
Table 4.22	Determined activity concentration of $^{32}\text{Si}$ . The data was kindly provided by Dr Karsten Kossert (Scientist, PTB, Germany). . . . .	119
Table 5.1	Overview of the progress on the different measurement techniques. . . .	122
Table 5.2	Overview of half-life values, similar to the preliminary value determined by the SINCHRON-collaboration. . . . .	124
Table 6.2.1	Compilation of the experimental cross section for the nuclear reaction: $^{\text{nat}}\text{V}(\text{p}, \text{x})^{44}\text{Ti}$ , used for comparison. Former value ( $\sigma$ ) and adjusted value ( $\sigma^*$ ) are reported. Please note, the reported values were initially stated in mb, while we report them after the adjustment in pb. . . . .	129
Table 6.2.2	Overview of the uncertainty sources in order to calculate the overall uncertainty budget (PLC = Point-Like Source). . . . .	130
Table 6.2.3	Specific relative uncertainties ( $\delta$ , in %) and their contribution to the total uncertainty budget ( $\delta_{\text{total}}$ , in %) for the $^{41}\text{Ca}$ samples. . . . .	131
Table 6.2.4	Specific relative uncertainties ( $\delta$ , in %) and their contribution to the total uncertainty budget ( $\delta_{\text{total}}$ , in %) for the $^{26}\text{Al}$ samples. . . . .	132





# List of Abbreviations

<b>A</b>	Activity
$A_{spec.}$	Specific Activity
ABLA	Evaporation/Fission Code (Simulation)
ADS	Accelerator-Driven System
AM	Axial Mode
AMS	Accelerator Mass Spectrometry
AMS-K1	AMS Sample Series No. 1 ( $K_2SFi_6$ )
AMS-S1	AMS Sample Series No. 1 ( $SiO_2$ )
AMS-S2	AMS Sample Series No. 2 ( $SiO_2$ )
ANL	Argonne National Lab (Lemont, USA)
ANU	Australian National University (Canberra, USA)
Apex-ACM	Sample Inlet System for ICP-MS with Actively Cooled Membrane
ArTTA	Argon-Trap Trace Analysis
ATLAS	Argonne Tandem Linear Acceleratory System
ATTA	Atom-Trap Trace Analysis
$\alpha$ -HIBA	$\alpha$ -Hydroxyisobutyric Acid
<b>Bq</b>	Becquerel
<b>CIEMAT</b>	Centro de Investigaciones Energetica Medioambientales Technological (Madrid, Spain)
CNET	CIEMAT/NIST Efficiency Tracing
COA	Certificate Of Analysis
CPM	Counts Per Minute
CRM	Certified Reference Material
CRs	Chelating Resins
CT	Conservative Tracer
<b>DCF</b>	Decontamination Factor
DGA Resin	Specialized Resin: Diglycolamide
DPM	Disintegrations Per Minute
DRS	Distillation Reference Solution
DSC	Dichroic Spectral Combiner
DTS	Distillation Trap Solution
DVB	Divinylbenzene
<b>EC</b>	Electron Capture
ECG	EURACHEM Guide
EPFL	École Polytechnique Fédérale de Lausanne (Lausanne, CHE)
ESS	European Spallation Source (Lund, SWE)

ETHZ	Eidgenössische Technische Hochschule Zürich (Zurich, CHE)
EXCO	Extraction Chromatography
<b>FEP</b>	Full Energy Peak
<b>GHG</b>	Greenhouse Gases
GUM	Guide to the Expression of Uncertainty in Measurement
<b>HD-PE</b>	High-Density Polyethylene
HDEHP	Di-(2-ethylhexyl)phosphoric acid
HETP	Theoretical Plate Heights
HFSA	Hexafluorosilicic acid
HIP A	High Intensity Proton Accelerator
HKM	Helium KED Mode
HPGe	High-Purity Germanium Detector
HPLC	High-Performance Liquid Chromatography
HTO	(Diluted) Tritiated Water
<b>IC</b>	Ionization Chamber
ICP	Inductively Coupled Plasma
IDMS	Isotope Dilution Mass Spectrometry
IER	Ion-Exchange Resin
INCL	Liège Intranuclear Cascade (Simulation)
IPA	Instrument Performance Assessment
IRA	Institute de Radiophysique (Lausanne, CHE)
ISO	International Organization for Standardization (London, GBR)
<b>K<sub>d</sub></b>	Distribution Coefficient
KED	Kinetic Energy Discrimination
KM	Kragten Matrix
<b>L-AscA</b>	L-Ascorbic Acid (Vitamin C)
LAMPF	Los Alamos Meson Physics Facility (Los Alamos, USA)
LANL	Los Alamos National Laboratory (Los Alamos, USA)
LEGe	Low-Energy Germanium Detector
LIP	Laboratory of Ion Beam Physics (Zurich, CHE)
LLC	Low-Level Counting
LN Resin	Specialized Resin: Lanthanides
LNS	Laboratoire National Saturne (Paris and Gif-sur-Yvette, FRA)
LoB	Limit of Blank
LoD	Limit of Detection
LoQ	Limit of Quantification
LSC	Liquid Scintillation Counting

<b>MC-(ICP-MS)</b>	Multi-Collector-(ICP-MS)
MILEA	Multi-Isotope-Low-Energy AMS System
MODUS	Mini Silicon Distillation Aparatus
<b>NCT</b>	Non-Conservative Tracer
NetCT	Net Count Rates
NIST	National Institute of Standards and Technology (Gaithersburg, USA)
NPL	National Physics Laboratory (Teddington, GBR)
<b>OES</b>	Optical Emission Spectrometry
OSA	Orthosilicic Acid
<b>PEG</b>	Polyethylene Glycol
PET	Positron Emission Tomography
PFA	Perfluoroalkoxy Alkanes
pH	Potentia Hydrogenii; Pondus Hydrogenii
pK	Dissociation Constant
PLC	Point-Like Source
PMMA	Polymethyl methacrylate
PMT	Photomultiplier Tube
PNNL	Pacific Northwest National Laboratory (Richland, USA)
PP	Polypropylene
PPB	Parts Per Billion
PPM	Parts Per Million
PS	Plastic Scintillation
PSI	Paul Scherrer Institut (Villigen, CHE)
PTB	Physikalisch-Technische Bundesanstalt (Braunschweig, DEU)
PTFE	Polytetrafluoroethylene
<b>R<sup>2</sup></b>	Correlation Coefficient
RM	Radial Mode
RS	Reference Solution (RS-2 and RS-5)
RSD	Relative Standard Deviation
<b>SF-H<sub>2</sub>O</b>	Silicate-Free Water
SF-(ICP-MS)	Sector-Field-(ICP-MS)
SINCHRON	<sup>32</sup> Si: A New Chronometer
SL	Spiez Laboratory (Spiez, CHE)
SINQ	Swiss Spallation Neutron Source
SLS	Silicon Load Solution
SNR	Signal-To-Noise-Ratio
SNSF	Swiss National Science Foundation (Bern, CHE)

STD	Standard Deviation
STF	Silicon Tetrafluoride
STIP	SINQ Target Irradiation Program
SUPL	Supplier
Sv	Sievert
<b>TDCR</b>	Triple-To-Double Coincidence Ratio
TEVA	Specialized Resin: Tetravalent Actinides
TLC	Thin-Layer Chromatography
(TO)DGA	Specialized Resin: N,N,N',N'-Tetraoctyl Diglycolamide
TQ-O	TotalQuant™-Option
TRIUMF	Canada's Particle Accelerator Centre (Vancouver, Canada)
tSIE	Transformed Spectral Index of the External Standard Spectrum
$T_{1/2}$	Half-Life
<b>USTC</b>	University of Science and Technology of China (Hefei, CHN)
UTP-H <sub>2</sub> O	Ultra-Pure Water (In-House Purified)
UV	Ultraviolet
<b>VB</b>	Vinylbenzene





# 1 Introduction

## 1.1 Environmental Research: The need for a new, suitable geochronometer

Nowadays, climate change on Earth has arisen great attention. Here, the emission of greenhouse gases (GHG), mainly carbon dioxide (CO<sub>2</sub>) and methane (CH<sub>4</sub>), have been identified as root of a key mechanism to cause accelerated global warming (e.g., [1]). The effects became apparent, especially during the past decade and continue a long-term trend of worldwide warming, mainly driven by rising GHG levels [2]. Therefore, the increased occurrence of natural catastrophes, such as droughts and floods [3], is perceived which sadly highlight those changes dramatically.

To understand and assess these highly complex issues, that significantly affect the environment and our society, records of past climate patterns help to investigate the mechanisms and driving forces for such changes. In this regard, very recently, the work of three scientists was recognized by awarding the 2021 Physics Nobel Prize [4] to Syukuro Manabe, Klaus Hasselmann [5] and Giorgio Parisi [6]. They demonstrated that our knowledge about the climate rests on a solid scientific foundation based on rigorous observations. Therefore, to have a sound base, new and innovative techniques are required to continuously broaden the knowledge of the involved processes in the future and to provide a reliable foundation for appropriate decisions.

On this subject, certain mineral formations, referred to as speleothems, have been widely established as terrestrial paleoclimate archives (e.g., [7]) and provide, i.e., the means for testing and validating general circulation models used to forecast future climate [8]. These mineral deposits accumulate over time in natural caves and contain certain trace elements, of which one is uranium that allows determining their absolute ages by measuring the <sup>230</sup>Th-<sup>238</sup>U ratio. With this, it is possible to reconstruct and study long-term climate records of up to 600'000 y (e.g., [9], [10]) while stable isotope ratios ( $\delta^{18}\text{O}$ ,  $\delta^{13}\text{C}$ ) are analyzed to study the shifts in temperature, and precipitation, respectively (e.g., [11]). However, besides these long-term records, precise studies of the more recent past are becoming more important, as they will contribute to an improved understanding of how glacier dynamics or ocean and atmospheric circulation have changed during a much shorter period, i.e., during the past millennium, thus focusing on the anthropogenic impact on the environment [12]. Here, paleoclimatic investigations using ice cores recovered from glaciers are of great use (e.g., [13]). Generally, radiometric dating is a recognized and established technique that has proved to be a versatile tool, i.e., well-known are argon-argon (<sup>40</sup>Ar/<sup>39</sup>Ar), radiocarbon (<sup>14</sup>C), thorium-uranium (<sup>230</sup>Th/<sup>238</sup>U), and uranium-lead (<sup>238</sup>U/<sup>206</sup>Pb) dating. A summary of those established isotopes is given in Table 1.1 together with their half-lives to indicate the suitable time-interval for dating.

**Table 1.1:** Overview of commonly used elements and element pairs to determine absolute ages.

	<sup>40</sup> Ar/ <sup>39</sup> Ar	<sup>14</sup> C	<sup>230</sup> Th/ <sup>238</sup> U	<sup>238</sup> U/ <sup>206</sup> Pb
Half-Life in years with uncertainty [14]	Stable / 268 ± 8	5700 ± 30	(7.538 ± 0.030) x 10 <sup>4</sup> / (4.468 ± 0.003) x 10 <sup>9</sup>	(4.468 ± 0.003) x 10 <sup>9</sup> / Stable
Representative Example	Development of the concept of Magnetostatigraphy	Age of the Ötztal Ice Man (Austria)	Age and magmatic evolution of the Stromboli volcano (Italy)	Proof of age for the oldest minerals – Zircon – (4.404 ± 0.008) x 10 <sup>9</sup> y ever discovered (Australia)
Year	1999	1994	1980	2001
Reference	[15]	[16]	[17]	[18]

Each dating technique is selected explicitly because of its individual  $T_{1/2}$  and can be applied up for time intervals of to eight times the half-life value. Moreover, the nuclides are also chosen based on their typical accumulation (e.g., in minerals) and thus their typical occurrence in the environment. Notably, both constant production and accumulation rates are therefore required. Hereof, sedimentary reconstructions play a vital role in revealing anthropogenic activities and providing important information (e.g., [19], [20], [21]). Typically,  $^{210}\text{Pb}$  ( $T_{1/2} = 22.20 \pm 0.22$  y, [14]) and  $^{14}\text{C}$  are used to access these data. Nonetheless, a precise radiometric dating method between those chronologies of  $^{210}\text{Pb}$  and  $^{14}\text{C}$  does not exist. Therefore, age-correlations between 100 to 1000 years cannot be provided, resulting in a visible dating gap (Fig. 1.1).

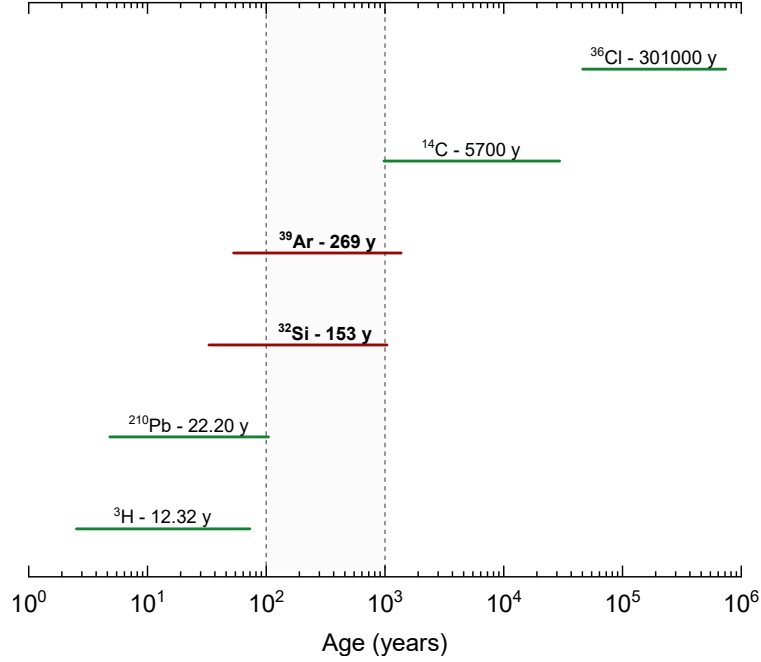


**Fig. 1.1:** Visible dating gap (red bars) between 100 to 1'000 years, whereby well-established chronometers are indicated by green bars. The bars represent the time range over which the nuclides can be used, as of their half-lives. Taken from Veicht et al. [22].

Yet, a suitable geochronometer would allow covering important epochs, such as the impact of European settlement and industrialization during the past 300 years, the Little Ice Age in the 17<sup>th</sup> and 18<sup>th</sup> century, and the last part of the Mediaeval Climatic Optimum [12]; or, generally spoken, to focus on age horizons associated with strong anthropogenic activity. Consequently, the importance of finding a suitable dating tool has been emphasized by many scientists in the field (e.g., [23], [24]). Among other potential candidates (Table 1.2), only two radionuclides can be considered to meet the required demands, namely  $^{39}\text{Ar}$  and  $^{32}\text{Si}$ , since they are the only naturally occurring isotopes, with a suitable half-life. Their half-life is in the necessary range of about  $10^2$  y, and their constant production and stable accumulation processes in Earth's ecosystem (geo-, bio-, cryo-, hydro-, and atmosphere) favor their application.

**Table 1.2:** Overview of suitable nuclides, based on their matching half-lives (range: 100 to 500 y), arranged in order of increasing half-lives. However, none of them are naturally occurring, thus must be produced exclusively artificially. Data taken from [14].

Nuclide	$^{63}\text{Ni}$	$^{209}\text{Po}$	$^{242}\text{Am}$	$^{158}\text{Tb}$	$^{192}\text{Ir}$	$^{249}\text{Cf}$	$^{241}\text{Am}$	$^{108}\text{Ag}$	$^{194}\text{Hg}$
$T_{1/2}$ (y)	101.2	122.9	141	180	241	351	432.6	438	447
Unc. (%)	1.5	1.9	1.4	6.1	3.7	0.6	0.1	2.1	11.6

A further common link between  $^{39}\text{Ar}$  and  $^{32}\text{Si}$  is their cosmogenic origin, hence their production in the upper atmosphere due to the bombardment of cosmic rays on natural  $^{\text{nat}}\text{Ar}$ . Typical, main production paths for  $^{39}\text{Ar}$  ([25], and references therein), and  $^{32}\text{Si}$  [26], including their averaged production rates are presented in Table 1.3.

**Table 1.3:** Summary of the primary, natural production paths, and their global atmospheric average intake.

	$^{39}\text{Ar}$	$^{32}\text{Si}$
<b>Main nuclear reaction pathways</b>	$^{40}\text{Ar}(\text{n},2\text{n})^{39}\text{Ar}$ $^{38}\text{Ar}(\text{n},\gamma)^{39}\text{Ar}$	$^{40}\text{Ar}(\text{p},2\alpha\text{p})^{32}\text{Si}$
<b>Global average surface injection*</b> (atoms $\times \text{cm}^{-2} \times \text{y}^{-1}$ )	$\approx 1 \times 10^5$	$\approx 5 \times 10^3$
<b>Integrated amount (globally)</b>	18.98 L of Ar $\approx$ 11.41 g or Ar	1.35 g of Si $\approx$ 2.53 g or $\text{SiO}_2$

\* The reported typical values for  $^{39}\text{Ar}$  and  $^{32}\text{Si}$  are taken from [27]. Contributions from oceanic production [28] are not considered. Moreover, the figures for the global average surface injection, i.e., for  $^{32}\text{Si}$ , may vary in literature [12, 29, 30].

With this being presented, a brief history of the efforts in the quantitative determination for both  $^{39}\text{Ar}$  and  $^{32}\text{Si}$  is described, although their situation concerning nuclear data has been rather poor, yet inconsistent, over the past 60 years, as presented in the following sections.

### 1.1.1 Argon-39 ( $^{39}\text{Ar}$ )

Referring to  $^{39}\text{Ar}$ , from a chemical perspective, it can be considered a suitable dating nuclide and a conservative tracer (CT) due to its noble gas properties. Hence as a CT, it is virtually not involved in bio- and geochemical processes, resulting in a low solubility in water, with approximately 6500 atoms [31] to 8500 atoms [32] per liter of atmosphere-equilibrated water. Further, it has an exceptionally low atmospheric abundance and, more importantly, this nearly hasn't been affected by the overground bomb tests in the 1950ies and early 1960ies [33], as opposed to, e.g., radiocarbon ( $^{14}\text{C}$ ) ([34], and references therein). Besides, isotopic fraction effects are insignificant with its comparatively low mass difference to the main isotope,  $^{40}\text{Ar}$  (natural abundance: 99.604%). Analyses of  $^{39}\text{Ar}$  have been early reported using Low-Level Counting (LLC) when first attempts were made to measure water samples of different origins [35, 36], while also determining and reducing the natural background of  $^{39}\text{Ar}$  for the proportional counters in the laboratory ([37], [38], and references therein). Consequently, such measurements were usually performed in specialized facilities like the LLC underground laboratory in Bern [37] or the Laboratori del Gran Sasso underground laboratory [39]. More recently, comprehensive tests to utilize this technique for determining ultra-low  $^{39}\text{Ar}$  concentrations [40] were performed at the Pacific Northwest National Laboratory (PNNL), including the preparation of PNNL's low-level  $^{39}\text{Ar}$  calibration standards to assist with improving the overall accuracy of  $^{39}\text{Ar}$  groundwater age-dating [41]. However, due to the low isotopic ratio in the atmosphere ( $^{39}\text{Ar}/\text{Ar} = 8.1 \times 10^{-16}$ , [42]) and a specific beta decay rate of approximately one Becquerel (Bq) per kg argon [39], typically 1500 to 5000 L of water were degassed in the field to provide the required amount of pure argon (0.5 to 2L, [31]). Obviously, due to these related efforts, the application of LLC for  $^{39}\text{Ar}$  routine analyses is constrained. In this regard, Accelerator Mass Spectrometry (AMS) seemed suitable, as it is a highly sensitive method of counting atoms instead of measuring decays. Typically, it can detect very low natural isotopic ratios (in the range of  $10^{-12}$  to  $10^{-16}$ ) while requiring only small sample sizes (some mg) and providing results after short (in some cases, less than one hour) measurement times [43]. However,  $^{39}\text{Ar}$  is rather difficult to measure because of its isobar,  $^{39}\text{K}$ . Recent advancements from Collon et al. [44] are promising, but the authors still report a consistently high  $^{39}\text{K}$  background that made measurements of  $^{39}\text{Ar}/\text{Ar}$  below  $(4.6 \pm 0.2) \times 10^{-13}$  impossible, which is three orders of magnitudes higher than expected natural isotopic Ar compositions. On this subject, it was highlighted already earlier by the authors that those system improvements are vital to measuring, e.g., ocean water samples with a precision below 5% in under ten hours of counting time [31]. However, it should be noted that this technique is generally somewhat challenging to implement for routine analyses because of its dependence on large accelerators, so the beam-time access for specialized AMS facilities can be a limiting factor (e.g., the 200 MeV ATLAS accelerator facility at the Argonne National Laboratory, U.S.A., [44]).

Consequently, recent developments at the University of Heidelberg are most promising as they allowed the first Argon Trap Trace Analysis (ArTTA) for glaciological applications in order to date alpine glacier ice samples [45]. Besides, a work from Tong et al. [46] describes the development of an Atom Trap Trace Analysis system with improved performance at the University of Science and Technology of China (USTC). The sample amount is in the range of one to five kg of either water or ice. Generally, such amounts are the key to the practical use of the dating technique, as it allows for the required spatial and thus temporal resolution [45]. Nonetheless, the authors conclude that age determination within 250 to 1300 years yields a 20% uncertainty, indicating significant systematic error sources. Generally, the evolution over the past ten years regarding ATTA has been quite remarkable (Table 1.4). While the technical challenges haven't been fully solved yet, steady improvements in the atom counts per hour are ongoing, thus helping to lower overall counting uncertainties.

**Table 1.4:** Overview of important contributions regarding Argon Trap Trace Analysis.

Contribution	Year and Reference	$^{39}\text{Ar}$ atom counts per hour
Analyses at and below $10^{-16}$ ( $^{39}\text{Ar}/\text{Ar}$ )	2011, [42]	0.2
First dating of groundwater	2014, [47]	up to $3.58 \pm 0.10$
Successful use as tracer in oceanography	2018, [48]	up to $7.00 \pm 0.70$
First dating of glacier ice	2019, [45]	up to $4.13 \pm 0.41$
Improving count rate by factor of two	2021, [46]	up to $10 \pm 1.00$
Further improvements (pre-enrichment)	2022, [49]	up to $200 \pm 11.5$

Although  $^{39}\text{Ar}$  has recently gained more attention and advanced further, this noble gas tracer actually poses further challenges in quantitative detection. Most notably, its subsurface production via  $^{39}\text{K}(\text{n,p})^{39}\text{Ar}$  can be significant in rocks, i.e., granites [32] that contain high U and Th contents. Consequently, the authors further describe elevated Ar levels above 100% of the modern atmospheric activity found. Furthermore, an essential aspect of  $^{39}\text{Ar}$  measurements is the questionable half-life which basically demands a redetermination. The only reported values are  $265 \pm 30$  y ([50], from 1952) and  $269 \pm 3$  y ([51], from 1965). As a result, the currently accepted  $T_{1/2}$  value is  $268 \pm 8$  y, and the 3% systematic uncertainty is preferred over the 1.1% statistical uncertainty [52]. However, to rely on only two measurements seems risky since high deviations from former recommended half-life values were already discovered for other radionuclides when reviewing new measurements. Such examples can be found in the literature, e.g., for  $^{60}\text{Fe}$  or  $^{146}\text{Sm}$  (Table 1.5).

**Table 1.5:** Overview of two examples where carefully performed redeterminations yielded quite different values for the half-life.

	$^{60}\text{Fe}$	$^{146}\text{Sm}$
Former recommended value	$(1.49 \pm 0.27) \times 10^6$ y	$(103 \pm 5) \times 10^6$ y
New recommended value	$(2.62 \pm 0.27) \times 10^6$ y	$(68.7 \pm 0.7) \times 10^6$ y
Deviation	+ 76%	- 33%
Literature	[53], and [54]	[55], [56], and [57]

This, undoubtedly, emphasizes the importance of precise knowledge of the half-life and thus generally calls for a reliable and, ideally, a more significant number of consistent and independent measurements.

### 1.1.2 Silicon-32 ( $^{32}\text{Si}$ )

In contrast to  $^{39}\text{Ar}$ , the situation is somewhat different for  $^{32}\text{Si}$ , as this nuclide is considered a non-conservative tracer (NCT). As opposed to a CT, silicon participates in environmental exchange processes, as, e.g., silica ( $= \text{SiO}_2$ ) can be brought into solution as monosilicic acid ( $\text{H}_4\text{SiO}_4$ ) and re-adheres to soil particulates [58]. That way, radiosilicon accumulates in typical environments, making it a perfect candidate for tracing it in environmental samples.

To begin with, radioactive  $^{32}\text{Si}$  was first identified in nature by Lal et al. [59] in 1959. However, its actual first discovery dates back to 1952, when Lindner [60] identified the nuclide as a by-product of a nuclear reaction, thus confirming its artificial production. Nowadays, its natural production path has been studied and summarized by Fifield & Morgenstern [12] via cosmic-ray-induced spallation of  $^{40}\text{Ar}$ . Subsequently, it is transferred to Earth's surface by precipitation and eventually deposited in terrestrial sediments, snow, and ice. Also, it can be carried away by water so that  $^{32}\text{Si}$  is enriched in limnic and/or oceanic sediments. These different geochemical pathways are summarized in Fig. 1.2.

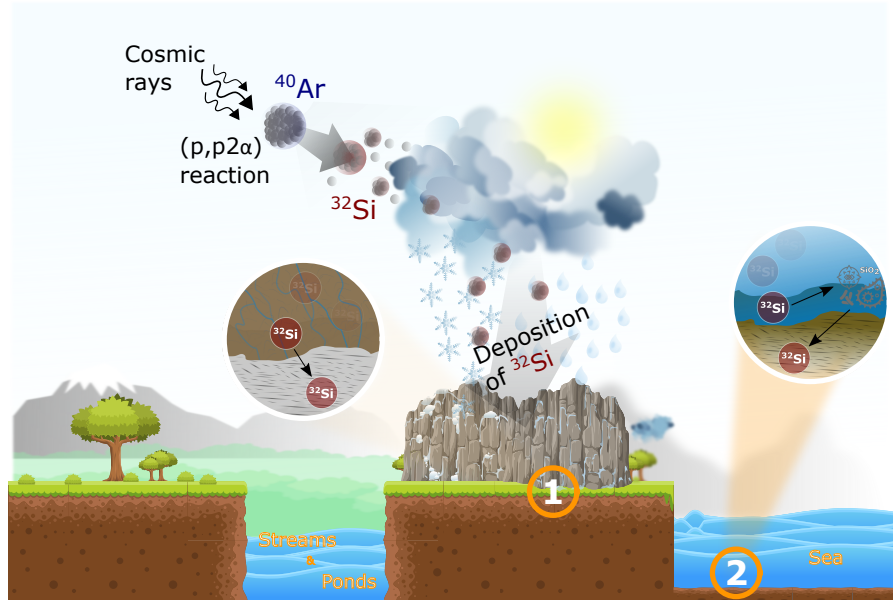


**Fig. 1.2:** The illustration is inspired by Orrell et al. [61] and shows the natural production, the involved transport mechanisms, and accumulation of  $^{32}\text{Si}$ . Apart from the enrichment in streams, ponds, or the sea,  $^{32}\text{Si}$  is eventually accumulated in (1) sediments and near-surface silicon deposits or in (2) where it is transported by biological,  $\text{SiO}_2$ -bearing organisms (Diatoms and Radiolaria), and are finally solidified in the sediments.

However, the meager production rates (Table 1.3) make it challenging to detect  $^{32}\text{Si}$  in natural samples, so radiometric detection methods have become necessary to determine its specific activity. As such, a pioneer work in the late 1950ies by Lal & Schink [62] marked the base for routine analyses focusing on gas-flow beta counters. Also, more recently scintillation spectrometry is applied (e.g., [63], [64]) whereby in all methods not  $^{32}\text{Si}$  directly, but the decay of the daughter  $^{32}\text{P}$  ( $T_{1/2} = 14.268 \pm 0.005$  d,  $E_{\beta_{max}} = 1.71$  MeV, [14]) in near-secular equilibrium is followed, after it has been radiochemically purified (e.g., [65], [66], and references therein). The advantages of that procedure are (I) higher sensitivity, and thus easier detection of the hard beta emitter, (II) smaller sample sizes due to phosphorous' extraction (referred to as milking, [59]). Examples of such successful measurements are, e.g., the analysis of marine sediments from Bangladesh ( $\approx 1000\text{g}$  sediment/sample; the Bay of Bengal, [67]) as well as limnic sediments from Russia ( $\approx 10\text{-}100\text{g}$  sediment/sample; the Lake Baikal, Siberia, [68]) or an early attempt of dating groundwaters in India [69].

Previously, AMS was already introduced as a highly sensitive method and is usually chosen when low quantities must be determined. However, when measuring  $^{32}\text{Si}$ , there is a further challenge that is directly linked to the low natural activities, namely the typically low  $^{32}\text{Si}/\text{Si}$  ratios in natural samples (sediments, sponges, and groundwaters), which range between  $10^{-15}$  and  $10^{-17}$  [70] or even  $10^{-18}$  [67]. Consequently, AMS cannot be used when dealing with elevated amounts of stable Si since some of these ratios are well below the detection limit ( $\approx 10^{-16}$ ). Thus, only ice or rain samples have been reported by Morgenstern et al. [26] to probably allow for  $^{32}\text{Si}/\text{Si}$  ratios ( $10^{-12}$  to  $10^{-13}$ ) being well above the detection limit. Another major obstacle is the stable mass isobar  $^{32}\text{S}$ . Recent advancements have thus focused on suppressing the isobar and were reported by Gong et al. [71] and He et al. [72], respectively. However, it is mentioned by the authors that a further suppression of the  $^{32}\text{S}$  signal is needed to measure  $^{32}\text{Si}$  in natural samples. But the proven system's sensitivity for  $^{32}\text{Si}$  ( $10^{-15}$  to  $10^{-14}$ ) will facilitate future measurements of the isotope's half-life, which is, in general, a crucial fact to aim for and is the principal challenge for its implementation as a suitable geochronometer.

The currently recommended half-life of  $^{32}\text{Si}$  is based on a weighted average of six independent measurements [73]. An overview of these results is provided in Fig. 1.3, and further details are stated in Table 1.6: a considerable scatter in the half-lives, including significant uncertainties, ranging from 2.3% to 17.8% are obvious. Based on that data, the recommended  $T_{1/2}$  for  $^{32}\text{Si}$  is  $153 \pm 19$  y, which yields an overall uncertainty of 12.4%.

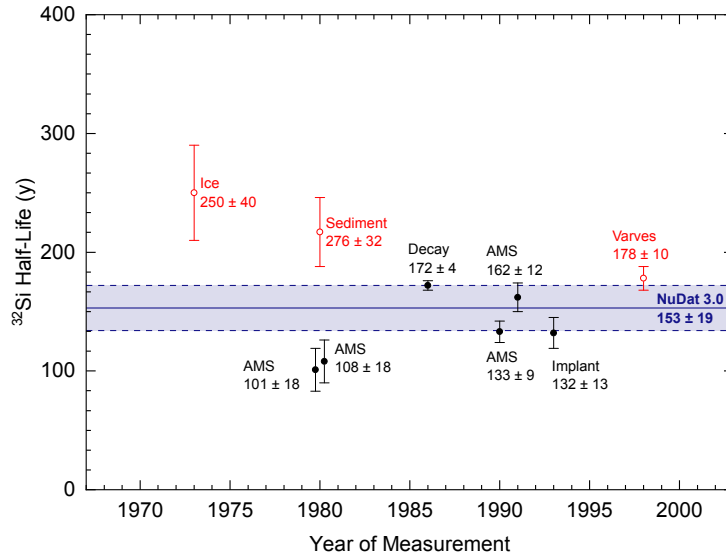


**Fig. 1.3:** Compilation of  $^{32}\text{Si}$  half-life determinations. Three measurements are excluded (marked with red) and haven't been used in the averaging procedure since they rely on  $^{32}\text{Si}$  accumulation rates (ice and sediments), which are not known well [73].

**Table 1.6:**  $^{32}\text{Si}$  activity that was involved in the experiments, which can be summed up to  $\approx 3.4$  kBq.

Year	$^{32}\text{Si}$ (y)	Method	Activity (Bq)	Reference
1980	$101 \pm 18$	AMS and LSC	5 to 10	[74]
1980	$108 \pm 18$	AMS and LSC	20	[75]
1986	$172 \pm 3$	Decay	300	[76]
1990	$133 \pm 9$	AMS and LSC	3000 50	[77]
1991	$162 \pm 12$	AMS and LSC	0.23	[78]
1993	$132 \pm 13$	Implantation	5	[79]

### 1.1.3 SINCHRON: $^{32}\text{Si}$ - a new chronometer

When climate archives shall be investigated, precise time information is vital. As such, the most crucial parameter is the nuclide's half-life. As previously presented, established radiometric techniques have precisely determined recommended half-lives with uncertainties ranging from, e.g., 0.07% ( $^{238}\text{U}$ ) to 0.5% ( $^{14}\text{C}$ ). The  $T_{1/2}$  is, however, in the case of  $^{32}\text{Si}$ , presently not known to the desired accuracy. Therefore, to implement the radionuclide as a promising new chronometer for nuclear dating, its half-life must be re-determined. In order to improve the current situation concerning the  $^{32}\text{Si}$  half-life, a primary goal of this PhD thesis focused on the supply of a sufficient amount of chemically pure  $^{32}\text{Si}$ , marking the cornerstone of the SNSF-funded SINCHRON-project (Silicon-32: a new chronometer). Moreover, as adding more data points to the initial measurements (Fig. 1.3) will not be a progress in refining the  $^{32}\text{Si}$  half-life, we want to provide our own set of half-life values based on complementary measurements within our collaboration (Table 1.7).

**Table 1.7:** Summary of the foreseen measurement methods and the involved institutions to determine the  $^{32}\text{Si}$ 's half-life.

Measurement	Method	Institution
Number of atoms	ICP-MS	PSI and Spiez Laboratory (SL)
Number of atoms	AMS	Laboratory of Ion Beam Physics (LIP) and Australian National University (ANU)
Activity Concentration	LSC	Physikalisch-Technische Bundesanstalt (PTB) and Institute of Radiation Physics (IRA)
Decay	PS/IC	Physikalisch-Technische Bundesanstalt (PTB)
Decay	PS	Institute of Radiation Physics (IRA)

Consequently, working with leading experts in the field of mass-spectrometry and metrology, one approach is measuring the specific nuclide's number of atoms (N) through inductively coupled plasma mass spectrometry (ICP-MS) and accelerator mass spectrometry (AMS) and the determination of the activity (A) - via liquid scintillation counting (LSC) - for the identical sample. Thus, the  $T_{1/2}$  can be determined from the relation (Eq. 1-1), which is referred to as the direct method:

$$T_{1/2} = \frac{N \times \ln(2)}{A} \quad (1-1)$$

Another approach follows the nuclide's decay after a given time interval. The decay constant ( $\lambda$ ) can then be derived from fitting procedures that fit the data to exponential decays. As a result, the half-life can be derived according to Eq. 1-2:

$$T_{1/2} = \frac{\ln(2)}{\lambda} \quad (1-2)$$

However, the long-term stabilities of both the sample and especially the measurement device (e.g., ionization chamber (IC), or Plastic Scintillation Counting (PS)) are vital.

To conclude, with the combined results from the foreseen measurements, we will contest to provide a new recommended half-life value for  $^{32}\text{Si}$  with a relative standard uncertainty ( $k=1$ ) of less than five percent.

## 1.2 Target material and isotope production: The artificial source of $^{32}\text{Si}$

The history of artificially created quantities of  $^{32}\text{Si}$  starts in 1953 when the production of  $^{32}\text{Si}$  was first reported by Lindner [60] as he described the bombardment of sodium chloride with 340-MeV protons using the Berkeley 184-inch cyclotron. With this experiment, the very first attempt was made to derive the  $^{32}\text{Si}$  decay characteristics, namely its half-life ( $T_{1/2} \approx 710$  y) and the determination of its emitting beta-energy ( $E_{\beta_{max}}^- \approx 100$  keV), while no gamma radiation was observed [60]. Further experiments have been performed with different proton energies at 420 MeV ([80], in 1964) and 52 MeV ([81], in 1978). Generally, in those experiments, silicon was produced via  $^{37}\text{Cl}$  (p, $\alpha$ 2p), and the studies focused on the determination of the endpoint energy ( $E_{\beta_{max}}^- = 213 \pm 7$  keV, [80]) and the cross-section [81] for the chlorine-plus-proton reaction. Sakamoto et al. [81] mention further that this reaction is most efficient in producing carrier-free  $^{32}\text{Si}$ . Nonetheless, a variety of other nuclear reactions can be considered, e.g., sequential routes with neutrons, such as  $^{31}\text{P}$  (n, $\gamma$ )  $^{32}\text{P}$  (n,p)  $^{32}\text{Si}$  [82] and  $^{32}\text{S}$  (n,p)  $^{32}\text{P}$  (n,p)  $^{32}\text{Si}$  [83], which also gives rise to, in general, a carrier-free product as virtually no stable silicon is involved.

Evaluating various production paths has the advantage of ultimately choosing an efficient and cost-effective way of nuclide production. Additionally, further circumstances have also to be considered. For instance, the production path from, e.g., Forberg [82], ultimately yield samples that are highly radioactive due to the formation of  $^{32}\text{P}$ , which in turn creates a lot of heat, and must be therefore taken into consideration during and after the irradiation process.

The production of the material used for this thesis was performed at the Swiss Spallation Neutron Source (SINQ), located at the Paul Scherrer Institut (PSI) as a part of the Swiss Spallation Neutron Source Target Irradiation Program (STIP-6). Usually, this program is dedicated to testing samples regarding material research (e.g., [84]), but some of the irradiation positions in the SINQ-Target can also be used for isotope production. Here, important considerations are related to the irradiation facility itself. For instance, the target material's selection for the production of  $^{32}\text{Si}$  is restricted by several boundary conditions, such as:

- Chemical elements with high neutron capture cross-section are not allowed (e.g.,  $^{10}\text{B}$  or  $^{155}\text{Gd}$ ), as they lower the neutron production (=neutron poison).
- Materials with high solubility in water (e.g., metal halide salts), low melting points, or explosion hazards (e.g., alkaline earth metals) are forbidden due to the high risk of contaminating or damaging the cooling circuit.
- Materials disturbing measurements (for instance, sulfur because of  $^{32}\text{S}$  as the isobar of  $^{32}\text{Si}$ , influencing the mass spectrometric measurements) must not be used, either.

Following these rules, high-purity vanadium discs were selected as the most suitable material. Moreover, because of the high chemical purity of the vanadium discs, only a small number of unwanted radionuclides were produced during the irradiation. In total, 150 metallic high-purity vanadium discs (= 63 g) were simultaneously irradiated for nearly two years (Fig. 1.4), using PSI's High-Intensity Proton Accelerator (HIPA) that delivers a proton beam up to 590 MeV [85]. After the irradiation process, the discs were stored at PSI to allow the short-lived isotopes, such as  $^{47}\text{Sc}$  ( $T_{1/2} = 3.3492 \pm 0.0006$  d), to decay, which is referred to as "Cool Down" (Fig. 1.4).

In this regard, Table 1.8 shows that among the shorter-lived isotopes (marked in yellow), which do not have a radioactive parent nuclide, only  $^{46}\text{Sc}$  ( $T_{1/2} = 83.79 \pm 0.04$  d) is of certain risk regarding the practical work. Due to its decay characteristics, it results in a very high dose rate, so a cool down period for, at least, ten  $^{46}\text{Sc}$ -half-lives ( $\approx 840$  d or  $\approx 2.3$  y) was necessary.

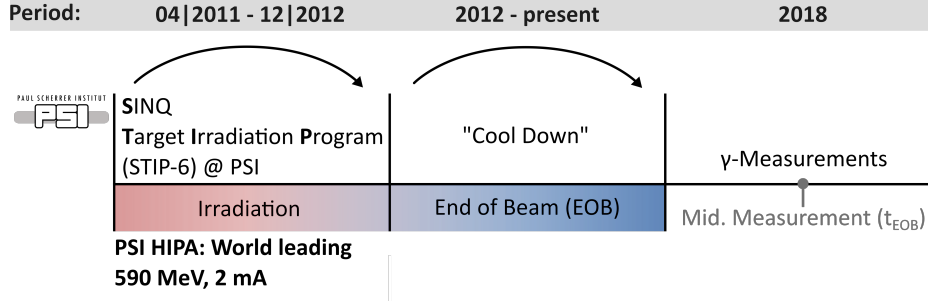


**Fig. 1.4:** Sequence of the different steps, starting from the irradiation, moving to the “Cool Down”-Phase, and the ultimate start of the SINCHRON-project, which began with  $\gamma$ -spectroscopic measurements of the vanadium discs.

However, isotopes such as the short-lived  $^{44}\text{Sc}$  must also be treated carefully. This nuclide is within 48 hours in secular equilibrium with its relatively long-lived parent  $^{44}\text{Ti}$  ( $59.1 \pm 0.3$  a, [86]), and causes a high dose rate because of the high-energy gamma emission ( $E_\gamma = 1157$  keV) with a high emission probability ( $I_\gamma = 99.9\%$ ). Moreover, because of the irradiation conditions, not only protons but also neutrons interacted with the target material. Consequently, expected activation products, due to (n,  $\gamma$ )- and (n, p)-reactions, were also identified throughout the separation process utilizing radioanalytical methods.

**Table 1.8:** Calculated activities of the main reaction products of SINQ Target 8, Rod 2. The initial calculations were based on 384 g metallic vanadium, whereas this overview has been adjusted to a processed amount of 63 g (= 150 V-discs).

Nuclide	Activity (Bq)	Number of atoms	Half-Life	Type of Radiation
<sup>49</sup> V	8.6E+11	3.5E+19	330 d	ε (Electron Capture) no γ
<sup>3</sup> H	1.4E+11	8.1E+19	12.32 y	β <sub>max</sub> <sup>-</sup> = 0.018 MeV
<sup>45</sup> Ca	4.9E+10	1.0E+18	162.6 d	β <sub>max</sub> <sup>-</sup> = 0.3 MeV
<sup>46</sup> Sc	4.5E+10	4.7E+17	83.3 d	β <sub>max</sub> <sup>-</sup> = 0.4; (1.5) MeV γ(99.9%) = 889 keV γ(99.9%) = 1121 keV
<sup>35</sup> S	7.6E+09	8.3E+16	87.4 d	β <sub>max</sub> <sup>-</sup> = 0.2 MeV
<sup>44</sup> Sc	9.0E+08	1.8E+13	3.97 h	γ(99.9%) = 1157 keV β <sub>max</sub> <sup>+</sup> = 1.5 MeV
<sup>44</sup> Ti	9.0E+08	2.4E+18	59.1 d	ε (Electron Capture) γ(96%) = 78.34 keV γ(94.4%) = 67.88 keV
<sup>39</sup> Ar	8.2E+08	1.0E+19	268 y	β <sub>max</sub> <sup>-</sup> = 0.6 MeV
<sup>42</sup> K	4.9E+08	3.1E+13	12.36 h	β <sub>max</sub> <sup>-</sup> = 3.5; 2.0 MeV γ(18%) = 1525 keV
<sup>42</sup> Ar	4.9E+08	7.3E+17	32.9 y	β <sub>max</sub> <sup>-</sup> = 0.6 MeV
<sup>37</sup> Ar	2.2E+08	9.7E+14	35 d	ε (Electron Capture) w/ X-ray emssions
<sup>22</sup> Na	5.0E+07	5.9E+15	2.6 y	γ(99.9%) = 1275 keV
<sup>32</sup> P	3.4E+07	6.0E+13	14.3 d	β <sub>max</sub> <sup>-</sup> = 1.7 MeV
<sup>32</sup> Si	3.4E+07	2.4E+17	153 y	β <sub>max</sub> <sup>-</sup> = 0.2 MeV
<sup>51</sup> Cr	2.5E+07	8.7E+13	27.7 d	γ(10%) = 320 keV β <sub>max</sub> <sup>-</sup> = 0.7 MeV
<sup>33</sup> P	6.5E+06	2.1E+13	25.3 d	β <sub>max</sub> <sup>-</sup> = 0.3 MeV
<sup>41</sup> Ca	6.4E+06	3.0E+19	9.9E+04 y	ε (Electron Capture) w/ X-ray emssions
<sup>36</sup> Cl	2.5E+06	3.5E+19	3.0E+05 y	ε (Electron Capture) w/ X-ray emssions β <sub>max</sub> <sup>-</sup> = 0.7 MeV
<sup>26</sup> Al	2.7E+04	8.9E+17	7.2E+05 y	ε (Electron Capture) γ(99.8%) = 1810 keV β <sub>max</sub> <sup>+</sup> = 1.2 MeV
<sup>40</sup> K	not calculated		1.2E+09 y	ε (Electron Capture) γ(11%) = 1460 keV β <sub>max</sub> <sup>+</sup> = (1.3) MeV

### 1.2.1 Isolation of $^{32}\text{Si}$ from irradiated materials

Generally, in order to study a nuclide in detail, any by-products must be entirely removed, in order to obtain the element of interest in a pure state. But, as different targets and production routes are usually available, a suitable separation technique must be adopted, that requires a thorough knowledge of the involved chemistry and physics.

Commonly, only a tiny quantity of any radionuclide is formed compared with the very large amounts of the target material from which it must be separated. In the present example of  $^{32}\text{Si}$  and  $^{\text{nat}}\text{V}$ , one compares around 80 ng  $^{32}\text{Si}$  (per disc), produced during the irradiation, with 420 mg  $^{\text{nat}}\text{V}$  (per disc). Besides, further challenges dealing with radiochemical separation procedures are related to the occurrence of some other, unwanted, radionuclides. Such nuclides can be possibly co-produced during the irradiation, by, e.g., competing nuclear reactions, daughter radionuclides (due to the decay of their respective parent), or metallic impurities initially present in the target material. For the isolation of the wanted radionuclides from individual irradiated targets, a wide range of chemical techniques are described in literature (e.g., [87]): (co-)precipitation, solvent extraction, distillation, electro-deposition, and ion-exchange chromatography. For these techniques, precise conditions have to be regarded, such as the ionic strength, and especially the pH. As these parameters play an essential role in the separation procedures, they require a careful investigation to obtain the best results.

From this perspective, the work of Polak et al. [88] is most interesting, as the authors also used vanadium targets, to produce  $^{32}\text{Si}$  through spallation. The metallic vanadium discs (typical mass  $\approx$  (!) 80 g, diameter  $\approx$  7.60 cm, thickness  $\approx$  3.0 mm) were bombarded over three years with 600 to 800 MeV protons (1 mA) at Los Alamos National Laboratory (LANL, Radioisotope Program) and their Meson Physics Facility (LAMPF). To recover  $^{32}\text{Si}$  from the active bulk vanadium matrix, a separation was carried out at high acidity by extraction of a heteropolycomplex (12-molybdosilicate) into 1-butanol and eventually purified by anion-exchange chromatography, yielding  $^{32}\text{Si}$  in a 1M NaOH matrix. However, the high number of both separation and purification steps led to low yields of Si-recovery. Therefore, the authors concluded that the procedure requires several improvements, e.g., silicon-poor reagents and the general avoidance of glassware are proposed to achieve a high specific  $^{32}\text{Si}$  activity.

Contrarily, in a work from Phillips et al. [89] the measurement of distribution coefficients on Sephadex<sup>®</sup> (dextran-based resin) for heteropolymolybdates of Si (among other elements), at varying pH are described, where a potassium chloride (KCl) target was used to produce  $^{32}\text{Si}$  by proton-induced spallation. Here, the authors present a sophisticated method based on the separation as silicon-molybdate complexes, followed by a final purification step on an anion-exchange resin. As precautions were taken during the whole separation process for one of the batches, a remarkably high specific activity (47.1 kBq per  $\mu\text{g}$  Si) was obtained. Finally,  $^{32}\text{Si}$  was reconstituted in 0.1M NaOH. Most notably, this method, developed at LANL, is used to produce  $^{32}\text{Si}$  on-demand [90, 91]. As the suggested target belongs to the metal halide salts, such a target would not have been allowed to be utilized in the SINQ Target due to safety restrictions.

### 1.2.2 Determination of cross-sections:

#### The interest in exotic nuclides such as $^{44}\text{Ti}$ , $^{41}\text{Ca}$ and $^{26}\text{Al}$

Rare and exotic isotopes, such as the cosmogenic ones,  $^{44}\text{Ti}$ ,  $^{41}\text{Ca}$ , and  $^{26}\text{Al}$  are urgently needed for applications in, e.g., nuclear medicine (e.g., [92]) or nuclear astrophysics (e.g., [93]). Usually, their production is very challenging, but these nuclides have been identified in exceptionally high quantities as by-products due to proton-induced spallation of metallic vanadium targets (see Table 1.8). For such predictions as shown, nuclear data are of fundamental importance as they provide necessary information of various physical interactions involving the nuclei of atoms and are commonly implemented into extensive data bases. In an attempt to further investigate vanadium as target material, the production cross-sections due to proton-induced spallation, of the cosmogenic nuclides  $^{44}\text{Ti}$ ,  $^{41}\text{Ca}$ , and  $^{26}\text{Al}$ , were also investigated and determined in this thesis. However, for this approach, different irradiated vanadium specimens were used. As opposed to the highly active vanadium samples from the SINQ-irradiation, here the information concerning the proton flux was available, which is vital for determining the cross-section, and excitation function, respectively. About the presented target element vanadium, the excitation function for  $^{44}\text{Ti}$  is of particular interest. The cosmogenic isotope belongs to the relatively long-lived isotopes with a half-life of 59.1 years and decays into  $^{44g}\text{Sc}$ , which decays further into  $^{44}\text{Ca}$  (Fig. 1.5).

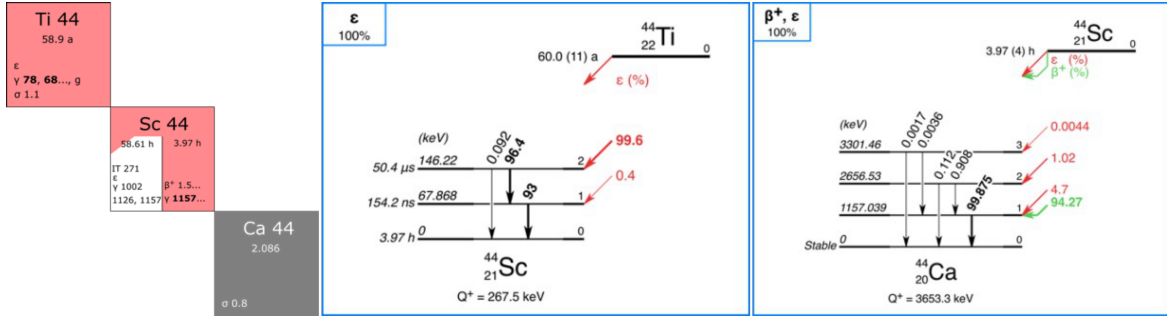


**Fig. 1.5:** Detailed decay schemes [94] of the relatively long-lived parent nuclide  $^{44}\text{Ti}$  and its daughter  $^{44g}\text{Sc}$ .

Especially over the recent years, the interest in  $^{44}\text{Ti}$  has gradually increased due to the versatility of the radionuclide's field of applications, with a focus on astrophysical applications (e.g., [94], [95]). Yet, most importantly, it is foreseen to be utilized as a possible radionuclide generator system ( $^{44}\text{Ti}/^{44g}\text{Sc}$ ), which would meet the demand for a convenient supply of  $^{44g}\text{Sc}$  concerning radiopharmaceutical applications (positron emission tomography (PET), [96]). Strategies for such a generator system were already investigated back in the 1960ies-1970ies ([97], and references therein), while more recent publications report already on improved designs [98, 99] and demonstrated the feasibility to obtain highly pure carrier-free  $^{44g}\text{Sc}$  fractions. From this point of view, the evaluation of a recently presented  $^{44}\text{Ti}/^{44g}\text{Sc}$  generator, based on the TEVA resin, is also tied to this topic, but suggests the development of new extractants suitable for  $^{44}\text{Ti}$  retention with improved efficiency [100]. As a result, providing  $^{44}\text{Ti}$  in sufficient amounts would enable a potential off-site availability without the need for a cyclotron and a subsequent chemical separation from the target. This is usually required, when considering the direct production routes used to produce  $^{44g}\text{Sc}$ :  $^{44}\text{Ca}$  (p,n)  $^{44g}\text{Sc}$  [101], and references therein), or alternatively via  $^{48}\text{Ti}$  (p,x)  $^{44g}\text{Sc}$  [102]. However, for such production routes, it is recommended to utilize an isotopically enriched target, which causes high production costs.

Moreover, complementary to the production route via spallation reactions (e.g.,  $^{nat}\text{V}(\text{p},\text{x})$ ),  $^{44}\text{Ti}$  can be produced by proton irradiation of natural  $^{45}\text{Sc}$  ( $\theta = 100\%$ ) using the  $^{45}\text{Sc}(\text{p}, 2\text{n})^{44}\text{Ti}$  reaction (Fig. 1.6), which was reported first in 1953 by Sharp & Diamond [103].

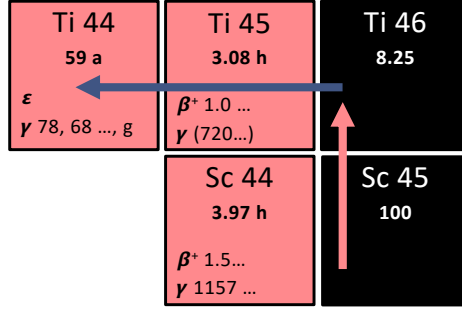


**Fig. 1.6:**  $^{45}\text{Sc}(\text{p},2\text{n})^{44}\text{Ti}$  production path.

Concerning  $^{41}\text{Ca}$  and  $^{26}\text{Al}$ , these are long-lived radionuclides with half-lives of  $(7.17 \pm 0.24) \times 10^5$  years [104] and  $(9.94 \pm 0.15) \times 10^5$  years [105], respectively. Calcium-41 decays to the ground state of  $^{41}\text{K}$  by pure electron capture (EC), emitting X-rays and Auger electrons of very low energy ( $<3.6$  keV, [105]). Since early on, its application was linked to, e.g., long-term biological studies of calcium kinetics in bones [106, 107], or for dating of meteorites shown by Klein et al. [108]. Aluminium-26 decays to the ground state of  $^{26}\text{Mg}$  by either EC or positron emission, with a distinct  $\gamma$ -ray ( $E_\gamma = 1808.7$  keV) and a high emission probability ( $I_\gamma = 99.76\%$ ) [105]. The nuclide is predominantly associated with astrophysical research and is well-known for being the first cosmic  $\gamma$ -ray emitter to be identified in the Universe [109].

Besides their actual practical application, a further scientific merit is given when specifically determining their excitation-functions for the  $^{nat}\text{V}(\text{p},\text{x})$  reaction. Generally, this allows for yield estimations that can be applied regarding, e.g., structural components and shielding, used in accelerator-driven systems (ADS). The ADS' components are usually exposed to intense, long-term particle irradiations. Depending on the chemical composition, numerous radioactive isotopes are generated and contribute to the resulting radiation dose rate. Knowledge of the  $^{nat}\text{V}(\text{p},\text{x})$  reactions' cross-sections helps thus estimating this dose rate concerning the potential vanadium content in the structure materials.

As an example, in the past seven decades, the proton-induced reactions on vanadium targets were described in over two dozen scientific reports and the production cross-sections of a multitude of nuclides at various incident proton beam energies were reported [110]. Interestingly, the production cross-sections of  $^{41}\text{Ca}$  and  $^{26}\text{Al}$  were never reported; potentially, due to difficulties in accurately determining the produced number of atoms or activity for  $^{41}\text{Ca}$  and  $^{26}\text{Al}$ . Generally, for their quantification highly sensitive measurement methods are required to accurately quantify them as spallation products, especially when the produced amounts are low. Besides their determination via gamma-spectrometry ( $^{26}\text{Al}$ ), and LSC ( $^{41}\text{Ca}$ ), AMS measurements have emerged as being the leading technique way of determining small amounts of these long-lived radionuclide (e.g., [111–114]), while tackling also technical difficulties, such as the  $^{41}\text{K}$ -signal suppression with respect to  $^{41}\text{Ca}$  measurements [115]. However, before such measurements, a radiochemical separation is required, followed by a careful sample preparation, to provide pure and suitable samples for the foreseen measurements.

## 1.3 Goal of the thesis

In the view of the previous assessment, the main goal of this thesis was to develop a robust and selective radiochemical separation procedure that will allow to isolate  $^{32}\text{Si}$  from the proton-irradiated metallic vanadium discs (STIP-6). Ultrapure  $^{32}\text{Si}$  samples shall be delivered with both high activity concentrations (kBq  $^{32}\text{Si}$  per g solution) and high specific activities (kBq  $^{32}\text{Si}$  per  $\mu\text{g}$  of Si). These samples should be chemically stable and  $^{32}\text{Si}$  needs to be available in sufficient amounts for basic scientific investigations and to produce reference material (e.g., AMS standards). Further, the following boundary conditions within the SINCHRON-collaboration were defined as follows:

- ① Duly manufacturing of a preliminary  $^{32}\text{Si}$  sample which is suitable to allow for the development and improvement of the involved measurement techniques.
- ② Studies on silicon chemistry for the development of long-time stable compounds.
- ③ Investigation of suitable sample matrices, suitable for producing samples for all of the intended measurements.
- ④ Development of a chemical purification procedure to remove ultra-traces of  $^{32}\text{S}$  (interfering isobar).
- ⑤ Ultimately, manufacturing a  $^{32}\text{Si}$  master solution, with a volume of 20 mL and a required total activity of  $A(^{32}\text{Si}) \approx 2 \text{ MBq}$  that will be used for a first iteration of the half-life determination.

Besides, due to the availability of a small batch of seven proton-irradiated vanadium discs (irradiation took place  $\approx 30$  years ago, in Sweden and France), we set further goals, apart from the ones aforementioned. Due to their much shorter irradiation time, these discs were considered as rather inactive. However, because of using a monitor function for the precise determination of the proton flux it appeared possible to determine production cross-sections for the nuclides of interest, which are created as by-products due to spallation. Consequently, the further goals to be accomplished were set:

- ⑥ Determination of the excitation function for  $^{\text{nat}}\text{V}(\text{p}, \text{x})^{44}\text{Ti}$
- ⑦ Determination of the production cross-section for  $^{\text{nat}}\text{V}(\text{p}, \text{x})^{41}\text{Ca}$
- ⑧ Determination of the production cross-section for  $^{\text{nat}}\text{V}(\text{p}, \text{x})^{26}\text{Al}$

As a result, further radiochemical separation procedures were to be developed to allow isolation of these nuclides from a vanadium matrix, and to determine their activity and hence their cross-sections.

Consequently, with the results of this thesis, we could extensively study vanadium as a target material and provide extremely rare, naturally, and non-naturally occurring isotopes in a pure state, of which  $^{32}\text{Si}$  is provided in a worldwide unique amount.



## 2 Theoretical Background

### 2.1 Chemical separations

In recent decades, the selective removal of toxic metal ions from diluted or concentrated solutions has received much interest [116]. Here, particularly the nuclear industry's requirements have significantly aided in the development of methods and materials for ion chromatography (IC). However, additional applications, such as the growing demand for cleaner water, have refocused attention on the need to improve existing treatments. As a result, IC is used in a wide variety of fields other than the nuclear industry, where distinct principles apply. Furthermore, while the fundamentals and theory of IC are covered in greater detail in a variety of textbooks (e.g., [116], [117], [118], [119]), this section will discuss the specific aspects of IC methodologies that are advantageous for following the processes developed and presented in this thesis.

#### 2.1.1 Separations using ion-exchange chromatography

Although commercially available exchange resins have a wide range of applications, they all share certain chemical and physical properties. Chemically, ion-exchangers are made up of a polymer skeleton and a functional group that is either directly connected (simple groups) or indirectly connected via another group (compose groups). The skeleton is typically composed of a cross-linked copolymer formed of vinylbenzene (VB) and divinylbenzene (DVB). DVB is chemically very similar to VB, except that it contains an additional vinyl group. The chains formed by the polymerization of VB are linked together via DVB groups (Fig. 2.1). A higher percentage of DVB used during polymerization results in a greater degree of chain cross-linkage. The advantages of higher cross-linked resins are that those resins swell less in aqueous solution and have increased mechanical strength. Simultaneously, however, the resin beads' porosity decreases. This means that the exchanger has fewer functional groups per volume. Although the solute is more easily absorbed by the functional groups, this results in a less quantitative ion-exchange process [120]. To balance the various effects, the majority of commercially available resins contain between 4% and 8% cross-linkages. Apart from the fact that DVB-based ion-exchange resins (IER) exhibit sufficient physical and chemical stability under a variety of conditions, it is relatively simple to introduce the ion-exchange sites that primarily govern an IER's chemical behavior, allowing for its classification. Four distinct types are used in general, each distinguished by its functional groups ( $R$  = Resin), also known as ionogenic groups. To exchange cations, strongly acidic (e.g., sulfonic,  $R\text{-SO}_3\text{H}$ ) or weakly acidic (e.g., carboxylic,  $R\text{-COOH}$ ) functional groups are introduced, whereas resins for exchanging anions contain basic functional groups such as quaternary amino groups (e.g.,  $R\text{-N}^+(\text{CH}_3)_3$ ) for strongly basic resins are used, and, e.g., secondary amino groups ( $R\text{-NH}^+(\text{CH}_3)_2$ ) characterise weak anion exchangers. Table 2.1 summarizes these differences. For example,  $R\text{-SO}_3\text{H}$  indicates that the ion-exchanger is in the  $\text{H}^+$  (hydrogen) form, while the  $\text{Na}^+$ ,  $\text{Ag}^+$ ,  $\text{Ba}^{2+}$  forms are also frequently used, allowing to have the resin in the sodium, silver, or barium form, respectively. For anion-exchangers, typically the  $\text{Cl}^-$  (chloride),  $\text{NO}_3^-$  (nitrate), and  $\text{OH}^-$  (hydroxide) forms are used.

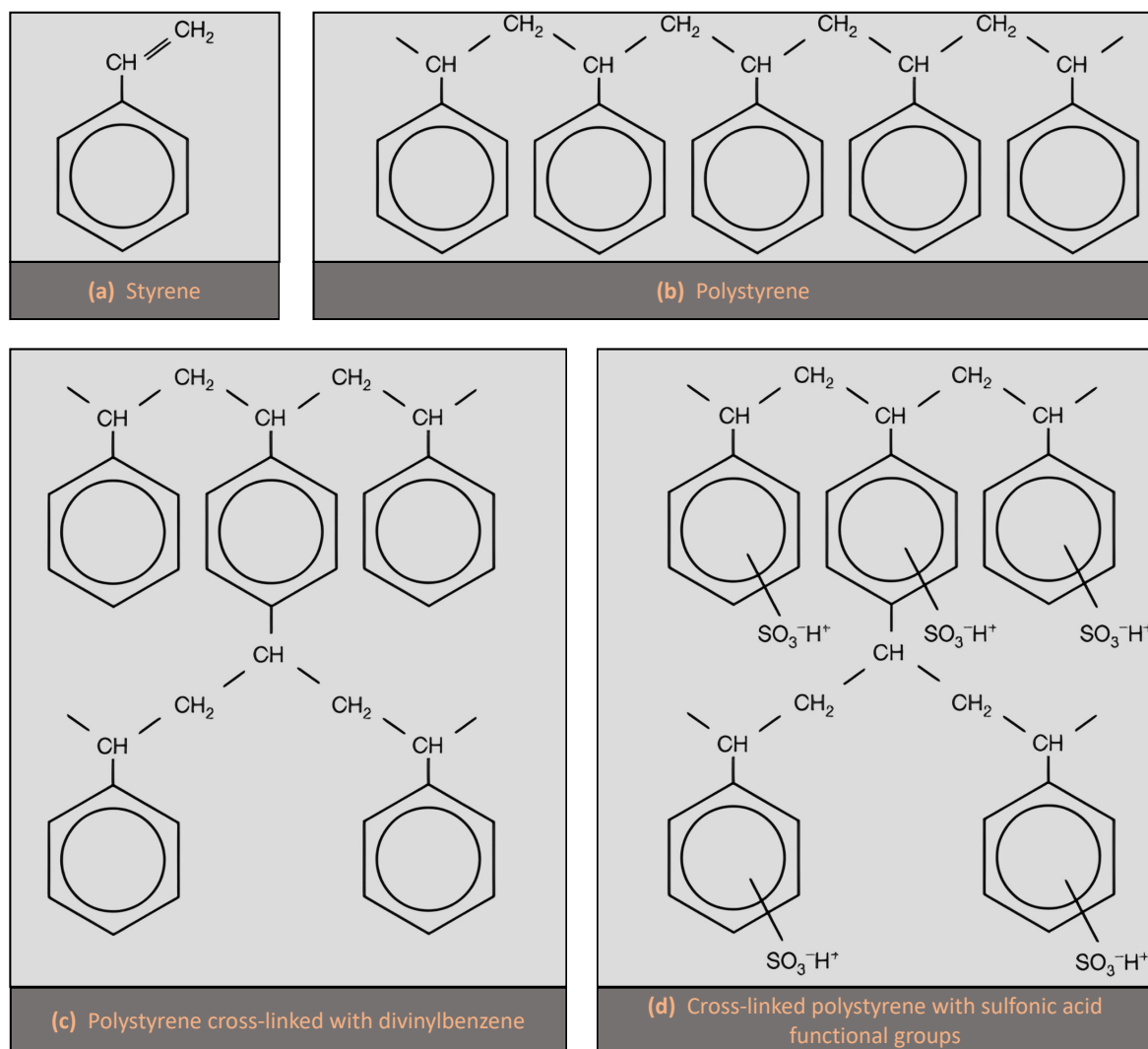


**Fig. 2.1:** The matrix of synthetic ion-exchange resin is composed of (b) polystyrene chains formed from (a) styrene. The matrix (c) of the resin is composed of polystyrene chains cross-linked with divinylbenzene. Adding functional groups to this matrix. The structure of a strong cation-exchange resin containing sulfonic acid functional groups is depicted in panel (d). Picture modified after Schönbächler & Fehr [121], and text adopted accordingly.

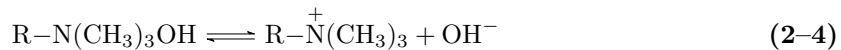
**Table 2.1:** Basic classification of ion-exchangers.

Ion Exchanger	Type	Ionogenic Group
Cation Exchanger	Strongly Acidic	R-SO <sub>3</sub> H; sulphonic
	Medium Acidic	R-PO(OH)O <sub>2</sub> ; phosphonic
	Weakly Acidic	R-COOH; carboxylic
Anion Exchanger	Strongly Basic	R-N <sup>+</sup> (CH <sub>3</sub> ) <sub>3</sub> (OH <sup>-</sup> ); Type I
		R-N <sup>+</sup> (CH <sub>3</sub> ) <sub>2</sub> C <sub>2</sub> H <sub>4</sub> OH (OH <sup>-</sup> ); Type II
	Medium Basic	Mixture of tertiary amines and quarternary ammonium groups
	Weakly Basic	amines, polyamines

Thus, based on this concept, acidic ionogenic groups in the  $H^+$  form dissociate with the release of the  $H^+$  ion, according to Eq. 2-3 (e.g., for strongly acidic cation-exchanger):



While the basic ionogenic groups in the  $OH^-$  form release  $OH^-$  ions, , according to Eq. 2-4 (e.g., for strongly basic anion-exchanger):



The aforementioned processes can be quantified using the apparent dissociation constants of the corresponding cation or anion-exchangers. These values are presented in Table 2.2 for several fundamental types of ionogenic groups, and thus cover a range of pH values relevant to the intended use in an experiment.

**Table 2.2:** Values of apparent dissociation constants of characteristic ionogenic groups of ion-exchangers ( $pK = -\log_{10}(K)$ ), and are R being the ion-exchanger's polymer backbone (= Resin).

Ion Exchanger	Ionogenic Group	$pK_a$ and $pK_b$
<b>Cation Exchanger</b>		
	R-SO <sub>3</sub> H	1
	R-COOH	4-5
	R-OH (phenolic)	9-10
<b>Anion Exchanger</b>		
	R- $\overset{+}{N}R_3$ ( $OH^-$ )	1
	R-NHR, R-NR <sub>2</sub>	3-5
	R-NH <sub>2</sub>	6-9

Additionally, when working with specific ionic forms, ion-exchanger affinity and selectivity become critical. Because ion-exchange is reversible, the exchange reactions between the stationary phase (the ion-exchanger) and the ions in a dissolved electrolyte can be expressed as follows (Eq. 2-5):



where G denotes the functional group's form of the ion-exchanger ( $G = H^+$ ,  $Na^+$  et cetera) and  $Z^+$  denotes the ion in solution. Equilibrium concentrations of ions involved in the exchange are not identical. It is critical to consider both the relative affinity of reacting ions for the ion-exchanger and their initial concentration.  $K_d$  studies on this subject indicate that ion affinity increases with ionic charge. As a result, polyvalent ions are more tightly bound to the exchanger than monovalent ions. Radii of hydrated ions are inversely proportional to affinities for similar charged ions. The literature contains a comprehensive series of affinity, also known as the lyotropic series. The order in which these series of affinities appear varies according to the exchanger and the conditions, respectively. Consequently, selectivity is a term that refers to the difference in the affinity of two ions. Notably, from the perspective of analytical practice, it is critical to control resin selectivity.

The following factors affect the ion-selectivity [118]:

- (i) The selectivity of the ion-exchanger increases as the amount of cross-linking substance increases.
- (ii) Ions with a smaller effective hydrated ionic radius are favored for adsorption.
- (iii) If the resin's ionogenic group forms an ionic pair with the reacting ion, the selectivity of the resin toward this type of ion is increased.
- (iv) If substances in the solution form compounds that are fairly little dissociated, ions that form compounds that are more dissociated are preferentially adsorbed.
- (v) As the temperature of the resin increases, its selectivity decreases. A fact that can be explained by the notion that the decrease in the ionic hydration shells causes the difference between the effective hydrated ionic radii of the reacting ions to decrease.

In this work, Dowex<sup>®</sup> 50WX8-200 (cation exchange resin) and Dowex<sup>®</sup> 1X8 (anion exchange resin) was used. During the development, these two resins were replaced with analytical grade (AG<sup>®</sup>) resins, which are then referred to as AG<sup>®</sup> 50WX8-200 and AG<sup>®</sup> 1X8 (TrisKem SAS, Bruz, France). The advantage over Dowex<sup>®</sup> is that these resin beads have a low extractable content, a narrower particle size distribution, and are extensively purified in advance to remove both organic and inorganic impurities [122], saving time owing to the absence of additional washing steps before their use.

#### 2.1.1.1 Specialized ion-exchange resins: Chelating resins

Chelating resins (CRs) are understood as a class of ion-exchange resins. But as opposed to traditional ion-exchange resins, the mechanism is not based on electrostatic action. CRs catch metal ions with a functional group that forms a chelate with the metal ion, thus readily coordinate with these [123]. The underlying mechanism is based on the general principle that two or more electron donor elements, e.g., nitrogen (N), sulfur (S), oxygen (O), and phosphorous (P) are needed (functional atoms) for coordinating to form a stable structure, similar to small molecule chelates. Examples include therefore the N-O type, S-N type, N-N type, O-O type, or the well-known iminodiacetic group  $[R-NCH_2COO^-]_2$  et cetera [124]. Because of these chemical properties, chelating resins exhibit a stronger binding force and higher selectivity with metal ions compared to the traditional ion-exchange resins. Typical applications include rare earth recovery [125] and the removal of trace impurities such as iron in hydrometallurgy [126]. In this work, the Monophos<sup>®</sup> resin (TrisKem SAS, Bruz France) was used and according to the supplier [127], this resin is comprised of a polymer support (Polystyrene-DVB) which has been functionalized with monophosphonic ( $R-PO(OH)_2$ ) and sulphonic acid ( $R-SO_3H$ ).

## 2.1.2 Separations using extraction chromatography

The idea behind the concept of extraction chromatography (EXCO) was already describe more than 40 years ago [119]. EXCO is considered a particular form of chromatography and is also referred to as solid-state extraction or reversed-phase partition chromatography. The term EXCO applies since liquid extractants are adsorbed onto the surface of inert solid support material. As a result, EXCO uses the favorable selectivity features of the organic compounds used in liquid-liquid extraction and allow separation of ions with similar ionic radii and charge. This enables a high degree of selectivity. Additionally, because it can be easily packed into columns, it benefits from the multistage nature of the chromatographic process. The active ingredient, the extractant (either a liquid itself or dissolved into a diluent) is absorbed onto a porous small-sized resin particle backing material. The system is very similar to ordinary liquid-liquid extraction, except that the solvent is in this case absorbed as a thin layer onto the surfaces and in the pores of the solid resin particles. Extraction of a metal is essentially a mass transport through the liquid-liquid interface driven by complexation with an organic soluble extractant and is therefore strongly dependent on the available surface. Thus, small, and uniform particle sizes result in large surfaces of the extraction chromatographic resin, which makes it efficient to achieve high separation factors. However, EXCO is well suited to remove trace-impurities (purification procedures) but less so for separations involving higher metal loadings (bulk matrix separations). The reason is that extraction chromatographic resins, being mostly porous polymeric backing material, exhibit a low volume concentration of the extractant. Therefore, typical working capacities ranges from a few mg to a few tens of mg metal per milliliter resin [128, 129]. For example, large-scale separations would require a large amount of resin, which would result in a large amount of liquid, and thus waste.

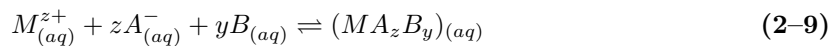
In contrast to the ion-exchange chromatography process, EXCO is based on complex processes involving a variety of different interactions and equilibria [119]. Generally, when a metal ion ( $M^{Z+}$ ) is extracted into an organic phase via the aqueous phase (Eq. 2-6), an equal amount of anions  $A^-$  is extracted as well (Eq. 2-7):



From there, two models can be used to describe the extraction process of a cation. Both models have a two-stage extraction process, but they differ slightly: According to Model I, the extractable neutral species are formed in the aqueous phase and then transformed into the organic phase. Thus, Eq. 2-6 shows the resulting extraction, whereby Eq. 2-8 describes the process at first:

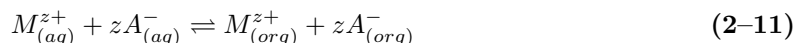


In order to obtain an extractable species, in many cases the complex  $MA_z$  must be solvated by organic molecules (B) having electron donor properties (lewis bases). Eq. 2-7 is therefore further expanded into Eq. 2-9, and Eq. 2-10, respectively, that ultimately describes the extraction process:





The second model (Model II) postulates that equal amounts of both cations and anions are transferred from the aqueous to the organic phase (Eq. 2-11) and then associate to form a neutral molecule following Eq. 2-12:



It is stressed that neither of the models is capable of accurately describing the extraction chromatographic process in its full extent. Thus, in the majority of cases, the extractable species is formed at the phase boundary, allowing for the formation or association of complexes to occur concurrently with the transfer process. However, because the extractable complex and extractant are both large hydrophobic molecules, their equilibrium concentrations are typically very low (in the aqueous phase). As a result, they are unimportant chemically during the EXCO.

The decision between the two approaches is driven primarily by practical considerations. Model I is particularly well-suited for describing the extraction of charged cations, whereas Model II is particularly well at describing the extraction of charged ions with large radii. Both contribute to a simplified description and understanding of the fundamental interactions that govern the magnitude of extraction and the differences in extractability between different cations [119].

The extraction resins used in this thesis were the LN and the DGA resin. LN was chosen, because its complexation mechanism allows for ideal extraction performance at lower acidities and, furthermore, the supplier provides extensive information concerning its distribution coefficients ([130], and references therein). Similarly, extensive data is provided for DGA ([131], and references therein), too, that allows to ideally alter the experimental conditions to reach favourable chemical conditions.

Chemically, The LN resin is impregnated with an organophosphorus extractant, HDEHP (di(2-ethylhexyl)orthophosphoric acid). DGA is either comprised of N,N,N,N'-tetra-n-octyldiglycolamide (normal) or N,N,N',N'-tetra-2-ethylhexyldiglycolamide (branched). The chemical structure of the LN resin and DGA (normal) resin is shown in Fig. 2.2

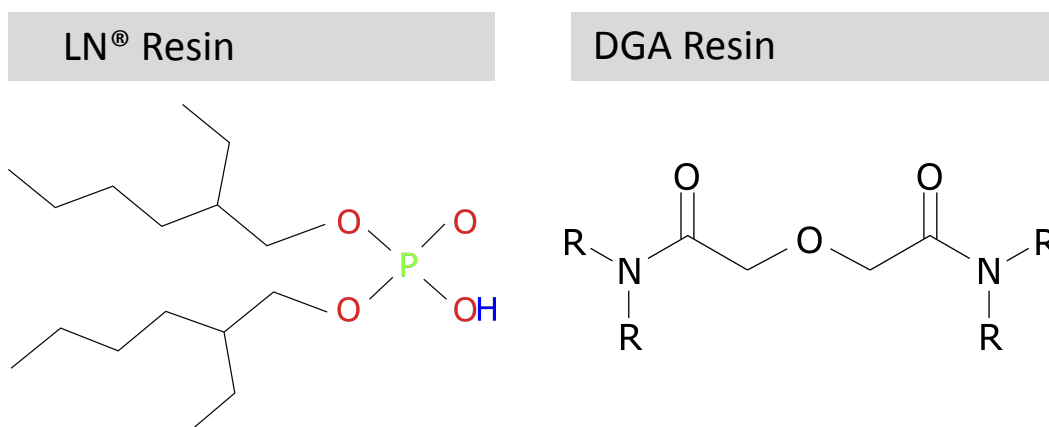


**Fig. 2.2:** Active component of LN<sup>®</sup>, namely the Di(2-ethylhexyl)orthophosphoric acid, and the active component of the DGA resin extractant with R = C8 ((CH<sub>2</sub>)<sub>7</sub>CH<sub>3</sub>).

## 2.2 General theory of column chromatography

The main performance characteristics regarding column chromatography are presented, as there are essential properties concerning the stationary phase, such as: Retention, Selectivity, Resolution, Capacity, Physical and Chemical stability. These characteristics are for ion-exchange and extraction chromatography similar, with some exceptions because of the different underlying mechanisms which are briefly introduced in the following sections.

### 2.2.1 Retention

The retention of a particular element (typically a dissolved metal) is determined by the distribution of the element between the stationary phase loaded on the support and the aqueous phase used as the eluent. Assume one can describe the distribution of a solute between the mobile phase and stationary phase using the equilibrium reaction (Eq. 2-13):



where  $S_{(mobile)}$  is the solute in the mobile and  $S_{(stationary)}$  is the solute in the stationary phase. Hence, to evaluate the efficacy of that process, one must consider the total concentration of the solute in each phase, which one refers to as the distribution coefficient ( $K_d$ ) and shown by Eq. 2-14:

$$K_d = [S_{(stationary)}] / [S_{(mobile)}] \quad (2-14)$$

Similarly, if extraction chromatography is considered, an equilibrium is reached (Eq. 2-15) as the solute is extracted from the aqueous phase ( $S_{(aq)}$ ) into the organic phase ( $S_{(org)}$ ):



Hence, the distribution coefficient is expressed by Eq. 2-16:

$$K_d = [S_{(org)}] / [S_{(aq)}] \quad (2-16)$$

Here, the equilibrium of the solute between the mobile phase and the stationary phase is essentially treated as identical to the equilibrium in a liquid-liquid extraction, but there is a significant distinction that must be considered. In a liquid-liquid extraction that occurs in a separatory funnel, the two phases are in constant contact, allowing for a true equilibrium. In chromatography, the mobile phase is continuously in motion. A solute that moves from the mobile phase to the stationary phase will equilibrate back into a different portion of the mobile phase; this does not accurately describe equilibrium. However if the mobile phase's velocity is slow, relative to the kinetics of the solute's movement, an equilibrium process can be assumed.

### 2.2.2 Selectivity

With respect to a chromatographic system, the term selectivity is a measure of how efficiently two components can be separated. Hence, it describes the ability of the stationary phase to display suitable distribution coefficients which is related to the preference of the resin for one specific ion over another ion. As a result, ions with a high relative selectivity readily replace those with a lower selectivity, whereas the converse reaction requires a large excess of the ion with the lower selectivity. Thus, the selectivity of a chromatographic system is strictly dependent on the nature of the stationary phase (e.g., cation ion-exchange resin or extractant), and ultimately results from a suitable combination of the aqueous/organic phase for the solute and eluent.

### 2.2.3 Resolution

As with any other type of chromatography separation (e.g., HPLC, TLC), the resolution of an ion-exchange experiment is critical. Here, the resolution is understood as the difference between the peak's maximum and its average base width. Therefore, the resolution is a measure of the relative separation of two peaks and can be used to ascertain whether further optimization of the chromatographic procedure is required [132].

Generally, the resolution capability of a chromatographic column is expressed in terms of theoretical plates. The theoretical plate heights (HETP) are useful for comparing column beds with varying dimensions. A column's HETP characteristics are determined by a variety of factors. When it comes to ion-exchange chromatography, for example, the resin particle size is critical. For EXCO, for example, the organic phase diffusion coefficient of the extracted complex is critical [119].

Additionally, the flow rate is vital in both systems, as it determines the time period during which the solution (mobile phase) can interact with the stationary phase. In general, such characteristics must be considered in order to achieve an entirely satisfactory separation between the peaks, and thus the various elements. Additionally, the resolution can be changed depending on the matrix involved, allowing a stepwise elution. From a practical standpoint, a well-known example is the lanthanide separation, which is well documented in the literature (e.g., [133]). Here,  $\alpha$ -Hydroxyisobutyric acid ( $\alpha$ -HIBA) is used to elute this series in steps. Obviously, a high resolution is required to obtain radiochemically pure fractions, and this is even more critical when using a stepwise elution method.

### 2.2.4 Capacity

This property of an ion-exchange resin quantifies its capacity to accumulate sorbed substances. Exchange chromatography requires a sufficient number of ion-exchange sites to accommodate and exchange the solute ions. Three of the most frequently used definitions, however, are introduced here:

- *Theoretical Specific Capacity*

Specifies the amount (mmol) of ionogenic group per mass (g) of dry ion-exchanger. If not otherwise stated, the capacity should be reported per mass (g) of the  $H^+$ -form of a cation-exchanger and of the  $Cl^-$ -form of an anion-exchanger.

- *Practical Specific Capacity*

It is usually expressed in milliequivalents (milliequivalent is the amount of substance needed to combine with 1 mL of 1M  $H^+$ ).

#### ■ *Break-Through Capacity of Ion-Exchange Bed*

It represents the quantity of ions sorbed by per gram of the dry ion-exchanger when the ion initially appears in the effluent or the ion concentration in the effluent reaches a specified value.

It is recommended that the number of exchange sites required for practical work remains well below the capacity of the resin, as the ion-exchange behavior changes as the resin approaches saturation [120]. In the distinguished case of EXCO, the capacity of an extraction chromatographic resin is proportional to the amount of extractant present in the column bed, and the maximum capacity is determined by the amount of extractant that can be loaded on the supporting material without being readily drained away by the eluting solutions [119].

### 2.2.5 Physical stability

Commercially available resins for use as stationary phase come in spheres or occasionally granules of a specific size and uniformity to meet the requirements of a particular application. The size and distribution of the particles are determined by the method of mesh analysis, and are a crucial parameter. Smaller particles, for example, provide higher resolution but typically require lower flow rates. In comparison, larger particles enable higher flow rates but result in decreased resolution. In terms of physical stability, such parameters must be known in order to create appropriate experimental conditions. For instance, deep resin beds, small diameter resin beds, extremely high flow rates, and frequent pumping or agitation can all contribute to resin attrition breakage. Thus, mechanical factors can be minimized by understanding the physical constraints imposed by the system and process. For example, if the chemical environment is altered to affect the resin's retention capacity, the resin may undergo rapid shrink-swell. As a result, attrition breakage can occur if the resulting osmotic shock weakens the resin beads' chemical morphology (e.g., [134, 135]). EXCO involves the adsorption of liquid extractants onto the surface of an inert solid support material. Thus, physical stability of the resin is defined here as the tendency for the stationary phase originally loaded on the support to be lost during elution. Extractant losses from the column can occur as a result of dissolution into the eluents or as a result of drainage of undissolved extractant that is retained on the supporting material but is barely retained by the eluent. They may result in the eluate containing an extractant, which is frequently undesirable, as well as a change in the column's characteristics. Although the majority of extractants used as stationary phases are insoluble in aqueous solutions, some of them dissolve significantly in the eluents.

### 2.2.6 Chemical stability

Apart from physical stability, chemical stability of a stationary phase is critical, as various conditions can exist during the experiments. For example, the stationary phase may be harmed by reactions with chemical agents present in the solutions, but the majority of stationary phases are stable in moderately oxidizing and reducing solutions [118]. However, if elevated concentrations of, e.g.,  $\text{HNO}_3$  are used, functional groups can be attacked. As an example, hydroxamates (ZR-resin) can be attacked with concentrations  $>6\text{M}$   $\text{HNO}_3$  which visually turns the resin entirely brown, while losing all of its selectivity at the same time [136]. Additionally, degradation can occur as a result of factors such as light, temperature, and, most notably, radiation ( $\alpha$ ,  $\beta$ ,  $\gamma$ ). During the separation process, the radioactive solution comes into close contact with the stationary phase, resulting in both direct

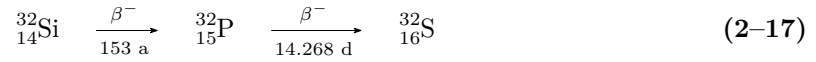
and indirect effects. In terms of the direct effect, radiation instantly ionizes the molecules of the ion-exchange resin, thereby altering their chemical properties. For example, loss of exchange capacity due to functional group degradation is a primary concern because it affects the ion-exchanger's kinetics. Additionally, direct radiation damage may result in an increase in resin solubility due to degradation of the carrier macromolecular skeleton. On the other hand, it may have an indirect effect of radiolysis of water, resulting in the formation of reactive radicals. These reactive products have the potential to further alter and modify the chemical properties of the stationary phase. Conventional inorganic ion-exchangers exhibit excellent thermal stability and resistance to radioactive substances in this application [118]. Concerning extractants, doubtlessly radiation stability is of vital importance for any solvent extraction ligand proposed for separation, as they find application in the nuclear fuel cycle process. Consequently, studies focusing on the radiolytic stability of, e.g., DGA and LN showed that these resins are quite resistant towards alpha-radiation [137]. Further, it was found that DGA degradation rate is five times higher in solvent extraction since the  $\alpha$ -particle is completely stopped in the solvent itself. With respect to EXCO, it could be demonstrated that the quantity of (TO)DGA that leaches from the resin is less than  $10^{-4}\%$  per bed volume. Therefore, EXCO provides enhanced stability of the system, due to the impregnation on the inert support.

## 2.3 Measurement methods

The round robin test, also known as an interlaboratory test, is a critical component of the SINCHRON-collaboration. As a result, multiple independent institutions will conduct measurements in parallel using the same method but with different equipment. To begin, there are several methods for determining a nuclide's half-life, which are discussed and illustrated in the following sections. Additionally, the fundamental principles concerning the measurement techniques are discussed, as well as details on calculating cross-sections using activity determinations.

### 2.3.1 Independent measurements

Equation 2-17 describes the decay of  $^{32}\text{Si}$  along the mass isobar  $A = 32$ , as illustrated in Fig. 2.3:



S 32 94.99	S 33 0.75	S 34 4.25	S 35 87.37 d	S 36 0.01
P 31 100	P 32 14.268 d $\beta^- 1.71066$ no $\gamma$	P 33 25.25 d	P 34 12.43 s	P 35 47.3 s
Si 30 3.092	Si 31 157.36 m	Si 32 153 a $\beta^- 0.2$ no $\gamma$ $\sigma < 0.5$	Si 33 6.11 s	Si 34 2.77 s
Al 29 6.56 m	Al 30 3.62 s	Al 31 644 ms	Al 32 33 ms	Al 33 41.7 ms
Mg 28 20.915 h	Mg 29 1.30 s	Mg 30 335 ms	Mg 31 236 ms	Mg 32 86 ms

**Fig. 2.3:** Part of the “Karlsruhe Nuclide Chart” (10<sup>th</sup> edition; [138]), in which the isobar ( $A = \text{const.} = 32$ ) is highlighted;  $^{32}\text{Si}$  is of special interest.

Related to this decay-scheme, LSC measurements are performed whereby  $^{32}\text{Si}$  is in secular equilibrium with its radioactive daughter  $^{32}\text{P}$ . However, what is also evident from Fig. 2.3 that stable  $^{32}\text{S}$  poses a problem for mass-spectrometric measurements, such as ICP-MS and AMS, as it has the same mass and is therefore a big concern for the determination of the absolute number of  $^{32}\text{Si}$  atoms. As a result, separating sulfur from the initial matrix has also been in the focus when developing the radiochemical separation procedure, which is presented in this thesis.

All in all, the measurements within the SINCHRON-collaboration will be seen as independent, and the reported values will be combined; although for determining the  $^{32}\text{Si}$  half-life, different approaches can be followed.

### 2.3.1.1 The direct method

As previously introduced (see section 1.1.3, Eq. 1–1), the half-life can be obtained by the relation  $T_{1/2} = N \times \ln(2)/A$ . Yet, these two parameters must be determined with high precision and accuracy. First, since  $^{32}\text{Si}$  and its progeny  $^{32}\text{P}$  are pure  $\beta$ /emitters, activity measurements can be obtained from LSC. However, these methods usually suffer from insufficient knowledge of the corresponding counting efficiency, as no commercial standards are available. For this reason, the Triple-To-Double-Coincidence (TDCR) method, and the CIEMAT/NIST Efficiency Tracing (CNET) technique will allow overcoming these problems. For further details refer here to, e.g., [139] or [140] (and references therein). For LSC measurements,  $^{32}\text{Si}$  and  $^{32}\text{P}$  need to be in secular equilibrium, which is achieved after a waiting time of more than 172 days ( $\approx 6$  months), after a chemical separation procedure which usually disturbs the radioactive equilibrium between mother and daughter.

Determining the number of atoms is even more difficult. Until now, the only direct method used was AMS, owing to the low  $^{32}\text{Si}$  abundances in the materials previously used. However, if the  $^{32}\text{Si}$  concentration is high enough, ICP-MS can also be used to determine the number of atoms. However, it is necessary to suppress or sufficiently remove the ubiquitous  $^{32}\text{S}$  via chemical separation procedures, as otherwise a precise separation between the two peaks is hampered. For ICP-MS, the application of isotope dilution mass spectrometry (IDMS), the state-of-the-art technique for quantification, will yield reliable and highly accurate results in this case. This technique has also been successfully applied to determining the half-life of  $^{60}\text{Fe}$  ([141], and see section 1.1.1, Table 1.5). Additionally, AMS will be used to perform independent measurements, which have the advantage of being free of molecular interferences (e.g.,  $^{16}\text{O}_2^+$ , [142]) and additional interferences (e.g.,  $^{64}\text{Ni}^{2+}$ , [142]). AMS is typically used to determine isotopic ratios (e.g.,  $^{41}\text{Ca}/^{40}\text{Ca}$  and  $^{26}\text{Al}/^{27}\text{Al}$ ), which necessitates the use of a reference standard for absolute measurements. However, such a standard does not exist for  $^{32}\text{Si}$ . As a result, the primary challenge for AMS is to determine the  $^{32}\text{Si}$  transmission efficiency in order to derive the total number of atoms. In general, the direct method is considered to produce extremely low uncertainties and is typically used for nuclides with a half-life greater than 100 years [143]. Along with the advancement of more precise measurement techniques, it enabled the reduction of statistical uncertainty and improvement of the accuracy of nuclear data. On this subject, a recent example is the measurement of the half-life of  $^{93}\text{Mo}$  ( $T_{1/2} = 4839 \pm 63$  y, [144]), which resulted in an uncertainty of only 1.3%. Consequently, a determination of the  $^{32}\text{Si}$  half-life would be possible, including a sufficiently low uncertainty.

### 2.3.1.2 The decay method

Similarly, the half-life of a radionuclide can also be deduced by its decay (see section 1.1.3, Eq. 1–2), whereby the relation  $T_{1/2} = \ln(2)/\lambda$  applies. Assuming sufficient material of a radioactive nuclide is available, the change in activity (and thus the instrument reading) over time yields a half-life value when the decay curve is fitted. Liquid Scintillation Counting, Plastic Scintillation, and Ionization Chamber are all applicable measurement techniques in this case. However, ionizing chamber measurements are difficult for a pure beta emitter, such as  $^{32}\text{Si}/^{32}\text{P}$ , due to the low ionization current produced by decay-related Bremsstrahlung. Thus, sources to be measured should have a total activity of  $>20$  MBq in order to achieve a reasonable net ionization current that is significantly greater than background. Additionally, the slope is small due to the long half-life, requiring a comparable long measurement time to achieve low uncertainty.

Therefore, this necessitates the use of highly stable measurement systems and sample material. One objective of this project is to prepare  $^{32}\text{Si}$  samples that can be monitored for an extended period of time using Plastic Scintillation or an Ionization Chamber. It should be stressed, however, that these measurements provide only preliminary results after approximately 3–4 years (e.g., [76]). For high-precision measurements, the data acquisition process should be extended significantly. According to a work from Pommé et al. [145] such a measurement time can also be estimated beforehand, in order to determine the measurement time. Thus, if the data are distributed evenly across time, a convenient uncertainty formula for the high-frequency component can be applied. A high-frequency component is described here, as a source of uncertainty that occurs at a rate that is higher than or comparable to the measurement of one data point. The typical example would be counting statistics.

Concerning the decay measurement of  $^{32}\text{Si}$ , only one half-life value of  $^{32}\text{Si}$  is based on such an experiment which was performed by Alburger et al. [76]. The campaign lasted approximately 48 months, beginning in February 1982. During this time period, a 1.6% decline in the count rate was observed, based on the analysis of 53 data points. However, because these changes in the net count rate are so small, the measurement system's stability is critical. Therefore, a  $^{36}\text{Cl}$  ( $T_{1/2} = (3.01 \pm 0.02) \times 10^5$  a) source was used to verify the system's stability. When  $\gamma$ -ray spectrometry is used to determine half-lives, it is common to select a reference source (e.g., [146]). Additionally, half-life determinations using an IC are remarkably precise, allowing for half-life values with uncertainties as low as 0.12% ( $^{65}\text{Zn}$  ( $T_{1/2} = 243.8 \pm 0.3$  d), [147]), or 0.22% ( $^{161}\text{Tb}$  ( $T_{1/2} = 6.9637 \pm 0.0029$  d), [148]). Therefore, this is an extremely promising method for determining the  $^{32}\text{Si}$  half-life. To achieve a comparable level of uncertainty of less than 1%,  $^{32}\text{Si}$  must be measured on a quarterly basis for approximately three years.

## 2.4 Instrumental analysis

The theory of analytical instruments and related procedures is described in detail here. These instruments and procedures were primarily used to develop (radio-)chemical separation procedures, but also to provide information on the samples' purity. Additionally, the validation of the analytical results, i.e., to ensure the results' traceability and comprehensiveness is presented, too.

### 2.4.1 Inductively coupled plasma optical emission spectroscopy

Inductively coupled plasma optical emission spectroscopy (ICP-OES) is a mean of chemical analysis that is commonly used for the quantification of certain elements in a sample. For the analysis, samples are generally dissolved to form an aqueous solution of known weight and dilution. Depending on the final uncertainty of the results, the sample can be prepared via volumetric or gravimetric traced dilution. For the measurements, a sample solution is placed into, e.g., an autosampler. Aspirating the solution into the nebulizer converts it to an aerosol. The aerosol then enters the plasma, where it is transformed into atoms and ions, which are excited and emit light at characteristic wavelengths (Fig. 2.4). The intensity of light for each element's wavelengths is proportional to its concentration.

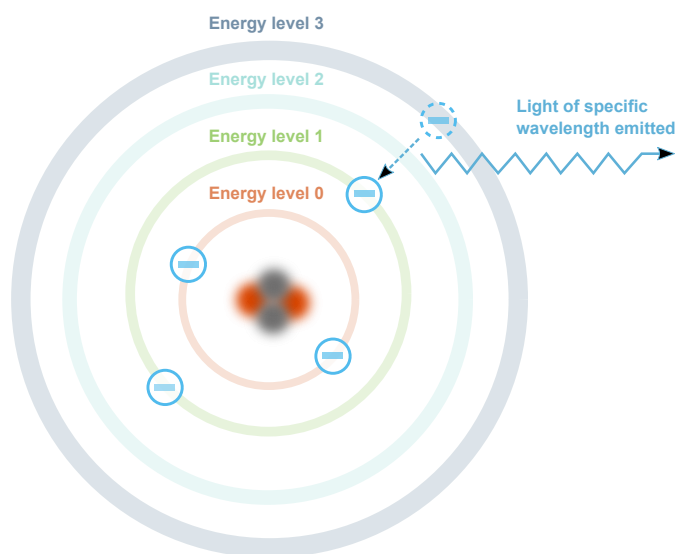


**Fig. 2.4:** When an electron returns from a higher energy level (e.g., Energy Level 3) to a lower energy level (e.g., Energy Level 1), light of a specific wavelength is emitted. The wavelength of the emitted light determines the type of atom or ion (i.e., which element it is) and is related to the energy levels in which the electron is moving (modified after [149]).

Plasma temperatures range typically between 6'000 and 10'000 Kelvin. To avoid a short circuit and subsequent meltdown, the plasma must be isolated. This is accomplished by passing the gas, typically argon or nitrogen, through the torch's outer tube. Additionally, that flow also sustains the plasma (plasma flow) and typically about  $12.0 \text{ L} \times \text{min}^{-1}$  are introduced. In principle, an ICP-OES torch is composed of three concentric tubes, referred to as the outer, middle, and inner tubes, which are typically made of fused silica. The torch's middle tube provides the support gas (auxiliary gas), and is used to elevate the bottom of the plasma from the injector tube (typically:  $1.0 \text{ L} \times \text{min}^{-1}$ ).

Finally, the sample aerosol is introduced into the plasma via the thin (inner) injector tube with a 1–2 mm aperture. Here, a thin jet of sample aerosol is emitted through this opening, which also follows a defined argon flow rate (typically:  $0.7 \text{ L} \times \text{min}^{-1}$ ) that is referred to as nebulizer flow. The torch itself is positioned in a coil, and coupling is accomplished by generating a magnetic field that is oriented vertically in the coil's vertical plane. Ionization of the flowing argon is initiated by a spark from a Tesla coil. The resulting ions and electrons from the Tesla coil then interact with the oscillating magnetic field. This generates sufficient energy to ionize more argon atoms through collision excitation. Electrons produced by the magnetic field are accelerated perpendicular to the torch. At high velocities, cations and electrons, also known as eddy current, collide with argon atoms to produce additional ionization, which causes a significant increase in temperature and allows for the ionisation of the analytes.

As each element emits several specific wavelengths of light in the ultraviolet visible spectrum that can be used for analysis, the selection of the optimal wavelength for a sample depends on a few factors, such as the other elements present in the sample matrix. The light emitted by an element's atoms must be converted to a quantifiable electric signal. This is accomplished by first resolving the light with a diffraction grating and then measuring the wavelength-specific intensity of each element emission line with a solid-state diode array or other photoelectric detector. The concentration of the elements in the sample is determined by comparing the intensity of the sample's emission signals to that of a solution containing the element at a known concentration (reference standard). Figure 2.5 illustrates a comprehensive example of such a measurement routine (Agilent 5110). The emitted light can be analyzed in either the "Radial Mode" (RM, red line) or the "Axial Mode" (AM, blue line). Finally, the Dichroic Spectral Combiner (DSC) technology will enable simultaneous axial and radial measurements. The RM is typically used to determine higher analyte concentrations, whereas the AM is used to determine lower analyte concentrations.

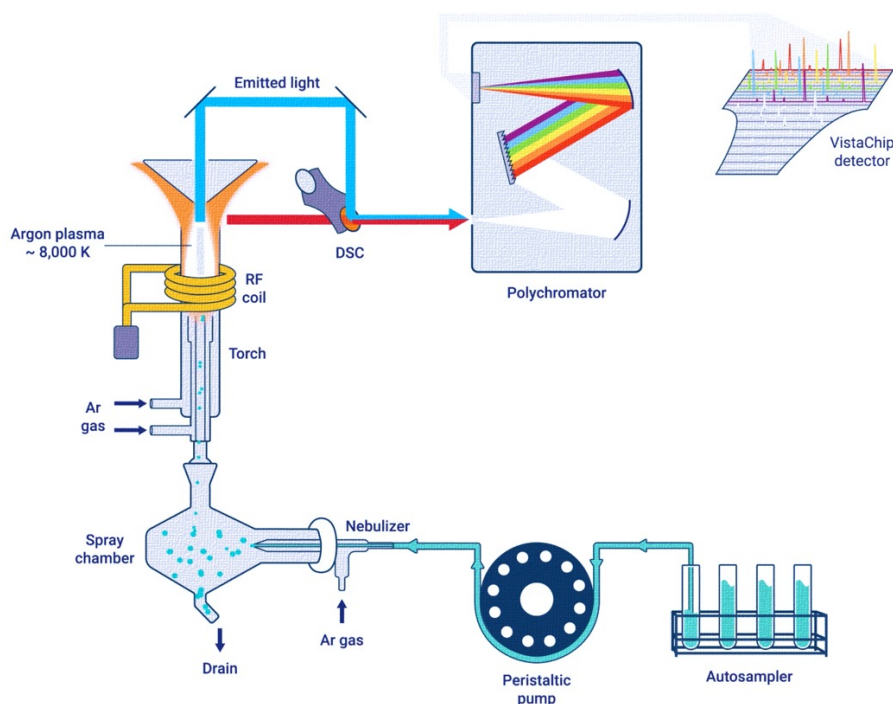


**Fig. 2.5:** Schematic of the ICP-OES principle as applied to an Agilent 5110 (modified after [149]).

## 2.4.2 Gamma-ray spectrometry

The functional principles of a semiconductor are illustrated in Fig. 2.6, as in this case, the High Purity Germanium (HPGe) detector. The valence band and conduction band are the bands that determine the electrical conductivity of the solid. In non-metals, the valence band is the highest range of electron energies in which electrons are commonly present at absolute zero temperature, while the conduction band is the lowest range of vacant electronic states. In semiconductors and insulators, the two bands are separated by a bandgap, while in conductors, the bands overlap. A bandgap is an energy range in a solid where no electron states can exist due to the quantization of energy. The electrical conductivity of non-metals is therefore determined by the susceptibility of electrons to excitation from the valence band to the conduction band. In the case of the HPGe detector, at room temperatures, a few electrons may gain sufficient thermal energy to overcome the bandgap to enter the conduction band. Once the electrons enter the conduction band, they can conduct electricity, as can the hole they left behind in the valence band. The hole is an empty state that allows electrons in the valence band some degree of freedom. This means that at room temperatures, there already exists a tiny current in the semiconductor, which is referred to as the dark current. In order to achieve a good signal-to-noise ratio (SNR), the HPGe detector is cooled down to around liquid nitrogen temperatures. Thus, the electrons would not have enough thermal energy to overcome the bandgap and enter the conduction band. The excitation of the electrons in the valence band could only be triggered by incoming particles with relatively high energies, creating electron-hole pairs. Under an electric field, the electrons are carried away and ultimately collected by the electronics, creating a pulse signal. The software helps record and analyze the incoming signals, and finally, a gamma-spectrum is obtained.

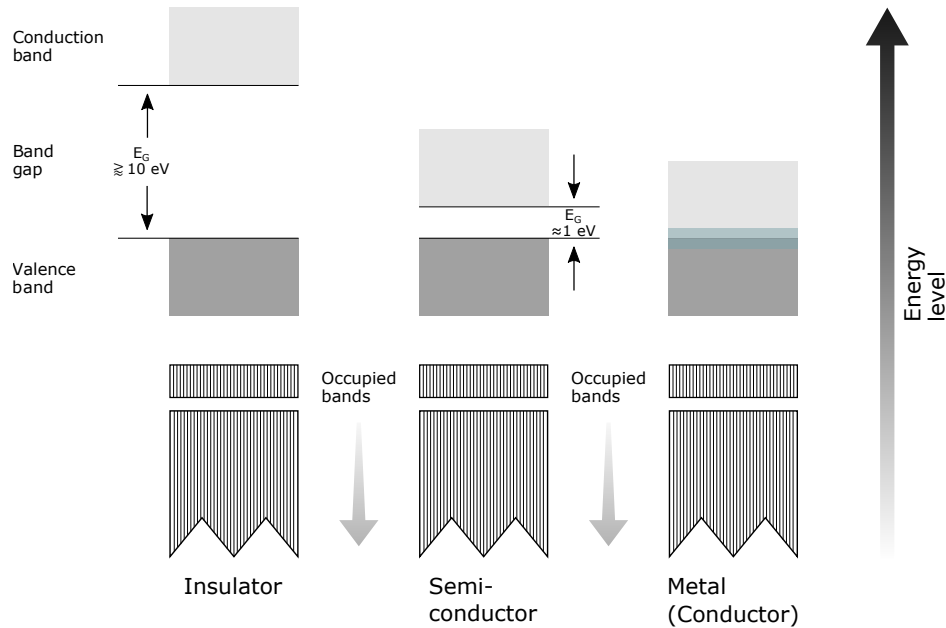


**Fig. 2.6:** Insulator: At room temperature, the valence band is separated from the conduction band by over  $\approx 10 \text{ eV}$ . Thermal excitation cannot promote electrons from the valence band up to the conduction band. Metal: The valence band and the conduction band overlap, so that free electrons are always present and can easily move from atom to atom, creating a current.

### 2.4.3 Liquid scintillation counting

Liquid scintillation counting (LSC) is a nuclear radiation measurement method suitable for both the qualitative and quantification detection of  $\alpha$ ,  $\beta^-$ ,  $\beta^+$ , and electron capture (EC) emitters. Notably, LSC is the only measurement method used in practice for pure, weak  $\beta$ -emitters, such as  $^3\text{H}$ ,  $^{14}\text{C}$ , or  $^{35}\text{S}$ , which are utilized as markers in biochemistry. Besides, LSC is employed to determine low-energy EC emitters such as  $^{41}\text{Ca}$  or  $^{55}\text{Fe}$ , which are considered essential nuclides regarding the dismantling of nuclear facilities [150]. The advantages of LSC are the possibility to measure solutions directly, combined with extraordinarily high efficiency (counting yield) in nuclear radiation measurement technology. Usually, the efficiency is greater than 50% for weak  $\beta$ -emitters- and EC emitters and virtually 100% for alpha and high-energy  $\beta$ -emitters. In contrast, a disadvantage is the laborious sample preparation since radiochemical separations may be required prior to the measurements. Moreover, the chemical compatibility of the sample with the scintillator cocktail must also be ensured. Before measurements, the radioactive sample is typically mixed with the scintillator cocktail directly in a suitable sample container (here: exclusively plastic vials). The interaction of the ionizing radiation with the scintillator cocktail produces flashes of light, which are converted into electrical pulses at the photomultiplier tube (PMT). The PMT consists of a photocathode and several dynodes arranged in a row. The photocathode releases individual electrons after the excitation due to electromagnetic radiation of the appropriate wavelength (usually: wavelength in the near UV range). Subsequently, secondary electrons are created, causing further secondary electron emissions. With this arrangement and the continuous interaction with each dynode, an amplification of the tiny current emitted by the photocathode is ultimately achieved; typically, an amplification of several orders of magnitude is possible (factor of  $10^6$ ). The operating principle of a PMT is shown in Fig. 2.7.

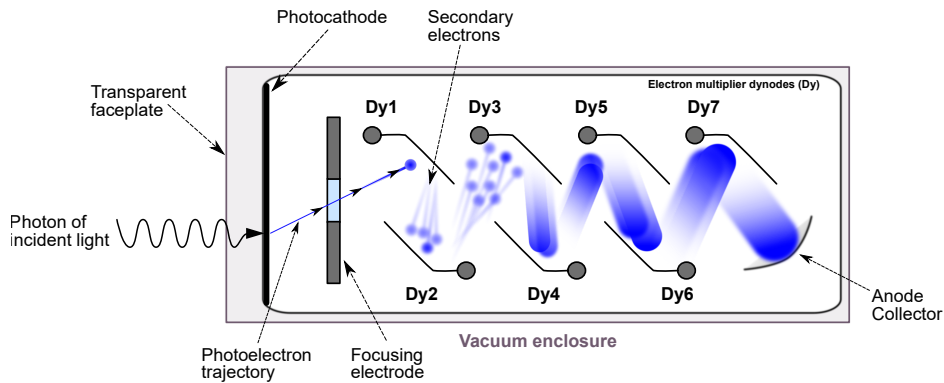


**Fig. 2.7:** Schematic principle of a photomultiplier tube (adopted after [117]).

The amplified electrical signals are sufficiently large to be detected by the measuring electronics. In order to suppress the always present, disturbing thermal noise of the PMT, common LSC instruments are equipped with two PMTs, which are operated in a coincidence circuit. This means that pulses are processed as the "true" signals of the sample are only processed if they are registered almost simultaneously by both photomultipliers. Radioactive decays produce a large number of light quanta so that they lead with a high probability to a coincidence signal. It is improbable that the noise will cause a pulse at both photomultipliers simultaneously.

Modern measuring instruments integrate all necessary components in one housing, sometimes even including the personal computer for evaluation, and are equipped with mechanical systems that automate the consecutive measurement of up to hundreds of samples.

The scintillator liquid usually consists of several components (solvent, primary and secondary scintillator, additives if necessary) and is generally purchased directly as a prefabricated mixture ("cocktail"). Various manufacturers offer a product that differs by adapted compatibility to the different types of samples or safety/environmentally optimized composition. The ionizing radiation emitted during radioactive decay is lost during energy as it passes through the scintillator cocktail until it is entirely decelerated. Its energy is transferred to the atoms of the solvent, which are the main component of the cocktail, and excites them. This excitation energy can exchange between solvent molecules without loss until it reaches the actual scintillator molecules present in the cocktail in comparably small concentrations. The de-excitation of the scintillator takes place via a fluorescence mechanism under the emission of light, which is usually in the near UV range. The number of light quanta generated in the scintillator cocktail is directly proportional to the energy deposited by the nuclear radiation. A so-called secondary scintillator (= wavelength shifter) is often added to the cocktail. The secondary scintillator absorbs the light emitted by the primary scintillator and emits light of larger wavelengths, which is in the optimal range for the photocathodes. Typically, aromatic substances are used as solvents, e.g., toluene, pseudocumene, or long-chain alkylbenzenes, since their  $\pi$ -electron systems are readily excited by the ionizing radiation and pass this excitation energy on well to the scintillator molecules. Many commercially available cocktails contain, in addition to the components required for the actual scintillation, also additives, such as surfactants, which improve the miscibility of aqueous samples with the hydrophobic cocktail. For the measurement, it is necessary that the cocktail is well miscible with the sample and that there is no two-phase formation or turbidity of the resulting mixture. Furthermore, the sample components must not react with the scintillator cocktail's components to avoid a potential chemical reaction between the two. Particularly, concentrated acids and alkalis can cause discoloration of the test solution or destruction of the scintillator.

Concerning LSC, these influences are summarized in the general expression of "Quenching". Regarding the Packard Tri-Carb<sup>®</sup> liquid scintillation counter (e.g., Tri-Carb<sup>®</sup> 2250CA), the quench indicating parameter is referred to as tSIE (Transformed Spectral Index of the External Standard Spectrum) and is calculated from the Compton Spectrum, induced in the sample by the device's standard source (e.g., <sup>133</sup>Ba or <sup>152</sup>Eu). The tSIE thus quantifies the degree of quenching: the value ranges between 0 (highly quenched) and 1000 (unquenched). A distinction is, however, made, and in essence, there are two different types of quenching:

#### **2.4.3.1 Chemical quenching**

Chemical Quenching is caused by the sample's components that absorb the excitation energy of the solution molecules before it can be transferred to the scintillator so that it is lost in terms of light yield. In particular, substances containing electronegative elements such as halogens, oxygen, or nitrogen are potent quenchers. These can be introduced due to organic (e.g., solvents) and inorganic (e.g., concentrated mineral acids) chemicals.

#### **2.4.3.2 Color quenching**

Color Quenching occurs due to the presence of dyes in the sample. These can absorb the light emitted by the scintillator before reaching the photomultiplier. Due to the typical waveband of the light emitted by the scintillator, samples stained with the complementary color yellow in a particular color, which often occurs in the measurement of biological or ferrous samples, exhibit strong color quenching.

The total effect results collectively in energy loss in the liquid scintillation solution. Consequently, as quenching increases, the efficiency of the measurement decreases, and the measured spectrum shifts towards lower energies.

Quenching concerns, therefore, mainly the counting efficiency, which must be considered for each individual sample. Quench correction curves are necessary to determine counting efficiencies, where samples with specific activity concentrations (mainly  $^3\text{H}$ ) are prepared and measured. Different amounts of, e.g., nitromethane is added to the cocktail to vary the counting efficiencies. As a result, an experimental determination of the counting efficiency as a function of tSIE can be provided, specific to the Liquid Scintillation Analyzer. In case the nuclide to be measured is not available to prepare such quench correction curves, different approaches can be followed, to determine the counting efficiency.

#### 2.4.3.3 CIEMAT/NIST efficiency tracing

The name, CIEMAT/NIST efficiency tracing (often abbreviated as: CNET) is linked to the collaboration between the Centro de Investigaciones Energeticas Medioambientales y Technological (CIEMAT) and the National Institute of Standards and Technology (NIST). The objective of the method is to obtain the counting efficiency quench correction curve of any nuclide, applicable to any commercial liquid scintillation analyzer, and any liquid scintillation cocktail [117]. The method is thereby centered on the experimental (measured) quench correction curve of a primary standard, such as  $^3\text{H}$  (e.g., experimental counting efficiency of  $^3\text{H}$  vs. tSIE). Here,  $^3\text{H}$  is chosen since it is considered one of the most suitable standard radionuclides for this method. It is readily available as an absolute standard (e.g., tritiated water), it has a relatively long half-life ( $T_{1/2} = 12.32\text{ y}$ ), and  $^3\text{H}$  provides more sensitive extrapolations to the low-energy portions of beta-particle spectra than higher-energy standards. For more details, the reader is advised to refer to the work from, e.g., Günther [151] or Kossert et al. ([139], and references therein).

Moreover, a dedicated example of applying the CNET Method is provided in the appendix (see section 6.1, Fig. 6.2). In the presented thesis, CNET was used in order to determine the absolute activity in units of disintegrations per minute (DPM), and allowed to eventually determine in-house the activity concentration, by accounting for the specific mass and thus specify the activity of  $^{32}\text{Si}$  and  $^{32}\text{P}$ , respectively, in kilobecquerel per gram solution (kBq/g).

## 2.4.4 Validation

The ISO definition of validation (ISO17025) is described as *"the confirmation by examination and provision of objective evidence that the particular requirements for a specific intended use are fulfilled"*. Further, when method validation is required, it needs to be proven that *"the analytical procedure used for a certain test is appropriate for its intended use"*.

The results from the method validation are then used to evaluate the quality, reliability and consistency of the analytical procedure and is, therefore, a vital part. As a result, some parameters and expressions are introduced that are directly linked to the method validation used in this thesis.

### 2.4.4.1 Limit of Blank (LoB), Limit of Detection (LoD), and Limit of Quantification (LoQ)

Generally, the limit of blank (*LoB*) is taken as the highest apparent analyte concentration expected to be found when replicates of a blank sample containing no analyte are tested [152]. Ideally, the blanks are prepared in a representative procedure in order to achieve the best comparability towards the samples and the respective matrix. Consequently, the limit of detection (*LoD*), is taken as the lowest concentration of an analyte in a sample that can be detected, but not necessarily quantified [152]. Else, if intensities are measured (e.g., using ICP-OES), an evaluation of the *LoB* is vital for each individual measurement, to establish a likely *LoD*, as it is required to reliably differentiate from the blank matrix. The *LoD*, expressed further as a concentration ( $c_{LoD}$ ), or an intensity ( $I_{LoD}$ ), is therefore calculated from the smallest signal which can be detected with reasonable certainty for a given analytical procedure. The value of  $I_{LoD}$  is expressed by Eq. 2–18:

$$I_{LoD} = \bar{x} + k \times s_{Blank} \quad (2-18)$$

where  $\bar{x}$  is the mean of the blank measurements,  $s_{Blank}$  is the standard deviation of the blank measurements, and  $k$  is a numerical factor chosen according to the level of confidence required. Here, the limit of detection is taken to be three times ( $k=3$ ) the standard deviation of the blank measurements, providing a 99.7% confidence level.

Furthermore, the limit of quantification (*LoQ*) may be determined, whereby the analyte can not only be reliably detected but at which some predefined goals for bias and imprecision are met [152]. The value of  $I_{LoQ}$  is expressed by Eq. 2–19:

$$I_{LoQ} = z \times I_{LoD} \quad (2-19)$$

The *LoQ* may be equivalent to the *LoD* ( $k=1$ ), but often  $k$  is set to ten, to ensure a clear signal from noise, with a good safe margin for, e.g., instrument drifts.

### 2.4.4.2 Robustness

The robustness of an analytical procedure is a measure of its capacity to remain unaffected by small, but deliberate variations in method parameters and provides an indication of its reliability during normal usage [153]. Examples of the factors that a robustness test could address are: changes in the

instrument, operator, or brand of reagent, concentration of a reagent, pH of a solution, temperature of a reaction, time allowed for completion of a process [154]. Hence, parameters which play an important role when working with irradiated (radioactive) materials and in the view of the development of a separation procedure that shall provide reproducible results.

#### 2.4.4.3 Selectivity

Selectivity is the degree to which a method can quantify the analyte accurately in the presence of interferences. Ideally, selectivity should be evaluated for any important interference likely to be present. It is particularly important to check interferences that are likely, on chemical principles, to respond to the test. Selectivity is expressed by decontamination factors ( $DCF$ ), which are calculated using Eq. 2–20:

$$DCF \geq \frac{x_i}{x_a} \quad (2-20)$$

Where  $x_i$  denotes, e.g., concentration, activity, net count rates in the initial (reference) sample, and  $x_a$  represents the determined value, e.g., after the treatment (after loading on the resin). Here, the criterion of acceptance for selectivity is  $DCF \geq 100$ , whereas higher values were the objective of method developments.

#### 2.4.4.4 Assessment of uncertainties

This work follows uncertainty estimation rules given in the "Guide to the Expression of Uncertainty in Measurement", abbreviated as GUM ([155], and references therein) and also based on the EURACHEM Guide (ECG) for "Quantifying Uncertainty in Analytical Measurement" [156].

The GUM classifies methods of uncertainty evaluation as either Type A or Type B. The former describes the method of evaluation by statistical analysis of a series of observations, while the latter assumes an a priori distribution for the data and is not based on statistical analysis of repeated measurements. Notably, for Type A, measurement uncertainty combines all parameters, associated with the result of a measurement, which characterises the dispersion of the values that could reasonably be attributed to the measurand. Uncertainty sets the limits within which a result is regarded accurate, i.e., precise, and true. Uncertainty of measurement is comprised of many components. In general, some of these components may be evaluated from the statistical distribution of the results of series of measurements and can be characterised by experimental standard deviations. The other components, which can also be characterised by standard deviations, are evaluated from assumed probability distributions based other information, e.g., from the distributor. According to the ECG the process for the estimation of measurement uncertainties is the following:

- (i) Specify the measurand, e.g., analyte concentration or activity.
- (ii) Identify uncertainty sources, e.g., sampling, instrument effects, uncertainty for certified reference materials (CRM), data processing et cetera.
- (iii) Quantify uncertainty sources by measuring or estimating the size of the uncertainty component associated with each potential source of uncertainty identified.
- (iv) Calculate the combined uncertainty.

Among these, to determine the combined uncertainty is very important. Before the uncertainty can be expressed as standard deviations, one must follow rules for converting an uncertainty contribution (component) to a standard deviation, expressed by Eq. 2-21:

1. Where the uncertainty component was evaluated experimentally from the dispersion of repeated measurements, it can readily be expressed as standard deviation theta ( $\vartheta$ ):

$$\vartheta = \sqrt{\frac{\sum(x_i - \bar{x})^2}{n - 1}} \quad (2-21)$$

Where  $x_i$  denotes the i-th value of the data set,  $\bar{x}$  denotes the arithmetic mean, and n corresponds to the number of data points in the set.

The relative standard deviation (*RSD*) is then given by Eq. 2-22:

$$RSD = \frac{\vartheta}{\bar{x}} \times 100\% \quad (2-22)$$

For results subjected to averaging, the standard deviation of the mean was used as follows (Eq. 2-23):

$$s_{\bar{x}} = \frac{\vartheta}{\sqrt{n}} \quad (2-23)$$

2. If limits (value  $\pm a$ ) are given without a confidence level and there is reason to expect that extreme values are likely, it was applicable to assume a rectangular distribution, with a standard deviation of  $\frac{a}{\sqrt{3}}$ .
3. If limits (value  $\pm a$ ) are given without a confidence level and there is reason to expect that extreme values are unlikely, it was applicable to assume a rectangular distribution, with a standard deviation of  $\frac{a}{\sqrt{6}}$ .
4. The general relation between the combined standard uncertainties ( $u_c(y)$ ) presented in this thesis, are based and calculated on uncorrelated input quantities. For simplification, calculations that involved only a sum or difference of quantities, e.g.,  $y = (a + b + \dots i)$ , the uncertainty is expressed according to Eq. 2-24:

$$u_c(y(a, b, \dots)) = \sqrt{u(p)^2 + u(q)^2 + \dots} \quad (2-24)$$

Where  $u_c(y)$  is the result of the positive square root of the sum of squares of the relative standard deviation. On the contrary, if calculations involved a product or a quotient, e.g.,  $y = (p \times q \times \dots i)$  or  $y = p/(q \times r \dots i)$  the combined standard uncertainty is written as follows (Eq. 2-25):

$$u_c(y(a, b, \dots)) = \sqrt{\left(\frac{u(p)}{p}\right)^2 + \left(\frac{u(q)}{q}\right)^2 + \dots} \quad (2-25)$$

Where the term  $(u_c(p)/p)$  et cetera, are the uncertainties in the parameters, expressed as relative standard deviations. For a validation of the calculation of the combined standard uncertainty in the case of non-correlating input quantities, the Kragten numerical method (KM) [157] was applied. This approach implies a modification of the propagation law of uncertainties concerning the sensitivity factor. As a result, each uncertainty contribution using the KM is calculated between two values of Y: one corresponding to the measured value and the other corresponding

to the measured value but corrected by a term which is the associated or measured uncertainty of this variable [158]. Thus, the advantage of using the KM is that it only requires the mathematical formula used to obtain the measure and the numerical values of the various variables, including their uncertainties. Notably, according to Kragten [157], this method considers also dependences of the variables within the mathematical formulation. This reduces the risks of calculation errors and allows the calculation of uncertainty fairly quickly. From the practical perspective, the analysis is carried out, using a spreadsheet in which a Kragten Matrix is built up to calculate each contribution. For a general example, the reader is advised to refer to the work from Kragten [157] (confer Table 1) in order to review the schematic representation of the spreadsheet method. Consequently, given the number of variables involved, the complexity of partial derivatives that can lead to calculation errors and the presence of dependence between variables is distinctly reduced by the KM.

At last, the expanded uncertainty can be computed. For this, the standard uncertainty ( $u_c$ ) is multiplied by the chosen coverage factor ( $k$ ) to obtain an expanded uncertainty. In this thesis, typically  $k=1$ , unless otherwise stated. Generally, the value of  $k$  is chosen based on the desired level of confidence to be associated with the interval. The expanded uncertainty is required in order to provide an interval which may be expected to encompass a large fraction of the distribution values which could reasonably be attributed to the measurand (Eq. 2-26):

$$u_y = k \times u_c \quad (2-26)$$

When the normal distribution applies and  $u_c$  is a reliable estimate of the standard deviation of  $y$ ,  $k = 1$  defines an interval having a level of confidence of approximately 68.3% ( $1\sigma$ ).

**Table 2.3:** Typical (major) uncertainties for the experimental procedures. Note that in some cases, the uncertainty is much larger e.g., low activities ( $\gamma$ -spectrometry) or low analyte concentrations (ICP-MS, and -OES). The typical uncertainty are the values assumed for in-house analyses only and do not account for measurements performed elsewhere (e.g., LSC at PTB or IRA).

Method	Component	$u(a)/a$ in %	Typical ( $1\sigma$ ) in %	Uncertainty
(SF)-ICP-MS	Pipetting	1-2	$\approx 2.5$	
	Ref. Standard	0.5-1		
	Calibration, Peak fitting	1-2		
ICP-OES	Pipetting	1-2	$\approx 5.0$	
	Ref. Standard	0.5-1		
	Standard Deviation Replicates	3		
	Calibration, Peak fitting	1-2		
$\gamma$ -spectrometry	Pipetting	1-2	$\approx 5.0$	
	Rel. Standard Deviation	1-15		
LSC	Pipetting	1-2	$\approx 3.0$	
	Rel. Standard Deviation	0.5-1		
	Model and decay data	1-2		

For several measurements performed in this thesis, further uncertainty contributions must be taken into consideration, from the likes of target mass, proton fluence, the nuclide's half-life, gamma emission probability, or uncertainties from the reference source (Type B uncertainties).

## 2.5 Nuclear spallation

About the target material vanadium, the production of the rare, exotic radionuclide  $^{32}\text{Si}$  was achieved due to proton-induced spallation, abbreviated in the following as:  $^{\text{nat}}\text{V}(\text{p},\text{x})^{32}\text{Si}$ . Besides radiosilicon, also other rare nuclides were produced during this process, such as  $^{44}\text{Ti}$ ,  $^{41}\text{Ca}$ , and  $^{26}\text{Al}$ , which are then denoted following the same schematic.

In order to provide the 590 MeV (almost 80% of the speed of light) high-energy protons, the irradiation was performed at PSI's acceleratory facility, using the large ring cyclotron HIPA (High Intensity Proton Accelerator). Protons entering the HIPA have already reached approximately 72 MeV (37% of the speed of light) in a pre-accelerator – Injector II, which is a smaller ring cyclotron. A Cockcroft-Walton accelerator serves as the first stage, from which protons are fed into Injector II [159].

The nuclear spallation generally occurs, when high-energy particles collide with individual nucleons in the target material. The spallation reaction is typically described as a two-step reaction: the intra-nuclear cascade ( $10^{-22}$  s) and a subsequent de-excitation ( $10^{-18}$  to  $10^{-16}$  s).

At first, the kinetic energy of the collision due to an incident particle is dissipated in target nucleus by a series of direct hit reactions with protons and neutrons, termed the intra-nuclear cascade (Fig. 2.8). By nucleon-nucleon energy transfer, secondary particles with energies between 20 MeV and the maximum energy of the initial particle are produced inside the nucleus. Some of these secondary particles are ejected from the target nucleus as a result of this intra-nuclear cascade, leaving the nucleus in a highly excited state (Fig. 2.8).

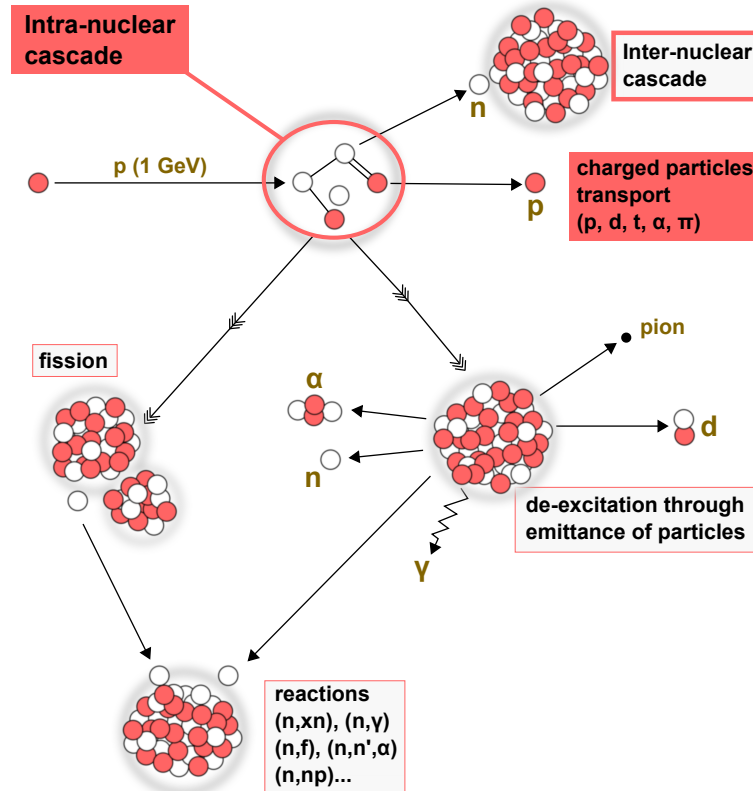


**Fig. 2.8:** Scheme of a nuclear reaction cascade (intra-nuclear cascade) in a target, induced by a high-energetic proton (1 GeV). Also shown the subsequent reactions, related to the inter-nuclear cascade. Figure was adopted from [160] and modified accordingly.

As a result of momentum transfer, secondary particles such as protons, neutrons, pions, and small groups of nucleons are emitted; these particles are all part of the subsequent de-excitation. These extremely energetic secondary particles may interact with other nuclei, resulting in a cascade of secondary spallation reactions. This inter-nuclear cascade generates an increased number of secondary particles and low-energy neutrons. By de-exciting the residual nucleus, the highly excited nucleus relaxes to its ground state. For heavy nuclei, this can happen in two ways: evaporation or high-energy fission. When the nucleus is excited above the energy required to separate one neutron, evaporation occurs. The excited nucleus emits nucleons or light(er) nuclei. If the energy of the target atoms is high enough, high-energy fission is the second important de-excitation channel, which competes with standard evaporation. All reactions caused by primary and secondary particles are accumulated in the so-called internuclear cascade.

### 2.5.1 Nuclear reaction cross-section(s)

When heavy metal targets, such as vanadium (atomic number  $Z = 23$ ) is bombarded with high-energy protons, a wide range of nuclear reaction products, known as residual nuclei, are produced, ranging from  $Z = 1$  to 24. Consequently, there are both stable and radioactive nuclides produced, which are a mix of evaporation and fission products. The amount of fission and evaporation products produced depends on the incident energy of the particle. Cross-sections are today used in all fields of high energy physics, but mainly associated with nuclear physics to indicate a measure of the probability of the interaction between particles (e.g., accelerated protons with atomic nuclei). Although this term is used to express the likelihood of a certain reaction, the dimension of the cross-section is represented by an area. Here, the unit barn is introduced. A barn is defined as  $10^{-28} \text{ m}^2$  ( $100 \text{ fm}^2$ ) and corresponds approximately to the cross-sectional area of a uranium nucleus. The general relation is expressed as follows (Eq. 2-27):

$$1 \text{ barn} = 1 \sigma = 10^{-28} \text{ m}^2 = 10^{-24} \text{ cm}^2 = 100 \text{ fm}^2 \quad (2-27)$$

But, instead of regarding this geometrical cross-sectional area of a nucleus ( $\pi r^2$ ) as a measure of this interaction probability, it is meaningful to ascribe to each nucleus an effective area  $\sigma$  perpendicular to the incident beam. Thus, if a bombarding particle impinges upon any part of such an imaginary surface, only then a reaction can occur. Related processes that can occur are, scattering, absorption and/or nuclear reaction, thereby becoming attenuated. However, the magnitude of a cross-section depends strongly upon the type of reaction (e.g., activation, or spallation), the flux, and the involved energy, respectively. Consequently, the graphical representation of the yield of such a reaction as a function of the particle energy, is referred to as excitation function and is vital when the production yields of radionuclides, e.g., due to spallation have to be estimated or calculated, respectively. Furthermore, the particle beam's intensity is also necessary to calculate the reaction cross-sections. To monitor the intensity, also referred to as flux, indirect determinations can be applied, by means of a well-known excitation function, the so-called monitor response. This method has the advantage that after the irradiation of the specimen, spectrometric analyses (e.g., via  $\gamma$ -spectrometry) can be performed, depending on the involved monitor function. For proton-beams, reactions such as  $^{63}\text{Cu}(p,2n)^{62}\text{Zn}$  (e.g., [161]), or  $^{27}\text{Al}(p,3p3n)^{22}\text{Na}$  (e.g., [162]) are used. In the example of  $^{22}\text{Na}$  ( $T_{1/2} = 2.6019 \pm 0.004 \text{ y}$ , [14]), the activity of the radionuclide can be easily determined, as it can be readily identified using  $\gamma$ -spectrometry, searching for its 1275-keV line. For such irradiation experiments, the stacked-foil technique is used (e.g., [163]), in which the monitor foils (e.g.,  $^{27}\text{Al}$ -foils) are placed between the target element foils. Choosing a suitable arrange of the foils, this allows to compute the flux density curve for the entire sample stack.

## 2.5.2 Determination of the activity in irradiated specimen

First, when a target T is irradiated with monoenergetic protons of energy E, the number of product nuclei ( $N_P$ ) generated by nuclear reactions T(p,x)P is proportional to the product of the cross-section ( $\sigma_E$ ), the flux ( $\Phi_E$ ), and the initial number of target nuclei ( $N_T$ ), according to Eq. 2-28:

$$\frac{\partial N_P(t)}{\partial t} = \sigma_E \Phi_E N_T(t) \quad (2-28)$$

The flux is the number of protons striking the target per unit time and area, whereas the cross-section is the probability of the reaction occurring at that energy, as introduced earlier. When the number of target nuclei  $N_T$  is significantly greater than the number of product nuclei  $N_P$  generated during the time of irradiation ( $t_{irr}$ ),  $N_T$  can be generally considered constant. Obviously, the irradiation time is understood as the time difference between the begin of the irradiation ( $t_{boi}$ ) and the end of irradiation ( $t_{eoi}$ ). Consequently, the relation  $N_T \gg \sigma_E \Phi_E t_{irr}$  usually applies. This condition is achieved with conservative estimation of the values in a very good approximation. As mentioned for the experimental studies, purified vanadium discs with a known averaged mass and chemical purity were initially used for the irradiations. Due to the irradiation, Eq. 2-28 expands further into the following differential equation (Eq. 2-29) by considering the decay of the radioactive product nuclides studied (e.g.,  $^{44}\text{Ti}$ ):

$$\frac{\partial N_P(t)}{\partial t} = \sigma_E \Phi_E N_T(t) - \lambda_p N_P(t) \quad (2-29)$$

where  $\lambda_p$  is the decay constant of the product nuclide. Under the initial condition  $N_P(t_{boi}) = 0$ , the solution of the differential equation becomes the activation equation (Eq. 2-30):

$$N_P(t) = \frac{\sigma_E \Phi_E N_T}{\lambda_p} [1 - e^{-\lambda_p(t-t_{boi})}] \quad \text{with } t_{eoi} \geq t \geq t_{boi} \quad (2-30)$$

In the case where the number of the product nuclei is obtained from the activity of the nuclide by means of  $\gamma$ -spectrometry at the end of irradiation, the following relation is regarded. After the end of the irradiation there are no new product nuclei being produced, and the number of the product nuclei simply follows the law of radioactive decay (Eq. 2-31):

$$N_P(t) = N_P(t_{eoi}) e^{-\lambda_p(t-t_{eoi})} = \frac{\sigma_E \Phi_E N_T}{\lambda_p} [1 - e^{-\lambda_p t_{irr}}] e^{-\lambda_p(t-t_{eoi})} \quad \text{with } t \geq t_{eoi} \quad (2-31)$$

The activity of product nuclei can be determined at the end of a measurement that begins at time  $t_{boc}$  and ends at time  $t_{eoc}$ . With the irradiation flux  $\Phi_E$  known, the activation equation (Eq. 2-30) can be used to calculate the cross-section of the production of the product nuclide, as represented by Eq. 2-32:

$$\sigma_E = \frac{A_p(t_{eoi})}{N_T \Phi_E} \frac{1}{1 - e^{-\lambda_p t_{irr}}} = \frac{C_E \lambda_p}{N_T \Phi_E \epsilon_\gamma I_\gamma} \frac{e^{\lambda_p(t_{boc}-t_{eoi})}}{(1 - e^{-\lambda_p t_{irr}})(1 - e^{-\lambda_p t_{eoc}})} \quad (2-32)$$

Here, the additional parameters such as the device's efficiency ( $\epsilon_\gamma$ ) and gamma-emission probability

( $I_\gamma$ ) need to be known, if the activity is determined via  $\gamma$ -spectrometry. Else, the presented equation also highlights the different sources of uncertainties, related to such experiments with irradiated specimen.

### 2.5.3 Simplification of the calculation of reaction cross-section(s)

With respect to the mentioned parameters ( $\epsilon_\gamma$ ,  $I_\gamma$ ), it is also possible to diminish the need for these two quantities (see section 2.5.3.1). As a result, a simplification of Eq. 2-32 is achieved, leading to Eq. 2-33:

$$\sigma_E = \frac{A_p(t_{eoi})}{N_T \Phi_E} \frac{1}{1 - e^{-\lambda_p t_{irr}}} \quad (2-33)$$

Here, the  $\gamma$ -ray measurement yields the sample's activity during the measurement time  $t_c$  ( $t_c = t_{eoc} - t_{boc}$ ). Given that the radionuclides of interest have a half-life  $T_{1/2} \gg t_c$ , it is worth to note that their activity is constant during the measurement; thus,  $A_p(t_{eoc}) = A_p(t_{boc}) = A_p(t_c)$ . To determine the activity at the end of irradiation, one can apply the simple radioactive decay law (Eq. 2-34):

$$A_p(t_{eoi}) = A_p(t_{boc}) e^{\lambda_p (t_{boc} - t_{eoi})} \quad (2-34)$$

Inserting Eq. 2-34 into Eq. 2-33, results then into Eq. 2-35:

$$\sigma_E = \frac{A_p(t_{boc}) e^{\lambda_p (t_{boc} - t_{eoi})}}{N_T \Phi_E (1 - e^{-\lambda_p t_{irr}})} \quad (2-35)$$

For our measurements, including the decay correction and defining  $t_w$  ( $= t_{boc} - t_{eoi}$ ), we determined all cross-sections, according to Eq. 2-36:

$$\sigma_E = \frac{A e^{\lambda t_w}}{N_T \Phi_E (1 - e^{-\lambda_p t_{irr}})} \quad (2-36)$$

#### 2.5.3.1 Cross-Sections: $^{nat}\text{V}(\text{p}, \text{x})^{44}\text{Ti}$ , $^{nat}\text{V}(\text{p}, \text{x})^{41}\text{Ca}$ , and $^{nat}\text{V}(\text{p}, \text{x})^{26}\text{Al}$

Initially, for  $^{44}\text{Ti}$ , we relied on in-house developed reference materials (see for details section 3.2.3.2). As these sources for the detector calibration were prepared in the same geometry as the measured samples for the activity determination, an efficiency calibration for the  $^{44}\text{Ti}$  activity in a particular geometry was obtained. These geometry-specific calibrations with the same radionuclide reduce the need for true-coincidence summing corrections as well as the need for precise knowledge of the photon emission probabilities and detector efficiency. Therefore, the count rate of the calibration solution can be compared to the known activity of the same geometry, which was meticulously determined in the beginning.

In contrast, AMS was used to determine the activity of  $^{41}\text{Ca}$  and  $^{26}\text{Al}$ , respectively. AMS measurements typically provide isotopic ratios between an artificially produced nuclide and a naturally abundant nuclide (referred to as carrier). The  $^{41}\text{Ca}/^{40}\text{Ca}$  and  $^{26}\text{Al}/^{27}\text{Al}$  ratios were made available by the Laboratory of Ion Beam Physics (LIP) at ETH Zurich. The activity (A) for the two nuclides was subsequently computed as follows (Eq. 2-37, Eq. 2-38):

$$A_{^{41}\text{Ca}} = ^{41}\text{Ca}/^{40}\text{Ca} \times N_{^{40}\text{Ca}} \times \lambda_{^{41}\text{Ca}} \quad (2-37)$$

$$A_{^{26}\text{Al}} = ^{26}\text{Al}/^{27}\text{Al} \times N_{^{27}\text{Al}} \times \lambda_{^{26}\text{Al}} \quad (2-38)$$

where  $N_{^{40}\text{Ca}}$  and  $N_{^{27}\text{Al}}$  corresponds to the number of atoms (added carrier),  $\lambda_{^{41}\text{Ca}}$  and  $\lambda_{^{26}\text{Al}}$  is the individual decay constant. Eventually,  $A_{^{41}\text{Ca}}$  and  $A_{^{26}\text{Al}}$  was used to determine the individual production cross-section, according to Eq. 2-36.

### 2.5.3.2 Theoretical cross-section calculations

The calculations were provided by Dr Jean-Christoph Davide (Commissariat à l'énergie atomique, Saclay, France). Here, the Liège intranuclear cascade model INCL++ [164, 165], combined with the de-excitation codes ABLA07 [166] were used to perform theoretical cross-section calculations. This model combination is commonly used to compute the production yields and characteristic particles and nuclei generated in spallation reactions [167]. The progenitors were taken into consideration to calculate the cumulative cross-sections as follows (Eq. 2-39):

$$\sigma_{D,cml} = \sigma_{D,ind} + \sigma_{M,cml} \times \frac{\lambda_M}{\lambda_M - \lambda_D} \quad (2-39)$$

where  $\sigma_{D,cml}$  is the cumulative and  $\sigma_{D,ind}$  is the independent cross-section,  $\sigma_{M,cml}$  is the cross-section of the parent nuclide,  $\lambda_M$  is the decay constant of the mother, and  $\lambda_D$  is the decay constant of the daughter. Obviously,  $\sigma_{M,cml}$  is calculated, such as  $\sigma_{D,cml}$  making the latter a sum of possibly numerous terms, according to the number of successive progenitors. The details can be found elsewhere [163, 167, 168].





## 3 Experimental Studies

### 3.1 Instrumental Analysis

#### 3.1.1 Gamma-ray spectrometry ( $\gamma$ -spectrometry) measurements

The measurements were performed with spectrometric systems comprising of either a low energy germanium Detector (LEGe) or a high purity germanium (HPGe) detector. Spectra analysis was performed with Genie 2000 gamma acquisition and analysis software (Canberra Industries, Inc., U.S.A.; now: Mirion Technologies, Inc., U.S.A.). For the different measurements, specific efficiency calibrations were used, according to the individual sample distance, and sample geometry. Therefore, these conditions are stated in each experimental section separately. Also, for some measurements (especially during the development of the separation procedure), a precise efficiency determination was not needed, since it was only about the qualitative detection of radionuclides left in solution. Thus, to maintain a precise energy calibration was more important. The energy calibration was checked and performed on a frequent schedule using a  $^{152}\text{Eu}$  point-source from PTB with  $A(^{152}\text{Eu}) = 149.3 \pm 2.1$  kBq (reference date: 01.01.2015). Moreover, background spectra were also recorded on regular schedule. Typical measurement times have been between 15 minutes (900 s) and 24 hours (86400 s), to be compared with the respective background spectrum.

#### 3.1.2 Liquid scintillation counting (LSC) measurements

LSC measurements were carried out using a Canberra Packard Tri-Carb<sup>®</sup> 2250CA liquid scintillation analyzer (PerkinElmer, Inc., Waltham, U.S.A.). Ultima Gold<sup>TM</sup>AB was used as scintillator cocktail. Principally, the sample preparation was carried out using 1 mL of aqueous phase, mixed with 15 mL of scintillator cocktail. This resulted in a ratio of 6.67% (aqueous/organic) and enhances the long-term sample stability [169]. In this work,  $^3\text{H}$  ( $E_{\beta_{max}} = 18.6$  keV) and  $^{32}\text{Si}$  ( $E_{\beta_{max}} = 227$  keV), with its daughter,  $^{32}\text{P}$  ( $E_{\beta_{max}} = 1710$  keV), were determined by LSC. Basically, the measurements of these samples, including background samples, yield experimental net count rates. In order to translate these into absolute activities, the corresponding counting efficiencies must be known. In this work the counting efficiencies were determined by means of a quench standard curve (for pure  $^3\text{H}$  in solution), as well as with the CIEMAT/NIST efficiency tracing (CNET) method (for pure  $^{32}\text{Si}$  and  $^{32}\text{Si}+^{32}\text{P}$  in solution). For the tritium quench curve (see section 6.1, Fig. 6.3), a commercially available product was used (Ultima Gold Quenched Standard (6007600), 15 mL, PerkinElmer, Inc., Waltham, U.S.A.), while for CIEMAT/NIST, experimental and theoretical data was provided by the Institute of Radiophysics (IRA) from Dr Y. Nedjadi (see section 6.1, Fig. 6.2). To monitor performance metrics, the Instrument Performance Assessment (IPA<sup>TM</sup>) was executed periodically. Therefore, one can follow instrument trends (e.g.,  $^3\text{H}$  and  $^{14}\text{C}$  counting efficiency) to ensure optimal performance at factory specifications (see section 6.1, Fig. 6.1). Further, the Tri-Carb<sup>®</sup> 2250CA offers up to three different windows (WinA, WinB, and WinC), in order to measure three different energy regions.

Typically,  $^3\text{H}$  was measured with  $\text{WinA} = 0\text{-}2000$  keV,  $\text{WinB} = 0\text{-}18.6$  keV,  $\text{WinC} = 2\text{-}18.6$  keV and  $^{32}\text{Si}/^{32}\text{P}$  was measured with  $\text{WinA} = 0\text{-}2000$  keV,  $\text{WinB} = 0\text{-}230$  keV,  $\text{WinC} = 230\text{-}2000$  keV. For all samples blanks with a matching matrix were prepared, too, to perform a background subtraction. The obtained net count rates are typically given as counts per minute (CPM). Thus, to derive the activity concentration, Eq. 3–40 was used:

$$DPM(\text{WinA})_{\text{Sample}} = \frac{CPM(\text{WinA})_{\text{Sample}} - CPM(\text{WinA})_{\text{Blank}}}{\epsilon_{\text{Nuclide}}} \times D_f \quad (3-40)$$

Here, the disintegrations per minute in WinA (DPM(A)) were derived, simply by dividing the computed net CPM (background subtracted) by the nuclide's efficiency ( $\epsilon_{\text{Nuclide}}$ ) which accounts in this thesis for  $^3\text{H}$ ,  $^{32}\text{Si}$  or  $^{32}\text{Si}+^{32}\text{P}$ , and  $D_f$  was the respective dilution factor. After the DPM(A) were determined, one can further apply Eq. 3–41 to finally calculate the activity concentration:

$$A_{\text{Sample}} = \frac{DPM(A)_{\text{Sample}}}{m(\text{Aliquot}) \times 60 \frac{\text{sec}}{\text{min}} \times 1000 \frac{\text{Bq}}{\text{kBq}}} \quad (3-41)$$

Where the mass (in g) of the added aliquot is respected, and two conversion factors were introduced to account for the denotation of the Becquerel ( $\text{s}^{-1}$ ), and for the unit's conversion to kilo ( $10^3$ ), respectively. Furthermore, LSC measurements were always performed for at least 60 minutes, or for the condition of  $2\sigma < 0.5\%$ , to obtain consistent results.

### 3.1.3 Hyphenated inductively coupled plasma (ICP-) techniques

#### 3.1.3.1 Optical emission spectrometry (OES)

ICP-OES was used for the on- and offline quantification of the elements of interest while performing experiments and for completed experiments, respectively. In this work, we were mainly working with an Agilent 5110 (Agilent Technologies, Inc., Santa Clara, U.S.A.) that replaced an older device, an OPTIMA 3000 (PerkinElmer, Inc., Waltham, U.S.A.).

For the sample preparation, care was taken to adjust the acidity between  $\approx 0.32\text{M}$  and  $\approx 0.80\text{M}$ , which translates to 2 wt.-% (weight-%)  $\text{HNO}_3$  and 5 wt.-%  $\text{HNO}_3$ , respectively. However, also measurements with  $\text{HCl}$ , and  $\text{HF}$  were performed. Therefore, blanks, standards and the device's wash bottle were prepared accordingly. Notably, in case of  $\text{HF}$ -containing samples, the Agilent 5110 was equipped with inert sample introduction components, which allowed running such samples directly, without requiring a neutralization step (e.g., with boric acid). For the element's identification, specific wavelengths were chosen (Table 3.1) and the results were carefully analyzed in order to exclude, e.g., influences from background analytes which could potentially interfere.

**Table 3.1:** Commonly used wavelengths for the analysis of the elements using ICP-OES. Care was taken to avoid interferences during the measurements, stemming from similar emission lines.

Atomic number (Z)	Element	Wavelength (nm)	Wavelength (nm)
13	Al	226.910	396.152
14	Si	250.690	251.611
16	S	180.669	181.972
20	Ca	317.933	373.690
22	Ti	307.866	368.520
23	V	270.093	326.769
26	Fe	238.204	261.382
28	Ni	216.555	221.648

Furthermore, the device’s performance was regularly checked with standard solutions, but also parts like the skimmer cone and the torch were cleaned regularly. Additionally, a detector and wavelength calibration were also performed to maintain performance metrics.

For the calibration curves, appropriate ranges in the ppb to ppm range were prepared, using exclusively TraceCERT® Single Element Standards (Merck KGaA, Darmstadt, Germany) with a certified relative standard of usually <0.5%. Moreover, pipette calibrations were regularly performed to ensure the low uncertainty range (0.8 to 1.0%), when working with volumetric dilutions. The resulting dilutions, specifically for the calibration curve, have been always controlled, and were evaluated by the correlation coefficient  $R^2$ . The criterion of acceptance was set to  $R^2 > 0.995$ . Moreover, the calibration curves were carefully prepared to work in the linear range, whereby linearity is understood as the ability of the method to obtain results proportional to the concentration of the analyte over the relevant concentration range.

### 3.1.3.2 Mass spectrometry (MS)

We performed ICP-MS measurements at the Institute of Chemical Sciences and Engineering (ISIC) that is part of EPFL’s associated campuses. These measurements were part of an EPFL-hosted course (CH-728, Mass spectrometry, Principles, and Applications) and performed with the supervision of Dr Natalia Gasilova (Scientist at ISIC’s Mass Spectrometry and Elemental Analysis Platform) using a NexION® 350 QC-ICP-MS (PerkinElmer, Inc., Waltham, U.S.A.). Furthermore, some measurements were performed using the machine’s collision mode (Helium Kinetic Energy Discrimination, He-KED). Here, a non-reactive gas (He) is introduced into the cell to collide with interfering ions with larger diameters, reducing their kinetic energy so they may be removed through He-KED (e.g., [170]).

## 3.2 Materials and experimental methods

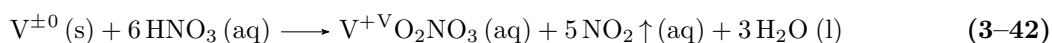
Unless otherwise stated, all declared chemical reagents used during the development of the separation procedure or sample preparation are commercially available and were used without further purification. However, we specifically ordered, e.g., high-grade acids that feature extremely low impurities and are used for trace-element analysis (in the ppb range). All required solutions were prepared by dissolution or dilution of commercial products with in-house purified water (utp-H<sub>2</sub>O, 18.2 M  $\Omega$  cm, Veolia S.A.) and volumetrically brought to the desired concentrations. Peristaltic pumps (REGLO Digital MS-2/8, Cole-Parmer Instrument Company, LLC., U.S.A.) were used for the separations, with the identical squeeze tubes (Ismaprene PharMed<sup>®</sup>, SC0307, Cole-Parmer Instrument Company, LLC., U.S.A.). Although working without a silicon-carrier, we refer intentionally to non-carrier added (nca) <sup>32</sup>Si in this work because of, e.g., the initial presence of stable silicon in the vanadium discs and other silicon sources due to the chemical processing, e.g., stated as a major impurity in hydrofluoric acid from the supplier. Hence, we learned from the literature that the final product's specific activity regarding <sup>32</sup>Si is drastically lowered by a factor of 25 [88] or up to nearly 100 [89] if one does not carefully consider the external sources for stable silicon. Noteworthy to mention that the laboratory equipment was carefully chosen in advance to prevent or minimize the addition of stable silicon from these sources during the whole work. Therefore, any glassware was avoided, and plastic (polypropylene (PP), polyethylene (PE), polymethyl methacrylate (PMMA), and polytetrafluoroethylene (PTFE)) was used instead.

### 3.2.1 Part 1 of 3: Characterisation of the target material

#### 3.2.1.1 Inactive V discs and the preparation for ICP-MS measurements

Originally, Goodfellow Cambridge Limited (U.K.) provided the inactive metallic vanadium discs (typical mass  $\approx$  420 mg, diameter  $\approx$  9.20 mm, thickness  $\approx$  1.0 mm, chemical purity of vanadium:  $\approx$  99.8%). The manufacturer's certificate states typical impurities (upper limit in %) to be Si ( $\leq$ 0.2), Nb ( $\leq$ 0.1), Mo ( $\leq$ 0.1), Ta ( $\leq$ 0.1), Al ( $\leq$ 0.05). However, as it was not possible to receive batch-specific information from the supplier, we decided to determine some elements ourselves, focusing on silicon. Therefore, we could receive a more detailed – batch-specific – analysis of the vanadium discs used for irradiation.

The initial preparations have been performed at PSI, using six inactive vanadium discs. The discs have been chosen based on their particular appearance (Table 3.2) and were each dissolved in six individual 15 mL PP-tubes with 5 mL 8M HNO<sub>3</sub>. A short overview with description is given in Table 3.2. Many ICP analyses require the sample's initial acidity to be between 2 wt.-% and 5 wt.-%, preferably in an HNO<sub>3</sub> matrix. While up to 5 wt.-% NO<sub>3</sub> is used for ICP-OES measurements, 2 wt.-% HNO<sub>3</sub> is required for ICP-MS measurements. Therefore, based on the dissolution reaction (Eq. 3-42):

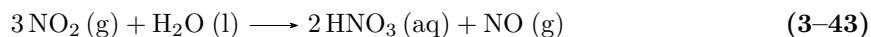


we determined the resulting acidity due to the neutralization of 6 moles acid (H<sup>+</sup>) per 1 mole vanadium, forming vanadium(V) nitrate, gaseous NO<sub>2</sub>, and H<sub>2</sub>O.

**Table 3.2:** Overview of the discs used for the ICP-MS analyses.

Sample	Weight (mg)	Metal concentration in solution (mg/mL)	Additional information	Identifier
1	418.87	83.77	<i>Both discs were shortly pre-cleaned with 3M HNO<sub>3</sub> and then cleansed with utp-H<sub>2</sub>O</i>	Cleaned
2	410.32	82.06		
3	417.86	83.57	<i>Brownish layer on the discs' surface. Discs were not cleaned and were considered: "dirty".</i>	Rusty
4	421.35	84.27		
5	418.93	83.79	<i>Both discs were regarded as "average" as they have not been cleaned and do not have a brownish surface color either.</i>	Average
6	414.52	82.90		
∅	416.89 ± 3.58	83.38 ± 0.72		

Nitrogen dioxide gas further reacts in water according to Eq. 3–43:



Consequently, during the dissolution reaction, HNO<sub>3</sub> is partially in-situ created. Since after the complete dissolution, on average, an H<sup>+</sup> concentration of  $c(\text{H}^+) \approx 2.5 \text{ M}$  was determined,  $\approx 12$  mmoles H<sup>+</sup> were additionally formed. Therefore, around 18 mmol NO<sub>2</sub> were consumed that allowed to eventually dissolve the entire vanadium disc. During the dissolution, the creation of NO<sub>2</sub> was readily visible due to the characteristic dense, brownish colored fumes that were partially escaping during the dissolution reaction. Thus, based on the assumption that the remaining acidity was about 2.5 M, we prepared samples with an acidity of 2% (vol-%) that would require a dilution factor of 8, if diluted with utp-H<sub>2</sub>O. However, as ICP-MS is a very sensitive measurement technique, we avoided high vanadium concentrations, and worked with 20-fold, 100-fold and 200-fold dilutions, respectively.

Besides, measurements with a reaction cell (using Helium) were performed that allows the kinetic energy discrimination (KED) and helps reducing ionic interferences, which are caused by the same mass-to-charge ratio, e.g., <sup>56</sup>Fe<sup>+</sup> with <sup>40</sup>Ar<sup>16</sup>O<sup>+</sup>. However, various polyatomic interferences are known and have numerous sources, such as the sample matrix, the reagents used for preparation, or the plasma gas (Ar, [171]). For a detailed overview, the reader is advised to refer to a work from May & Wiedmeyer [142]. Further, for the determination of the absolute amounts of the trace metal content, Eq. 3–44 was used:

$$m(\text{Element}) = \frac{\Gamma \times D_f \times V_{\text{initial}}}{\frac{\Lambda}{m_{\text{disc}} \times 100 \%}} \quad (\mathbf{3-44})$$

where  $\Gamma$  is the conversion ((ng mL)/(1000 µg/ng)),  $D_f$  the dilution factor,  $V_{\text{initial}}$  represents the volume (mL),  $\Lambda$  a further conversion (1000 µg/mg) and  $m$  the mass of a vanadium disc (g).

### 3.2.1.2 Determination of aluminium, iron, and trace elements

First, samples with a 20-fold and a 200-fold dilution factor were prepared (Table 3.3). Yttrium standard was added to each sample in order to reach a final yttrium concentration of about ten ng/g (ppb). Using yttrium as internal standards allowed us to monitor whether, e.g., matrix effects, beam defocusing, or space charge effects occurred [172]. Blanks were prepared accordingly, mixing 50  $\mu\text{L}$  of the 1 ppm Y-Std. with 4950  $\mu\text{L}$  2% (vol.-%)  $\text{HNO}_3$ . Using the recovery rates of the internal standard, it was then possible to decide whether a further dilution of the sample was needed for the experiments, or if the results were reliable. For the determination of the trace elements using the TotalQuant™ Option, the samples were diluted 100-fold (Table 3.4).

**Table 3.3:** Sample preparation for the ICP-MS measurements: With calibration curves.

D <sub>f</sub>	Sample	Sample ( $\mu\text{L}$ )	2% $\text{HNO}_3$ ( $\mu\text{L}$ )	Yttrium Std., 1 ppm ( $\mu\text{L}$ )	Final D <sub>f</sub>
20	1				
	3	200	3800	40	20.2
	5				
20	1				
	3	20	3980	40	202
	5				

**Table 3.4:** Sample preparation for the ICP-MS measurements: With TotalQuant™.

D <sub>f</sub>	Sample	Sample ( $\mu\text{L}$ )	2% $\text{HNO}_3$ ( $\mu\text{L}$ )	Yttrium Std., 1 ppm ( $\mu\text{L}$ )	Final D <sub>f</sub>
100	1				
	3	50	4900	50	100
	5				

### 3.2.1.3 Determination of the <sup>nat</sup>Si content with ICP-MS

The analyses were performed with and without KED and again with 20x and 200x dilution. The preparation of the different samples was done according to Table 3.5. Again, Blanks were prepared correspondingly, mixing 50  $\mu\text{L}$  1 ppm Y-Std. with 4950  $\mu\text{L}$  2%  $\text{HNO}_3$  (vol.-%).

**Table 3.5:** Summary of the sample preparation for the ICP-MS measurements (for <sup>nat</sup>Si).

D <sub>f</sub>	Sample	Sample ( $\mu\text{L}$ )	2% $\text{HNO}_3$ ( $\mu\text{L}$ )	Yttrium Std., 1 ppm ( $\mu\text{L}$ )	Final D <sub>f</sub>
20	1				
	3	250	4700	50	20
	5				
200	1				
	3	25	4925	50	200
	5				

#### 3.2.1.4 Determination of the $^{nat}\text{Si}$ content with ICP-OES

As the laboratory's Agilent 5110 can be equipped with both an inert sample introduction system and a PTFE-torch, measurements of the natural silicon content have also been performed, in order to compare the obtained results for the silicon content in the vanadium discs.

For such an analysis, an inactive vanadium disc was dissolved in 5 mL 1:1 8M HCl/HNO<sub>3</sub>. Then, 8 mL 0.5M N<sub>2</sub>H<sub>4</sub> were added and the solution subsequently diluted to 100 mL with utp-H<sub>2</sub>O. Following a separation on a Dowex<sup>®</sup> 50WX8-200 cation-exchange resin,  $^{nat}\text{Si}$  can be measured interference-free with the ICP-OES, since most of the cations in solution were retained. Moreover, the very same approach was used, when developing the separation scheme, since this experiment also provided an elution profile from  $^{nat}\text{Si}$  on Dowex<sup>®</sup> 50WX8-200. Thus, each collected fraction consisted of 5 mL and was measured without prior dilution.

For the determination of the  $^{nat}\text{Si}$ -content commonly two approaches were followed: (i) Measurement without the addition of Si (nca-amount):  $^{nat}\text{Si}$  content solely from the disc's impurities, or (ii) with the addition of a known amount of Si (Si-spike) to the initially dissolved disc that is eventually subtracted to the determine the  $^{nat}\text{Si}$  content from the disc's impurities.

In case where a Si-spike was added, 300  $\mu\text{L}$  ( $\approx 300 \mu\text{g}$ ) of a single-element standard (1000 ppm, TraceCERT<sup>®</sup>, 2 wt.-% NaOH, Merck KGaA, Darmstadt, Germany) was used.

## 3.2.2 Part 2 of 3: Development of radiochemical separation procedures

### 3.2.2.1 Preparation for distillation experiments

Lindner & Polak pioneered in the early 1980ies on the production of no-carrier-added  $^{32}\text{Si}$  [173] by separating radiosilicon using a distillation apparatus. Yields of 60 to 80%, combined with a fast transfer of silicon (within one hour), appeared as a promising method to separate  $^{32}\text{Si}$ , initially present as  $\text{H}_2\text{SiF}_6$ . Therefore, attempts were made to distill  $^{32}\text{Si}$  from the vanadium matrix.

To begin with, 10 mL of a «distillation reference solution (DRS)» was prepared, of which 5 mL were used for the distillation experiment, while the remaining 5 mL were kept for determining the initial amount of silicon. This allowed to determine relative yields. The DRS was prepared using 1000 ppm ICP-standard solution (TraceCERT®, 2 wt.-%  $\text{HNO}_3$ , Merck KGaA, Darmstadt, Germany) in a  $\text{HNO}_3/\text{HF}$ - (for Si) or  $\text{HNO}_3$ -matrix (for V). The final composition was chosen as summarized by Table 3.6:

**Table 3.6:** Final composition of the representative sample matrix used for the distillation experiments.

Element	Concentration mmol/mL)	(in	Concentration (in ppm)	Volume (in mL)
Silicon	1.8	50		10
	0.9	25		10
Vanadium	1.8	90		10
	0.9	45		10

Moreover, hydrofluoric acid (HF) was added to be stoichiometric with the formation of  $\text{H}_2\text{SiF}_6$ , but with an 10% excess to ensure its speciation in solution. Finally, the matrix of each of the DRS contained about 2% (vol.-%)  $\text{HNO}_3$ , to match the requirements for the ICP-OES measurements.

In the course of the experiments, an amount of 25 ppm and 50 ppm ( $^{\text{nat}}\text{Si}$ ) was chosen, to evaluate if the yield of the distillation depends on the concentration of the silicon in solution.

In order to catch the volatalized silicon, a «distillation trapping solution (DTS)» was prepared. Here, a mixture of 0.32 M  $\text{HNO}_3$ /0.36 mM HF was used, which allowed direct measurements of the solution with ICP-OES. For this reason, 5 mL of the DTS was placed in a 15 mL centrifuge tube and connected to the distillation appartus, accordingly.

In order to test the system and to apply it at the envisaged experimental conditions, a distillation setup was built up as follows: Nitrogen ( $\text{N}_2$ ) was being used as a carrier gas; A 100 mL round-bottom PTFE-flask (Bohlender GmbH, Grünsfeld, Germany) was placed in a bath of PEG-400, which in turn, was on top of a heating plate to bring the 5 mL aliquot of the DRS to boil. The heating plate was set to maximum ( $\approx 300\text{ }^\circ\text{C}$ ) to achieve the desired temperature of around  $135\text{ }^\circ\text{C}$ . We assumed the heat transfer to be equal between the bath and the distillation flask and were therefore monitoring the temperature of the PEG-400, which was used as a bath. After approximately 1 to 1.5 hours, the 5 mL aliquot was completely evaporated to dryness. Consequently, the DTS was then brought to a final volume of 10 mL using a graduated plastic cylinder. The yield was then determined with an OPTIMA 3000 ICP-OES (PerkinElmer, Inc., Waltham, U.S.A.).

### 3.2.2.2 Preparation for column chromatography experiments

Generally, the procedure is composed of five steps:

- (i) a Preconditioning Step, where the resin is wetted using a suitable volume of aqueous solution which corresponds to the matrix which is used during the second step;
- (ii) a Loading Step (Load) in which the initial solution is brought into contact (loaded) with the stationary phase;
- (iii) a Washing Step (Wash), particularly meant to remove all remaining non-binding elements from the resin;
- (iv) an Elution Step (Elute), employed to remove the metal ion of interest from the resin;
- (v) after the completion of the separation, the resin was washed thoroughly and inspected (e.g. formation of air bubbles) in order to start again with (i) and is referred to as post-conditioning.

While the separation procedure was developed to process approximately 150 proton-irradiated vanadium specimens, we also focused on high reproducibility and a generalized purification procedure to account for the different irradiation conditions, leading to a diverse nuclide inventory for each of the vanadium discs. Column operations were carried out under ambient conditions and the time required for the different procedures may vary and strongly depend on the chosen parameters, such as the flow rate ( $\text{mL} \times \text{min}^{-1}$ ). Peristaltic pumps (REGLO Digital MS-2/8, Cole-Parmer Instrument Company, LLC., U.S.A.) were used throughout the separations to provide a constant flow. Flow rates, however, were set for each experiment and stated individually. For all separation procedures, the identical squeeze tubes (Ismaprene PharMed®, SC0307, Cole-Parmer Instrument Company, LLC., U.S.A.) were used. These squeeze tubes are described to have a good chemical resistance to acids, alkali, and oxidants, and have a recommended tubing life of about 1000 hrs (0.7 bar). Attention was paid when working with other tube materials (in the separation circuit), where PTFE tubes were chosen. The method development focused primarily on non-active (cold) model solutions precisely matching the chemical composition of the active solutions. For each individual experiment, a typical load solution with a representative matrix was prepared in order to investigate the behavior of silicon during the separation. However, the procedure was ultimately also applied to active solutions to study and to confirm the element's behavior in the respective matrix. Therefore, inactive model solutions were used to investigate mainly silicon's behavior but also to determine if other nuclides were sufficiently retained under these conditions. The cold model solutions were also used to establish elution profiles, analyzing the individual fractions with ICP-OES. In addition, specific nuclides have been chosen for the experiments, as some radionuclides might interfere with LSC measurements, such as  $^3\text{H}$ ,  $^{41}\text{Ca}$ ,  $^{55}\text{Fe}$ , and  $^{59}\text{Ni}$ .

### 3.2.2.3 Cation-exchange chromatography: Dowex® 50WX8-200

Cation-exchange chromatography (Dowex® 50WX8-200, 200–400 mesh; Sigma-Aldrich, Germany) was initially used, hosting the resin in tailor-made PMMA columns (length = 300 mm; inner diameter = 10 mm) to a height of 220 mm. To ensure that no resin particles were lost, 30  $\mu\text{m}$  PTFE frits (006FR-10-30, Diba Industries, Inc., Cambridge, UK) were placed at the end of the PMMA column and on the resin, respectively. Before use, a typical resin-batch was pre-cleaned with 25 mL 6 M HCl,

further treated with 50 mL 3 M  $\text{HNO}_3$ , and washed with 50 mL utp- $\text{H}_2\text{O}$ . Using 6M  $\text{HCl}$ , traces of metal (Fe, Ni, Zn) should be removed, while 50 mL 3M  $\text{HNO}_3$  prior to the separation conditions the column accordingly to the final elution. Finally, utp- $\text{H}_2\text{O}$  is used to bring the pH to  $\approx 4$ .

The matrix solution was loaded at a fixed flow rate of  $1.50 \text{ mL} \times \text{min}^{-1}$ . The Wash consisted of 20 mL utp- $\text{H}_2\text{O}$  and was collected together with the initial Load, which was then marked as  $^{32}\text{Si}$  fraction ( $V_{\text{total}} = 120 \text{ mL}$ ). For the elution 50 mL 3 M  $\text{HNO}_3$  was necessary, to remove all cations which were retained on the column. Generally, that solution was kept and appropriately stored for further radiochemical separations of other products of interest. Finally, post-conditioning of the resin-batch was done with utp- $\text{H}_2\text{O}$  until pH reached 4 (typically 50 mL). For active discs, each resin batch was used on average six to ten times before replacement with a fresh batch. The finalized preparation for the chemical separation procedure consisted of the following stepwise approach:

- (i) Place an empty 15 mL PP-tube into an ice-water mixture;
- (ii) Add a single, proton-irradiated vanadium disc into the tube and add an acidic cocktail composed of 2.5 mL 8M  $\text{HCl}$  and 2.5 mL 8M  $\text{HNO}_3$  for dissolution. Unlike a non-irradiated disc, the dissolution of an irradiated disc takes a substantial amount of time. Therefore, the vanadium disc was left to dissolve for around 16 hours. Such a dissolution behavior was already described during the early experiments of Polak et al. [88]. Besides, to diminish the escape of gaseous species ( $\text{NO}_x$ ,  $^3\text{H}_2$ ,  $^3\text{HCl(g)}$ ,  $^{39}\text{Ar}$ ,  $^{42}\text{Ar}$ ) that were created during the disc's dissolution, a cylindrical cap filled with activated carbon was screwed on the PP-tube and replenished after each dissolution procedure;
- (iii) Add 50 mL utp- $\text{H}_2\text{O}$  and 8 mL 0.5M  $\text{N}_2\text{H}_4$  to a 100 mL wide-neck PP-bottle. Then, add the dense, dark-blue-colored vanadium solution and stir immediately;
- (iv) Wash the PP-tube thoroughly with 3x4 mL utp- $\text{H}_2\text{O}$  and discard the PP-tube (active waste);
- (v) Add further 30 mL of utp- $\text{H}_2\text{O}$  to obtain a total volume of 100 mL (dilution 1:20) and let the solution rest for around two hours;
- (vi) Perform the ion-exchange chromatography (Dowex<sup>®</sup> 50WX8-200) to separate  $^{32}\text{Si}$  from the bulk vanadium;
- (vii) Wash with 20 mL utp- $\text{H}_2\text{O}$  over the column, to quantitatively recover the  $^{32}\text{Si}$ ;
- (viii) Store the  $^{32}\text{Si}$  fraction ( $= 120 \text{ mL}$ ) from a single recovery procedure for further purification;
- (ix) Elute all remaining cations with 50 mL 3M  $\text{HNO}_3$  ( $K_d < 10^1$ ) and store the solution for further radiochemical separations to recover the by-products:  $^{26}\text{Al}$ ,  $^{41}\text{Ca}$ ,  $^{44}\text{Ti}/^{44}\text{Sc}$ ;

The cation-exchange resin was used about six to ten times before being replaced by a new, fresh batch. After the separation procedure, each  $^{32}\text{Si}$  fraction was typically measured for around one hour to ensure that only some expected impurities (e.g.,  $^{22}\text{Na}$ ,  $^{44}\text{Ti}/^{44}\text{Sc}$ ,  $^{60}\text{Co}$ ,  $^{94}\text{Nb}$ ) were visible in the  $\gamma$ -spectrum. Due to the different irradiation conditions, some discs have been more active than others, resulting in higher or lower activities of the respective radionuclides.

#### 3.2.2.4 Purification of the $^{32}\text{Si}$ fractions: Removal of trace impurities

In contrary to experiments with radioactive solutions (non-carrier added), we used for the experiments with cold solutions elevated natural Si concentrations, to be able to perform more accurate ICP-OES measurements, as the solutions were subsequently measured without prior dilution.

Further, the solutions for both the LN<sup>®</sup> resin (Purification Step I) and Monophos<sup>®</sup> resin (Purification Step II) were prepared identically. The typical Load with a representative matrix was prepared in order to investigate the behavior of silicon during the separation procedure. 1000 µL Si solution (TraceCERT<sup>®</sup> silicon standard 1000 µg/mL, 2 wt.-% NaOH, Merck KGaA, Germany) were added to 119 mL 0.05 M HCl/0.05 M HNO<sub>3</sub> which was used as Load with  $c(\text{Si}) = 8.33 \text{ µg mL}^{-1}$ . For these experiments, an extended wash (40 mL utp-H<sub>2</sub>O) was used to clearly identify, whether tailing of silicon occurs. Finally, it could be determined, how much utp-H<sub>2</sub>O was needed to quantitatively recover Si from these purification procedures.

### 3.2.2.5 LN<sup>®</sup> resin series: Purification step I

As only trace impurities had to be removed (ppb to ppt-range), an in-house-made PMMA column (length = 100 mm; inner diameter = 10 mm) was prepared, filled with 35 mm LN<sup>®</sup> resin (20–50 µm; TrisKem SAS, Bruz, France), which is composed of di(2-ethylhexyl)orthophosphoric acid (HDEHP) impregnated onto an inert support.

To ensure that no resin particles were lost, 20 µm PTFE frits (006FR-10-20, Diba Industries, Inc., Cambridge, UK) were placed at the end of the PMMA column and on the resin, respectively. Before the purification, the resin was preconditioned with 20 mL 0.05M HCl/0.05M HNO<sub>3</sub> to account for the expected solution's matrix of the <sup>32</sup>Si fraction, as the pH was typically measured to be  $1.00 \pm 0.05$ . The solution was loaded at a fixed flowrate of  $1.25 \text{ mL} \times \text{min}^{-1}$ . Same conditions were then applied also for the final <sup>32</sup>Si fractions. Concerning expected impurities, it is noteworthy to mention that we did not work with, e.g., inactive titanium since available single element standards (e.g., TraceCERT<sup>®</sup>, Merck KGaA, Germany) contain titanium commonly as  $\text{TiF}_6^{2-}$  anion and could possibly distort the experimental observations. Therefore, the subsequent purification of radioactive <sup>32</sup>Si-solutions was then monitored using  $\gamma$ -spectrometry, to see whether <sup>44</sup>Ti was selectively removed.

### 3.2.2.6 Monophos<sup>®</sup> resin: Purification step II

Monophos<sup>®</sup> (100–200 mesh; TrisKem SAS, Bruz, France) resin was used in this step as this chelating ion-exchange was tested for its performance on removing <sup>94</sup>Nb(V). However, as compared to the previous purification step, we did forgo the actual separation of Nb(V) during the method development and focused solely on silicon's behavior.

In this regard, like for titanium, a typical commercially available single element standard (e.g., TraceCERT<sup>®</sup>, Merck KGaA, Germany) provides niobium in an HNO<sub>3</sub>/HF matrix, where Nb is present in solution as the  $\text{Nb(V)F}_6^-$  anion. Due to these speciation issues, the experimental design aimed only to investigate silicon's behavior during the separation, while working with radioactive solutions to see, whether <sup>94</sup>Nb(V) was successfully removed by this approach. Here, one can follow the two distinct  $\gamma$ -emission lines at 871.1 keV ( $I_\gamma = 100\%$ ), and 702.6 keV ( $I_\gamma = 97.9\%$ ), respectively.

The preparatory steps for these experiments were identical to the LN-based purification (Step I), except that the PMMA column was replaced by a smaller ISOLUTE<sup>®</sup> PE reservoir (length = 60 mm; inner diameter = 9 mm, Biotage Sweden AB, Sweden), and the Monophos<sup>®</sup> bed's height was shortened to 30 mm. Also, to ensure that no resin particles were lost, 20 µm PE frits (Biotage Sweden AB, Sweden) were placed at the end of the reservoir and on the resin, respectively.

### 3.2.2.7 Evaporation to dryness: Removal of $^3\text{H}$ and $^{39,42}\text{Ar}$

In this step, we followed two different experimental procedures for developing an approach for the removal of volatile species. Generally, it concerned the use of the two different reducing agents: L-ascorbic acid (L-AscA), and hydrazine ( $\text{N}_2\text{H}_4$ ). As we studied quantitatively the behavior of the volatile species, these experiments were exclusively performed using radioactive  $^{32}\text{Si}$  solutions, since LSC measurements could be performed to accurately determine the activity of the pure  $\beta$ -emitters.

Consequently, for samples treated with L-AscA, a rotary evaporator (RotaVap) was used. First, a 130 mL  $^{32}\text{Si}$ -solution was transferred into a 500 mL one-neck receiving PFA-flask (Bohlander GmbH, Germany) and the RotaVap was set to: 55 °C bath temperature (PEG-400), 72 mbar internal pressure, and rotating the flask at 60 revolutions per minute (Fig. 3.1). After the evaporation to near dryness, 50 mL of utp- $\text{H}_2\text{O}$  was filled in successively, reaching a total of twelve evaporations. Utilizing LSC, we analyzed the  $^3\text{H}$ -content, whereby the sample (= 100  $\mu\text{L}$ ) was taken from the receiving flask, after each of the utp- $\text{H}_2\text{O}$ -additions.

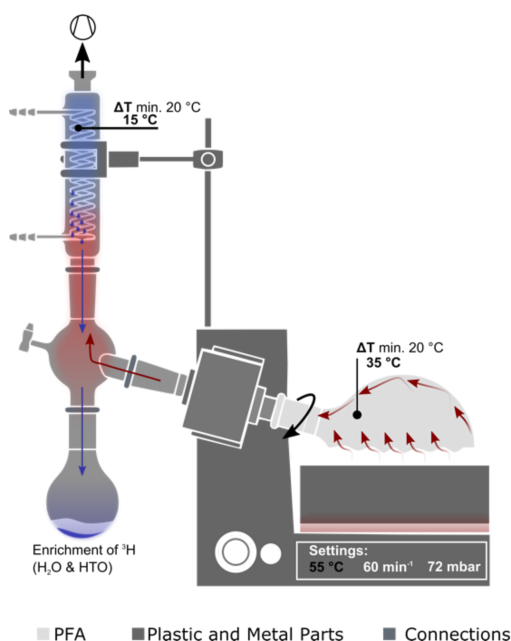


**Fig. 3.1:** Schematic view of the experimental setup used for the evaporation of L-AscA samples.

For the  $^{32}\text{Si}$  fractions treated initially with  $\text{N}_2\text{H}_4$ , we decided to use a PTFE evaporating dish (flat shape, 25 mL,  $\varnothing = 65$  mm,  $H = 12$  mm, Laborshop24 GmbH, Gross-Zimmern, Germany) to prevent any contamination with stable silicon and to efficiently recover the dried residue. The dish was placed on a hot plate (Fisherbrand® Isotemp® 4 × 4, Thermo Fisher Scientific Inc., U.S.A.) with the temperature set to  $175 \pm 5$  °C. After evaporating the full 130 mL, and eventually reaching complete dryness, 25 mL utp- $\text{H}_2\text{O}$  were added and re-evaporated. The procedure was repeated in total nine consecutive times to reach a total evaporated volume of 250 mL. From each sample, an aliquot was analyzed using LSC, and the data analysis was initially performed with the help of Dr Nataša Lalović (at that time, post-doctoral researcher at the Physikalisch-Technische Bundesanstalt (PTB), Germany). Finally, the  $^{32}\text{Si}$  recovery was achieved by washing the dish twice with 1 mL 1 M HF, topped up to 10 mL with utp- $\text{H}_2\text{O}$ . For an intermediate storage, each sample was transferred into a 50 mL conical centrifugation vial (PP), sealed with Parafilm®, and stored in a fridge.

### 3.2.2.8 Anion-exchange chromatography: Dowex® 1X8 200-400

#### 3.2.2.8.(I) $K_d$ studies

Most systems, like Dowex® 1X8 – HCl – H<sub>2</sub>O or Dowex® 1X8 – HNO<sub>3</sub> – H<sub>2</sub>O are having well-determined distribution coefficients ( $K_d$ ) for various anions (e.g., [118]). However, in the presented work, we wanted to have specific values for the system Dowex® 1X8 – HF – H<sub>2</sub>O, as no data was available for silicon. Thus, we adopted an in-house procedure reported by TrisKem (e.g., [174]), and adjusted it regarding the equilibration time, because of the practical use in our laboratory.

The resin was dried overnight at 60 °C and allowed to cool down in a desiccator before it was used. Around 50 mg of dried resin were weighed into a 2 mL Eppendorf vial, while marking each tube with the precise amount of resin added: typically,  $50 \pm 3$  mg. Then, 400  $\mu$ L of acid (HF, HCl) of individual concentrations were added, followed by 30 mins of pre-conditioning using an overhead shaker, to homogenize the samples. After 30 mins, 1 mL of the element's solution ( $c(\text{Element}) \approx 50 \pm 1.5$   $\mu$ g/mL) was added to the Eppendorf vial and left on the overhead shaker for 16 hours.

The element's matrix was individually prepared to account for the specific acidic matrix in each individual series. The matrices were chosen as follows:  $c(\text{HCl})$ : 0.1M, 0.5M, 1.0M, 1.5M, and  $c(\text{HF})$ : 0.01M, 0.05M, 0.10M, and 0.20M. Each series was centrifuged using a micro centrifuge (Eppendorf® 5415C, Eppendorf, Hamburg, Germany). First, for one minute at 2000 rpm (= x325 relative centrifugal force), followed by two minutes at 6000 rpm (= x2949 relative centrifugal force). For the instrumental analysis, 1 mL was taken out and diluted 1:10 with 2% HNO<sub>3</sub>, before measured with ICP-OES. The same was also done for the initial stock solution, to precisely determine the initial concentration for each of the fractions. Generally, for each element, and each acid concentration, three samples were prepared to achieve reliable results. The average of the three independent measurements was reported for the  $K_d$  ( $\text{cm}^3 \times \text{g}^{-1}$ ) value. For calculating the distribution coefficient, Eq. 3–45 was used:

$$K_d = \frac{C_0 - C_{\text{Aliquot}}}{C_{\text{Aliquot}}} \times \frac{V}{m} \quad (3-45)$$

Where  $C_0$  denotes the initially added concentration ( $\mu$ g/mL),  $C_{\text{Aliquot}}$  the concentration of the supernatant ( $\mu$ g/mL),  $V$  represents the volume ( $\text{cm}^3$ ), and  $m$  corresponds to the dry mass of the resin (g).

#### 3.2.2.8.(II) Ultra-trace removal of sulfur

Prior to the development of this experimental scheme, we realized during our experiments the removal of <sup>32</sup>P while gathering higher activities of <sup>32</sup>Si on an anion-exchange resin (Dowex® 1X8, 200-400 mesh, Merck KGaA, Germany). Suggesting a similar speciation in aqueous solution of both P and S, we intended to develop a single-step procedure which would yield highly reproducible results.

First, the column (ISOLUTE® 3 mL (9 mm diameter), Biotage Sweden AB, Sweden) was filled with anion-exchange resin to reach a bed height of  $\approx 3$  cm. For each experiment, the resin was pre-conditioned with 50 mL 0.1M HF. The peristaltic pump's speed was set to  $1.50 \text{ mL} \times \text{min}^{-1}$ . Silicon ( $\text{SiF}_6^{2-}$ ), vanadium ( $\text{VO}_2^+$ ), and sulfate ( $\text{SO}_4^{2-}$ ) were added from ICP-OES standard solutions (TraceCERT®, Merck KGaA, Germany).

Additionally, a 10'000 ppm standard solution ((NH<sub>4</sub>)<sub>2</sub>SO<sub>4</sub>, SPEX CertiPrep™, U.S.A.) as a sulfur source was utilized. All measurements were performed with the Agilent 5110 ICP-OES. Since the sulfur removal takes place while gathering the hexafluorosilicate anion on the exchange resin, ideal conditions had to be found, allowing the quantitative elution of sulfur while retaining <sup>32</sup>SiF<sub>6</sub><sup>2-</sup>. For the sulfur removal, we forwent the preparation of K<sub>d</sub> studies and directly decided to verify the experimental conditions using column chromatography. In each of the experiments, sulfur was first added to the Load solution (= 0.1M HF matrix).

For small-scale experiments, a typical “Silicon Load Solution” (SLS) consisted of 100 mL 0.1M HF, spiked with 400 µg Si, and 200 µg V, respectively. This resembled an averaged amount of five Si-fractions, eventually obtained from the “SINCHRON-separation” scheme. Additionally, 10 mg of sulfur was added, which accounts to 200 ppm sulfur per SLS. A varying HCl-concentration was then used to determine the threshold value above which sulfur commence eluting. To ensure the retention of Si, HF was added to each individual HCl-fraction to maintain c(HF) = 0.1M.

For up-scale experiments, the amount of ten processed Si-fractions was used (200 mL 0.1M HF; 800 µg Si; 400 µg V), however, with elevated sulfur amounts of 30 mg, equal to 600 ppm sulfur per SLS. Furthermore, experiments were performed, to screen for the recovery of, e.g., calcium, whose isotope <sup>41</sup>Ca could potentially cause problems for LSC. For this reason, stable calcium was added to the matrix and followed, whether it could be detected in the final 0.5M HCl <sup>32</sup>Si fraction. For these experiments a small-scale experiment was prepared, with the exception that 500 µL calcium ICP-OES standard solution (TraceCERT®, Merck KGaA, Germany) was added to the SLS. These experiments were employed to determine the final parameters of this step, thus, to prove the selectivity, robustness, and feasibility of the experimental design.

### 3.2.2.8.(III) Characterisation of the final product: <sup>32</sup>Si in 0.5M HCl

Here, the experimental preparation for the final characterisation of a prospective <sup>32</sup>Si master solution is described. Its production was performed on December 23, 2020. For this experiment, six entirely purified <sup>32</sup>Si solutions were used. The solutions were chosen based on their activity concentration (see Table 3.7), which was determined originally in-house using LSC and the CIEMAT/NIST Efficiency tracing method. We assumed the solutions to be in secular equilibrium.

**Table 3.7:** Overview of the <sup>32</sup>Si fractions that were used to produce a <sup>32</sup>Si master solution.

Disc N°	31	32	33	40	41	42	SUM
Activity concentration (kBq/g)	15.9	17.3	17.2	24.5	23.6	22.7	121.7 ± 3.6

Afterwards, the typical Load procedure, using anion-exchange chromatography, was applied. An overview of the procedure is given by Table 3.8. Assuming slightly lower recovery yields of around 90%, we wanted to ensure that the final <sup>32</sup>Si solution has an activity concentration of >100 kBq/g. The summed activity concentration of all six individual samples will yield ≈ 122 kBq/g. If <sup>32</sup>Si would quantitatively be recovered from all fractions, whereby an estimated 90% yield would still allow us to obtain ≈ 110 kBq/g. To confirm the fraction's final radiochemical and radionuclidic purity, a long-term γ-spectrum was measured, while comparing this spectrum later with a background spectrum.

Furthermore, using LSC and the CIEMAT/NIST Efficiency tracing method, we were also able to calculate the activity concentration of the final  $^{32}\text{Si}$  fraction. For this, 100  $\mu\text{L}$  were taken from the solution, diluted 1:100 (with 0.5M HCl), and then 100  $\mu\text{L}$  were subsequently added to 15 mL scintillation cocktail. Finally, 900  $\mu\text{L}$  of 0.5M HCl was added, to achieve a ratio of 1/15 (aqueous phase/organic phase).

**Table 3.8:** Sequence of the experimental procedure to produce the prospective  $^{32}\text{Si}$  master solution.

Time	$\Delta t$ (min)	Disc N° or Identifier	Volume (mL)	Matrix	Remark
07:44 am	0	31			
07:58 am	14	32			
08:12 am	14	33	20	0.1M HF	Six Load solutions with determined activity concentrations
08:27 am	15	40			
08:41 am	14	41			
08:57 am	16	42			
09:12 am	15	Sulfur Wash 1	50	0.10M HF/ 0.10M HCl	600 ppm sulfur ( $\approx 30 \text{ mg } ^{\text{nat}}\text{S}$ )
09:52 am	40	Sulfur Wash 2	50	0.10M HF/ 0.13M HCl	Removes further sulfur
10:33 am	41	Sulfur Wash 3	25	0.10M HF/ 0.16M HCl	Ensures no contamination in the final $^{32}\text{Si}$ fraction
10:54 am	21	Collection $^{32}\text{Si}$	20	0.5M HCl	Elution of $^{32}\text{Si}$ : final fraction
11:11 am	17	<b>Separation Process ended</b>			Time stamp: Ingrowth of $^{32}\text{P}$

### 3.2.2.9 Sample preparation for AMS: $^{32}\text{SiO}_2$ and $\text{K}_2^{32}\text{SiF}_6$

For measurements with AMS, it was necessary to convert the liquid  $\text{H}_2^{32}\text{SiF}_6$  (in 0.5M HCl) matrix into solid  $^{32}\text{SiO}_2$  and  $\text{K}_2^{32}\text{SiF}_6$  samples, respectively, with each set having suitable  $^{32}\text{Si}/^{28}\text{Si}$  ratios. First, we prepared samples using a  $^{32}\text{Si}$  stock solution with  $A(^{32}\text{Si}) = 14.4 \text{ kBq/g}$ , but also prepared samples from the  $^{32}\text{Si}$  stock solution with  $A(^{32}\text{Si}) = 108.9 \text{ kBq/g}$ . In order to provide appropriate  $^{32}\text{Si}/^{32}\text{Si}$  ratios, we assumed that an average vanadium disc contains  $80 \mu\text{g } ^{\text{nat}}\text{Si}$ . However, referring to the isotopic abundance of  $^{28}\text{Si}$  (92.223%) that translates to  $73.784 \mu\text{g } ^{28}\text{Si}$  per disc. Due to the two different stock solutions, we also needed to account for different silicon contents, as presented in Table 3.9.

**Table 3.9:** Overview of the stock solutions used for the preparation of individual sample sets for the AMS measurements at ETH Zurich (Laboratory for Ion Beam Physics, LIP).

Activity concentration (kBq/g)	Disc(s)	$^{28}\text{Si}$ content per disc ( $\mu\text{g}/\text{disc}$ )	$^{28}\text{Si}$ content ( $\mu\text{g}$ )	Solution's volume (mL)	$c(^{28}\text{Si})$ in $\text{M} (\times 10^{-4})$	$^{32}\text{Si}/^{28}\text{Si}$ ( $\times 10^{-3}$ )
14.4	x1	78.784	78.784	20	1.318	1.330
108.9	x6		472.704		6.587	1.994

### 3.2.2.9.(I) $^{32}\text{SiO}_2$ samples

The sample preparation was based on an in-house developed procedure that yielded the highest precipitation rate and provided pure  $\text{SiO}_2$  samples. For the required solutions, 3.098 g of  $\text{H}_3\text{BO}_3$  was dissolved (Suprapur<sup>®</sup>, 99.9999%, Merck KGaA, Germany) together with 1.325 g of  $\text{Na}_2\text{CO}_3$  (anhydrous, Puratronic<sup>™</sup>, 99.997%, Fisher Scientific, Waltham, U.S.A.) in a 50 mL volumetric flask using silicate-free water (NANOCOLOR, silicate-free water (sf- $\text{H}_2\text{O}$ ), Macherey & Nagel, Germany)). This yielded a 0.25M  $\text{Na}_2\text{B}_4\text{O}_7$  solution. Further, 10.5988 g of  $\text{Na}_2\text{CO}_3$  were dissolved in sf- $\text{H}_2\text{O}$  a separate 50 mL volumetric flask, to obtain a 2M solution. As we had to provide  $^{32}\text{Si}/^{28}\text{Si}$  in the range of  $10^{-14}$  to  $10^{-10}$  we followed first two different ways of diluting the stock solution, while preparing the subsequent dilutions for the different isotopic ratios equally. For the dilution, a diluent solution was prepared from a 10'000 ppm commercially available silicon standard (04713-100ML TraceCERT<sup>®</sup> (Merck KGaA, Darmstadt, Germany), and 038723-AE Specpure<sup>™</sup>(Alfa Aesar, Haverhill, U.S.A.)). To avoid any hydrolysis of silicon, 38 mL of the standard solution was transferred into a 50 mL PP-Tube and 2 mL 20M HF (prepared from Suprapur<sup>®</sup>, 40 wt.-% HF ( $\approx 22.5\text{M}$ ), Merck KGaA, Darmstadt Germany) was added to reach a final HF-concentration of 1M. Moreover, the resulting  $^{28}\text{Si}$  concentration was calculated based on the certificate of analysis (COA), providing the silicon concentration within an uncertainty of  $\approx 0.7\%$  ( $k=1$ ). Preparations for all the different steps have been gravimetrically traced, to provide both a low uncertainty and a high reproducibility. A more detailed overview for each dilution is given in the appendix. Generally, an aliquot of each dilution was mixed with 4.5 mL of diluent solution. From this solution 4 mL were removed and mixed with 4.7 mL 0.25 M  $\text{Na}_2\text{B}_4\text{O}_7$  solution and 6.1 mL 2 M  $\text{Na}_2\text{CO}_3$  in a 50 mL PP-tube. The solutions were left in the dark for around 12 hours. Then the samples were centrifuged for 1 minute at 2000 rpm, and 2 minutes at 4000 rpm, respectively. In total, the samples were washed three times with 15 mL sf- $\text{H}_2\text{O}$  each time. Between each washing step, the samples were again centrifuged with the same sequence, to avoid losses during decanting.

After washing the samples, the 50 mL PP-tubes were placed into an oven (70-75 °C), and left there for around 20h. The dried precipitate was transferred into an alumina crucible and burned for around 4 hours at 400 °C. Noteworthy to mention that the preparation starts with the lowest  $^{32}\text{Si}/^{28}\text{Si}$  ratio ( $= 10^{-14}$ ) to avoid contaminations, e.g., during the process of burning in the furnace. Table 3.10, and Table 3.11, provide an overview of the different samples that have been delivered to ETHZ for measurements. The samples were finally provided as amorphous  $\text{SiO}_2$  and each sample weighed around 50 mg. During the method development, the final procedure was tested with ICP-OES, to confirm that sodium and boron are quantitatively removed and, thus, to provide pure samples for the AMS measurements.

**Table 3.10:** Overview of the first batch of (test) samples (AMS Series SiO<sub>2</sub> (S-I)), based on the <sup>32</sup>Si stock solution with an activity concentration of 14.4 kBq/g for <sup>32</sup>Si. The scheme "D-" refers to the dilution's step number.

AMS-S-I	D-1	D-2	D-3	D-4	D-5
<sup>32</sup> Si/ <sup>28</sup> Si	$5.63 \times 10^{-9}$	$1.01 \times 10^{-9}$	$1.00 \times 10^{-10}$	$9.94 \times 10^{-12}$	$9.84 \times 10^{-13}$
<sup>32</sup> Si stock (mL)	0.1				
Diluent (mL)	9.9	4.5	4.5	4.5	4.5
Dilution 1		1			
Dilution 2			1		
Dilution 3				1	
Dilution 4					1

**Table 3.11:** Overview of the second batch of samples (AMS Series SiO<sub>2</sub> (S-II)) based on the <sup>32</sup>Si stock solution with an activity concentration of 108.9 kBq/g for <sup>32</sup>Si. The scheme "D-" refers to the dilution's step number.

AMS-S-II	D-1.1	D-1.2	D-2	D-3	D-4	D-5
<sup>32</sup> Si/ <sup>28</sup> Si	$4.18 \times 10^{-8}$	$4.14 \times 10^{-9}$	$7.53 \times 10^{-10}$	$7.51 \times 10^{-11}$	$7.49 \times 10^{-12}$	$7.45 \times 10^{-13}$
<sup>32</sup> Si stock (mL)	0.1					
Diluent (mL)	9.9	9	4.5	4.5	4.5	4.5
Dilution 1.1		1				
Dilution 1.2			1			
Dilution 2				1		
Dilution 3					1	
Dilution 4						1

### 3.2.2.9.(II) K<sub>2</sub><sup>32</sup>SiF<sub>6</sub> samples

In contrast, sample preparation for K<sub>2</sub><sup>32</sup>SiF<sub>6</sub> samples was requiring a less chemical treatment as the speciation in solution was already matching the salt's composition. The sample preparation was based on an in-house developed procedure that yielded the highest precipitation rate and provided pure K<sub>2</sub><sup>nat</sup>SiF<sub>6</sub> samples.

First, 10 mL of a saturated potassium chloride (99.999%, (trace metal basis), Fisher Scientific, Waltham, U.S.A.) solution was prepared. The solubility is around 34 g/100mL (at 20 °C) so that 3.5 g of solid were added to 10 mL that finally yields a  $\approx$  4.6M solution of KCl. Again, as we had to provide <sup>32</sup>Si/<sup>28</sup>Si in the range of 10<sup>-14</sup> to 10<sup>-10</sup> we followed first two different ways of diluting the stock solution, while preparing the subsequent dilutions for the different isotopic ratios equally. For the dilution, a diluent solution was prepared from a 10'000 ppm commercially available silicon standard (Cat. number: 456012Y, VWR International, Radnor, U.S.A.). Besides, to avoid any hydrolysis of silicon, 38 mL of the standard solution was transferred into a 50 mL PP-Tube and 2 mL 20M HF (prepared from Suprapur<sup>®</sup>, 40 wt.-% HF ( $\approx$  22.5M), Merck KGaA, Darmstadt, Germany) was added in order to reach a final HF concentration of 1M.

Moreover, the resulting  $^{28}\text{Si}$  concentration was calculated based on the certificate of analysis (COA), providing the silicon concentration within an uncertainty of  $\approx 2.4\%$  ( $k=1$ ). After the final preparation of the samples (Table 3-12), they were left untouched for around 24 hours. Afterwards, the samples were centrifuged for 1 minute at 2000 rpm, and 2 minutes at 4000 rpm. respectively. In total, the samples were washed three times with 3 mL utp- $\text{H}_2\text{O}$  each time. Between each washing step, the samples were again centrifuged with the same sequence, to avoid losses during decanting. After washing the samples, the 15 mL PP-tubes were placed into an oven ( $\approx 50\text{ }^\circ\text{C}$ ), and left there for around 20 hours. The sample amount was determined to be in the range of 80 mg per sample.

**Table 3.12:** Overview of the third batch of samples (AMS Series  $\text{K}_2\text{SiF}_6$  (K-I)) based on the  $^{32}\text{Si}$  stock solution with an activity concentration of 108.9 kBq/g for  $^{32}\text{Si}$ . The scheme "D-" refers to dilution's step number, and K indicates the potassium.

AMS-K-I	D-K-1.1	D-K-1.2	D-K-2	D-K-3	D-K-4	D-K-5
$^{32}\text{Si}/^{28}\text{Si}$	$4.00 \times 10^{-8}$	$3.95 \times 10^{-9}$	$9.83 \times 10^{-10}$	$9.74 \times 10^{-11}$	$9.60 \times 10^{-12}$	$9.52 \times 10^{-13}$
$^{32}\text{Si}$ stock (mL)	0.1					
Diluent (mL)	9.9	9	2.25	2.7	2.7	2.7
Dilution 1.1		1				
Dilution 1.2			0.75			
Dilution 2				0.3		
Dilution 3					0.3	
Dilution 4						0.3

### 3.2.3 Part 3 of 3: Preparation for determining cross-sections

#### 3.2.3.1 Irradiated vanadium discs and their characterisation

As opposed to the irradiated metallic vanadium discs used as targets during the STIP-6, we received seven additional vanadium discs from Prof. Rolf Michel (Leibniz University Hannover). The natural metallic vanadium discs (on average: mass  $\approx 132$  mg, diameter  $\approx 1.50$  cm, chemical purity of vanadium: 99.8%) were initially also provided by Goodfellow Cambridge Limited (U.K.). The manufacturer's certificate states typical impurities to be (in parts per  $10^6$ ): Cu  $<1$ , Ca  $<1$ , Mg  $<1$ , Mn  $\leq 1$ , Ag  $\leq 1$ , Al  $\leq 2$ , Cr  $\leq 15$ , Fe  $\leq 70$ , and Si  $\leq 300$ . These seven discs differ mainly in their mass, and in their irradiation time. The main reason for receiving these vanadium discs was to determine the excitation function for  $^{44}\text{Ti}$ ,  $^{41}\text{Ca}$ , and  $^{26}\text{Al}$ . As a result, a radiochemical separation procedure, that is described in detail in one of the following sections, was developed.

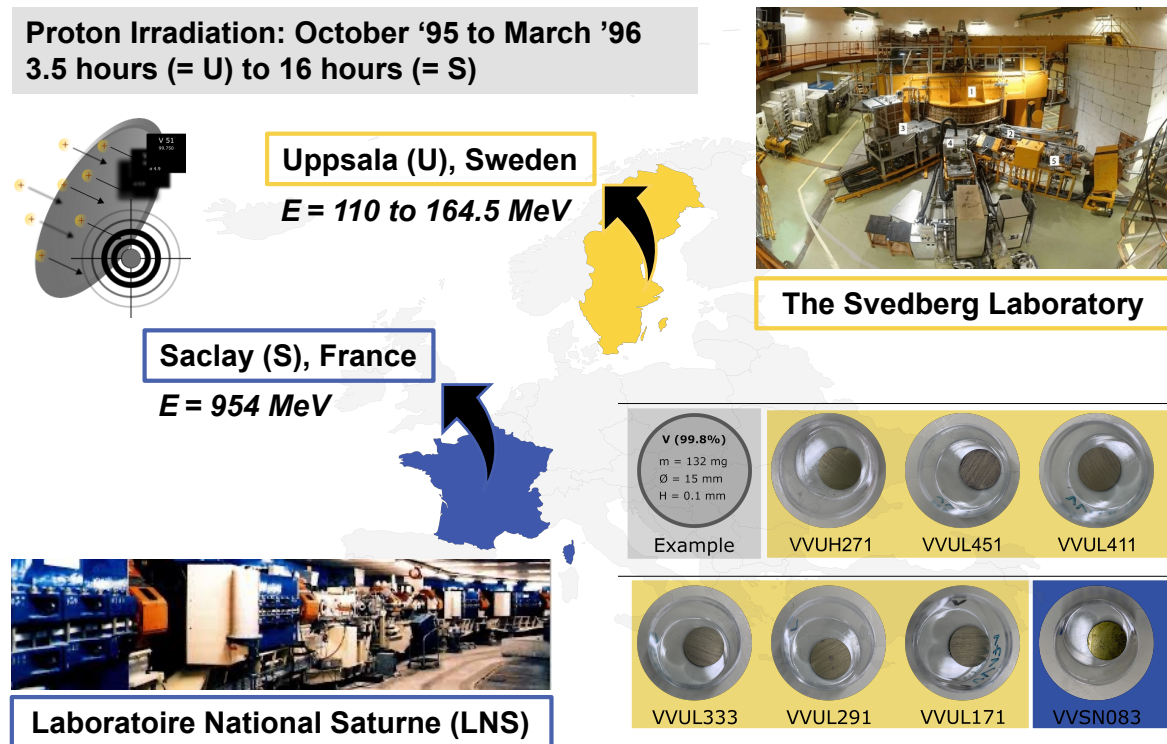


**Fig. 3.2:** Overview of the irradiation locations and conditions. Also, initial seven irradiated vanadium discs are shown, with their different appearance, which is likely caused by partial oxidation. Photos are taken from [175], [176], and [177], respectively.

As seen in Fig. 3.2, the irradiation took place between October 1995 and March 1996 and covered proton energies ranging from 111 to 954 MeV. The experiments' initial target preparation was carried out in cooperation with the University of Cologne and the Leibniz University in Hannover. A detailed description of the target preparation can be found elsewhere [163]. Further, the irradiation experiments with protons were performed at two facilities in Europe: the Laboratoire National Saturne (Saclay, France) and the Svedberg Laboratory (Uppsala, Sweden). The samples were marked accordingly (Fig. 3.2).

**Table 3.13:** Overview, characterising the analyzed vanadium specimen. The mass was determined based on measurements, but the mass differences were suspected to, e.g., partial oxidation of the metal (Fig. 3.2). In order to be consisted with the previous work [178], an averaged disc mass of  $132 \pm 1.32$  mg was considered.

Sample	Proton Energy (MeV)	Proton flux ( $\times 10^{11}$ ) ( $\text{cm}^{-2} \text{ s}^{-1}$ )	Irradiation time (s)	Target mass (mg)
VVUH271	$111 \pm 1.3$	$1.068 \pm 0.021$	11400	132.3
VVUL451	$129 \pm 1.4$	$1.447 \pm 0.024$		133.4
VVUL411	$134.9 \pm 1.3$	$1.466 \pm 0.024$		148.3
VVUL333	$145 \pm 1.2$	$1.505 \pm 0.024$	12360	145.9
VVUL291	$150.2 \pm 1.2$	$1.523 \pm 0.024$		140.2
VVUL171	$164.5 \pm 1.0$	$1.576 \pm 0.024$		138.5
VVSN083	$954 \pm 1.6$	$0.02430 \pm 0.00053$	60480	151.2

### 3.2.3.2 Determination of the $^{44}\text{Ti}$ activity with $\gamma$ -spectrometry

Although a separation procedure from  $^{44}\text{Ti}$ -traces from proton-irradiated vanadium is described by [179], we decided to forgo a radiochemical separation of  $^{44}\text{Ti}$ , to exclude possible losses and could thus perform our calculations based on a 100% yield. Gamma-ray attenuation in the acidic vanadium matrix was considered negligible. Furthermore, working with  $^{44}\text{Ti}$  has the advantage to allow measuring the 1157-keV  $\gamma$ -line of the daughter nuclide  $^{44g}\text{Sc}$ , and to calculate the  $^{44}\text{Ti}$  activity based on the daughter's activity. By this, difficulties of determining the gamma-spectrometer's efficiency precisely in the low-energy range can be circumvented. Therefore, care should be taken to ensure that the reference standard (RS), used for calibration, precisely represents the samples to be counted. For this reason, the RS and samples should be, e.g., identical in dimensions, shape, density (media), spatial distribution of active material. Moreover, the source position is also important, in particular for close geometries, as we used during our measurements. In order to accurately determine the  $^{44}\text{Ti}$  activity in each vanadium disc sample, in-house prepared calibration sources, guaranteeing the same geometry as the investigated samples, were prepared. At first, the initial specific  $^{44}\text{Ti}$ -activity of a purified, in-house carrier-free  $^{44}\text{Ti}$ -solution (in 1 M HCl) was measured as a point-like source (PLC). The PLC was prepared by gravimetrically traced droplet deposition ( $\approx 20$   $\mu\text{L}$  per droplet) using a self-made pycnometer, followed by an immediate evaporation of the solution on a circular polyethylene foil with a diameter of 2.5 cm (specified density =  $21.3 \pm 1.8$   $\text{mg} \times \text{cm}^{-2}$ ). The PLC was then placed on an efficiency calibrated position of a High-Purity Germanium (HPGe) detector at a distance of  $140 \pm 1$  mm in air on a 1.2-mm thick Al support. Consequently, the activity concentration of this in-house solution was determined with =  $(1.140 \pm 0.013)$  Bq/mg. Utilizing  $^{44g}\text{Sc}$  in secular equilibrium with its parent,  $^{44}\text{Ti}$ , has a twofold advantage: (i) The emission branching ratio for  $^{44}\text{Sc}$  is accurately known ( $I_{\gamma,1157\text{keV}} = 99.9(4)\%$ ) and (ii) The use of the high energy region of the HPGe avoids unnecessary complications caused by complex background and steep changes in the efficiency curve, as it is the case for the low energy region. Subsequently, from the calibrated stock solution, two RS with volumes of 2 mL (RS-2) and 5 mL (RS-5), respectively, were also gravimetrically prepared in the same high-density polyethylene (HD-PE) LSC-vials. For each sample, 1 mL of the  $^{44}\text{Ti}$  stock solution was used, and either 8M  $\text{HNO}_3$  (for RS-2) or 8M HCl (for RS-5) was added to reach the final volume and to account for the specific matrix.

These solutions were then used for the relative efficiency calibrations of both the Low Energy Germanium (LEGe) detector and HPGe detector used for determination of  $^{44}\text{Ti}$  activity in the specific sample (Fig. 3.3).

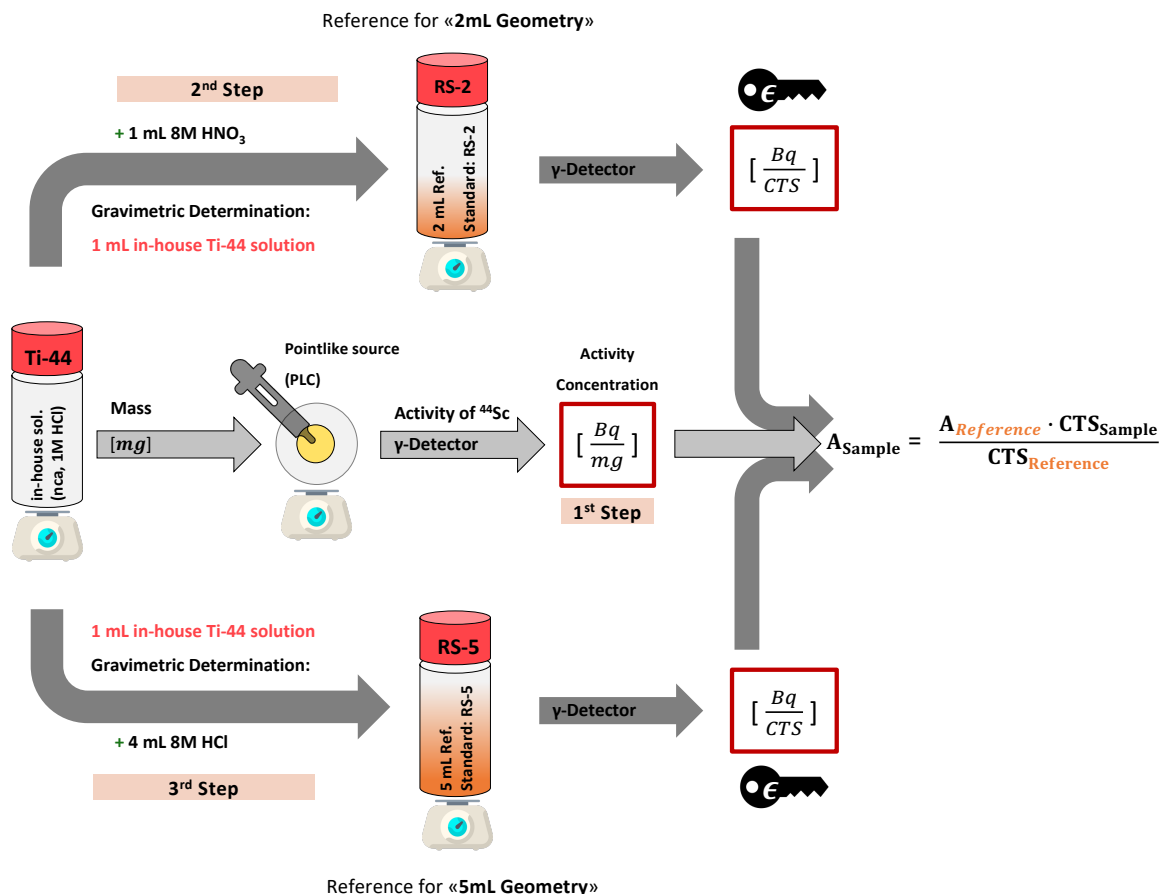


**Fig. 3.3:** Overview of the sample preparation and the measurements by means of  $\gamma$ -spectrometry. All involved steps were mass-controlled using a high-precision scale (XS225 DualRange, Mettler Toledo, Switzerland).

### 3.2.3.2.(I) Preparation for LEGe measurements: 2 mL Reference

Initially, each vanadium disc was placed into an HD-PE LSC vial (diameter: 27 mm, height: 58 mm) and dissolved in 2 mL 8 M nitric acid, which was prepared from concentrated nitric acid (Semiconductor Grade MOS PURANAL,  $\text{HNO}_3$  (69 wt.-%), Merck KGaA, Germany.). Due to the experience with the previous vanadium discs from the STIP-6, these discs were also dissolved in vials, which were placed in an ice-water mixture to quench the exothermic dissolution reaction. Again, this procedure was necessary to prevent the formation of a solid residue (likely vanadium pentoxide,  $\text{V}_2\text{O}_5$ ) which was always visible when the vial was not cooled during the dissolution process. After the complete disc's dissolution, each sample was subsequently  $\gamma$ -spectrometrically measured using the LEGe.

### 3.2.3.2.(II) Preparation for HPGe measurements: 5 mL Reference

In order to provide a reliable comparison with the  $\gamma$ -spectrometric previous results, obtained from the LEGe, a further measurement for each sample was considered. This time, on a HPGe. Since these measurements were performed several months after the initial measurements, each sample was reprocessed to account, e.g., for changes in the volume concerning the sample geometry; such a change was suspected due to the sample's storage and possible evaporation.

Consequently, each HD-PE LSC vial was heated up gently with an open lid to achieve complete dryness. To dissolve remaining residues on the inner walls of the LSC vial entirely, the sample walls were then treated several times with concentrated hydrochloric acid (ACS reagent, fuming, HCl (37 wt.-%), Merck KGaA, Germany). After a further evaporation to dryness, the samples were re-dissolved using 5 mL of 8 M HCl. On this subject, the resulting matrix with a strong complexing ion, such as chloride, proofed to provide a suitable matrix for the solution's long-term stability (no early precipitation of  $V_2O_5$ ) and was therefore later added as part of the acidic cocktail used for the dissolution of the irradiated vanadium discs from the STIP-6. Moreover, choosing an elevated HCl concentration for the dissolution, vanadium forms various chemically stable and soluble chloro complexes ensuring reliable measurements regarding the sample's geometry, as the spatial distribution of the activity is maintained (e.g., no formation of solids). Since the 2 mL and 5 mL reference sources were prepared in the same geometry and with the same radionuclide, as the dissolved vanadium samples, we were able to diminish both the need for true-coincidence summing corrections and precise knowledge of the photon emission probabilities. Moreover, the efficiency response curve for energies other than the nuclide specific ones was not required since it was immediately determined through the count rates at the 67.9 and/or 78.3 keV  $\gamma$ -lines from its decay. Therefore, with our specified geometry we obtained our efficiency calibration as counts per second per becquerel ( $CT \times s^{-1} \times Bq^{-1}$ ) of  $^{44}Ti$  activity in the solution of the specified geometry (Fig. 3.3).

As a result, this allowed comparing the count rate of the samples, with unknown activity, with the known activity of the calibration sources of the same geometry, in order to determine the  $^{44}Ti$  activity (Fig. 3.3) and to finally characterise each reference solution (Table 3.14). The final  $^{44}Ti$  activity was projected with a specified reference date: August 31, 2019, (defined as "end of measurement";  $t_{eoc}$ ).

**Table 3.14:** Overview of the different reference sources used for the activity determination respecting different sample geometries.

Reference Standard	Detector	$^{44}Ti$ activity (Bq/mg)	Added $^{44}Ti$ solution (mg)	Resulting activity (Bq)	Nuclide ( $\gamma$ -energy in keV)
PLC	HPGe	$1.140 \pm 0.013$	$86.35 \pm 0.01$	$98.45 \pm 1.13$	$^{44g}Sc$ (1157)
2 mL	LEGe		$1021.12 \pm 1.02$	$1167.70 \pm 13.42$	$^{44}Ti$ (67.9, 78.3)
5 mL	HPGe		$1024.26 \pm 1.02$	$1167.47 \pm 13.48$	$^{44}Ti$ (78.3)

### 3.2.3.3 Development of a separation procedure for $^{41}\text{Ca}$ and $^{26}\text{Al}$

It is noteworthy to mention that the presented separation procedure was successfully developed as part of a master's thesis, which, however, had to regard some experimental boundary conditions prior to the development:

- (i) The separation of either  $^{41}\text{Ca}$  or  $^{26}\text{Al}$  had to be performed initially with 3M  $\text{HNO}_3$  to account for the matrix, with which the irradiated STIP-6 samples were eluted from the Dowex<sup>®</sup> 50WX8-200 resin (bulk separation).
- (ii)  $^{32}\text{Si}$ , as a proven by-product due to proton-induced spallation on vanadium targets, had to be separated, too.
- (iii)  $^{32}\text{Si}$ ,  $^{41}\text{Ca}$ , and  $^{26}\text{Al}$  will be measured using AMS and must be therefore separated with a carrier which must be added prior to the separation. This is necessary to provide enough (solid) sample material and to disregard losses, as AMS measures isotopic ratios and, if losses occur during the separation procedure, then both for the stable and radioactive nuclide.

Moreover, as this separation procedure was developed in a rather early phase of the SINCHRON-project, L-AscA was used for the reduction of vanadium. We decided later, to forgo the addition of L-AscA since it requires later a separation of  $^{32}\text{Si}$  from the L-AscA matrix. Referring to (i) and (ii), the samples were initially dissolved in 5 mL 8M HCl. Therefore, to fulfill these requirements, a matrix change was needed, and, additionally implementing the simultaneous separation of  $^{32}\text{Si}$  from the vanadium matrix, while (iii) working with ppm instead of nca amounts.

#### 3.2.3.3.(I) Change of matrix and separation of carrier-added $^{32}\text{Si}$

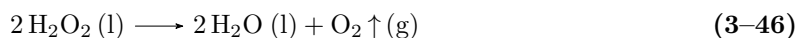
A  $300 \pm 3$  mL plastic graduated cylinder was pre-filled with 100 mL utp- $\text{H}_2\text{O}$ . The initial 5 mL acidic vanadium solution was added to the graduated cylinder. The HD-PE vial was then rinsed twice, with 5 mL utp- $\text{H}_2\text{O}$  and the washing solutions were combined with the initial vanadium solution into the same graduated cylinder. Then, 2 mL of 1M ascorbic acid (L-AscA) solution to reduce the vanadium was added. Since the samples were intended for AMS measurements, carriers for both calcium and aluminium were added before the separation. Thus, 2 mL of a single-element standard (1000 ppm, TraceCERT<sup>®</sup>, Merck KGaA, Germany) were added successively. Before introducing 2 mL silicon standard solution (1000 ppm, 2 wt.-% NaOH, TraceCERT<sup>®</sup>, Merck KGaA, Germany), the solution's volume was adjusted to 180 mL using utp- $\text{H}_2\text{O}$ . After the addition of the silicon standard, the final volume of 200 mL was reached by further dilution with utp- $\text{H}_2\text{O}$ . Diluting the sample by a factor of 40, the initial acidity decreased to  $\approx 0.2\text{M}$  HCl. The first separation step was performed using Dowex<sup>®</sup> 50WX8-200 (Merck KGaA, Germany) cation-exchange resin, hosted in a tailor-made polymethyl methacrylate (PMMA) column with an inner diameter of 10 mm and a resin bed height of 140 mm. The Load consisted of 200 mL matrix solution, followed by the Wash of 30 mL utp- $\text{H}_2\text{O}$ , to wash-off the silicon entirely. The two fractions were collected in a single 250 mL PE-Bottle. Most importantly, the Elute allowed to introduce the actual matrix change, since 50 mL 3M  $\text{HNO}_3$  were used here for the elution, and it was collected as a single fraction. As a result, we could provide the starting solution and start the development using the same matrix.

### 3.2.3.3.(II) $^{41}\text{Ca}$ separation using DGA (normal)

Again, a tailor-made PMMA column (length = 100 mm; inner diameter = 10 mm) was chosen, to host 60 mm of DGA (normal) resin. After pre-conditioning the resin with 3M  $\text{HNO}_3$ , the initial 50 mL 3M  $\text{HNO}_3$  fraction was passed through, followed by 20 mL 3M  $\text{HNO}_3$  to clean the column from remaining matrix-components. The final volume for this, so called aluminium-fraction (Al-Fraction), was finally 70 mL (3M  $\text{HNO}_3$ ). Subsequently, the elution of calcium from the DGA-column was achieved using 30 mL of 3M  $\text{HCl}$ .

### 3.2.3.3.(III) $^{26}\text{Al}$ separation using Dowex® 50WX8-200

The strongly acidic cation-exchange resin was used (bed height: 140 mm), filled in the tailor-made 300 mm PMMA-column. To the initial fraction of 70 mL (matrix: 3M  $\text{HNO}_3$ ), 7 mL of concentrated  $\text{H}_2\text{O}_2$  (30 wt.-%, Merck KGaA, Germany) was added and the solution was heated up for around ten minutes in a water bath (keeping at  $\approx 60^\circ\text{C}$ ) to decompose excess  $\text{H}_2\text{O}_2$ . The solution's heating for around ten minutes in a water bath was necessary to decompose excess  $\text{H}_2\text{O}_2$ , which was accompanied by the release of large gas bubbles. This step was quite significant since excess  $\text{H}_2\text{O}_2$  could also decompose during the actual separation procedure on the column, according to Eq. 3-46



leading to a formation of oxygen, which would, in turn, greatly affect the separation procedure since gas inclusions could occur within the resin. It is known that a similar increase in the rate of decomposition of hydrogen peroxide can be achieved by homogeneous, heterogenous catalysis, e.g.,  $\text{Fe}^{3+}$ , or  $\text{Mn}(\text{II})$  oxide, or also via enzymatic catalysis. However, neither did we want to introduce any further metal additive nor to work with enzymes (also critical conditions considering 3M  $\text{HNO}_3$ ). Thus, we decided to forgo the use of either an inorganic or enzyme catalyst. As a result, we optimized the experimental conditions for the separation, using heat to facilitate the hydrogen peroxide's decomposition. After the solution was allowed to gently boil, the PE-bottle was immediately placed in ice. For the actual separation, the sample was then further diluted to 310 mL using a graduated cylinder and was then used as Load fraction. In the case of  $^{26}\text{Al}$ , we succeeded in choosing a gradual elution from the vanadium matrix employing a novel technique for the separation, which isn't described as such in the literature. This approach focuses on vanadium's low retention in the oxidation state +V.

To remove vanadium entirely, three different  $\text{HNO}_3$  concentrations (0.75M, 1M, and 3M) were used, applying the concept of gradual elution. First, during the load and the wash with 0.75 molar  $\text{HNO}_3$ ,  $\text{V}^{+V}$  species were fully removed. Secondly, increasing the  $\text{HNO}_3$  molarity to 1 M,  $\text{V}^{+IV}$ , which exhibits a higher affinity towards the ion-exchange resin, was partially starting to elute. Then, using 3M  $\text{HNO}_3$  as eluent, both  $\text{V}^{+IV}$  and  $\text{Al}^{3+}$  are eluted, so care was taken to obtain pure  $\text{Al}^{3+}$ -fractions, which was achieved by performing a test utilizing a high-resolution elution profile (5mL-Fractions) to screen for the breakthrough of vanadium and aluminium, respectively. As a result, the separation scheme then included a wash with 30 mL 0.75M  $\text{HNO}_3$  (= 340 mL), followed by 10 mL 1 M  $\text{HNO}_3$ . For the consecutive separation of remanent  $\text{V}^{+IV}$ , 20 mL 3M  $\text{HNO}_3$  were added, followed by 30 mL 3M  $\text{HNO}_3$ , in which aluminium was eventually collected. Those volumes result from the continuous optimization to achieve the best separation using gradual elution.

### 3.2.3.4 Sample preparation for AMS: $^{41}\text{CaF}_2$ and $^{26}\text{Al}_2\text{O}_3$

#### 3.2.3.4.(I) Preparation of $^{41}\text{CaF}_2$ AMS-samples

Each  $^{41}\text{Ca}$ -fraction was evaporated to dryness using a 5 mL conical glass vial (Reactivial®), while successively adding the 3M HCl solution. The heat was applied by an external electric heating coil with the temperature set to 150 °C. The obtained solid residue was dissolved in 500  $\mu\text{L}$   $\text{H}_2\text{O}$  and the resulting solutions were transferred to a 2 mL centrifuge plastic vial. Moreover, 250  $\mu\text{L}$  1M HF was added to account for the stoichiometry, and the solutions were left undisturbed overnight for a complete  $\text{CaF}_2$  precipitation. Following this procedure, the dispersion was then centrifuged, and the supernatant was discarded. The solid precipitate was washed with 750  $\mu\text{L}$  utp- $\text{H}_2\text{O}$  and the centrifugation process was repeated. The obtained solids were dried for 24h at 80 °C. The  $^{41}\text{Ca}$  AMS measurement was performed at the 300 kV MILEA AMS located at the Laboratory of Ion Beam Physics (ETH Zurich, [180]).

#### 3.2.3.4.(II) Preparation of $^{26}\text{Al}_2\text{O}_3$ AMS-samples

The optimized procedure to obtain solid samples, suitable for AMS measurements, is explained in the following paragraph. The procedure was optimized towards high precipitation yields while achieving reproducible results. At first, the separated  $^{26}\text{Al}$  solutions with an initial volume of 30 mL in 3M  $\text{H}_2\text{O}$  were reduced to about 5 mL. The solutions were concentrated through evaporation using a zirconium vessel, placed on a hot plate ( $T = 180$  °C). The concentrated solutions were transferred to a 50 mL PP conical centrifugation tube (PP). To this solution, 10 mL freshly prepared half-concentrated ammonia solution (prepared from Ammonia solution 28.3 wt.-% (from the COA), Suprapur®, Merck KGaA, Germany) was added, followed by 3 mL (2x 1.5 mL) concentrated ammonia solution. After the addition of the second 1.5 mL, the visible precipitation of aluminium hydroxide ( $\text{Al}(\text{OH})_3$ ) occurred. The precipitate was allowed to settle overnight, the solution was centrifuged, the supernatant was discarded, and the hydroxide-residual washed twice with half-concentrated ammonia solution. Eventually, using three to four times 500  $\mu\text{L}$  half-concentrated ammonia solution, the residual was transferred into glazed crucibles and dried for 24h at 105 °C. Once completely dried, the solids were calcined at 900 °C for 8h (netto burning time), and each sample was transferred into a single, dedicated 2 mL Cryovial and sealed with Parafilm®. The  $^{26}\text{Al}$  AMS measurement was performed at the 300 kV MILEA AMS facility, located at the Laboratory of Ion Beam Physics (ETH Zurich, [180]).



## 4 Results and Discussion

### 4.1 Characterisation of the target material

Two tasks were followed to characterize the target material, including an individual sample preparation. Generally, we focused on the determination of metallic impurities as well as the quantitative determination of the  $^{nat}\text{Si}$  content in the vanadium discs, which was considered the main objective of this task.

#### 4.1.1 Task I: Determination of impurities

- 20x, 100x, and 200x (volumetric) dilution of the initial sample matrix
- Calculations based on the precisely determined amount of vanadium (gravimetric)
- Quantitative detection of aluminium and iron for a further comparison
- Semi-Quantitative detection of trace impurities using TotalQuant™
- With and without using the Helium KED (**K**inetic **E**nergy **D**iscrimination) mode

First, the measurements of  $^{27}\text{Al}$  and  $^{56}\text{Fe}$  were performed. Given the isotopic abundances ( $\Theta$ ) of the elements,  $^{27}\text{Al}$  ( $\Theta = 100\%$ ) and,  $^{56}\text{Fe}$  ( $\Theta = 91.754\%$ , [181]) the elements' quantitative detection with ICP-MS was considered a routine analysis. However, the Helium KED mode (HKM) was necessary in order to suppress the known polyatomic interferences for  $^{27}\text{Al}$ , but especially for  $^{56}\text{Fe}$ . As seen in Fig. 4.1 and Fig. 4.2, respectively, the “Rusty” disc yields the highest aluminium and iron contents. But, in contrast, the  $^{27}\text{Al}$  and  $^{56}\text{Fe}$  contents between all discs do not show high deviations. Yet an apparent trend between the 20-fold and 200-fold dilution is visible, leading to higher element concentrations when analyzing the 200-fold diluted samples. This difference can be however explained when comparing the yields of the  $^{89}\text{Y}$  recovery rate (Fig. 4.3) that was used as internal standard. Looking at the results for the 20-fold dilution, the measurements with and without the KED mode are not satisfying for these low diluted samples. Consequently, the lower recovery yield suggests an underestimation of the  $^{27}\text{Al}$  and  $^{56}\text{Fe}$  content. Contrary to these results, the recovery rate of  $^{89}\text{Y}$  for 200x dilutions is within limits (Fig. 4.3), and, therefore, the results from the 200-fold dilution are considered more reliable. Moreover, the HKM was also used here to demonstrate the improvements in the measurement performance, e.g., especially visible for the 20-fold dilution series.

The determined amounts for  $^{27}\text{Al}$  and  $^{56}\text{Fe}$  with the 200-fold dilutions indicate that likely these impurities have only been present at the surface, which can explain higher concentrations of the “Rusty” discs, as opposed to rather shiny looking discs (“Average”) or the “Cleaned” discs, respectively. The obtained results are well below any expected concentrations for these elements, estimated from the maximum metallic contents, given by the suppliers' certificate. Nevertheless, nuclear reactions must also be considered for production routes from such impurities, stemming from (p, x) or (n,  $\gamma$ ) reactions.

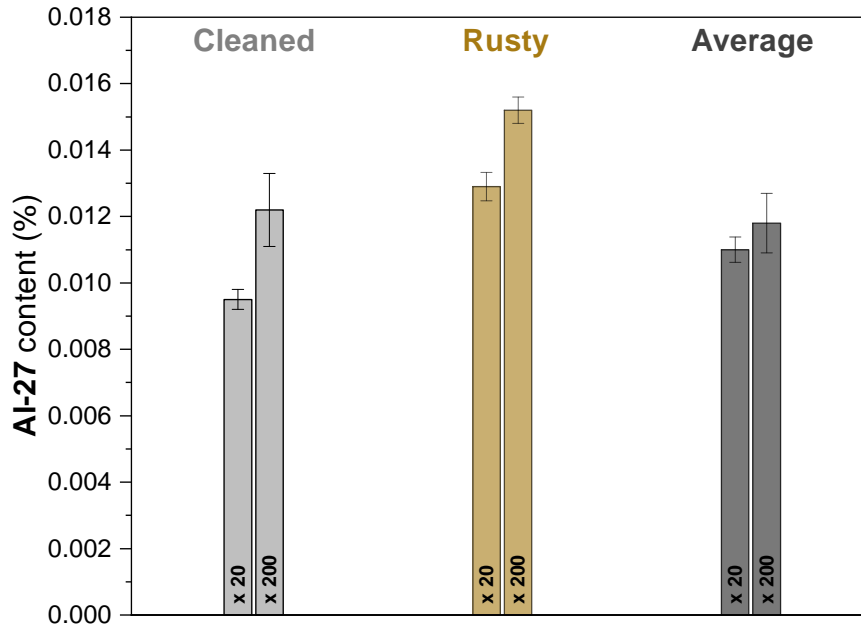


**Fig. 4.1:** Results for the  $^{27}\text{Al}$  content from the ICP-MS measurements. A comparison is shown for the different samples (1, 3, 5) and at different dilutions; x 20 and x 200, respectively.

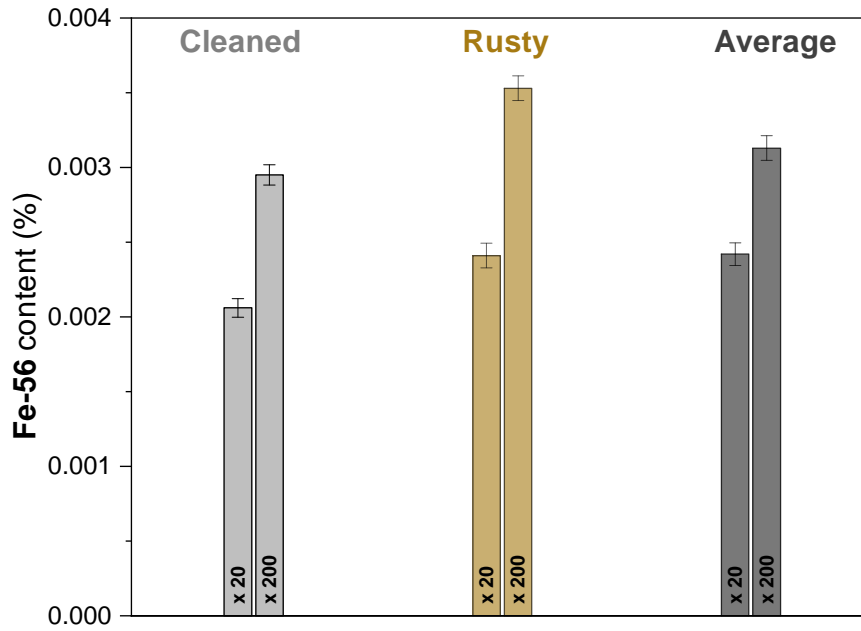


**Fig. 4.2:** Results for the  $^{56}\text{Fe}$  content from the ICP-MS measurements. A comparison is shown for the different samples (1, 3, 5) and at different dilutions; x 20 and x 200, respectively.

Since the average  $^{27}\text{Al}$  and  $^{56}\text{Fe}$  amounts were precisely determined, we used them further to verify measurements that were performed with the TotalQuant™Option (TQ-O). The TQ-O works with an internal calibration for the atomic mass units from 6 to 232 and allows to screen for nearly all elements of the periodic table. However, the determination is only semi-quantitative but allows for screening of several other metallic impurities that would yield further reaction-products during an irradiation. Considering that the samples seemed somewhat similar overall, for TQ-O, three independent samples were prepared, whereby the determined content is reported as the average of all three samples.

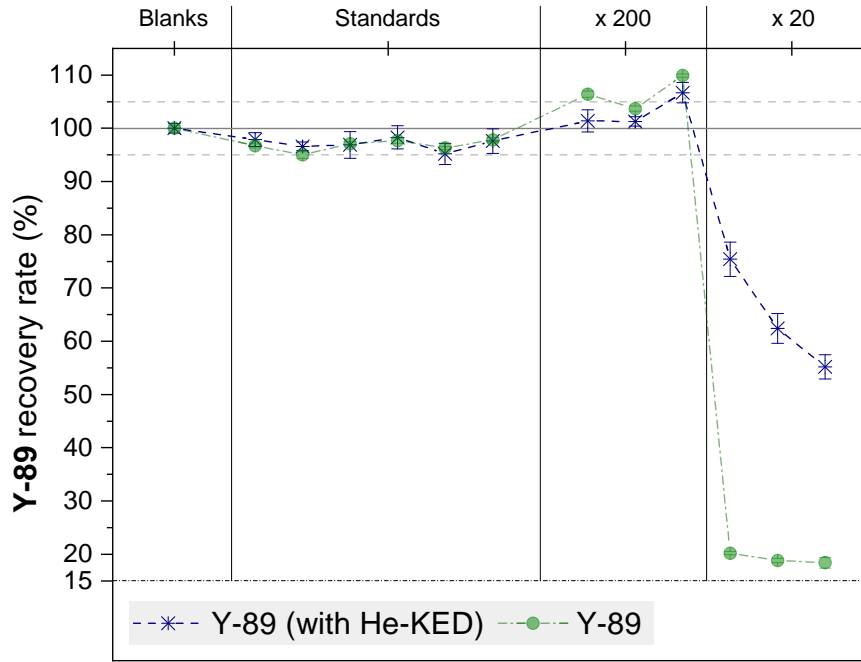


**Fig. 4.3:** Relative recovery yields for the 10 ppb  $^{89}\text{Y}$  from the samples (1, 3, 5). The average is indicated by the solid line, uncertainties by the grey dashed line ( $\pm 5\%$ ).

With an uncertainty of 50%-100% this measurement method is considered of more qualitative analytical character. Therefore, Table 4.1 suggests that the calculated metal content of Al and Fe is in good agreement with the previous measurement, which has been performed using a dedicated calibration curve. Therefore, the order of magnitude is usually correct, whereas a subsequent measurement with a matching calibration curve is always recommended.

**Table 4.1:** Comparison of the  $^{27}\text{Al}$  and  $^{56}\text{Fe}$  results for the two different measurement techniques.

	Aluminium ( $^{27}\text{Al}$ ) in wt.%		Iron ( $^{56}\text{Fe}$ ) in wt.%	
	x20	x200	x20	x200
Quantitative Detection	0.011	0.013	0.002	0.003
<b>Average</b>		<b>0.012</b>		<b>0.003</b>
Dilution	x100			
<b>TotalQuant<sup>TM</sup></b>		<b>0.015</b>		<b>0.005</b>

As stated in the supplier's product sheet, Al, Nb, Mo, and Ta could be identified with the TQ-O since they belong to the group of main contaminants. Further, we could identify Fe, Ni, Co, W, Zr, Zn, Cu, and Hf, since their intensities were clearly above the detection limit and above the blank values (Fig. 4.4). The detected nuclides likely explain the presence of, e.g.,  $^{94}\text{Nb}$  ( $T_{1/2} = (2.03 \pm 0.16) \times 10^4$  y), and  $^{60}\text{Co}$  ( $T_{1/2} = 5.2747 \pm 0.038$  y) in the proton irradiated vanadium samples, as they are the result of neutron activation of the stable nuclides:  $^{93}\text{Nb}$  (n, $\gamma$ )  $^{94}\text{Nb}$ ,  $^{94}\text{Mo}$  (n,p)  $^{94}\text{Nb}$  and  $^{59}\text{Co}$  (n, $\gamma$ )  $^{60}\text{Co}$ ,  $^{60}\text{Ni}$  (n,p)  $^{60}\text{Co}$ .

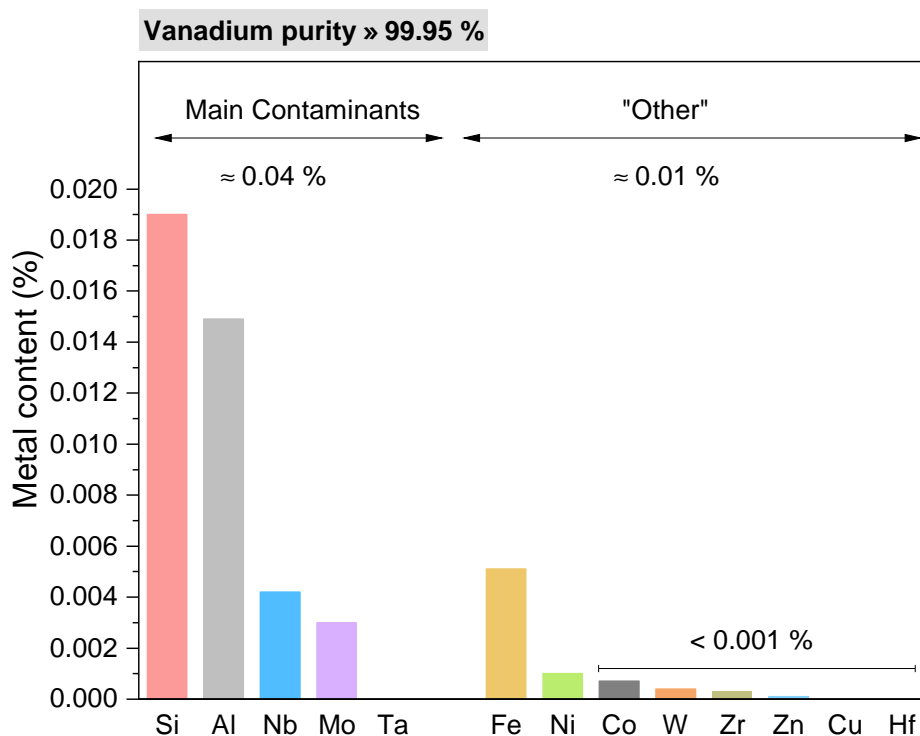


**Fig. 4.4:** Semi-quantitative determination of the elements detected in the vanadium disc, using the TQ-O. The measurements are reported as an average for samples 1, 3, and 5. Note that the Si-content was already added, too, but will be discussed in detail in the next section.

In addition to the clearly identifiable elements, also other nuclides could be identified, but rather in the ppb concentration range ( $\leq 0.001$  wt.-%). A summary of these nuclides with their relative concentration is given in Table 4.2.

**Table 4.2:** Determined metal content (EPFL) in the inactive vanadium discs compared with the certified maximum content of the supplier (SUPL), Goodfellow (Cambridge Ltd., England).

	Main Contaminants					"Other"						
EPFL	Al	Nb	Mo	Ta	Fe	Ni	Co	W	Zr	Zn	Cu	Hf
ppm	150	40	30		50	10	7	4	3	1		
ppb				110							310	55
Sum	≈ 220 ppm					≈ 75 ppm						
SUPL												
ppm	≤500	≤1000	≤1000	≤1000	individual amounts: n.a.							
Sum	≤3500 ppm					≤500 ppm						

2

When comparing the measurement results with the stated upper maximum metal contaminations given by the supplier, it is obvious that the received batch of vanadium discs contain much less metallic contaminants, in comparison to the expected upper limit. Therefore, the amount of the metallic contaminants is in the range of  $\approx 300$  ppm, whereas they can be as high as  $\approx 4000$  ppm (here: without silicon). As a result, the determined purity of the vanadium discs is 99.97% and we could provide a batch-specific analysis for the experiments. Further, the stated purity regards also the content of natural silicon, which is presented in the subsequent section.

### 4.1.2 Task II: Determination of the Si content

- 20x and 200x (volumetric) dilution of the initial sample matrix
- Precisely determined amount of vanadium (cross-check)
- With and without using the Helium KED (**K**inetic **E**nergy **D**iscrimination) mode

As we refer to non-carrier added (nca) silicon, it was important to know how much stable Si is initially present. Thus, it allows us to estimate a general specific activity of  $^{32}\text{Si}$  while being additionally able to provide a reference for further ICP-MS measurements concerning our  $^{32}\text{Si}$  solution(s).

Natural silicon consists of the isotopes  $^{28}\text{Si}$ ,  $^{29}\text{Si}$ , and  $^{30}\text{Si}$ .  $^{28}\text{Si}$  is the most abundant isotope, thus yields the most accurate and reliable results, regarding the applied ICP-MS measurements. However, again, polyatomic interferences must be considered, which are for each of the silicon isotopes summarized in Table 4.3.

**Table 4.3:** Summary of possible polyatomic interferences, taken from [142].

Isotope	m/z	Abundance (%)	Possible Interferences
$^{28}\text{Si}$	28	92.223	$^{14}\text{N}_2^+$ and $^{12}\text{C}^{16}\text{O}^+$
$^{29}\text{Si}$	29	4.658	$^{14}\text{N}^{15}\text{N}^+$ ; $^{14}\text{N}_2^+ \text{H}^+$ ; $^{13}\text{C}^{16}\text{O}^+$ ; $^{12}\text{C}^{17}\text{O}^+$ ; $^{12}\text{C}^{16}\text{O}^1\text{H}^+$
$^{30}\text{Si}$	30	3.092	$^{15}\text{N}_2^+$ ; $^{14}\text{N}^{15}\text{N}^1\text{H}^+$ ; $^{14}\text{N}^{16}\text{O}^+$ ; $^{12}\text{N}^{18}\text{O}^+$ ; $^{13}\text{C}^{17}\text{O}^+$ ; $^{13}\text{C}^{16}\text{O}^1\text{H}^+$ ; $^{12}\text{C}^{17}\text{O}^1\text{H}^+$ ; $^{14}\text{N}_2^+ \text{H}_2^+$ ; $^{12}\text{C}^{16}\text{O}^1\text{H}_2^+$

As visible from Table 4.3, not only is  $^{30}\text{Si}$  the isotope with the lowest isotopic abundance, but measurements on the atomic mass unit of 30 are very likely influenced by various polyatomic species related to carbon, hydrogen, nitrogen, and oxygen. These elements are ubiquitous, as they are usual impurities present in the plasma gas (e.g., Argon 5.0), or in the used acid ( $\text{HNO}_3$ ). Therefore, we already expected relatively high differences between the measurements for the different silicon isotopes in advance. The results of the  $^{\text{nat}}\text{Si}$  determination are seen in Fig. 4.5 and Fig. 4.6. As the measurements on the NexION® 350D ICP-MS were performed with the usual sample introduction system made from glass, the reported uncertainties are generally higher than usually expected from ICP-MS. However, this is a known issue, as the quantitative detection of silicon is generally considered a rather challenging task (e.g., [182]).

First, when working without the Helium KED mode (HKM), it is evident that especially the results with the 20-fold dilution show much higher contents compared to the data obtained from the 200-fold dilution. Here, a difference of about two becomes apparent. However, the results themselves are consistent within the dilution series, for the individual silicon isotopes. Referring to Fig. 4.3 the  $^{89}\text{Y}$  recovery rate for samples with low dilution is very low. Generally, this suggests matrix effects, that are usually affecting the consistency of, e.g., ionization in the plasma, beam defocusing. Such matrix effects can affect the quantification, so that the results from the more diluted samples (x 200) likely provide a more reliable value, concerning the silicon content. For this reason, a value of  $70 \pm 14 \mu\text{g}$  per disc for silicon is assumed, regarding the measurements performed without the HKM (Table 4.4). Further, measurements with the HKM demonstrate that the different dilution series yield overall consistent results, regarding both the different dilutions as well as silicon isotopes (Fig. 4.6). However, only one value yields – in comparison to this series – an exceptionally high content ( $145 \pm 15 \mu\text{g}$  per disc).

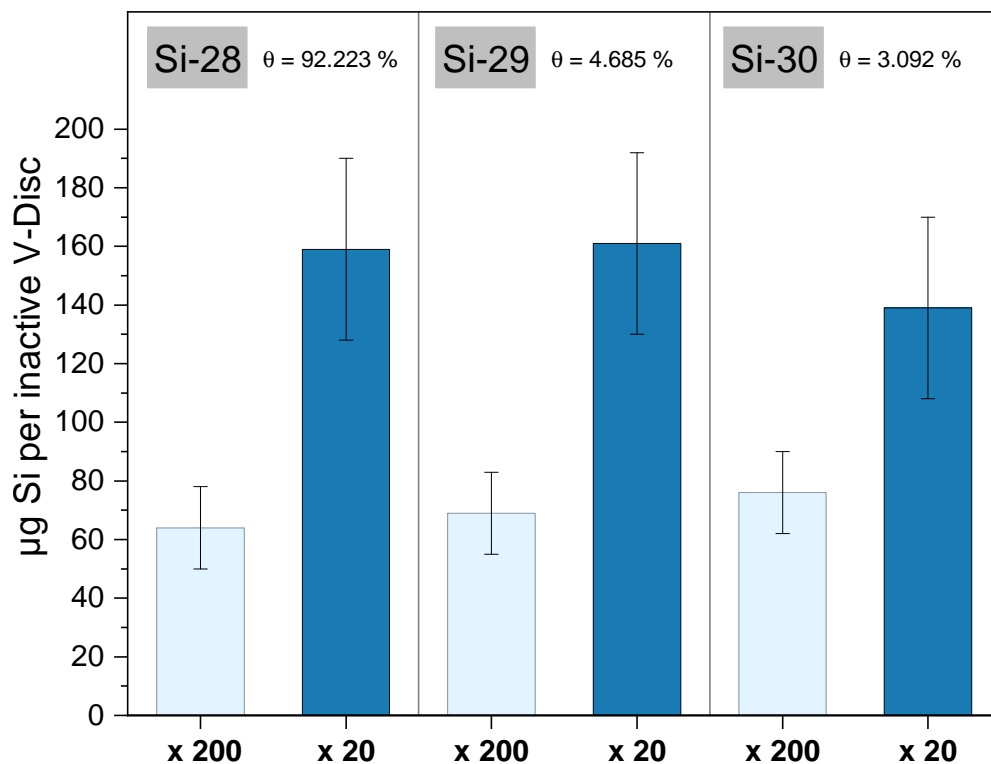


**Fig. 4.5:** Results of the determination of the silicon content in the vanadium discs without Helium KED mode. The determined results are reported as the average of the samples 1, 3, and 5.

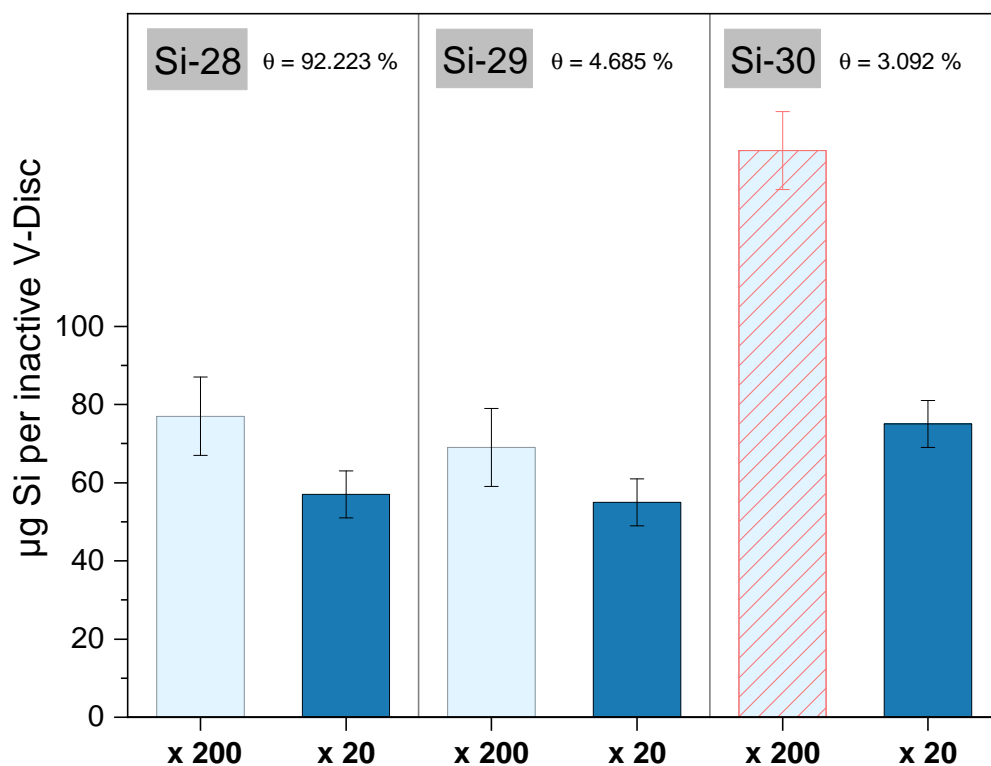


**Fig. 4.6:** Results of the determination of the silicon content in the vanadium discs with Helium KED mode. The determined results are reported as the average of the samples 1, 3, and 5.

**Table 4.4:** Overall uncertainties are considered 20% (w/o HKM), and 10% (w/ HKM). Note, that the value for  $^{30}\text{Si}$  (x200 dilution) has been excluded from the calculations (see discussion in the text).

	Silicon-28		Silicon-29		Silicon-30		$\emptyset$ $^{\text{nat}}\text{Si}$	
Dilutions	x20	x200	x20	x200	x20	x200	x20	x200
w/o HKM ( $\mu\text{g}$ )	159	64	161	69	139	76	150	70
w/ HKM ( $\mu\text{g}$ )	57	77	55	69	75	(145)	62	73

Since elevated silicon concentrations were found during measurements without the HKM but only at lower dilution, such a value with the HKM and with higher dilution was regarded as an outlier and was therefore not considered for the average in this series (Table 4.4). As a result, we obtain obviously a more consistent and reliable data set.

Consequently, from the data evaluations, it appears that highly diluted samples can be measured without HKM, while low dilutions can still be accurately measured using the HKM. However, due to the low isotopic abundance and given the plethora of interferences, measurements for  $^{30}\text{Si}$  are somewhat biased and should be avoided for a comparison. Therefore, using the results from  $^{28}\text{Si}$  and  $^{29}\text{Si}$ , we could determine a likely upper limit (UL) of the Si content. We defined that to be  $90 \mu\text{g } ^{\text{nat}}\text{Si}$  per vanadium disc and quantified the silicon content within a 10% uncertainty (based on  $^{28}\text{Si}$  only), which yields the quantity of  $^{\text{nat}}\text{Si}$  to be  $68 \pm 7 \mu\text{g}$  per vanadium disc.

For a further comparison, we also obtained data on the  $^{\text{nat}}\text{Si}$  content of other vanadium discs (from the same batch though) by means of ICP-OES (Agilent 5110) using a PTFE sample introduction system. The results from selected measurements are shown in Table 4.5.

**Table 4.5:** Overview of the ICP-OES results to determine the  $^{28,29,30}\text{Si}$  content. Here, samples with and without an additional Si-Spike were used, and different vanadium discs were used (but from the same batch).

Measurement date	With Spike: $\mu\text{g}$	Without Spike: $\mu\text{g}$ or Substracted
04-Feb-2020	$392 \pm 20$	$92 \pm 5$
04-Feb-2020		$85 \pm 4$
18-Nov-2021		$103 \pm 5$
11-Feb-2022	$417 \pm 21$	$117 \pm 6$
Average (Spiked)		$105 \pm 8$
Average (Unspiked)		$94 \pm 6$

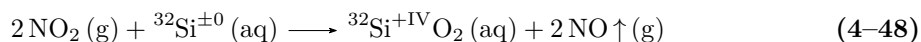
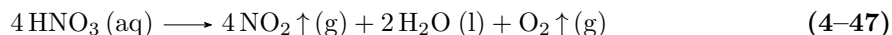
The results between spiked and unspiked samples agree well within the given uncertainties and allow to have a further comparison concerning the  $^{\text{nat}}\text{Si}$  content. Hence, based on the results of both the ICP-MS and ICP-OES measurements, we consider the UL to be around  $100 \mu\text{g } ^{\text{nat}}\text{Si}$  per vanadium disc. However, for our experimental work, we refer to an expected average of about  $70 \mu\text{g}$  to  $80 \mu\text{g } ^{\text{nat}}\text{Si}$  per vanadium disc, as this value is consistent regarding the ICP-MS measurements for the x200 dilutions (Table 4.4, with and without HKM). Therefore, when performing cold (=inactive) experiments, an amount of  $80 \mu\text{g } ^{\text{nat}}\text{Si}$  and multiples of that amount (added with single element standard solutions) was used in order to mimic the radioactive vanadium matrix as close as possible. Furthermore, the obtained value of  $80 \mu\text{g } ^{\text{nat}}\text{Si}$  corresponds to 0.02 wt.-% or 190 ppm per vanadium disc and is, again, in the lower range of the manufacturer's certificate of  $\leq 0.2$  wt.-% or up to 1900 ppm.



## 4.2 Radiochemical separation: V targets from STIP-6

### 4.2.1 Silicon tetrafluoride: Distillation of the volatile Si species

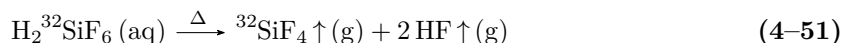
First, the metallic vanadium discs must be dissolved in an acid, such as  $\text{HNO}_3$ . Utilizing an oxidizing acid ( $\text{HNO}_3$ ), it is ensured that metallic silicon is oxidized to its stable oxidation state +IV, and, thus, all silicon is present in solution as  $^{32}\text{SiO}_2$  or  $^{32}\text{Si}(\text{OH})_4$ , respectively. Working with nca- $^{32}\text{Si}$  low-level concentrations of about 60 ppb ( $\approx 60 \text{ ng/mL}$ ), one can expect that such carrier-free solutions do not form colloids under the chosen conditions, and silicon is completely dissolved [183], thus present as non-dissociated molecules of orthosilicic acid [184]. Consequently, the following chemical reactions can be assumed during the dissolution process (Eq. 4-47, Eq. 4-48, Eq. 4-49):



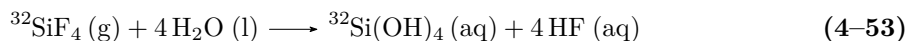
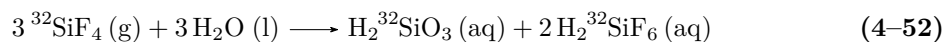
Orthosilicic acid (OSA) is a weak acid ( $\text{pK}_{\text{a}1} = 9.86$ ,  $\text{pK}_{\text{a}2} = 13.1$ , [185]) so that protonation under mildly acidic conditions in the  $\text{HCl}/\text{HNO}_3$ -media will not occur. Therefore, after adding stoichiometric quantities of hydrofluoric acid (HF), OSA reacts further according to Eq. 4-50:



Hexafluorosilicic acid ( $\text{H}_2\text{SiF}_6$ , HFSA) is rather a strong acid [185], whereas the second deprotonation is weak, with a  $\text{pK}_{\text{a}2}$  value between 1.5 [186] to 4.2 [187]. Here, the formation of HFSA is still considered as an intermediate step in the distillation since the volatilization of silicon only occurs when HFSA is thermally decomposed (Eq. 4-51) to form the volatile silicon tetrafluoride ( $\text{SiF}_4$ , STF):



Although it seems rather effortless to obtain the required silicon species in solution, the actual quantitative recovery of silicon as STF is complicated because of the apparatus' requirement. The temperature to decompose HFSA starts at around  $110^\circ\text{C}$ . Since this exceeds the water's boiling point,  $\text{H}_2\text{O}$  is also brought into the gas phase. Yet, the difficulty is linked to STF's strong affinity for water that, in turn, forms various non-volatile reaction products [188], e.g., Eq. 4-52 and Eq. 4-53:



Therefore, reported yields from Lindner & Polak [173] potentially suffered from a loss due to the formation of non-volatile species, which are then deposited in the apparatus. Concerning the used apparatus, not many details are stated in their paper, apart from “*using an all-Teflon apparatus heated in a silicon oil bath in combination with a nitrogen stream to facilitate the transfer*”. Thus, for practical implementation, we referred to the work from Holt [189] to construct an own distillation apparatus (see section 6.3, Fig. 6.4, Fig. 6.5) that focused on these main features:

- (i) Closed system to prevent any losses due to leakages, but more importantly, also prevent the escape of hazardous hydrogen fluoride;
- (ii) Uniformly heated apparatus to avoid condensation of water, and silicon, respectively;
- (iii) Chemically inert materials that are not attacked by the different acids and do not react with silicon either;

However, during the procedure’s development, we also had further difficulties, such as using an older ICP-OES (OPTIMA 3000, PerkinElmer Inc., U.S.A.), which was exclusively equipped with glass parts so that we usually dealt with high Si background intensities. As a result, repeated measurements could not accurately determine the actual silicon content, resulting in high uncertainties (see Fig. 4.7 and Fig. 4.8), and not satisfying results so that we have abandoned the idea of developing this procedure further.

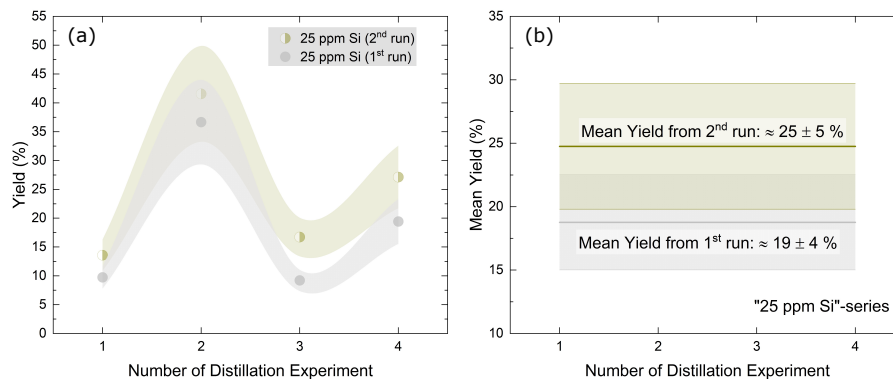


**Fig. 4.7:** (a) Silicon yield (25 ppm series) determined in a series of distillation experiments. The yields from the 1<sup>st</sup> run have been usually lower than from the 2<sup>nd</sup> run, indicating a built-up of silicon in the system. (b) Generally, with a mean yield between 19 to 25%, the recovery rate was considered too low.

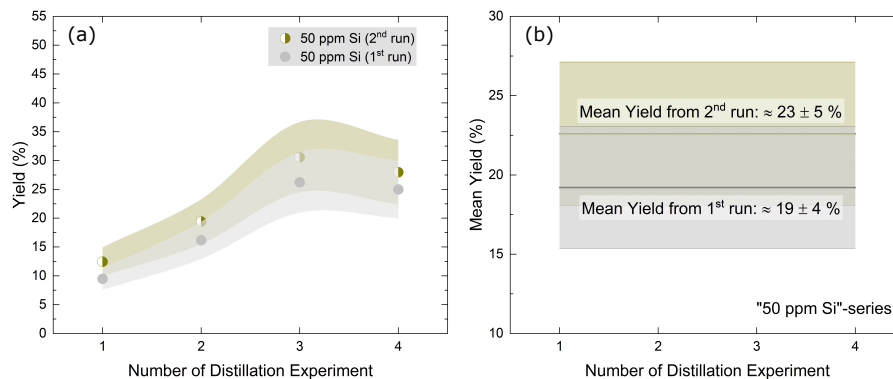


**Fig. 4.8:** (a) Silicon yield (50 ppm series) determined in a series of distillation experiments. Here, a slight trend is visible, also indicating a built-up of silicon, and generally, the apparent recovery rate from the 1<sup>st</sup> run is also lower than for the 2<sup>nd</sup> run. (b) Again, the recovery rate was considered too low, with a mean yield between 19 to 23%. Moreover, an apparent concentration dependence questioned the use with solutions, as no silicon carrier was usually added.

## 4.2.2 Column Chromatography: Exchange, extraction, and chelating

Parts presented in this section are based on the article: ➡ “Radiochemical separation and purification of non-carrier added silicon-32” and appeared in *Radiochimica Acta* **109**(10), (2021). The work was authored by Veicht et al. [22].

### 4.2.2.1 Separation from the bulk vanadium matrix:

#### Cation-exchange chromatography: Dowex® 50WX8-200

Carrier-free solutions of silicon contain non-dissociated molecules of OSA. But, depending on the concentration and pH, OSA tends to form polynuclear compounds of various compositions, referred to as polysilicic acids. However, the element’s speciation is vital when working with chromatographic methods. The chemical conditions should aim for a certain speciation of the element of interest to achieve high accuracy and reproducibility. To obtain chemically pure  $^{32}\text{Si}$  fractions, the very small quantity of  $^{32}\text{Si}$  must be separated from a large amount of the target material. Therefore, the first separation step aimed to separate the bulk matrix, as well as the simultaneous retention of interesting by-products (e.g.,  $^{26}\text{Al}$ ,  $^{41}\text{Ca}$ ,  $^{44}\text{Ti}/^{44}\text{Sc}$ ) using ion-exchange chromatography. Here, an extensive study regarding the determination of distribution coefficients ( $K_d$ ) [118] provides information about the nuclide’s specific sorption behavior on various ion-exchangers (e.g., AG® 50W-X8, a strongly acidic cation-exchange resin) and for multiple systems, such as  $\text{HNO}_3\text{--H}_2\text{O}$  and  $\text{HCl--H}_2\text{O}$ . Table 4.6 and Table 4.7 provide the information of the  $K_d$  as a function of pH for vanadium(IV) and vanadium(V).

**Table 4.6:** Values for the distribution coefficients taken from [118] for vanadium(IV, V) in the system: AG® 50W-X8 – HCl –  $\text{H}_2\text{O}$ .

Ion	c(HCl in mol/L)						
	0.1	0.2	0.5	1.0	2.0	3.0	4.0
V(IV)	-	230	44	7.20	-	-	-
V(V)	13.9	7.0	5.0	1.10	0.7	0.2	0.3

**Table 4.7:** Values for the distribution coefficients taken from [118] for vanadium(IV, V) in the system: AG® 50W-X8 –  $\text{HNO}_3$  –  $\text{H}_2\text{O}$ .

Ion	c( $\text{HNO}_3$ in mol/L)						
	0.1	0.2	0.5	1.0	2.0	3.0	4.0
V(IV)	495	157	35.6	14.0	4.7	3.0	2.5
V(V)	20	10.9	4.9	2.0	1.2	0.8	0.5

Using this data, we were able to estimate our resulting distribution coefficients according to the resulting matrix, which is highlighted in green for vanadium(IV) and vanadium(V), respectively. It can be seen from Table 4.6 and Table 4.7 that vanadium’s retention gradually decreases with a lower pH. Moreover, vanadium(IV) generally shows a much higher affinity towards the cation-exchange resin than vanadium(V), resulting in a difference of one order of magnitude.

Therefore, in order to enhance the retention of vanadium, thus, to retain the bulk vanadium on the strong cation-exchange resin, these requirements were considered:

- Due to the initial use of  $\text{HNO}_3$  (oxidizing acid), a suitable reducing agent must be added to reduce the vanadium from oxidation state  $+V$  to  $+IV$ .
- A decrease in  $\text{H}^+$  concentration is necessary to yield overall higher retention for all cations present in the solution. However, strong bases must be avoided (e.g.,  $\text{NaOH}$ ,  $\text{KOH}$ ), to respect the resin's exchange capacity.
- Because of its good chemical resistance (e.g., towards oxidizing agents and solutions, e.g., higher concentrated acids), styrene-DVB-based resins should be considered.

To decrease the  $\text{H}^+$  concentration, we diluted the sample by a factor of 20 with  $\text{utp-H}_2\text{O}$ , which resulted in a  $\text{pH}$  of  $0.92 \pm 0.05$ . This  $\text{pH}$  range was already sufficient to result in reasonably high retention of the cations. Therefore, a strong base was not needed. The observed differences in the solution's  $\text{pH}$  are likely caused by the uncertainty in the vanadium discs' masses:  $417 \text{ mg} \pm 4 \text{ mg}$  ( $k=1$ ), but the relatively narrow  $\text{pH}$  range was acceptable for the intended separation.

Besides the  $\text{pH}$ , a key aspect of obtaining reliable and reproducible results from the separation process was the reduction of vanadium(V) to vanadium(IV). In the first attempts, the reduction of  $\text{V}^{+V}$  to  $\text{V}^{+IV}$  was achieved upon adding 1.2 mL 1M L-ascorbic acid (L-AscA) to the solution. Although L-AscA is known as an effective reducing agent that also reduces  $\text{V}^{+V}$  to  $\text{V}^{+IV}$  (e.g., [190], [191]), some issues were soon identified. Severe drawbacks of utilizing L-AscA is its ability to coordinate with various metals to form complexes ([192], and references therein). Moreover, its multiple protonation and oxidation states lead to different metal-ligand binding modes. The data from [193] suggest that for a  $\text{pH} < 1$ , the predominant species of  $\text{Ti(IV)}$  is  $\text{Ti(HAscA)}^{3+}$ , while for  $1 < \text{pH} < 1.6$ ,  $\text{TiO(HAscA)}^+$  is present in aqueous solution. We would assume that such titanium species exhibit lower retention on a cation-exchanger because of the larger coordination sphere and the reduced charge. As a result, indeed, using  $\gamma$ -spectrometry, we determined much higher  $^{44}\text{Ti}$ -activities than we expected from our estimations based on given  $K_d$  values. Besides, it is known that L-AscA undergoes further oxidative decomposition to various organic compounds (xylonic acid, threonic acid, and oxalic acid [193]), which will, in turn, have unexpected effects on further separations or on the quantitative measurements, e.g., concerning the long-term stability of the matrix. Another disadvantage of employing L-AscA will be explained more in detail (see section 4.2.2.4.(I), L-AscA as a reducing agent), as it concerns the fundamental problem of removing the volatile species ( $^3\text{H}$ ,  $^{39,42}\text{Ar}$ ) from the solution.

As a result, hydrazine ( $\text{N}_2\text{H}_4$ ) was chosen as alternative reductant. The advantage of using  $\text{N}_2\text{H}_4$  is that its decomposition products, namely ammonia ( $\text{NH}_3$ ), nitrogen ( $\text{N}_2$ ), and hydrogen ( $\text{H}_2$ ) are all volatile and escape upon drying. Since  $\text{N}_2\text{H}_4$  is also a weak base ( $\text{p}K_B = 5.90$ ), a slight increase in  $\text{pH}$  ( $1.25 \pm 0.05$ ) of the finally diluted sample was observed. While working with a cation-exchange resin, an increase in the  $\text{pH}$  is generally beneficial for an increased retention of metal cations. Besides, it could also be noticed that  $\text{N}_2\text{H}_4$  ensured the long-term stability of  $\text{V}^{+IV}$ . Similar to solutions without any additive, solutions previously treated with L-AscA gradually changed the color into green, indicating both the presence of  $\text{V}^{+IV}$  and  $\text{V}^{+V}$ , whereby solutions containing hydrazine keep their blue color during storage (Fig. 4.9). This is also an important aspect for the long-term storage, as further separations of other nuclides of interest ( $^{44}\text{Ti}/^{44}\text{Sc}$ ,  $^{41}\text{Ca}$ ,  $^{26}\text{Al}$ ), will also still require the separation from the bulk matrix, whereby  $\text{V}^{+IV}$  is certainly the preferred oxidation state.

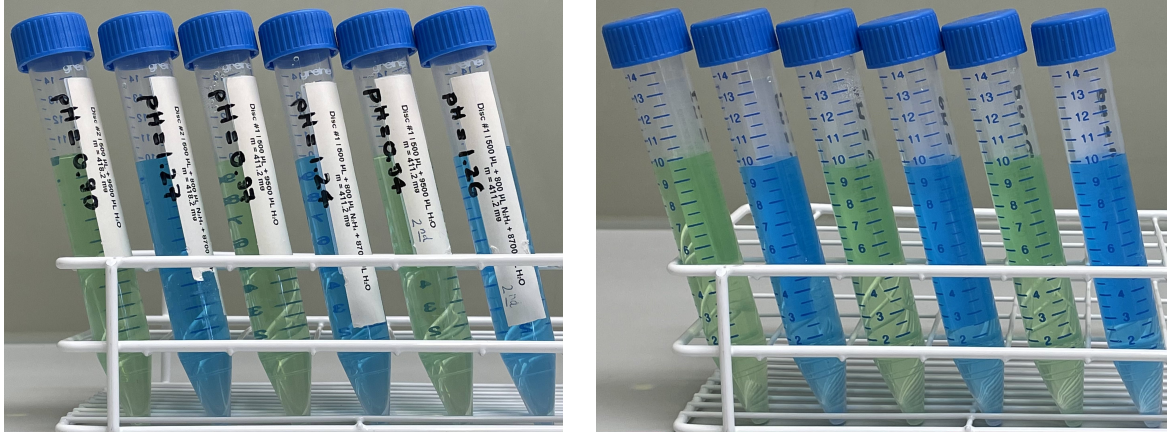


**Fig. 4.9:** Samples from the development phase were prepared on January 28, 2020, and the picture was taken on March 23, 2022. While the green color occurs usually quite rapidly (within a week) and indicates a mixture of  $V^{+IV}$  and  $V^{+V}$ , the solutions treated with hydrazine apparently remain stable for even time frames of  $>2$  years, since they maintain their intense, blue color, which is in aqueous solution typical for  $V^{+IV}$ .

Generally, identifying  $^{22}\text{Na}$  ( $T_{1/2} = 2.6018 \pm 0.0022$  y) and  $^{42}\text{K}$  ( $T_{1/2} = 12.355 \pm 0.007$  h) as impurities after the first separation was not a big concern; however, the presence of  $^{42}\text{K}$  showed that it is in equilibrium with its parent nuclide,  $^{42}\text{Ar}$  ( $T_{1/2} = 32.9 \pm 0.11$  y). Na(I) and K(I) exhibit a rather simple chemistry in aqueous solution, as they belong to the first main group of elements. Additionally, thanks to the ICP-OES measurements, it was also possible for us to screen for elements that would be not easily detectable during the separation procedure through radioanalytical methods.

Elements, such as  $^{41}\text{Ca}$  ( $T_{1/2} = (9.94 \pm 0.15) \times 10^4$  y),  $^{55}\text{Fe}$  ( $T_{1/2} = 2.744 \pm 0.009$  a), and or  $^{59}\text{Ni}$  ( $T_{1/2} = (7.6 \pm 0.5) \times 10^4$  y), do not emit any gamma-rays and would be difficult to detect using LSC, because of their low-energy  $\beta$ -spectrum. Therefore, the ICP-OES results were taken to exclude their presence after the first separation step.

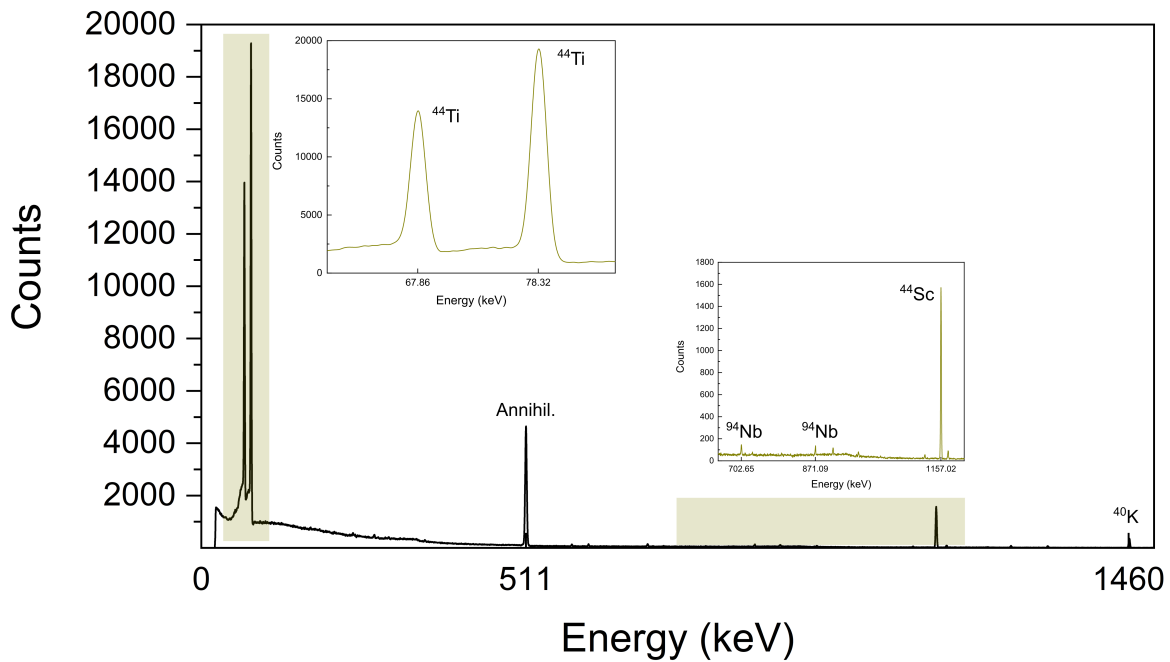


**Fig. 4.10:** Gamma spectrum (recorded for 4.5h) confirms the typical impurities after the first separation step. However, using cation-exchange chromatography, vanadium can be quantitatively separated, leading only to trace impurities of other radionuclides which are summarized by Table 4.8.

**Table 4.8:** Overview of the nuclides typically present in the  $^{32}\text{Si}$  fraction after the separation from the bulk vanadium matrix.

Nuclide	$\gamma$ -line(s); Energy (keV)	Species	IUPAC Group Number	Comment	Separated
Main Group Elements					
<sup>22</sup> Na	1274.5	Na <sup>+</sup>	1 Hydrogen and Alkali Metals	Low K <sub>d</sub> ; Breakthrough	X
<sup>40</sup> K	1460.8	K <sup>+</sup>		Background radiation	X
<sup>42</sup> K	1524.7	K <sup>+</sup>		Daughter of <sup>42</sup> Ar (T <sub>1/2</sub> = 32.9 y)	X
Transition Metals					
<sup>44</sup> Sc	1157.0	Sc <sup>3+</sup>	3 Scandium Group	Daughter of <sup>44</sup> Ti (T <sub>1/2</sub> = 59.1 y)	X
<sup>172</sup> Lu	810.1, 1093.6	Lu <sup>3+</sup>		Daughter of <sup>172</sup> Hf (T <sub>1/2</sub> = 1.87 y)	X
<sup>173</sup> Lu	272.1	Lu <sup>3+</sup>		Likely formation of chloro-complex	X
<sup>44</sup> Ti	67.9, 78.3	Ti <sup>4+</sup>	4 Titanium Group	Likely formation of chloro-complex	X
<sup>172</sup> Hf	125.8	Hf <sup>4+</sup>		Likely formation of chloro-complex	X
<sup>94</sup> Nb	702.6, 871.1	Nb <sup>5+</sup>	5 Vanadium Group	Likely formation of chloro-complex; hydrolysis	X
<sup>60</sup> Co	1173.2, 1332.5	Co <sup>2+</sup>	9 Cobalt Group	Likely formation of chloro-complex	X
Gaseous Species					
<sup>3</sup> H	Pure $\beta^-$ emitters	<sup>3</sup> H <sub>2</sub> O, <sup>3</sup> HOH	1 Hydrogen and Alkali Metals	Dissolved, isotopic exchange with water	X
<sup>40</sup> Ar		Ar	18 Noble Gases	Dissolved	X
<sup>42</sup> Ar		Ar		Dissolved	X

But because of their reported high  $K_d$  values on the cation-exchange resin (Table 4.9 and Table 4.10, we expected Ca, Ni, and Fe to be well retained under the chosen conditions and, therefore, not to be detected .

**Table 4.9:** Values for the distribution coefficients taken from [118] for calcium, nickel and iron in the system: AG<sup>®</sup> 50W-X8 – HCl – H<sub>2</sub>O.

Ion	c(HCl in mol/L )						
	0.1	0.2	0.5	1.0	2.0	3.0	4.0
Ca(II)	<b>3200</b>	<b>790</b>	151	42.3	12.2	7.3	5.0
Ni(II)	<b>1600</b>	<b>450</b>	70	21.9	7.2	4.7	3.1
Fe(III)	<b>9000</b>	<b>3400</b>	225	35.5	5.2	3.6	2.0

**Table 4.10:** Values for the distribution coefficients taken from [118] for calcium, nickel and iron in the system: AG<sup>®</sup> 50W-X8 – HNO<sub>3</sub> – H<sub>2</sub>O.

Ion	c(HNO <sub>3</sub> in mol/L)						
	0.1	0.2	0.5	1.0	2.0	3.0	4.0
Ca(II)	<b>1450</b>	<b>480</b>	113	35.3	9.7	4.3	1.8
Ni(II)	<b>1140</b>	<b>384</b>	91	28.1	10.3	8.6	7.3
Fe(III)	<b>&gt;10<sup>4</sup></b>	<b>4100</b>	362	74	14.3	6.2	3.1

As a result, Fig. 4.11, Fig. 4.12, and Fig. 4.13 show that, on average, the detected atomic emission intensities for Ca, Ni, and Fe are below the background intensity. However, in the 10mL-, and 105mL-fraction elevated concentrations of Ca were found. Including the higher measurement uncertainties, related to intensities very close to the detection limit, Ca is quantitatively retained on the cation-exchange resin.

In contrast, Ni does have lower distribution coefficients (Table 4.9, Table 4.10), but suggest still a sufficiently high retention. According to Fig. 4.12, the 10mL-fraction – alike Ca – showed some apparent intensity which is slightly above the detection limit, but again, only visible in the two fractions.

Generally, the results are somewhat biased, but are overall in good agreement, indicating that nickel is retained during this step, too. A similar behavior can also be seen in Fig. 4.13 for Fe, whereby here one of the blanks has the highest intensity. All other measured fractions have intensities well below the detection limit.

As a result, Ca, Ni, and Fe should not be present in the obtained  $^{32}\text{Si}$  fraction after separating them from the bulk vanadium matrix. The somewhat higher intensities for Ca and Ni in the 10mL-fraction can be likely explained by a contamination of, e.g., the used PP-tube and do not suggest a breakthrough of the elements. With respect to V, Fig. 4.14 shows the behavior during the different stages of the initial separation. Some V – likely  $\text{V}^{+V}$  – is washed out during the separation process. An increase in the V intensities can be clearly observed during the Wash fraction. But besides, V intensities are also clearly above the detection limit during the Load. Only the Blanks show the absence of V. The amount of V that is finally transferred into a  $^{32}\text{Si}$  fraction was, on average,  $\approx 10\text{ }\mu\text{g}$  ( $\approx 1\text{ ppm}$ ). But regarding the initial amount of  $\approx 420\text{ mg}$  vanadium, this translates into a decontamination factor of  $\approx 4.2 \times 10^4$  in a single step, and fulfills the requirement for the successful separation of the bulk matrix.

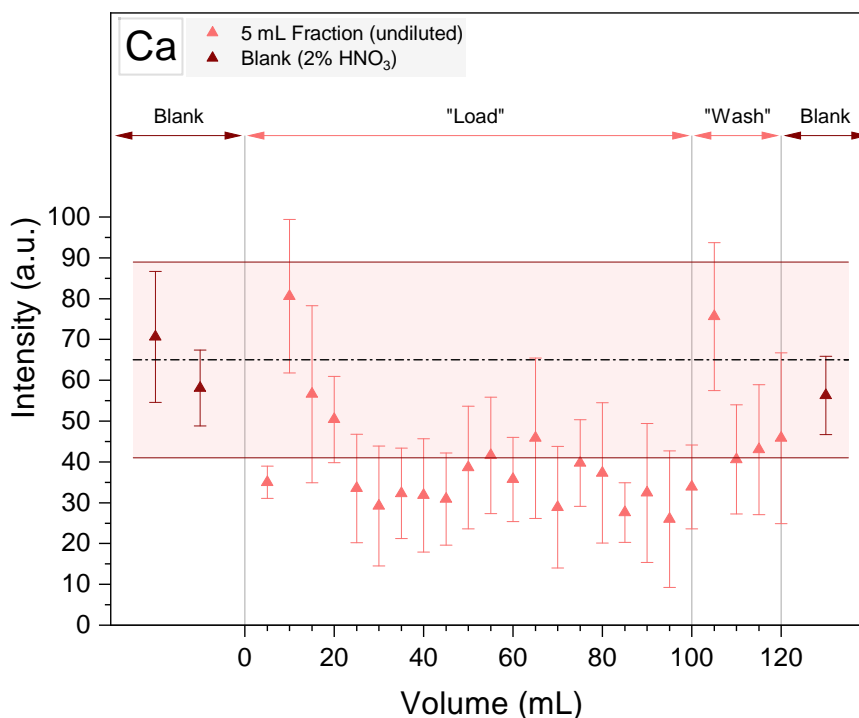


**Fig. 4.11:** Calcium intensities as a function of volume during the first separation step. The «dash-dot»-line represents the averaged intensities of the three blanks, including a confidence band with  $k=3$  ( $3\sigma$ ):  $65 \pm 24$  (a.u.).

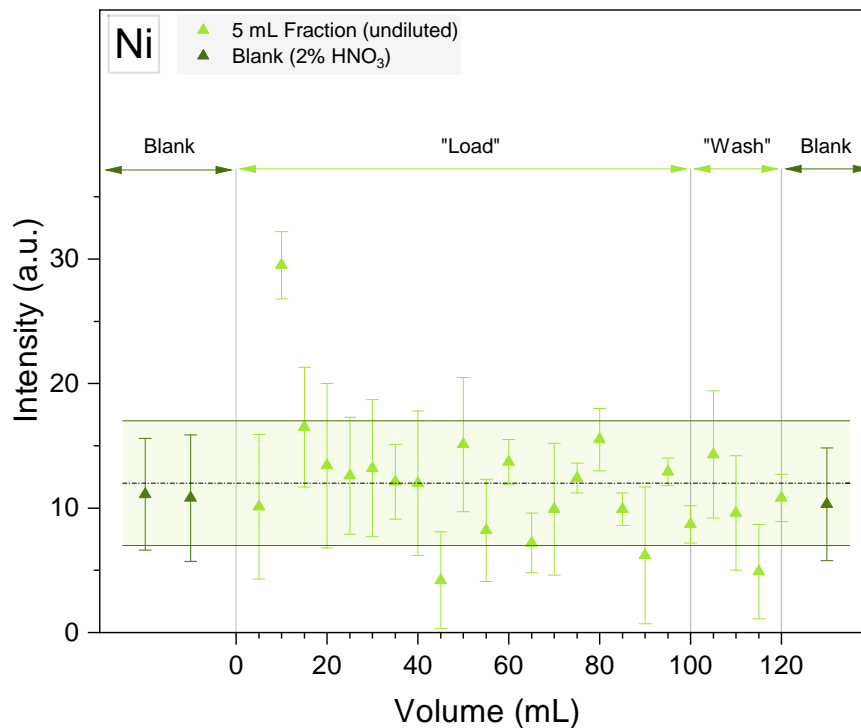


**Fig. 4.12:** Nickel intensities as a function of volume during the first separation step. The «dash-dot»-line represents the averaged intensities of the three blanks, including a confidence band with  $k=3$  ( $3\sigma$ ):  $12 \pm 5$  (a.u.).

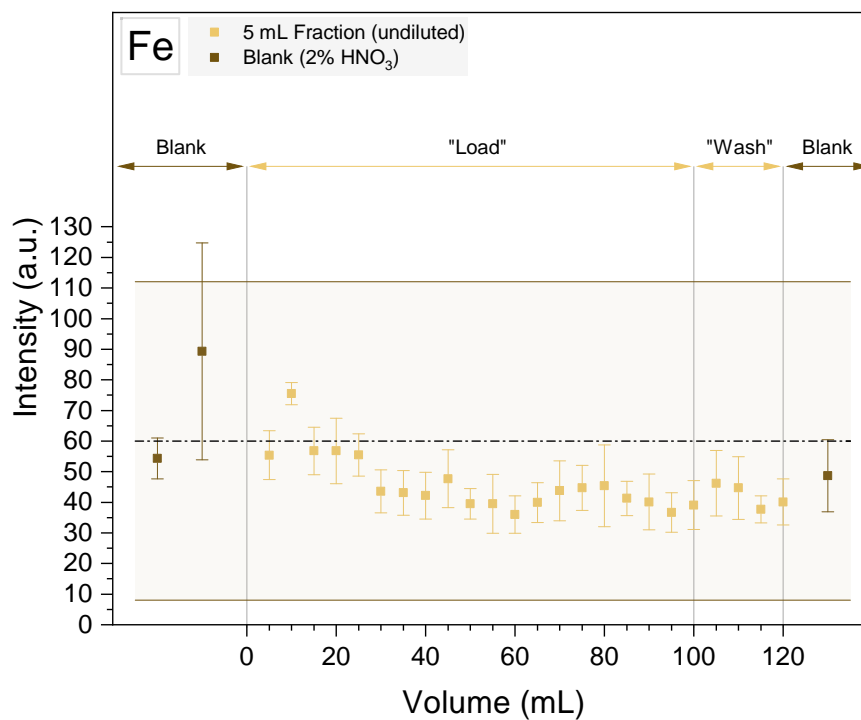


**Fig. 4.13:** Iron intensities as a function of volume during the first separation step. The «dash-dot»-line represents the averaged intensities of the three blanks, including a confidence band with  $k=3$  ( $3\sigma$ ):  $60 \pm 52$  (a.u.).

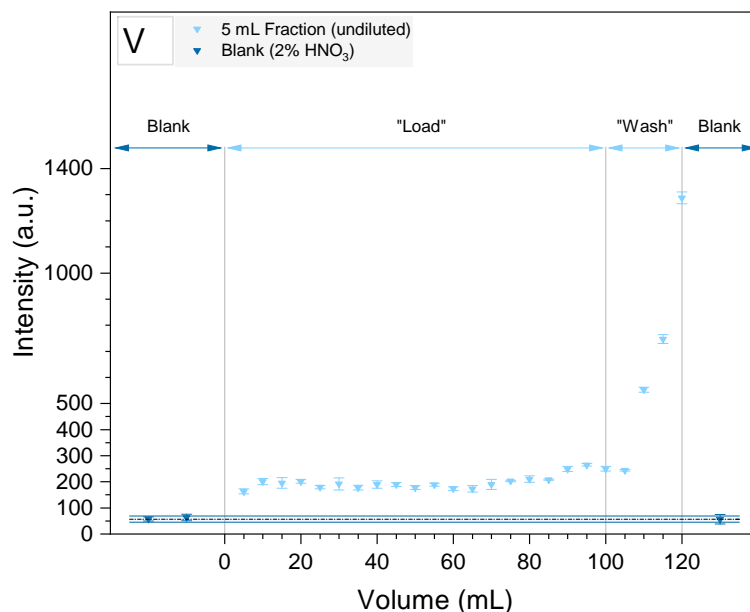


**Fig. 4.14:** Vanadium intensities as a function of volume during the first separation step. The «dash-dot»-line represents the averaged intensities of the three blanks, including a confidence band with  $k=3$  ( $3\sigma$ ):  $57 \pm 12$  (a.u.).

Concerning silicon we assumed fully protonated orthosilicic acid ( $\text{Si}(\text{OH})_4$ ) in our solution. Since OSA is a neutral compound, neither cation- nor anion-exchange resins will retain it under these conditions and should be quantitatively recovered. Moreover as the vanadium chemistry is a very colorful one, the success of the final separation from the bulk vanadium could be easily witnessed since the obtained  $^{32}\text{Si}$ -fraction was colorless (Fig. 4.16(a)). This was also in agreement with the obtained ICP-OES results, that showed only  $\approx 1$  ppm V in a  $^{32}\text{Si}$  fraction. Furthermore, in the presented example (Fig. 4.15), the Si concentration is observed to be almost constant, which demonstrates that Si is completely unretained by the strongly acidic cation-exchange resin. Due to the addition of the silicon spike, the undiluted fractions yield, on average, about  $4 \mu\text{g/mL}$   $^{32}\text{Si}$ , which is in excellent agreement with the expected Si concentration, marked by the solid line.

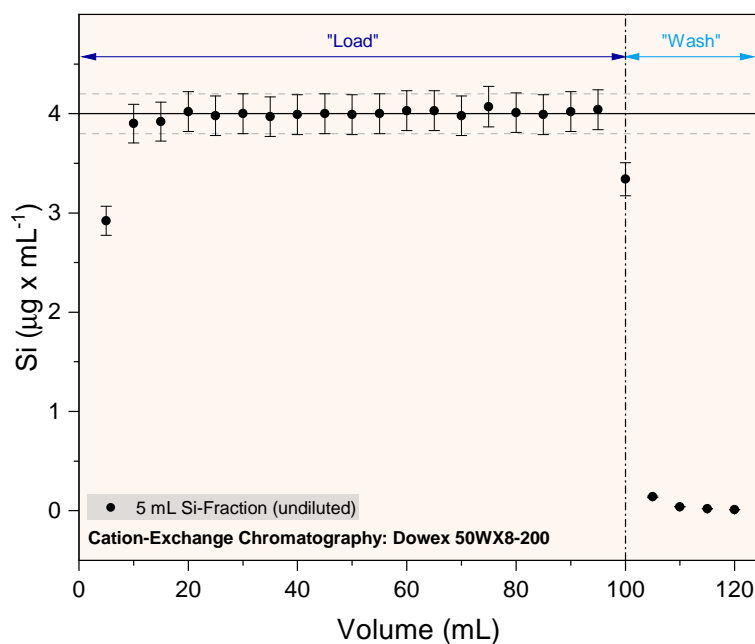
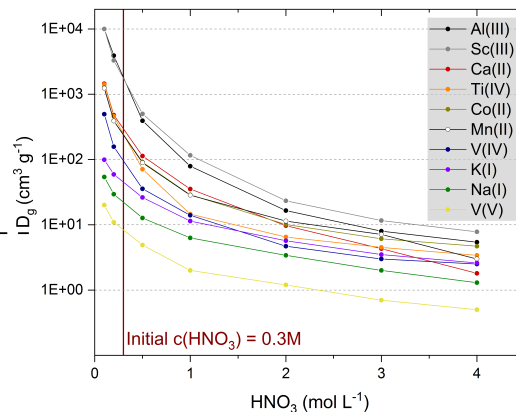
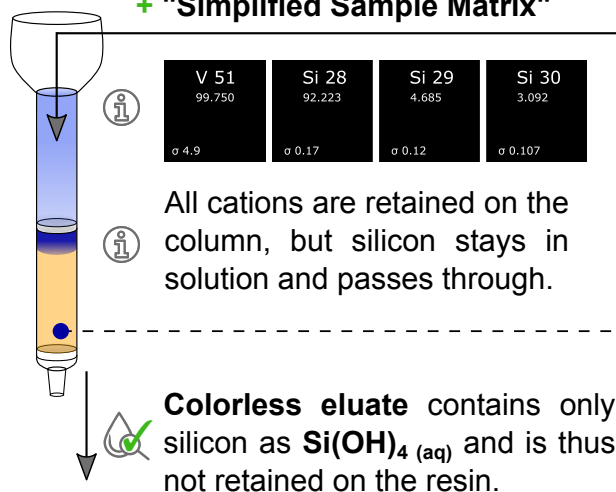


**Fig. 4.15:** Example of silicon's elution profile during the separation with the Dowex® 50WX8-200 resin (220 mm bed height,  $\varnothing = 10$  mm, PMMA column).

Dowex® 50WX-200 (H<sup>+</sup> form)  
Cation Exchange Resin

(a)

+ "Simplified Sample Matrix"



Dowex® 50WX-200 (H<sup>+</sup> form)  
Cation Exchange Resin

(b)

+ 3M HNO<sub>3</sub>

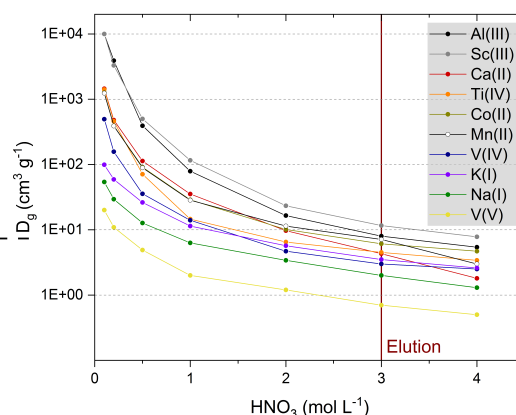
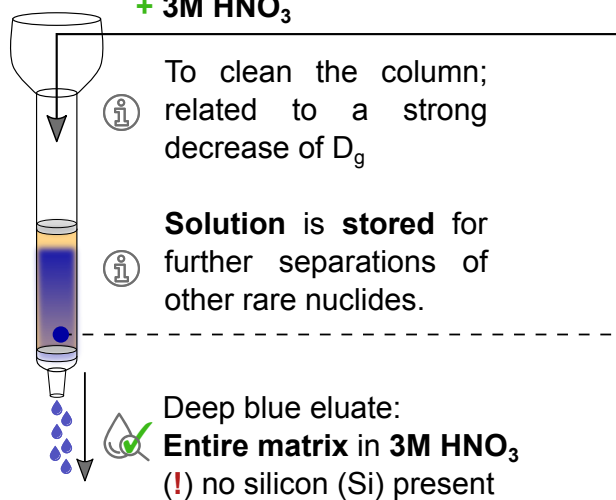
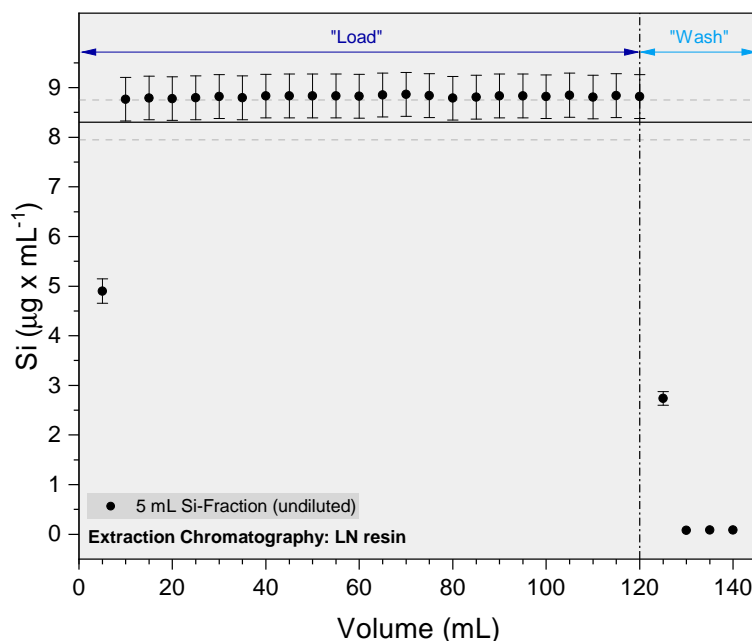


**Fig. 4.16:** (a) Example of the bulk separation, allowing to separate silicon from the majority of the target material. Here,  $\text{V}^{+IV}$  is visibly retained on the cation-exchange resin. Besides, also other cations (e.g., impurities, spallation-products) are retained on the strongly acidic cation-exchange resin, which is expected due to high (typically  $> 10^2$ ) distribution coefficients. At the end of this procedure, a colorless eluate is obtained that contains silicon. (b) After the separation of Si, all remaining cations (except Sc) are eluted using 3M  $\text{HNO}_3$ , while the collected 50 mL fraction is stored until further use.

Finally, when working with radioactive solutions, measurements with a dose rater meter (e.g., Automess 6150AD®) confirmed the absence of most of the  $\gamma$ -emitting cations, such as  $^{60}\text{Co}$ ,  $^{22}\text{Na}$ , since the dose rate for the obtained  $^{32}\text{Si}$ -fraction was in the range of  $< 1 \mu\text{Sv/h}$ , as opposed to the initial solution, which was typically measured in the range of  $250 \mu\text{Sv/h}$  up to  $5 \text{mSv/h}$ . Eventually, the remaining matrix, that is retained by cation-exchange resin was eluted using 3M  $\text{HNO}_3$  and stored for further radiochemical separation procedures (Fig. 4.16).

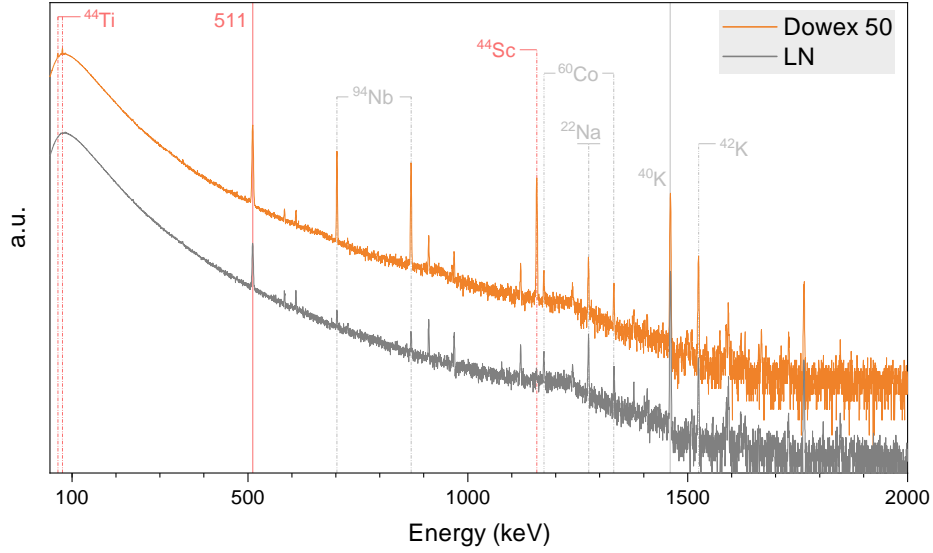
#### 4.2.2.2 Purification of the $^{32}\text{Si}$ -fractions: LN<sup>®</sup> resin series

If we consider the remaining nuclides that were typically noticeable after the first separation, a bulk separation was not needed anymore. Therefore, we refer to the subsequent separation steps as purification, since only trace contaminants had to be removed from the  $^{32}\text{Si}$  fractions. Choosing the LN<sup>®</sup> resin enabled the first step towards purifying the  $^{32}\text{Si}$  fractions. In order to see whether the LN<sup>®</sup> resin's functional group also extracted  $^{32}\text{Si}$ , we performed a pre-analysis confirming that  $^{32}\text{Si}$  is quantitatively recovered during the separation procedure.



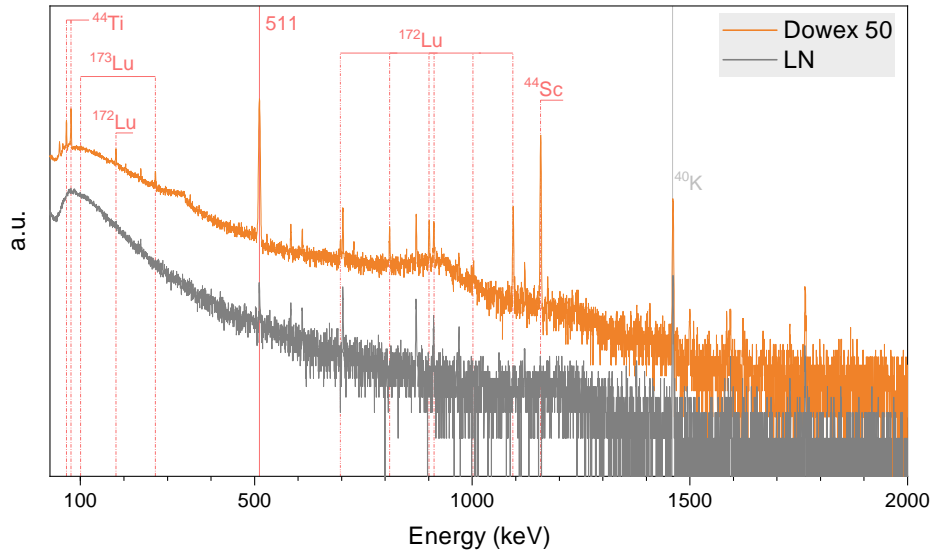
**Fig. 4.17:** Silicon's elution profile during the separation with the LN<sup>®</sup> resin (35 mm bed height,  $\varnothing = 9$  mm, ISOLUTE PE column).

Fig. 4.17 shows that, similar to the results from the first bulk separation, silicon is steadily washed out, which implies that there is no interaction with the LN<sup>®</sup> resin's functional group. We recovered >99% of the silicon within 125 mL in the presented example. Using an extended "Wash" fraction and a short resin height, it is apparent that one needs only 5 mL utp-H<sub>2</sub>O to recover the silicon. In the remaining fractions (130-140 mL), the silicon content is negligible. Obviously, the silicon concentration ( $c(\text{Si}) \approx 8.8 \mu\text{g/mL}$ ) is, on average, higher than expected ( $c(\text{Si}) \approx 8.3 \mu\text{g/mL}$ ). But the concentration is still within the uncertainties and the expected range. The observed increase is likely related to the used silicon standard. During our work, the Si single element standards may have increased in concentration since they were not exclusively stored in a fridge but at room temperature in the laboratory environment. With regard to the separation procedure, we established the required volume for the Wash fraction (= 5 mL). Since it was not possible to find appropriate standard solutions (only HF-complexes of Ti, Nb), we performed experiments with active  $^{32}\text{Si}$  fractions to determine whether the typical impurities were removed during this procedure. After such a separation, the comparison of the two  $\gamma$ -spectra (Fig. 4.18) showed the absence of  $^{44}\text{Ti}/^{44g}\text{Sc}$ , while ICP-OES gave us confidence that no silicon was lost during the procedure. Since  $^{44g}\text{Sc}$  is the daughter of  $^{44}\text{Ti}$ , it is not necessary to separate  $^{44g}\text{Sc}$ , as it will eventually decay. But the advantage of following the emission line of  $^{44g}\text{Sc}$  allowed to exclude the  $^{44}\text{Ti}$  presence in the fraction, after allowing for its radiochemical equilibrium.



**Fig. 4.18:** Example of  $\gamma$ -ray spectra ( $\approx 1$  hr) of a  $^{32}\text{Si}$  fraction after processing with Dowex<sup>®</sup> 50WX8-200 resin (orange) and the subsequent purification using the LN<sup>®</sup> resin (gray). Contaminants which were to be removed are highlighted in red.

Please note, we also focused on removing hafnium ( $^{173}\text{Hf}$ ) and lutetium ( $^{172,173}\text{Lu}$ ), as some  $^{32}\text{Si}$  fractions contained these radionuclides. An example is presented in Fig. 4.19, whereby a highly contaminated  $^{32}\text{Si}$  solution was used to observe the LN<sup>®</sup> resin's performance. Hafnium could not be directly identified but via its short-lived daughter,  $^{172}\text{Lu}$ . Due to the different irradiation conditions for each of the vanadium discs, we had to find a very robust resin to receive reliable results throughout the separation process, as these elements had to be removed, too. According to Fig. 4.19, a comparison of the spectra confirmed that after the LN-purification step, the nuclides of interest (= contaminants) were successfully removed as they could not be detected anymore.



**Fig. 4.19:** Example of  $\gamma$ -ray spectra ( $\approx 1$  hr) of a  $^{32}\text{Si}$  fraction after processing through Dowex<sup>®</sup> 50WX8-200 resin (orange) and the subsequent purification using the LN<sup>®</sup> resin (gray). Contaminants which were to be removed are highlighted in red.

As a result, we confirmed the resin's high selectivity, allowing separating several  $^{32}\text{Si}$  fractions per day before a replacement would be needed. For the LN<sup>®</sup> resin, this was typically done after

six to ten independent purification procedures while constantly measuring the final fractions using  $\gamma$ -spectroscopy. Only if these measurements confirmed the absence of  $^{44}\text{Ti}/^{44}\text{Sc}$ ,  $^{173}\text{Hf}$ ,  $^{172,173}\text{Lu}$ , the solutions were ready for the following separation step. In this way, comparing the 511-keV  $\gamma$ -line, the typical decrease also confirmed the successful separation of the  $\beta^+$ -emitting nuclides.

#### 4.2.2.3 Purification of the $^{32}\text{Si}$ -fractions: Monophos<sup>®</sup> resin

Although no information concerning Nb(V) was available, the TrisKem's Monophos product sheet suggests that the resin shows a wide range of tendencies for various cations of different groups, including other oxidation states. Figure 4.20 shows that silicon was not retained during a separation with Monophos since it could be quantitatively recovered. Similar to the separation with the LN<sup>®</sup> resin, an excellent indication is the constant silicon concentration for each fraction that implies no interaction with the resin's functional group. Since we were also using small column volumes, an additional wash of only 5 mL utp-H<sub>2</sub>O was required. Consequently, we tested it to remove Nb(V) and could demonstrate that the radionuclide was quantitatively removed from the  $^{32}\text{Si}$  fraction. Again, this was proven by long-term  $\gamma$ -measurements (Fig. 4.21). The Monophos-purification separation has also proven to be very robust and highly selective. Due to the relatively low  $^{94}\text{Nb(V)}$  quantities, we decided to replace a Monophos<sup>®</sup> resin batch on average after ten separations which account for around 1200 mL active solution.

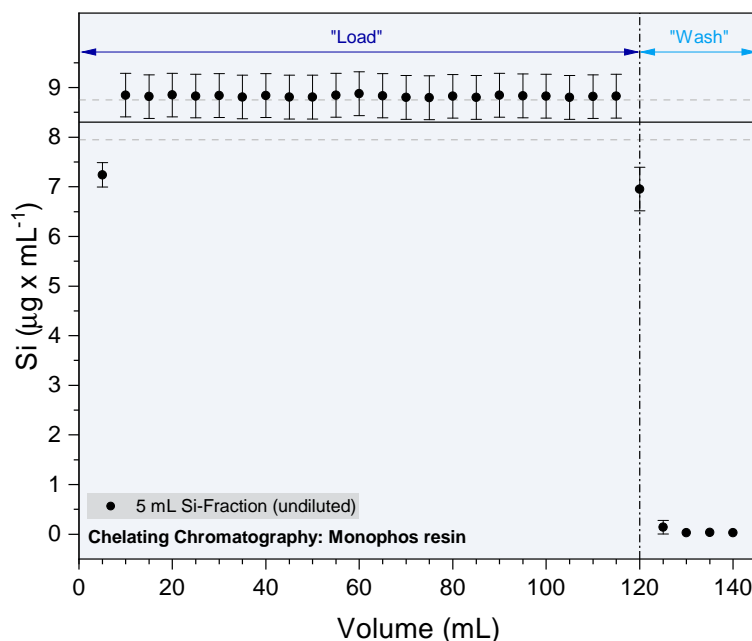


**Fig. 4.20:** Silicon's elution profile during the separation with the Monophos<sup>®</sup> resin (30 mm bed height,  $\varnothing = 9$  mm, ISOLUTE PE column).

After this separation step, radioisotopes of  $\text{Na}^+$ ,  $\text{K}^+$ , and  $\text{Co}^{2+}$  were still indentifiable in the  $\gamma$ -spectrum. However, at this stage, an anion-exchange resin was foreseen to purify the silicon fraction. Thus, according to the prospective separation, those nuclides left in solution would not interfere with a separation on an anion-exchange resin as these elements do not form any stable fluoro-complexes. Consequently, ions like  $\text{Na}^+$ ,  $\text{K}^+$ , and  $\text{Co}^{2+}$  will not be retained under our conditions and can simply be washed off the column.

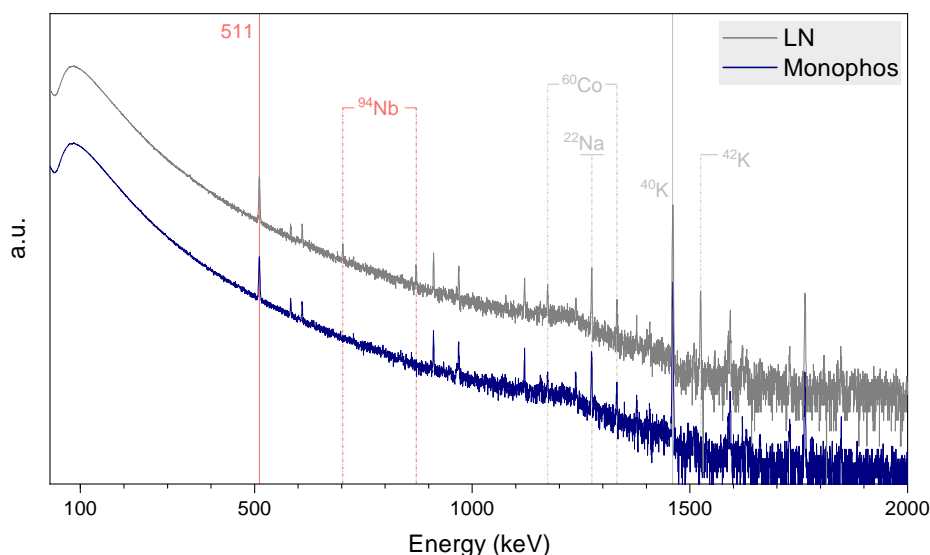


**Fig. 4.21:** Example of  $\gamma$ -ray spectra ( $\approx 1$  hr) of a  $^{32}\text{Si}$  fraction after purification through LN<sup>®</sup> (grey) and the subsequent purification using the Monophos<sup>®</sup> resin (blue). Nuclide of interest is highlighted in red.

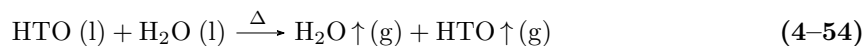
#### 4.2.2.4 Removal of volatile species:

##### Evaporation to dryness

While employing ICP-OES during the method development with inactive solutions, the analysis of volatile species, was impossible. However, referring to the number of atoms,  $^3\text{H}$  is the main product, produced during spallation. Moreover, considerable amounts of the argon isotopes,  $^{39}\text{Ar}$  and  $^{42}\text{Ar}$ , were also calculated (see section 1.2, Table 1.8). The presence of  $^{42}\text{Ar}$  in solution was already visible, searching for the emission of 1525 keV gamma-rays due to the daughter's nuclide ( $^{42}\text{K}$ ,  $T_{1/2} = 12.36$  h) decay. Thus,  $^{42}\text{K}$  would be already decayed if not in equilibrium with its parent. In order to remove these elements from the solution, evaporation to complete dryness was required. Notably, a further advantage of the evaporation to dryness is related to the subsequent recovery of silicon, allowing a precise matrix composition. Therefore, these steps ensure the removal of volatile species and silicon's speciation in a well-defined matrix.

##### 4.2.2.4.(I) L-AscA as a reducing agent

First, in total, three samples have been treated with L-AscA before  $\text{N}_2\text{H}_4$  was used for further separations. Generally, it concerns three irradiated V-discs used for testing purposes during August 19, 2019, and November 07, 2019, and were marked accordingly. As described in section 4.2.2.1, first problems with L-AscA were encountered because of its ability to form ascorbato complexes. Yet, the further problem was that a  $^{32}\text{Si}$ -fraction, previously coming from a solution treated with L-AscA, could not be evaporated to complete dryness. Overall, we measured a decrease of  $^3\text{H}$ -activity with increasing evaporation series, but still, even after the twelve repeated evaporation, we could not ultimately remove tritium (Fig. 4.22). As a result, only the complete evaporation to dryness of the  $^{32}\text{Si}$  solution could allow for tritium's quantitative removal. If not, then the hydrogen isotope exchange reaction is assumed where tritium (T) is involved and reacts, e.g., with water according to Eq. 4-54, and thus to form isotopically enriched HTO:



Such exchange reactions have been also studied (e.g., [194]), stating that molecules with COOH and OH groups preferentially undergo hydrogen exchange with HTO. Generally, this also accounts for organic molecules, thus a further potential problem related to using L-AscA. Noteworthy that, unlike  $^3\text{H}$ , both  $^{39}\text{Ar}$  and  $^{42}\text{Ar}$  would not undergo an isotopic exchange with, e.g., water and are thus much easier to remove from the matrix. Yet, the resulting isotopic exchange of tritium requires a complete evaporation to dryness, in order to remove this radionuclide from the solution quantitatively.

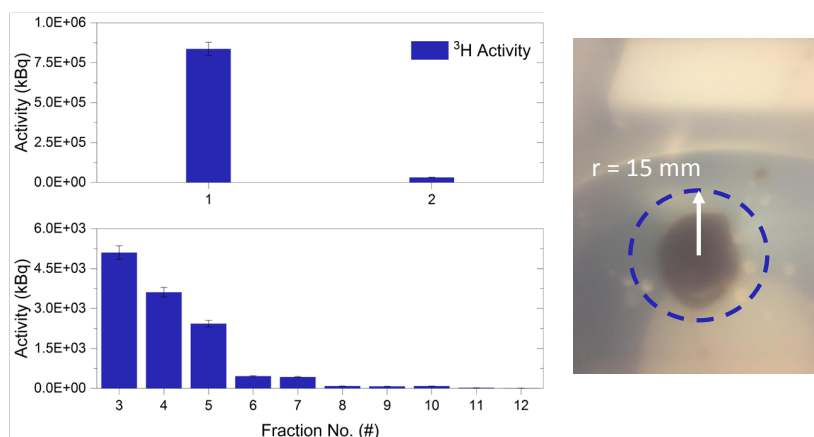


**Fig. 4.22: (Left)** Determined activity of tritium using LSC as a function of repeated evaporations (Fraction No.). The values are reported as sum (in kBq) for each individual recovered fraction. Initially,  $\approx 800$  MBq  $^3\text{H}$  were present in a single  $^{32}\text{Si}$  fraction (obtained from processing one irradiated V-Disc). **(Right)** Residue in the PTFE-one-neck flask, after a typical evaporation step using the RotaVap. The residue was somewhat tacky and could never be evaporated to complete dryness.

#### 4.2.2.4.(II) Hydrazine as a reducing agent

Similar to the procedure with L-AscA, we followed the decrease in tritium activity, shown in Fig. 4.23 and Fig. 4.24. Due to the material constraints, a temperature limitation was given so that we set the temperature to  $175 \pm 5$  °C (Fisherbrand® Isotemp® 4x4, Thermo Fisher Scientific Inc., U.S.A.). After reaching complete dryness, 25 mL utp- $\text{H}_2\text{O}$  was added and re-evaporated. Especially in Fig. 4.24, it is apparent that after five consecutive evaporations to dryness, the activity in the “low-energy” region has greatly decreased, in contrast to the samples treated with L-AscA. A comparison with “initial solution – before evaporation” shows that the count rate in the low energy region (0-20) decreased by nearly three orders of magnitude. Moreover, the “Actual Si-32 fraction 1:100 diluted” does not show any peak in the low energy region, which demonstrates that tritium could be successfully removed by this procedure. Although five evaporations seemed to provide a threshold for the tritium evaporation the procedure was repeated in total nine consecutive times to reach a total evaporated volume of 250 mL. Finally, after the last evaporation to dryness, the  $^{32}\text{Si}$  was recovered by washing the PTFE dish twice with 1 mL 1M HF, topped up to 10 mL with utp- $\text{H}_2\text{O}$ , and eventually transferred it into a 50 mL PP-Tube for intermediate storage of the solution (= 20 mL 0.1M HF matrix). For each  $^{32}\text{Si}$ -fraction, a new PTFE evaporating dish was used to avoid cross-contaminations and, more importantly, to prevent volatilization of  $^{32}\text{Si}$  due to residuals of HF or  $\text{H}_2\text{SiF}_6$ , respectively, left on the evaporating dish.

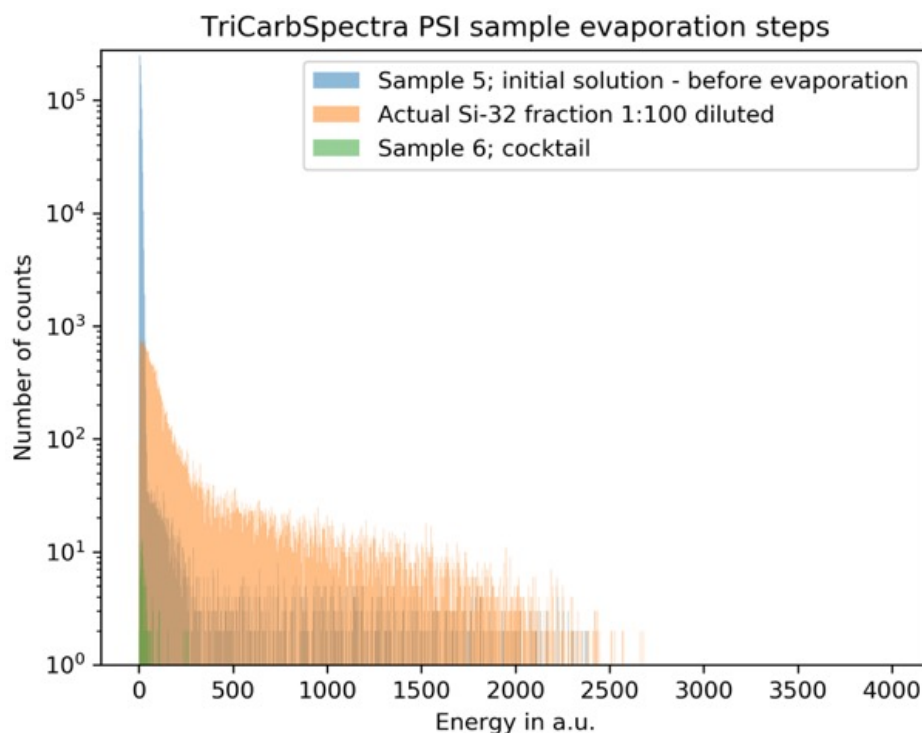


**Fig. 4.23:** Spectral comparison between an initial solution  $^{32}\text{Si}$  solution (Sample 5; before evaporation), the actual sample (1:100 diluted), and a blank (Sample 6; cocktail). Spectra were recorded using a Tri-Carb<sup>®</sup> 2250CA (PSI) and analyzed by Dr Nataša Lalović (former postdoctoral research at PTB).

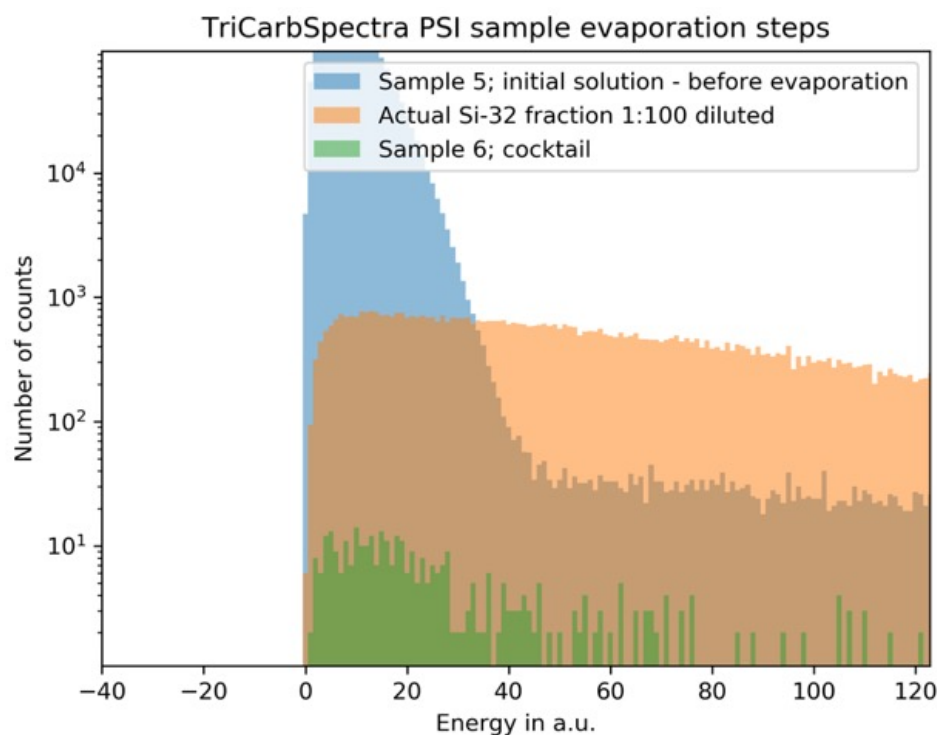


**Fig. 4.24:** Detail of the spectral comparison between an initial solution  $^{32}\text{Si}$  solution (Sample 5; before evaporation), the actual sample (1:100 diluted), and a blank (Sample 6; scintillation cocktail). Spectra were recorded using a Tri-Carb<sup>®</sup> 2250CA (PSI) and analyzed by Dr Nataša Lalović (former postdoctoral research at PTB).

#### 4.2.2.5 Preparation of the final $^{32}\text{Si}$ solutions:

##### Anion-exchange chromatography: Dowex<sup>®</sup> 1X8

With each processed active metallic vanadium disc, a 20 mL 0.1 M HF  $^{32}\text{Si}$  solution is finally obtained. Under these conditions, silicon is present as hexafluorosilicate ( $\text{SiF}_6^{2-}$ ). Hence, using an anion-exchange resin, any metallic impurity with a similar chemical behavior to Si will hinder a further separation, which concerns therefore ions known to form stable, anionic fluoride complexes. For this reason, the LN<sup>®</sup> and Monophos<sup>®</sup> resins removed those elements from the solution. As such, complexation reactions with various halogenides, e.g., the formation of stable chloro- or fluoro-complexes, do not occur. However, it is well-known that transition metals, e.g., Ti, Sc, and Nb, form stable complexes with halogenides, and, more importantly, so does Si. Yet the final separation, and the purification of the  $^{32}\text{Si}$  fractions was already foreseen using an anion-exchange resin. Elements like Ti, Sc, and Nb had to be removed first, as they could not be separated while employing the anion-exchange resin. Therefore, we decided to use highly specific resins to remove those impurities from the matrix. First, optimal separation conditions for Si were investigated by employing dedicated batch studies for the expected matrix, including known trace impurities. A similar approach is also described in the literature [195], thus providing the basis for separating alkali and alkaline-earth metal cations and cobalt and vanadium by using a mixture of HF/HCl. But, more importantly, this last purification step combines two more features, apart from the separation of the remaining radionuclides.

##### 4.2.2.5.(I) "Pre-Concentration" of several individual $^{32}\text{Si}$ fractions

A high distribution coefficient of Si is required to achieve a "Pre-Concentration" of radiosilicon on the anion-exchange resin. Since Si forms in the presence of HF a stable fluoro complex, we deduced from Fig. 4.25 that working with  $c(\text{HF}) = 0.1\text{M}$  will work for our final separation scheme. Under these conditions, a corresponding  $K_d$  of  $872 \pm 44 \text{ cm}^3 \times \text{g}^{-1}$  ( $\log_{10}(K_d) \approx 3$ ) results. While the  $K_d$  increases with a decrease in HF concentration, we specifically chose a higher HF concentration to maximize the recovery yields from the evaporating dish and eventually work with reasonable volumes after the subsequent 1:10 dilution. To finally elute  $^{32}\text{Si}$  from the column, a sufficiently low  $K_d$  of  $9.2 \pm 0.92 \text{ cm}^3 \times \text{g}^{-1}$  ( $\log_{10}(K_d) \leq 10^0$ ) was found for  $c(\text{HCl}) > 0.5\text{M}$ . In contrast, HCl concentrations of less than 0.5M could likely yield an incomplete elution of silicon, since the  $K_d$  gradually increases in the range of  $c(\text{HCl})$  0.5M to 0.1M, while eventually reaching a  $K_d$  value of  $32.2 \pm 3.22 \text{ cm}^3 \times \text{g}^{-1}$  ( $\log_{10}(K_d) \approx 1.5$ ).

Here, tests with other acids, such as  $\text{HNO}_3$ , were not performed since  $\text{HNO}_3$  can influence the stability of organic solvents and scintillation cocktails due to its oxidation and nitration powers connected to quenching effects, which represent big concerns for LSC measurements. Consequently, we decided to elute the  $^{32}\text{Si}$  fraction with 0.5M HCl (Fig. 4.25). Titanium (Fig. 4.26) shows its high retention at these conditions, too. Therefore, it would not have allowed to separate  $^{32}\text{Si}$  in the presence of  $^{44}\text{Ti}$ , as they exhibit a very similar behavior on the anion-exchange resin: In the 0.1M HF matrix, titanium's  $K_d$  is  $1777 \pm 89 \text{ cm}^3 \times \text{g}^{-1}$  ( $\log_{10}(K_d) \approx 3$ ), while for the 0.5M HCl matrix, titanium would be easily co-eluted with silicon, since a  $K_d$  of  $13.1 \pm 1.12 \text{ cm}^3 \times \text{g}^{-1}$  ( $\log_{10}(K_d) \approx 1$ ) was observed.

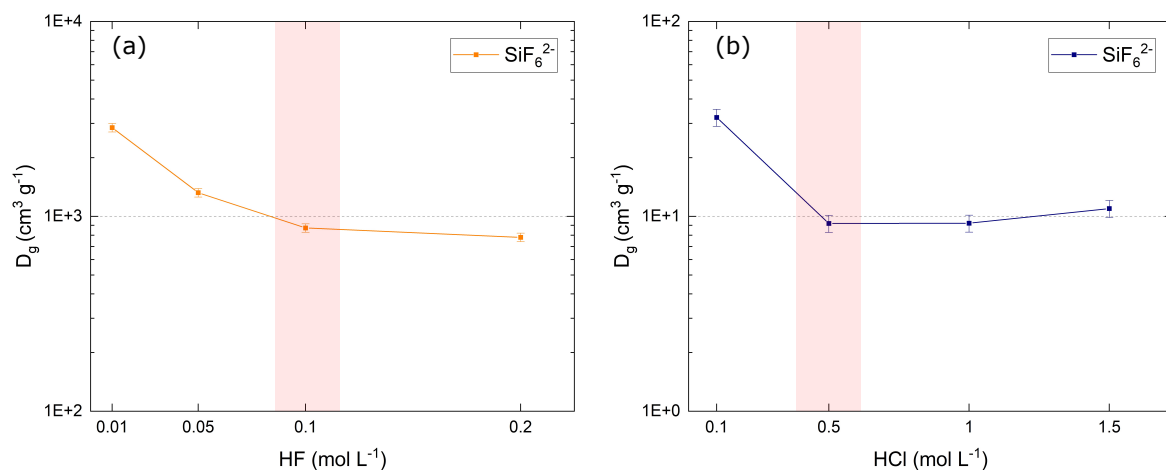


**Fig. 4.25:** (a) Distribution coefficient as a function of HF concentration for silicon, and (b) distribution coefficient as a function of HCl concentration. The red ribbon highlights the chosen experimental conditions.

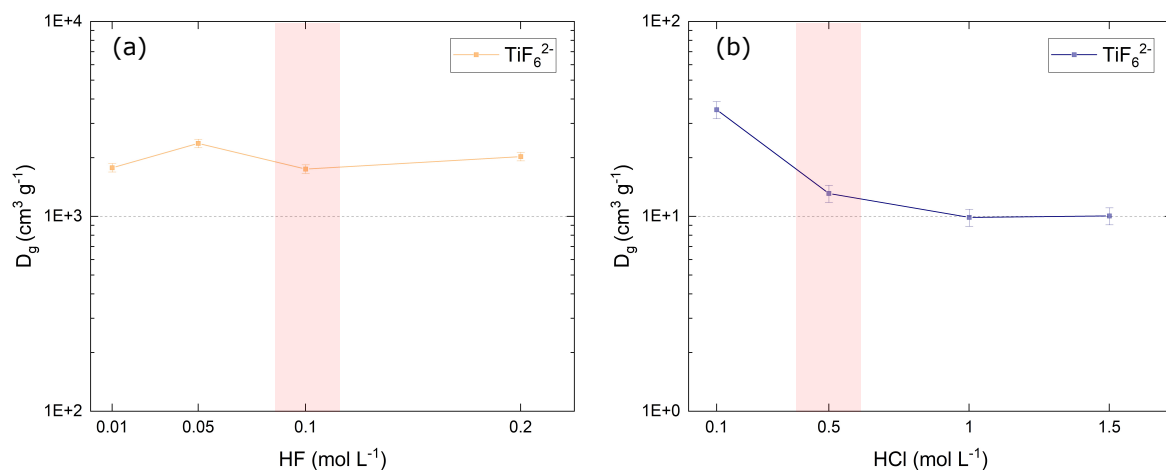


**Fig. 4.26:** (a) Distribution coefficient as a function of HF concentration for titanium, and (b) distribution coefficient as a function of HCl concentration. The red ribbon highlights the chosen experimental conditions.

Therefore, it was vital that nuclides that are also forming fluoro complexes (e.g., Ti) had to be removed prior to the anion-exchange chromatography. Regarding the target element, vanadium, it is also known to form fluoro complexes. But the complex is seemingly less stable and thus allows a separation on the anion-exchange resin. In that particular case, we decided to forgo  $K_d$  studies for V, and studied the behavior of V during different experimental series.

#### 4.2.2.5.(II) Removal of the isobaric interference $^{32}\text{S}$

Since the removal of sulfur should ideally be implemented while gathering the hexafluorosilicate anion on the resin, again, ideal chemical conditions had to be determined for the quantitative removal of S while retaining Si. First, in each of the experiments, S was added to the inactive load solution in order to investigate the behavior under HCl-free conditions, thus in a 0.1M matrix. As seen from Fig. 4.27, during the Load, S and Si are quantitatively retained under these conditions as they are not

detectable. However, some amounts of vanadium seem to be eluted during this procedure. On this subject, it cannot be excluded that this behavior is related to remanent HCl since vanadium was not always detected in the Load fraction. It is assumed that this is likely related to previous experiments, given that the same column was used repeatedly. Therefore, we assume that the retention of vanadium is 0.1M HF is fairly high and thus comparable to Si.

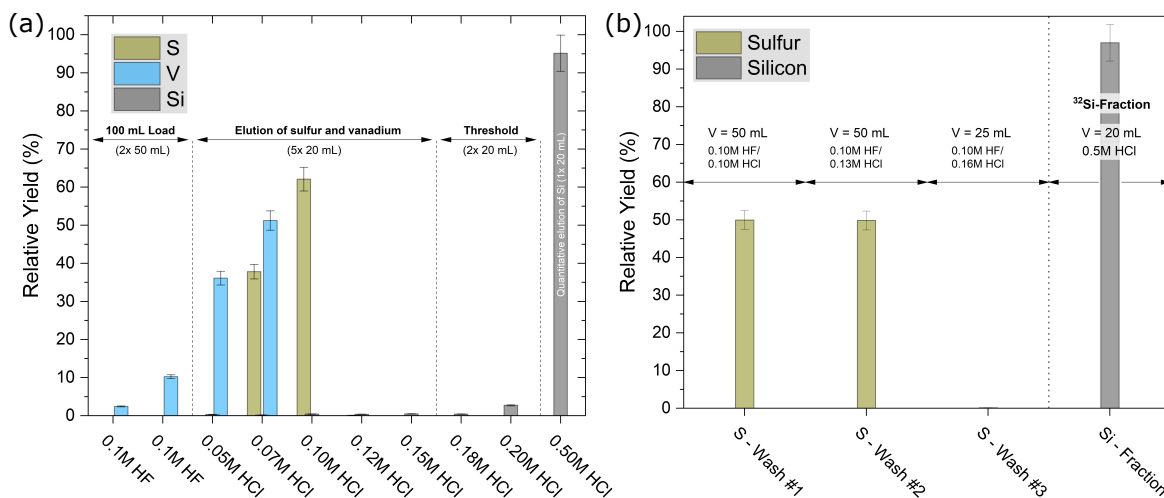


**Fig. 4.27: (a)** Exemplary elution profile to study the behavior of S, V, and Si, respectively, under varying HCl concentrations. Sulfur, together with silicon, is retained by the anion-exchange resin, while vanadium is partially retained. **(b)** Exemplary elution profile to highlight the quantitative removal of sulfur. Silicon was in none of the sulfur samples detected, and thus the quantitative recovery (98-100%  $\pm$  3%) of Si was constantly observed in the final fraction.

In contrast, working with small HCl concentrations (50 to 70 mM), in combination with 0.1M HF, vanadium and sulfur start to elute from the column, while no silicon is detected. As a result, a first threshold for the elution of both sulfur and vanadium can be found in the region of 0.05M to 0.07M HCl, indicating their low retention, working in HCl-HF media. With respect to vanadium, in the shown example, 36% can be determined in the 0.05M fraction, and 51% in the 0.07M fraction. The yields would be accordingly higher, if the detected amounts during the “Load” ( $\approx$  13%) would be distributed on these fractions. Further, when exceeding these concentrations, the results for 0.10M HF/0.10M HCl show that most of the sulfur ( $\approx$  60%) was found in this fraction, while still only trace amounts of silicon are present ( $\leq$  0.5%). Therefore, we considered this concentration as a threshold value for commencing a quantitative elution of both vanadium and sulfur. Therefore, utilizing HCl concentrations  $\geq$  0.10M, the quantitative removal of sulfur is certainly achieved. However, in order to find the highest possible HCl concentration under which silicon is still retained, we learned that Si elution commences from 0.10M HF/0.18M HCl onwards, limiting the HCl concentration and setting the threshold to avoid Si losses during this procedure. Consequently, we determined a relative Si yield of up to  $\approx$  3% in the 0.10M HF/0.20M HCl fraction. Furthermore, when finally analyzing the 0.5M HCl fraction, we were able to obtain reproducible results, yielding a recovery rate for  $^{nat}\text{Si}$  of 98-100%  $\pm$  3%. Further, when comparing the sulfur contents (as intensities, a.u.) of the 0.5M HCl fraction with a 0.5M HCl Blank, no differences were detected, confirming the successful removal of stable sulfur. Based on these results, we were setting the boundary conditions, and finalized the procedure as follows:

- After the initial load of up to ten independent vanadium discs (= 200 mL 0.10M HF solution), 30 mg  $^{nat}\text{S}$  is subsequently added in 50 mL 0.10M/0.10M HCl matrix, that is referred to as Sulfur Wash 1, while sulfur is not retained.

- When increasing the HCl concentration (Sulfur Wash 2), sulfur is quantitatively removed from the column, with 50 mL 0.10M/0.13M HCl.
- In order to avoid any contamination with sulfur in the final  $^{32}\text{Si}$ -fraction, 25 mL of 0.10M/0.16M HCl (Sulfur Wash 3) is added.
- Finally,  $^{32}\text{Si}$  is quantitatively recovered with 20 mL 0.5M HCl.

Using anion-exchange chromatography, we demonstrated that Si is highly retained in a relatively wide range of HF concentrations (0.01M to 0.20M). Due to practical reasons, we chose to work with a 0.1M HF matrix, which allowed us to achieve a maximal recovery yield for Si and keep the final volumes comparatively small. This procedure also allows producing various activity concentrations since the amount of processed  $^{32}\text{Si}$  can be chosen from, e.g., one up to ten  $^{32}\text{Si}$  fractions. Furthermore, we proved that sulfur, along with vanadium impurities, was quantitatively removed from the matrix under the chosen conditions, and the results agree very well with the observations reported in [195]. The removal of ultra-traces of sulfur is vital for ICP-MS measurements since it is an interfering isobar.

Additionally, we also carried out studies focusing on  $^{41}\text{Ca}$ , as this was of particular concern regarding LSC measurements. While calcium's presence can be actually excluded due to its high retention on the cation-exchange resin (see Table 4.9 and Table 4.10), an assumption was followed in which calcium could be transferred, together with  $^{32}\text{Si}$ , into the final 0.1M HF fraction, which is typically used in order to produce the final  $^{32}\text{Si}$  product. Following calcium's elution profile on the anion-exchange resin, Fig. 4.28 shows that the measured concentrations are slightly less than expected, which is indicated by the black line. On average,  $4.6 \pm 0.4$  ppm are recovered, instead of the expected average of  $5.0 \pm 0.3$  ppm. Therefore, analyzing the 20 individual 5mL-fractions, the overall recovery yield of calcium accounts for around 90% (455  $\mu\text{g}$  out of 500  $\mu\text{g}$ ), during the Load.

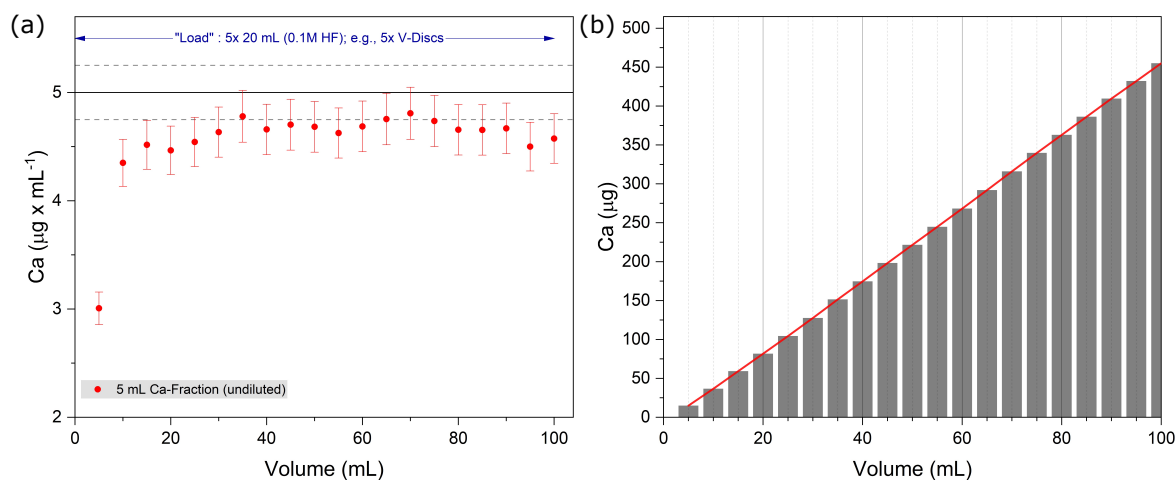


**Fig. 4.28:** (a) Elution behavior of calcium on the anion-exchange resin during the “Load” (= 0.1M HF), shown for a small-scale experiment, mimicking the load of e.g., five  $^{32}\text{Si}$  fractions. (b) Monitoring the sum of the calcium concentration, reaching in total about 90% recovery rate.

With these experiments, dedicated to study the behavior of  $^{41}\text{Ca}$ , it could be demonstrated that, regardless of whether  $^{41}\text{Ca}$  would be present until the final separation stage, using the anion-exchange, the element is quantitatively removed from the matrix. Although Ca is apparently not entirely washed off during the Load, it is eventually washed off during the different sulfur wash procedures. Combining the masses for calcium from S-Wash 1, S-Wash 2, S-Wash 3 yields 100% of the purposely added Ca tracer (see Fig. 4.29 and Table 4.11). Therefore, we conclude that its presence in the final  $^{32}\text{Si}$  is strongly diminished, and interferences during LSC measurements, stemming from  $^{41}\text{Ca}$ , are not expected.

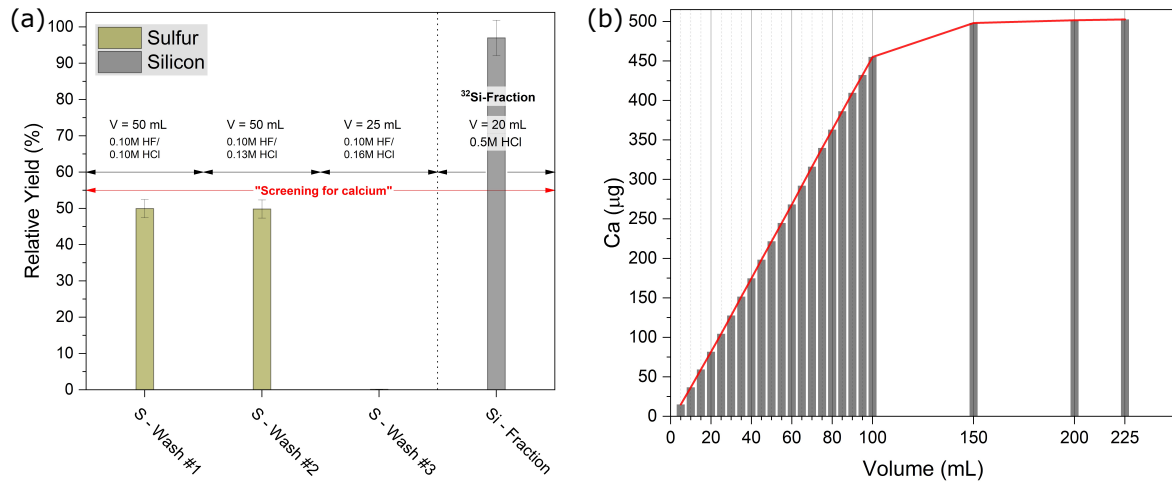


**Fig. 4.29:** (a) Screening for calcium in the three sulfur wash fractions, and in the final  $^{32}\text{Si}$  fraction. (b) After another 125 mL of solution, calcium was quantitatively recovered, reaching a total of  $503 \mu\text{g} \pm 25 \mu\text{g}$ .

**Table 4.11:** Overview of the Ca recovery rates (in  $\mu\text{g}$ ) for the different fractions.

Identifier	Total volume (mL)	Mass of Ca ( $\mu\text{g}$ )	Reovered Ca (%)
Fraction 1 to 20	100 (5 x 20)	$455 \pm 23$	$90.5 \pm 4.5$
S-Wash 1	50	$43 \pm 2.2$	$8.6 \pm 0.4$
S-Wash 2	50	$3.5 \pm 0.2$	$0.7 \pm 0.04$
S-Wash 3	25	$1 \pm 0.1$	$0.2 \pm 0.01$
Si-fraction	20	< Detection Limit	-

#### 4.2.2.6 Characterisation of the final product: $^{32}\text{Si}$ in 0.5M HCl

After the final separation procedure, the master solution ( $\approx 20$  mL) was measured on an HPGe  $\gamma$ -detector for around 95 hours (see Fig. 4.30). The separation of the typical impurities (Table 4.12) was confirmed by absence of their typical  $\gamma$ -lines. Moreover, the long-term gamma measurement was also compared to a background measurement, recorded for the same amount of time, to confirm these findings. The comparison also confirmed that no other nuclides than the typically known background nuclides (e.g., see [196]) are observed.

**Table 4.12:** Overview of the nuclides typically present in the  $^{32}\text{Si}$  fraction after the separation from the bulk vanadium matrix.

Nuclide	$\gamma$ -line(s); Energy (keV)	Species	IUPAC Group Number	Comment	Separated
Main Group Elements					
<sup>22</sup> Na	1274.5	Na <sup>+</sup>	1 Hydrogen and Alkali Metals	Removed by Dowex® 1X8 (unretained)	✓
<sup>40</sup> K	1460.8	K <sup>+</sup>		Background radiation	✓
<sup>42</sup> K	1524.7	K <sup>+</sup>		Removed as <sup>42</sup> Ar is evaporated	✓
Transition Metals					
<sup>44</sup> Sc	1157.0	Sc <sup>3+</sup>	3 Scandium Group	Removed by LN®	✓
<sup>172</sup> Lu	810.1, 1093.6	Lu <sup>3+</sup>		Removed by LN®	✓
<sup>173</sup> Lu	272.1	Lu <sup>3+</sup>		Removed by LN®	✓
<sup>44</sup> Ti	67.9, 78.3	Ti <sup>4+</sup>	4 Titanium Group	Removed by LN®	✓
<sup>172</sup> Hf	125.8	Hf <sup>4+</sup>		Removed by LN®	✓
<sup>94</sup> Nb	702.6, 871.1	Nb <sup>5+</sup>	5 Vanadium Group	Removed by Monophos®	✓
<sup>60</sup> Co	1173.2, 1332.5	Co <sup>2+</sup>	9 Cobalt Group	Removed by Dowex® 1X8 (unretained)	✓
Gaseous Species					
<sup>3</sup> H		<sup>3</sup> H <sub>2</sub> O, <sup>3</sup> HOH	1 Hydrogen and Alkali Metals		✓
<sup>40</sup> Ar	Pure $\beta^-$ emitters	Ar	18 Noble Gases	Removed through evaporation to complete dryness	✓
<sup>42</sup> Ar		Ar			✓

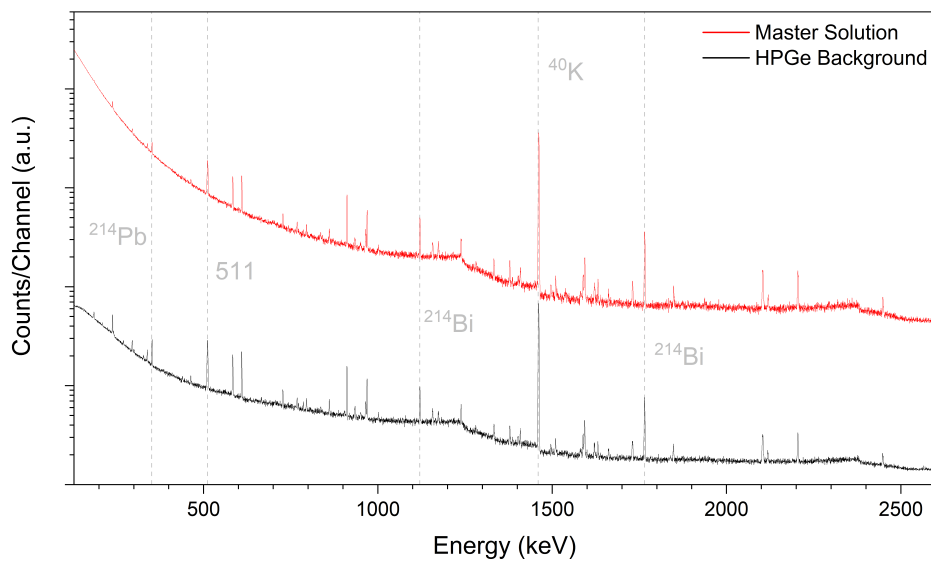


**Fig. 4.30:** Spectral comparison of 95 h  $\gamma$ -ray measurements, obtained using an HPGe detector. Both spectra show only the presence of typical background nuclides. As an example, some  $\gamma$ -emissions from  $^{214}\text{Pb}$ ,  $^{214}\text{Bi}$ , and  $^{40}\text{K}$  are shown, including the “511”-keV line.

In order to further characterize the obtained  $^{32}\text{Si}$  fraction, we also performed a LSC measurement from a x100-fold diluted aliquot of the  $^{32}\text{Si}$  master solution. Here, we wanted to confirm that the procedure yielded the required activity concentration of  $>100$  kBq/g. The measurement was completed within one hour after the separation procedure, to diminish the contribution in count-rate from the daughter,  $^{32}\text{P}$ . As a result, we obtained the following data (Table 4.13) from the LSC measurement, which we considered as measurement day zero ( $\Delta T = 0\text{d}$ ).

**Table 4.13:** Results from the LSC measurements, determined at different time intervals.

$\Delta T$ (d)	CPM(WinA) ( $\text{min}^{-1}$ )	Dilution Factor	CPM(WinA) ( $\text{min}^{-1}$ )	tSIE (-)	Efficiency (-)	DPM(WinA) ( $\text{min}^{-1}$ )	mass (mg)	DPM(WinA) ( $\text{min}^{-1} \times \text{mg}^{-1}$ )	kBq/g
0	6251	100	625110	526	0.9476	659708	101	6531.8	108.9
92	12750	100	1274967	490	1.9446	655651	101	6491.6	108.2
								$\varnothing$ 6511.7	$\varnothing$ 108.6

Noteworthy,  $^{32}\text{P}$  was quantitatively removed during the separation on the anion-exchange resin (Fig. 4.31), which suggests that the associated phosphorous speciation in aqueous solution (e.g,  $\text{H}_2\text{PO}_4^-/\text{HPO}_4^{2-}$ ) exhibits a very low retention. This can be demonstrated by measuring the freshly obtained  $^{32}\text{Si}$  fraction with LSC, whereby  $<0.1\%$  net count rates were observed from Window C ( $E_{\text{WinC}} = 230$  keV to 2000 keV), which would solely correspond to  $^{32}\text{P}$ , as the maximum beta energy of  $^{32}\text{Si}$  is 227 keV.

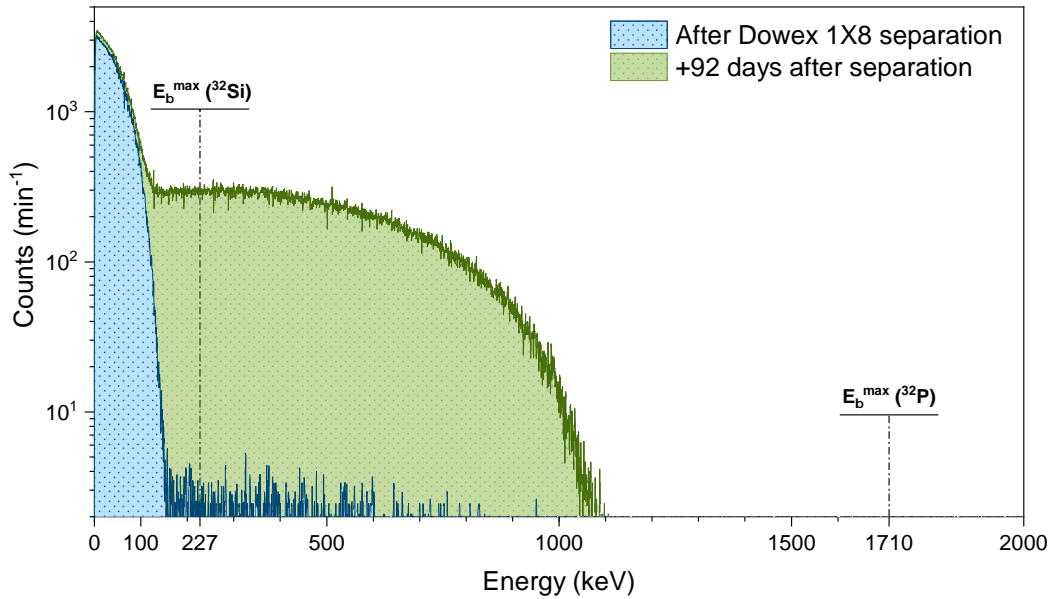


**Fig. 4.31:** Comparison of two LSC spectra, immediately after the separation (After Dowex<sup>®</sup> 1X8 separation) and 92 days later, to allow in-growth of the daughter,  $^{32}\text{P}$  ( $T_{1/2} = 14.268$  d).

As a result, the  $^{32}\text{Si}$  activity could be solely determined using  $^{32}\text{Si}$ 's counting efficiency of 0.9476 (Table 4.13). In order to compare the initially determined activity concentration, the sample was measured once more. As the in-growth of the  $^{32}\text{P}$ -daughter takes places gradually, we were considering the counting efficiencies for both  $^{32}\text{Si}$  and  $^{32}\text{P}$ , respectively (Table 4.13). Referring to Fig. 4.31, as the sample was measured again after 92 days this corresponded to a  $^{32}\text{P}/^{32}\text{Si}$  ratio of 0.9894 (based on  $T_{1/2}(^{32}\text{Si}) = 153$  y). Thus, the activity of  $^{32}\text{P}$  at that point of time corresponds to 98.94% of  $^{32}\text{Si}$ . However, a ratio of 1.000 is only achieved after around 172 days which is equal to  $\approx 12$  half-lives of  $^{32}\text{P}$  (Fig. 4.32).

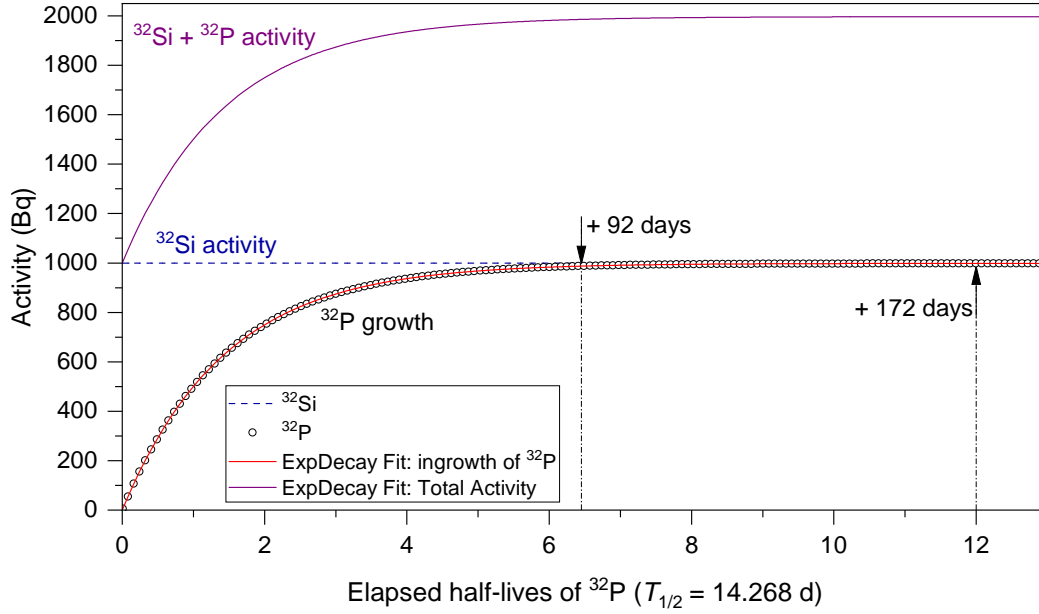


**Fig. 4.32:** Example of  $A(^{32}\text{Si}) = 1 \text{ kBq}$ , which shows the activity increase after separation due to the in-growth of the daughter nuclide. Ideally,  $A(^{32}\text{Si}) = A(^{32}\text{P})$  is reached after  $\approx 172$  days.

Based on the CIEMAT/NIST Efficiency Tracing, we were able to quantify the initial  $^{32}\text{Si}$  content to be:  $108.6 \pm 3.3 \text{ kBq/g}$ . Together with the gravimetrically traced weight of the mother solution, we calculated a total activity of  $A(^{32}\text{Si}) = 2.19 \pm 0.07 \text{ MBq}$ . With the production of this  $^{32}\text{Si}$  solution, we could fulfill the key aspect of the SINCHRON-project: “The production of a sufficient amount of  $^{32}\text{Si}$  in ultrapure quality in a stable matrix, suitable for each of the envisaged measurements”.

Further, during the separation scheme, we also traced the losses of  $^{32}\text{Si}$ , during the Load and during the Wash, as we were measuring undiluted 1 mL aliquots of each of the separately collected fractions. By combining the determined activities, we were able to determine the final yield of  $^{32}\text{Si}$  recovery to be 93.57%, while some activity losses (6.37%;  $A(^{32}\text{Si}) \approx 150 \text{ kBq}$ ) only occurred during the "Sulfur Wash 3" (0.10M HF/0.16M HCl). However, we accept these losses, as this step prioritizes the quantitative removal of  $^{32}\text{S}$ . Therefore, our experimental data confirms the high retention of  $^{32}\text{Si}$  in the used matrices, since only 0.06% of the activity ( $\approx 1.4 \text{ kBq}$ ) were eluted.

Due to mass spectrometric results, we could also determine the specific activity of  $^{32}\text{Si}$  in the prospective master solution. The  $^{\text{nat}}\text{Si}$  content in the solution was determined to be  $18 \mu\text{g}$  per g solution. Since the specific activity ( $A_{\text{spec.}}$ ) is expressed as  $A(^{32}\text{Si})/m(\text{Si})$ , the  $A_{\text{spec.}} \approx 5.9 \pm 0.4 \text{ kBq (k=2) per } \mu\text{g Si}$ . Important to note that  $18.3 \mu\text{g Si per g solution}$  yields eventually around  $61.4 \pm 2.7 \mu\text{g (k=2) Si per V disc}$  if one considers  $20.1 \text{ g initial } ^{32}\text{Si solution}$  and that six irradiated V discs were used for its production. Hence, a contribution to the  $^{32}\text{Si}$  content, stemming from the spallation process, appears to be negligible as the value is in excellent agreement with our ICP-MS determinations (Table 4.4), whereby non-irradiated V discs were used. Afterwards, aliquots (individual, requested amounts) from this finally purified  $^{32}\text{Si}$  solution were sent to each of the partners to work along with the development and improvements. At this step, it was very important to receive an independent determination of the activity concentration, which was provided by PTB, and confirmed the value, obtained from our previously performed LSC measurements (Table 4.13). As the sample's weight was gravimetrically traced during the storage and before and after the aliquots were taken out, ideal storage conditions had to be elaborated to diminish losses, e.g., due to evaporation (loss of matrix ( $\text{H}_2\text{O}$ ,  $\text{HCl}$ )). Figure 4.33 shows that, within 21 days, a loss of about 30 mg could be determined during the samples' storage under ambient conditions, while in parallel being measured on the HPGe.

Consequently, we decided to place the sample into a fridge for storage and further chose to seal the  $^{32}\text{Si}$  master solution in a multi-layered poly-nylon bag (wall thickness: 90  $\mu\text{m}$ ), which was then again sealed in an aluminium bag (wall thickness: 170  $\mu\text{m}$ ); both bags were commercially available. As a result, we can see from the trendline that losses are generally diminished, and a long-term storage of the solution should not lead to significant losses of the sample's volume. A similar principle is also applied for commercially available (ICP) standard solutions (e.g., Sigma-Aldrich).

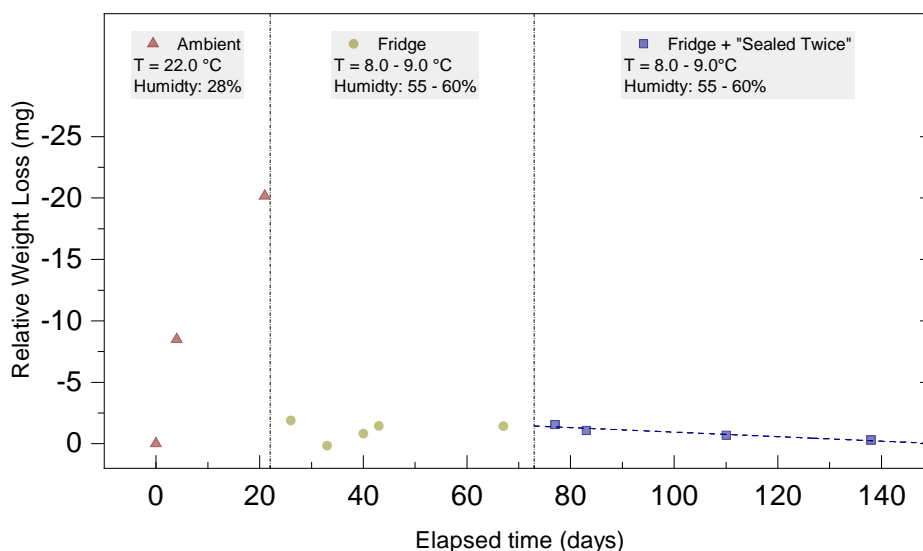


**Fig. 4.33:** Overview of the relative weight losses of the  $^{32}\text{Si}$  master solution, traced for a period of around five months.

### 4.2.3 Summary: Radiochemical separation of $^{32}\text{Si}$

Although the distillation of radiosilicon based on  $\text{H}_2^{32}\text{SiF}_6$  appeared as a suitable method for conveniently separating  $^{32}\text{Si}$ , neither could we reach the reported yields from [173], nor could we obtain reproducible results from our distillation setup. Although we eventually reached a final design of a prospective distillation apparatus, a key point, namely the uniform heat to avoid condensation of water, and silicon, respectively, was a challenge that we ultimately could not solve. Moreover, considering further implementations, such as to regard radio-protective measures, would be rather difficult since the smallest leakages in the system would lead to, e.g., the escape of hazardous hydrogen fluoride, but also radioactive gaseous species. From this perspective, we concluded that it was not possible to develop a reliable, fully working setup for the distillation of  $^{32}\text{Si}$ .

Concerning the duly production of a suitable  $^{32}\text{Si}$ -sample for the SINCHRON-collaboration, we moved over to means of column chromatography. Since more than 150 proton-irradiated V-discs were processed, this method turned out to be more suitable and allowed us to process such amounts more conveniently. We focused on the stepwise development of a wet-chemical separation scheme while first removing the bulk vanadium matrix. While performing radioanalytical analyses, we determined further unexpected nuclides hampering the processing, since specific resins had to be found for a reliable separation. As a result, a series of purification steps involving extraction, chelating chromatographic resins, evaporation to dryness, and finally, an anion-exchange resin was chosen to obtain pure  $^{32}\text{Si}$  fractions.

Furthermore, using silicon’s speciation in HF-media, we were able to find a procedure to ultimately provide a solution with remarkably high activity concentration ( $>100$  kBq/g) and further remove radiosilicon’s isobar,  $^{32}\text{S}$ . The slightly acidic matrix (0.5M HCl) has also proven to be beneficial for LSC measurements, as no oxidizing acid (e.g.,  $\text{HNO}_3$ ) was used that potentially influences the long-term stability. The overall results demonstrated that the separation scheme provides a robust and reliable method with a high recovery of  $^{32}\text{Si}$ . Therefore, enough  $^{32}\text{Si}$  can be provided to perform a range of individual measurements, focusing initially on a precise determination of the half-life of  $^{32}\text{Si}$ .

Furthermore, the proton-induced spallation reactions within the vanadium discs are considered to be a valuable production path for other rare and valuable carrier-free radionuclides (such as  $^{44}\text{Ti}/^{44g}\text{Sc}$ ,  $^{41}\text{Ca}$ , and  $^{26}\text{Al}$ ) that can also be recovered from the existing metal matrix.

The final “SINCHRON-Separation” scheme is shown in Fig. 4.34. Interestingly, because of the scheme’s versatility, it is possible to implement other highly specific resins to, e.g., separate further impurities that would be mainly stemming from different irradiation conditions during the exposure in the SINQ-Target.

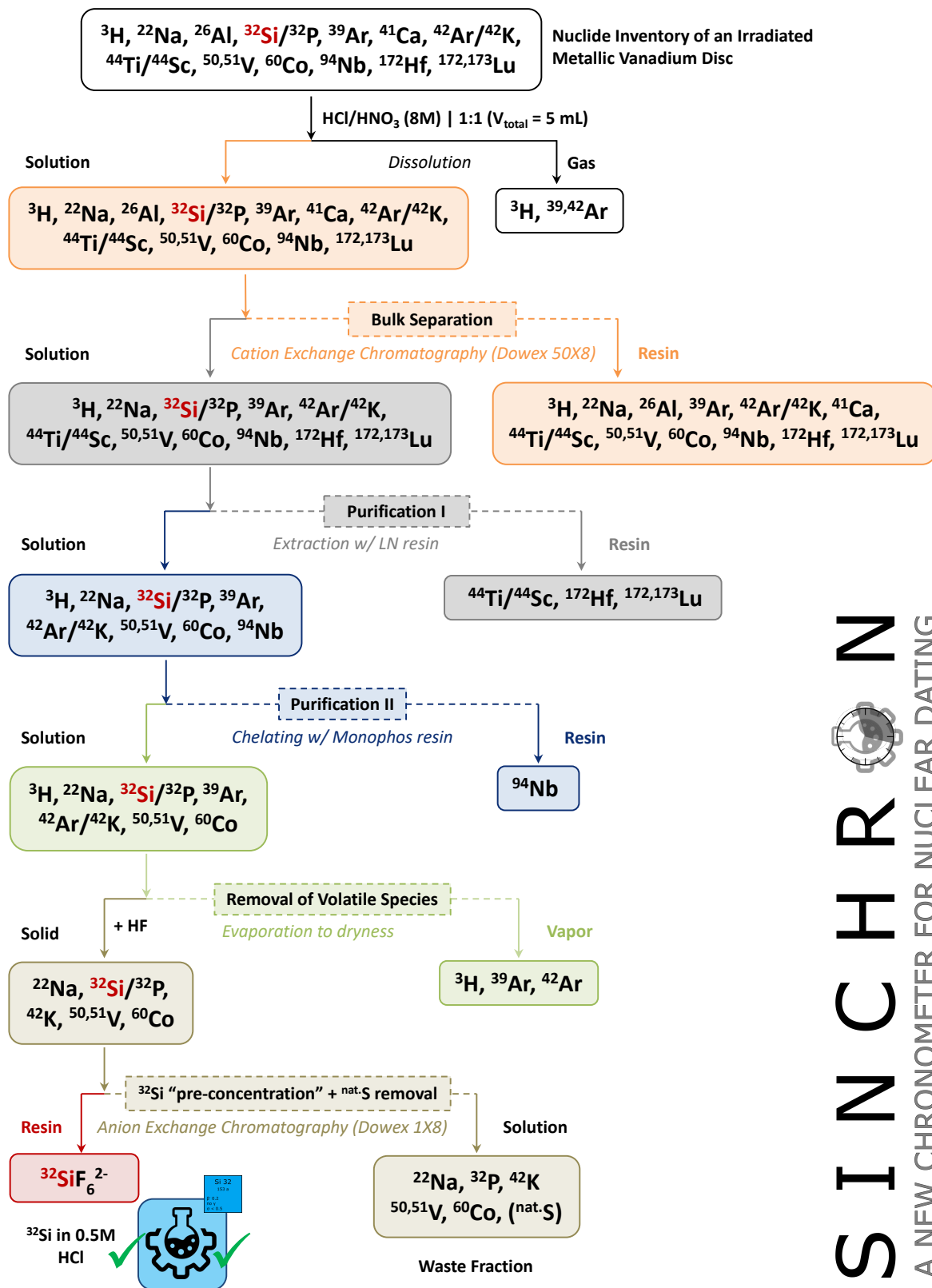


**Fig. 4.34:** Stepwise separation of nca  $^{32}\text{Si}$  from proton-irradiated vanadium matrix. The “SINCHRON-Separation” scheme has been carefully developed to provide a robust and reliable scheme that allowed to prepare >40 purified  $^{32}\text{Si}$  fractions. As a result, the Laboratory of Radiochemistry (LRC) at PSI has a unique worldwide amount of  $A(^{32}\text{Si})\ 22 \pm 2\ \text{MBq}$  at its disposal.



### 4.3 Determination of the cross-section: $^{nat}\text{V}(\text{p}, \text{x})$

The excerpt presented in this Section is based on the article: ➡ “*Experiment-based determination of the excitation function for the production of  $^{44}\text{Ti}$  in proton-irradiated vanadium samples*” and appeared in Physical Review C **104**(1), 014615 (2021). The work was authored by Veicht et al. [177].

#### 4.3.1 $^{nat}\text{V}(\text{p}, \text{x})^{44}\text{Ti}$

After validating the counts of each sample, the subsequent determination of the sample’s  $^{44}\text{Ti}$  activity is presented in Table 4.14. Notably to mention is the very low activity of the samples that range from around 0.04 Bq to 0.67 Bq. These meager  $^{44}\text{Ti}$  production yields have also been identified early as the major challenge in determining the excitation function. However, with the presented approach, it was possible to determine these low activities with relatively low uncertainties, ranging from 2.74% up to 15.33%.

**Table 4.14:** Overview of the measured activities of  $^{44}\text{Ti}$  from proton irradiated vanadium discs.

	VVUH271	VVUL451	VVUL411	VVUL333	VVUL291	VVUL171	VVSN083
	$A(^{44}\text{Ti})$ in Becquerel						
LEGe	$0.30 \pm 0.01$	$0.55 \pm 0.01$	$0.61 \pm 0.01$	$0.65 \pm 0.01$	$0.66 \pm 0.02$	$0.62 \pm 0.01$	$0.04 \pm 0.01$
HPGe	$0.33 \pm 0.01$	$0.055 \pm 0.01$	$0.64 \pm 0.01$	$0.67 \pm 0.01$	$0.67 \pm 0.01$	$0.69 \pm 0.01$	$0.04 \pm 0.01$
Arithmetic mean	$0.32 \pm 0.02$	$0.55 \pm 0.02$	$0.62 \pm 0.02$	$0.66 \pm 0.02$	$0.67 \pm 0.02$	$0.65 \pm 0.04$	$0.04 \pm 0.01$
Uncertainty (%)	5.31	2.84	3.42	2.97	2.74	5.81	15.33

To determine the cross-section values, the unweighted arithmetic mean of obtained  $^{44}\text{Ti}$  activity values was used. Consequently, knowing the integrated proton current and the activity of produced  $^{44}\text{Ti}$ , the production cross-sections were calculated as displayed in Table 4.15. Our experimental data show an excellent agreement compared to those from the unpublished work of Protoschill’s diploma thesis [178], in which the cross-sections were studied over a similar energy range (Fig. 4.35). Notably, the uncertainties of the obtained cross-sections are significantly lower in our work than from the data taken from Protoschill [178]. Moreover, for a further comparison, the cross-sections from Zaitseva et al. [197] are reported with an uncertainty of  $\pm 20\%$  and are, therefore, also considerably higher. In our work, only the sample VVSN083 shows a high uncertainty as this is related to the exceptionally low  $^{44}\text{Ti}$  activity (one order of magnitude lower than the average).

**Table 4.15:** Measured production cross section of  $^{44}\text{Ti}$ .

	VVUH271	VVUL451	VVUL411	VVUL333	VVUL291	VVUL171	VVSN083
	$A(^{44}\text{Ti})$ in Becquerel						
Energy (MeV)	$111 \pm 1.3$	$129 \pm 1.4$	$134.9 \pm 1.3$	$145 \pm 1.2$	$150.2 \pm 1.2$	$164.5 \pm 1.0$	$954 \pm 1.6$
Cross-section ( $\mu\text{b}$ )	$592 \pm 34$	$697 \pm 24$	$782 \pm 31$	$803 \pm 28$	$805 \pm 27$	$761 \pm 46$	$576 \pm 89$
Uncertainty (%)	5.77	3.48	3.95	3.55	3.36	6.11	15.52

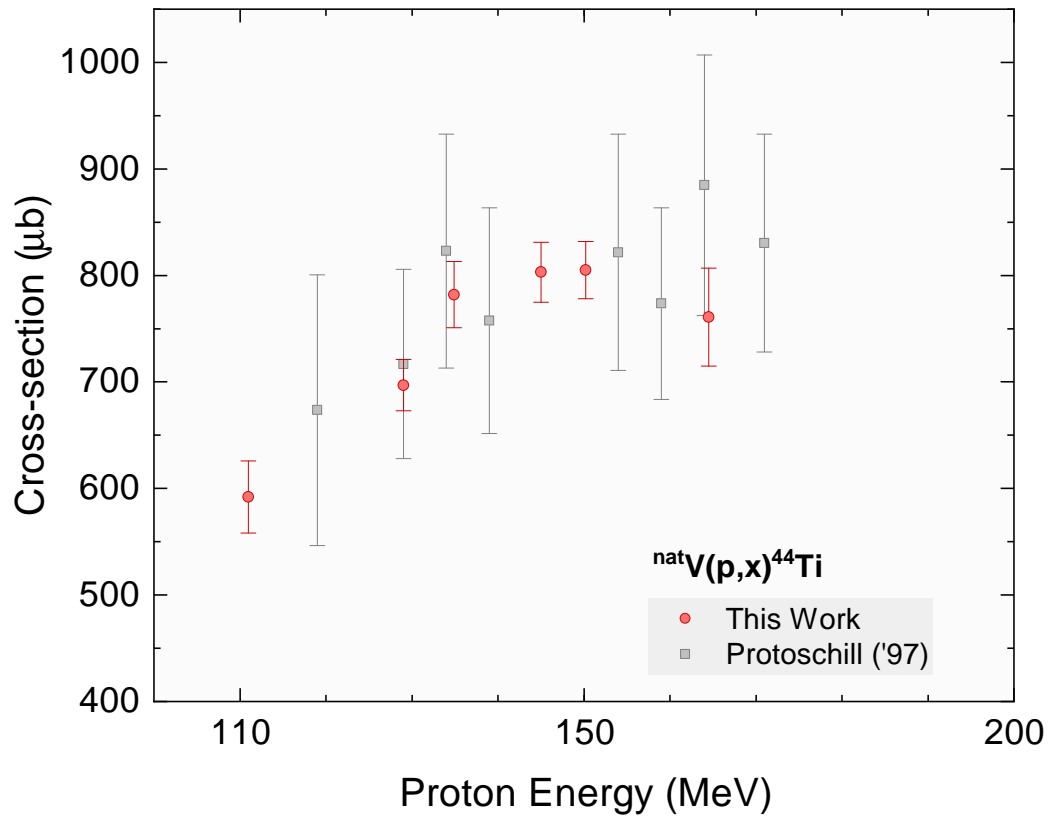


**Fig. 4.35:** Experimental excitation function to produce  $^{44}\text{Ti}$  from proton-induced reactions. A comparison between the two data sets is shown.

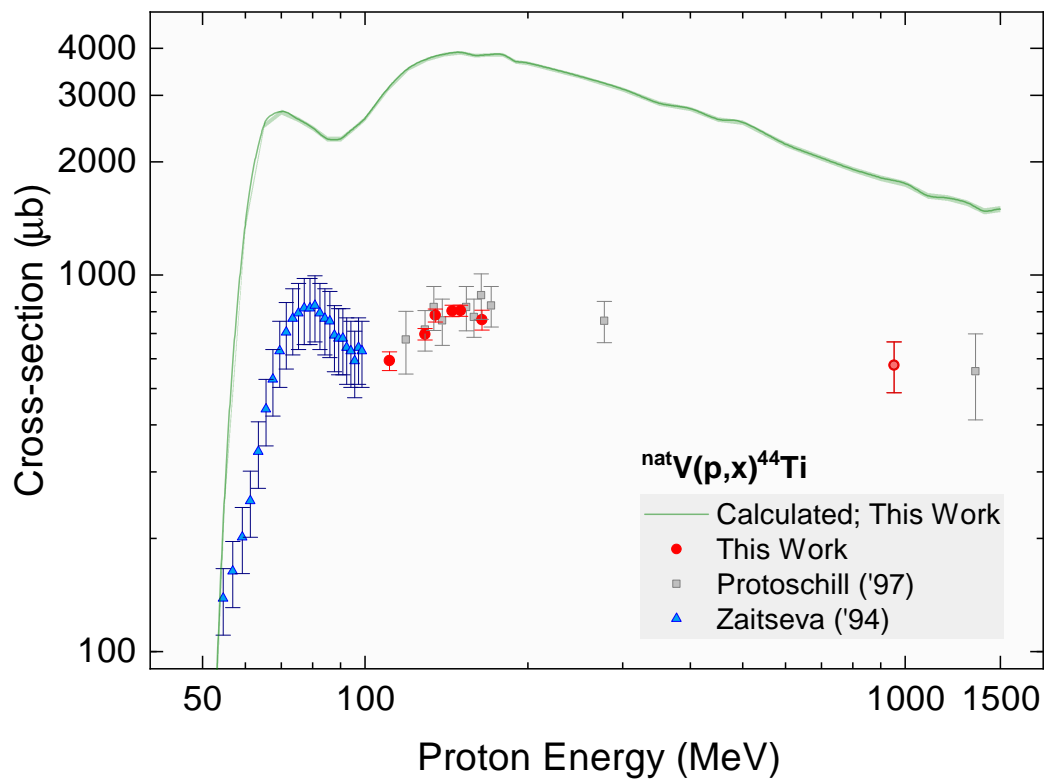


**Fig. 4.36:** Further comparison of the excitation function for the  $^{44}\text{Ti}$  production with additional data in the low-energy range (data taken from [197]) as well as theoretical calculations.

First, if we compare the experimental data with the predictions of the INCL++ and ABLA 07 codes (Fig. 4.36), it can be seen that the theoretical data indicate a consistent shift towards much higher cross sections. The experimental data, hence, suggest that the codes are overestimating the excitation function. Furthermore, from the calculations, it can be derived that the maximum is located in the mid-energy range, which is here reached at 150 MeV. This is consistent with our experimental data. Accordingly, our data agree with the predicted energy of the maximum cross section with  $803 \pm 28$   $\mu\text{b}$  at an energy in the region of  $145 \pm 1.2$  MeV and with  $805 \pm 27$   $\mu\text{b}$  at  $150.2 \pm 1.2$  MeV, respectively. For a comparison, in the work from Zaitseva et al. [197], the cross section maximum is reached at an energy of  $80.8 \pm 2$  MeV, yielding  $830 \pm 166$   $\mu\text{b}$ . Here, the experimental data differ, since according to the computational predictions, a global maximum for the cross section is localized at 150 MeV. However, derived from our experimental data, it is obvious that a second maximum is reached at 150 MeV, although the value is not much higher than compared to the maximum value of the lower-energy region. But, as the values obtained from Zaitseva et al. [197] are given within a 20% uncertainty, the actual cross-section values in that range might be actually lower. Therefore, a global maximum at 150 MeV could be expected; a further investigation and, thus, more experimental data in the low-energy region would be required. Moreover, as the cross sections in the range of  $>70$  MeV are consistently high and even constant in the range from 100 to 150 MeV, also thick targets can be considered for proton irradiations [177]. Yet, to mention the overestimation of the model, the new data set allows to provide a reliable reference for the comparison, based on experimental data. As a result, the model's overestimation will require further investigation. However, these new data, can help to improve the codes. Concerning the practical application, our results show, using this production path, the production of sufficient amounts of  $^{44}\text{Ti}$  requires several hundred hours of dedicated beam time. About a practical application, for instance, to produce 370 MBq  $^{44}\text{Ti}$  (corresponding to ten millicurie – the smallest unit of, e.g., the commercially available  $^{68}\text{Ge}/^{68}\text{Ga}$  generator [198]) using an average cyclotron with 100  $\mu\text{A}$  proton beam current, around 30 days irradiation time would be required. Moreover, the chemical separation of the  $^{44}\text{Ti}$  from the irradiated matrix material Sc requires exceptionally high decontamination factors. Because of the requirements, e.g., for medical applications, the wanted  $^{44g}\text{Sc}$  is the same chemical element as the irradiated matrix material. Any remaining stable Sc in the  $^{44}\text{Ti}$  fraction would contaminate the  $^{44g}\text{Sc}$  fraction eluted from the generator. This could not only hinder the labeling of the medically active molecule but, in the worst case, poison the patient. Considering these circumstances, spallation represents a promising alternative production route. Given the possibility of dedicated irradiation positions in large-scale spallation facilities, for instance, near the beam dump or at particular positions in the spallation target, no additional beam time is needed to perform long-term irradiations over several months or even years. Such an opportunity is given, e.g., by the spallation target of the SINQ facility at PSI. Besides, several high-power spallation sources worldwide, such as the Spallation Neutron Source in Oak Ridge (U.S.A.) [199], the Japan Spallation Neutron Source in Tokai (Japan) [200], TRIUMF in Canada [201] or the still under construction European Spallation Source (ESS) in Lund (Sweden) [202] are potential sites for such an application [177]. Therefore, besides the radiochemical separation of purified nca  $^{44}\text{Ti}$  from the STIP-6 vanadium discs, obtaining the necessary precise knowledge about the production cross-section of  $^{44}\text{Ti}$ , is a further step in realizing a potential  $^{44}\text{Ti}/^{44g}\text{Sc}$  generator.

Clearly, the differences between the experimentally obtained data and the model calculations are not discussed further in detail. The reader is advised to have a careful look into to the work from Veicht et al. [177]. Yet, as also mentioned by the authors, that new data allows to have a reliable reference for the comparison, and are very important in order to improve the theoretical codes.

### 4.3.2 $^{\text{nat}}\text{V}(\text{p}, \text{x})^{41}\text{Ca}$ and $^{\text{nat}}\text{V}(\text{p}, \text{x})^{26}\text{Al}$ : Radiochemical separation procedures

The excerpt presented in this section is based on the article: ➡ “Radiochemical separation of  $^{26}\text{Al}$  and  $^{41}\text{Ca}$  from proton-irradiated vanadium targets for cross-section determination by means of AMS” and was published online by the time this thesis was finally submitted. This work was authored by Veicht et al. [203].

#### 4.3.2.1 Change of matrix and separation of carrier-added $^{32}\text{Si}$ from $^{41}\text{Ca}$ , $^{26}\text{Al}$ , and $^{\text{nat}}\text{V}$

The initial separation procedure, employing Dowex® 50WX8-200 ion-exchange resin, was required to change the chemical matrix content from 8M HCl to 3M HNO<sub>3</sub>. Under the slightly acidic conditions after the dilution ( $\approx 0.2\text{M}$  HCl), the resin retained all cations, including Ca, Al, and V. Also, the resulting pH ( $\approx 0.7$ ) was in a range that allowed to separate silicon as neutral species Si(OH)<sub>4</sub>. Here, the separation of  $^{32}\text{Si}$  was introduced since it was earlier identified as a spallation product from proton-irradiation vanadium targets [22]. Finally, 3M HNO<sub>3</sub> was used for elution, whereby Ca, Al, and V were eluted with 50 mL of the eluent. The elution profile is represented in Fig. 4.37 and shows the excellent separation of Si from Ca, Al, and V.

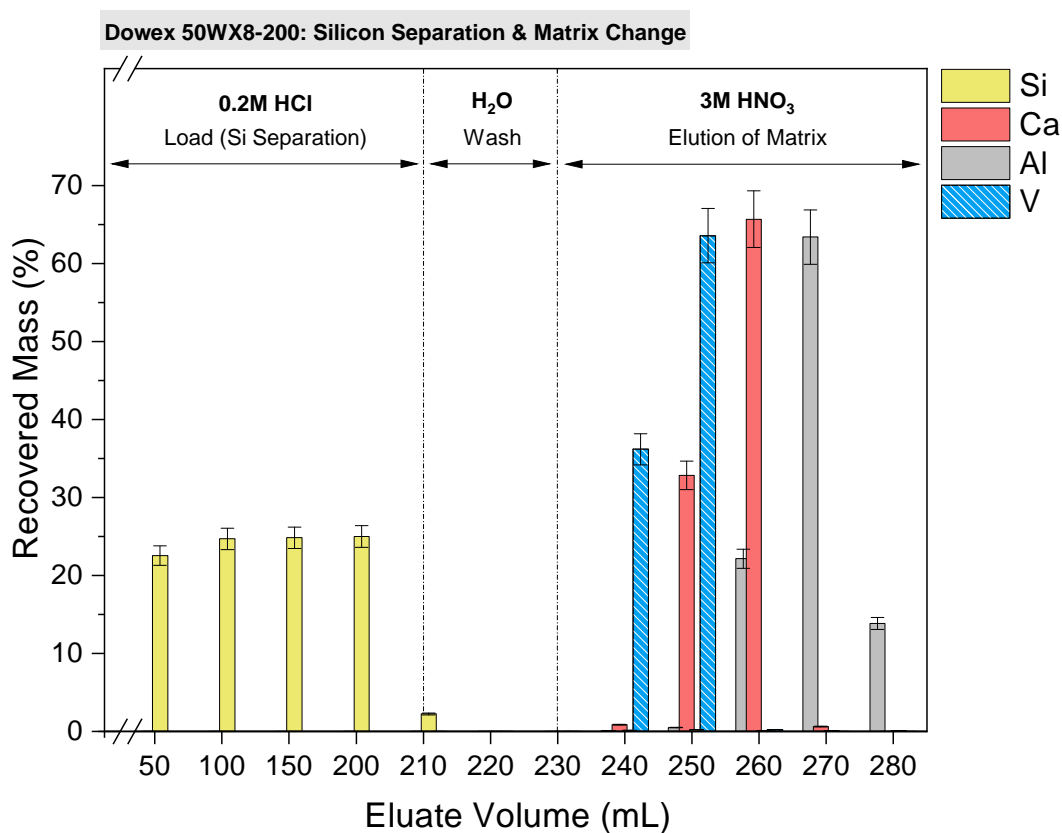


**Fig. 4.37:** Example of an elution profile: during the Load, Si is unretained and thus gathered within 230 mL. Afterwards, Ca, Al, and V are eluted from the column with 50 mL (230 mL to 280 mL) 3M HNO<sub>3</sub>.

### 4.3.2.2 Calcium-41 separation with DGA (normal)

Continuing the experimental scheme, the separation of calcium was achieved. As stated, calcium's affinity towards DGA in 3M HNO<sub>3</sub> is very high, which is shown in (Fig. 4.38), as it cannot be detected during the Load. In contrast, Al and V do not show any retention under these conditions. To avoid any contamination in the Ca fraction, a wash of 20 mL 3M HNO<sub>3</sub> was used, whereby Al and V were quantitatively recovered. Afterwards, the Ca elution took place, using 30 mL 3M HCl. Analyzing the Ca fractions with ICP-OES, a typical Ca recovery of >99% was confirmed (Fig. 4.38). Noteworthy to mention that the same recovery yield was achieved for the sample VVUL171, although the value is not shown in Fig. 4.38. This was traced back to a faulty sample preparation for the ICP-OES measurement, which could therefore not yield accurate results (sample too concentrated). However, given the separation scheme's robustness as well as looking at the sample amount of the AMS samples (see section 4.3.4, Table 4.17), the Ca recovery yield is very likely >99%, too.

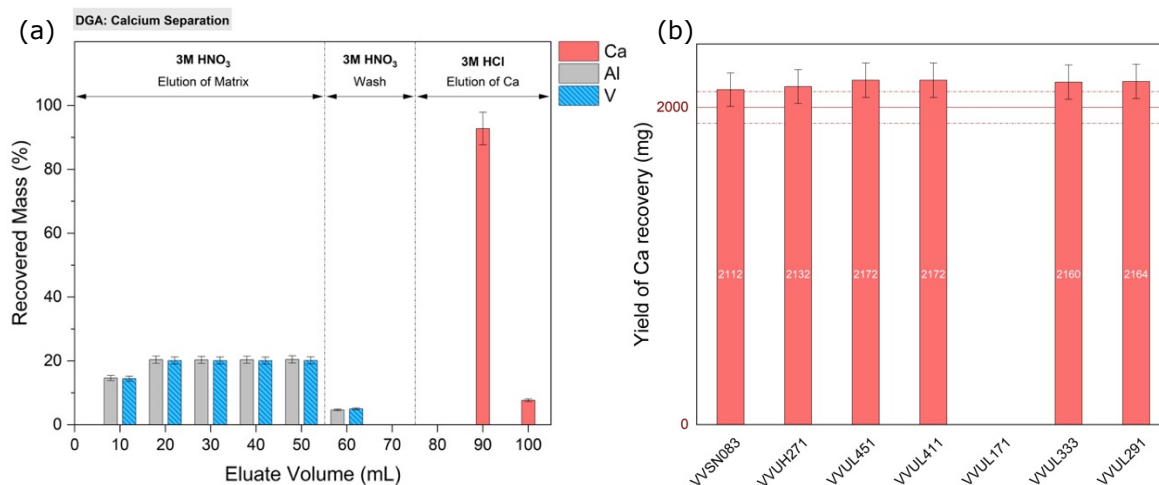
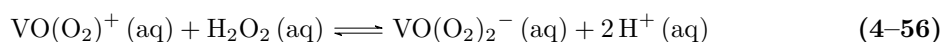
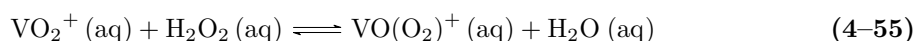


**Fig. 4.38:** (a) Example of an elution profile: during the Load, Ca is retained, while Al and V are unretained. Eventually, Ca is eluted with 30 mL 3M HCl (70 mL to 100 mL) (b) Confirmation of the yield of Ca recovery which was on average >99%.

Referring to the separation results of Ca, our data is also in excellent agreement with other literature. First, in the work from Dirks [174] a series of comprehensive batch studies was performed, whereby the  $K_d$  values of various elements, such as Ca, Al, and V were evaluated using the DGA resin (TrisKem SAS, Bruz, France). Comparing these values, we found that in 3M HNO<sub>3</sub>, Ca is highly retained ( $K_d \approx 10^3 \text{ cm}^3 \text{ g}^{-1}$ ) while vanadium and Ti repeatedly have no retention, resulting in a  $K_d < 10^1 \text{ cm}^3 \text{ g}^{-1}$ . Besides, a further study performed by Pourmand & Dauphas [204] determined distribution coefficients of 60 elements on the (TO)DGA resin as a function of nitric acid and hydrochloric acid concentration. Consequently, Al<sup>3+</sup> and V<sup>5+</sup> retention in HNO<sub>3</sub>-media remain very low up to 8M, while the  $K_d$  for Ca<sup>2+</sup> increases, with a peak at around 1M. Ultimately, a work from Mueller et al. [205] describes the separation of <sup>47</sup>Sc from an enriched <sup>46</sup>Ca target. In order to extract <sup>47</sup>Sc, the irradiated calcium target was dissolved in 3M HCl and then loaded onto a column containing DGA (normal) resin. Calcium remained in solution and was eluted in the initial 3M HCl matrix. Therefore, highly reproducible results can also be reported for our experiments, using proton-irradiated vanadium as starting material.

### 4.3.2.3 Aluminium-26 separation using Dowex® 50WX8-200

At first, upon the addition of  $\text{H}_2\text{O}_2$ , the solution turned red, indicating the formation of the oxo-peroxo cationic complex  $(\text{VO}(\text{O}_2)^+)$ . As described by Butler et al. [206], in an aqueous solution, hydrogen peroxide readily coordinates to vanadium(V), forming mono-, di-, tri-, and even tetraperoxo complexes. However, the highly pH-dependent equilibrium distribution suggests that in acidic solution ( $\leq \text{pH } 2$ ), the red oxo-peroxo  $(\text{VO}(\text{O}_2)^+)$  is formed (Eq. 4–55), while a yellow anionic oxo-diperoxo complex  $((\text{VO}(\text{O}_2)_2^-))$  can be reached, too (Eq. 4–56). For that species, the pH has to be raised to 2 and above [206].



Since vanadium(V) exhibits relatively low retention on the cation-exchange resin, we expected the oxo-peroxo cation to have similarly low retention, too. This can be confirmed according to Fig. 4.39(a) since during the Load, most of the vanadium passed through the cation-exchange resin. However, after the Load, traces of vanadium were still detectable: on average ( $n=3$ )  $3.6 \pm 0.3\%$  ( $\approx 475.2 \pm 1.4 \mu\text{g}$ ). Detecting vanadium in the fractions (350 to 370 mL) with elevated  $\text{HNO}_3$  concentrations (3M) suggested that vanadium  $\text{V}^{IV}$  was also present in solution, as it has a higher affinity towards the strong cation-exchange resin than  $\text{V}^{+V}$  or its red oxo-peroxo complex. Therefore, it was not eluted during the Load given the initial  $\text{HNO}_3$  concentration of 0.75M. Thus, with the gradual elution (1M  $\text{HNO}_3$ , followed by 3M  $\text{HNO}_3$ ) it was possible to determine the breakthrough of Al, whereby V was completely separated before. Ultimately, we analyzed each Al-fraction with ICP-OES in order to confirm the yield and purity. As seen from Fig. 4.39(b), we were able to recover on average  $1995 \pm 10 \text{ mg Al}$  which translates into a yield of  $>99\%$ . At the end of the separation procedure, the 0.75M- $\text{HNO}_3$ -, 1M- $\text{HNO}_3$ - and partially the 3M- $\text{HNO}_3$ -fraction were discarded as they contained only vanadium.

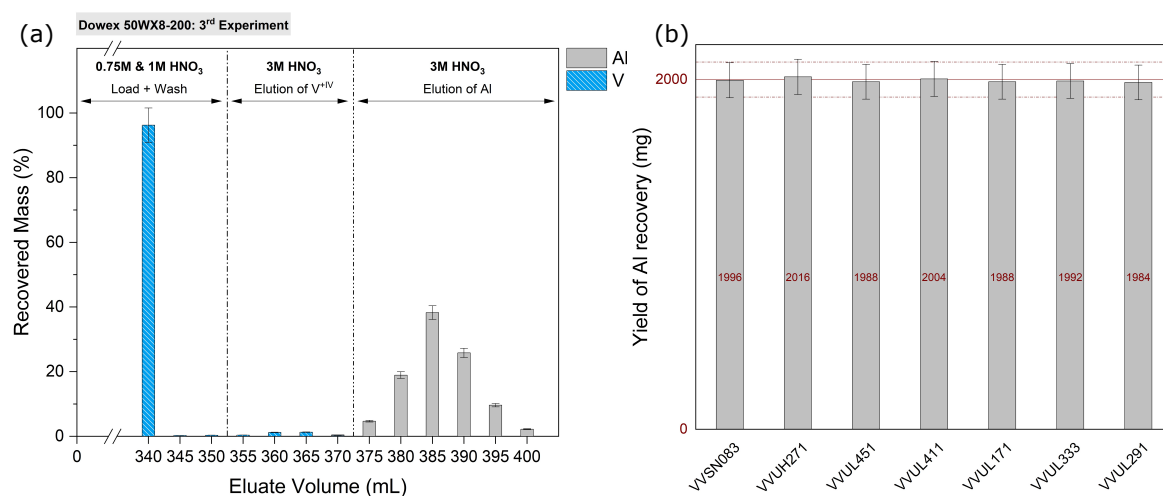


**Fig. 4.39:** (a) Example of an elution profile, showing the successful separation of Al from the bulk vanadium matrix using gradual elution and (b) yield of Al recovery was on average  $>99\%$ .

### 4.3.3 Summary: Radiochemical separation of carrier-added $^{32}\text{Si}$ , $^{41}\text{Ca}$ , and $^{26}\text{Al}$

The developed scheme for separating the cosmogenic radionuclides,  $^{32}\text{Si}$ ,  $^{41}\text{Ca}$ , and  $^{26}\text{Al}$ , has proven to allow for pure samples, combined with high separation yields. In the case of the provided vanadium samples, we performed these separations with the addition of a carrier (each 2 mg) since we specifically aimed for AMS measurements. After completing the entire separation scheme (Fig. 4.40), we produced around 0.37 L waste fraction per fully processed vanadium disc while providing the separated elements in fractions as summarized in Table 4.16.

**Table 4.16:** Overview of the three fractions obtained per each fully processed vanadium disc.

Element	Isotope	Volume (mL) per fraction	Matrix composition
Silicon	$^{32}\text{Si}$	230	$\approx 0.17\text{M HCl}$
Calcium	$^{41}\text{Ca}$	30	3M HCl
Aluminium	$^{26}\text{Al}$	30	3M $\text{HNO}_3$

Since the final waste fraction is not highly radioactive and clearly  $<1$  CS, one can chemically treat these solutions accordingly and dispose of them as inactive waste. Here, just to be aware that these solutions contain elevated heavy metal concentrations (vanadium). Moreover, since titanium was initially not separated, we assumed that Ti(IV) could potentially follow vanadium along the entire separation process due to their similar behaviors on both the strong cation-exchange resin (Dowex® 50WX8-200) and the extraction resin (DGA normal). Finally, the calcium and aluminium samples have been further processed to obtain suitable AMS samples. At this point, the sample preparation was not performed for silicon since there is currently no  $^{32}\text{Si}$ -AMS-Standard available. However, a procedure to obtain suitable samples (either  $\text{SiO}_2$  or  $\text{K}_2\text{SiF}_6$ ) is described elsewhere in this thesis and can be eventually applied to these sample solutions. However, a purification scheme to separate  $^{32}\text{Si}$  from its L-AscA matrix needs to be developed first.

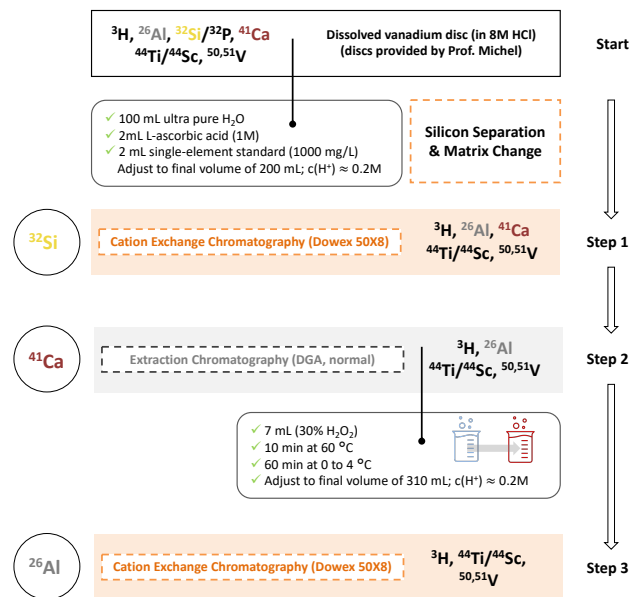


**Fig. 4.40:** Stepwise separation of carrier-added  $^{32}\text{Si}$ ,  $^{41}\text{Ca}$ , and  $^{26}\text{Al}$  from proton-irradiated vanadium discs. The “DOGADO-Separation” scheme has been carefully developed to provide a quantitative recovery, with virtually no losses during the separation. Consequently, we obtained pure samples, which were further chemically processed, to obtain solid AMS samples.

#### 4.3.4 Sample preparation for AMS: $^{41}\text{CaF}_2$ and $^{26}\text{Al}_2\text{O}_3$

Since the samples' chemical shapes for AMS were already known, samples for calcium and aluminium were prepared accordingly:  $^{41}\text{CaF}_2$  and  $^{26}\text{Al}_2\text{O}_3$ , respectively. The sample weight for calcium fluoride was, on average, around 94%, while we reached on average 67% for aluminium oxide (Table 4.17). Here, we first assumed the lower sample yield of aluminium was related to losses during the chemical separation. However, it was proven that we reached a recovery of  $\geq 99\%$ , and losses were therefore excluded. Also, when carefully reviewing the dedicated method development for the precipitation of  $^{26}\text{Al}_2\text{O}_3$  we usually dealt with 65% to 70% recovery yields, which is in excellent agreement with the finally obtained amounts of aluminium oxide. Although we were working at a high pH, we did not reach a pH, e.g., greater than 11 or 12, in which aluminium turns into a soluble complex: tetra hydroxo aluminate  $[\text{Al}(\text{OH})_4]^-$ . Thus, we can consider these losses must happened during the sample transfer. In contrast, the recovery yields for calcium are higher, whereby only the sample VVSN083 yielded smaller amounts. Here, we used a non-optimized procedure which was then further optimized to produce the other samples. Nevertheless, the AMS measurements can be performed with quantities of  $\approx 2$  mg sample, so we did not have any issues regarding the amounts themselves.

**Table 4.17:** Overview of the recovery yields for the AMS samples.

Sample	$\text{CaF}_2$		$\text{Al}_2\text{O}_3$	
	mg	%	mg	%
VVUH271	3.9	100.0	2.8	74.1
VVUL451	4.0	102.5	2.4	63.5
VVUL411	4.3	110.2	2.6	68.8
VVUL333	3.3	84.6	2.4	63.5
VVUL291	3.9	100.0	2.8	63.5
VVUL171	4.1	105.1	2.8	66.2
VVSN083	2.1	53.8	2.6	68.8

At the low energies available at MILEA, the  $^{41}\text{Ca}$  isobars cannot be clearly separated as with the gas ionization detector (GID), but the intensity of K can be significantly reduced by selecting  $\text{CaF}_3^-$ . Furthermore, the contribution of  $^{41}\text{K}$  to the mass 41 counts can be monitored by measuring the isotope  $^{39}\text{K}$  and a correction can be applied assuming a constant (natural)  $^{41}\text{K}/^{39}\text{K}$  ratio. Standards were used for normalization with nominal values taken from [111]. A blank correction based on the average of three blanks was applied and an uncertainty of 3% was added to the relative uncertainty.

Further,  $^{26}\text{Al}$  was measured in charge state 2+ for high transmission and efficiency, but it required a gas absorber cell in front of the final detector to stop the m/q interference of  $^{13}\text{C}^+$ . However, the samples here showed too much  $^{13}\text{C}$  and thus the 1+ charge state was selected, although it has a lower transmission. But molecular interferences were sufficiently reduced by increasing the stripper gas pressure. The measured  $^{26}\text{Al}/^{27}\text{Al}$  ratios of the irradiated samples were between  $10^{-12}$  and  $10^{-11}$  whereas the blanks were at  $10^{-14}$  and thus not relevant. The measurement was normalized to the ETHZ in-house standard (ZAL02) having a nominal  $^{26}\text{Al}/^{27}\text{Al}$  ratio of  $(46.4 \pm 0.1) \times 10^{-12}$ , which, in turn, was calibrated against the primary standard KN 01-4-1 (nominal  $^{26}\text{Al}/^{27}\text{Al}$  ratio  $(74.44 \pm 2.68) \times 10^{-12}$ ) reported by Nishizumi [207]. A 1% uncertainty was added to the final error.

### 4.3.5 Determination of the excitation function: ${}^{\text{nat}}\text{V}(\text{p}, \text{x}) {}^{41}\text{Ca}$ and ${}^{\text{nat}}\text{V}(\text{p}, \text{x}) {}^{26}\text{Al}$

Noteworthy to mention that with this data, we present the first experimentally determined excitation functions for  ${}^{41}\text{Ca}$  and  ${}^{26}\text{Al}$ , originating from the proton-induced spallation reaction using high-purity metallic vanadium discs as targets. First, we look at the results for the reaction  ${}^{\text{nat}}\text{V}(\text{p}, \text{x}) {}^{41}\text{Ca}$  (Fig. 4.41(a) and (b)). The experimental values show a very good agreement with the predicted theoretical model. As seen from the detail, the shape of the curve is well reproduced, while the experimental values are only slightly lower (factor of  $\approx 1.5$ ). Consequently, the data confirm both the accuracy and predictive power of the theoretical models, which means that the mechanisms involved in the nuclear reactions are well implemented.

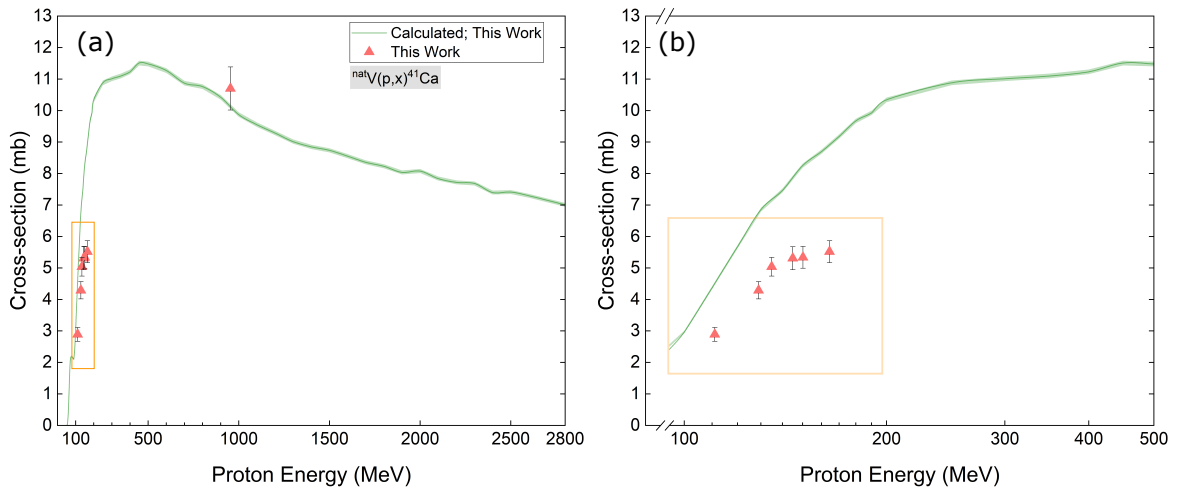


**Fig. 4.41:** (a) Comparison between the calculated and experimentally obtained excitation function for the  ${}^{\text{nat}}\text{V}(\text{p}, \text{x}) {}^{41}\text{Ca}$  reaction and (b) detail of the low-energy region.

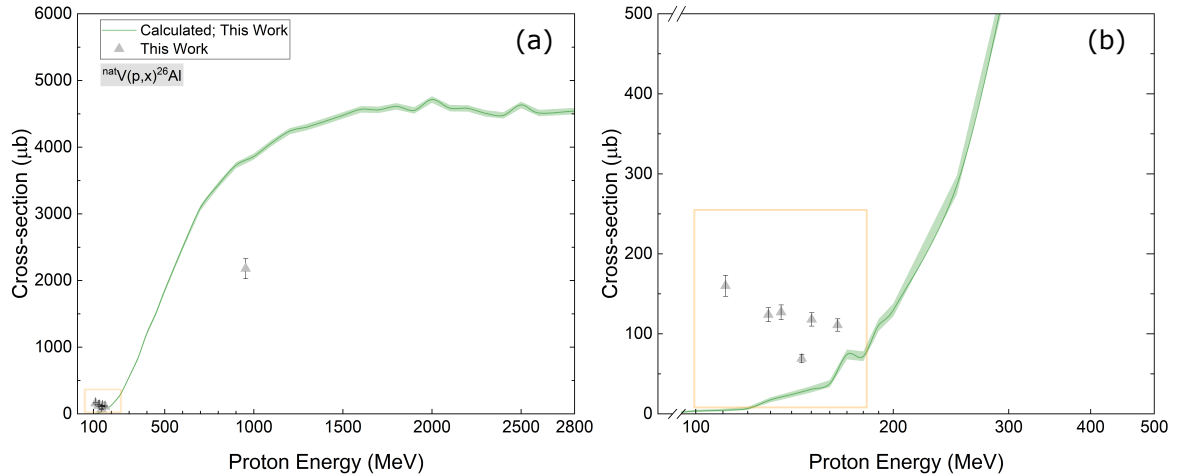


**Fig. 4.42:** (a) Comparison between the calculated and experimentally obtained excitation function for the  ${}^{\text{nat}}\text{V}(\text{p}, \text{x}) {}^{26}\text{Al}$  reaction and (b) detail of the low-energy region.

Again, comparing the predicted excitation function with the experimental values, however, to produce  ${}^{26}\text{Al}$ , the results from the model calculations seem to slightly underestimate the cross-sections values at low proton energy ( $<200$  MeV) and to overestimate it at higher energy, which is represented

by sample VVSN083 ( $E_{\text{Proton}} = 954$  MeV) (Fig. 4.42(a) and (b)). Nevertheless, the experimental data confirm the predicted low reaction probability for  $^{26}\text{Al}$  production, regarding the  $^{\text{nat}}\text{V}(\text{p}, \text{x})$ -reaction.

Interestingly, such deviations are visible for both  $^{41}\text{Ca}$ , and  $^{26}\text{Al}$  from the theoretical models have also been described earlier ([208], [177]), and in the work of Veicht et al. [177], some considerations regarding this already earlier observed systematic overestimation of neutron-poor residues are given, that will trigger new approaches in order to improve the predictions performed by the model calculations. Ultimately, details concerning the values for the experimentally obtained cross-section values are presented in Table 4.18 ( $^{41}\text{Ca}$ ) and Table 4.19 ( $^{26}\text{Al}$ ), respectively. Briefly, in the case of  $^{41}\text{Ca}$ , the total uncertainty averages at 6.0%, with the relative contributions (on average) from the activity determination (78%), the decay constant (9%), the proton flux (=8%), and from the number of atoms (=5%). The average uncertainty associated with the cross-section values for  $^{26}\text{Al}$  yields 7.3%. In the same way, the relative contributions are from the activity determination (=76%), the decay constant (18%), the proton flux (=5%), and from the number of atoms (=2%).

**Table 4.18:** Overview of the measured production cross-section of the  $^{\text{nat}}\text{V}(\text{p}, \text{x})^{41}\text{Ca}$  reaction for the different vanadium specimens, including experiment-specific details.

	VVUH271	VVUL451	VVUL411	VVUL333	VVUL291	VVUL171	VVSN083
Energy (MeV)	$111 \pm 1.3$	$129 \pm 1.4$	$134.9 \pm 1.3$	$145 \pm 1.2$	$150.2 \pm 1.2$	$164.5 \pm 1.0$	$954 \pm 1.6$
$^{41}\text{Ca}/^{40}\text{Ca}$ ( $\times 10^{-10}$ )	$1.88 \pm 0.07$	$4.10 \pm 0.14$	$4.82 \pm 0.17$	$5.28 \pm 0.18$	$5.37 \pm 0.19$	$5.75 \pm 0.20$	$84 \pm 6.1$
A ( $\times 10^{-3}$ ) (Bq)	$1.21 \pm 0.05$	$2.65 \pm 0.09$	$3.11 \pm 0.11$	$3.41 \pm 0.12$	$3.46 \pm 0.12$	$3.71 \pm 0.13$	$0.54 \pm 0.04$
Measurement date	October 01, 2021						
$N_{^{40}\text{Ca}}$ (atoms)	$(2.92 \pm 0.04) \times 10^{19}$						
$\lambda_{^{41}\text{Ca}}$ ( $\text{s}^{-1}$ )	$(2.21 \pm 0.03) \times 10^{-13}$						
Cross-section (mb)	$2.89 \pm 0.17$	$4.29 \pm 0.24$	$5.04 \pm 0.27$	$5.31 \pm 0.30$	$5.34 \pm 0.30$	$5.52 \pm 0.31$	$10.70 \pm 0.91$
Overall uncertainty (%)	5.8	5.6	5.4	5.6	5.6	5.6	8.6

**Table 4.19:** Overview of the measured production cross-section of the  $^{\text{nat}}\text{V}(\text{p}, \text{x})^{26}\text{Al}$  reaction for the different vanadium specimens, including experiment-specific details.

	VVUH271	VVUL451	VVUL411	VVUL333	VVUL291	VVUL171	VVSN083
Energy (MeV)	$111 \pm 1.3$	$129 \pm 1.4$	$134.9 \pm 1.3$	$145 \pm 1.2$	$150.2 \pm 1.2$	$164.5 \pm 1.0$	$954 \pm 1.6$
$^{27}\text{Al}/^{26}\text{Al}$ ( $\times 10^{-10}$ )	$6.81 \pm 0.42$	$7.75 \pm 0.36$	$7.95 \pm 0.35$	$4.47 \pm 0.24$	$7.75 \pm 0.37$	$7.58 \pm 0.35$	$11.2 \pm 0.5$
A ( $\times 10^{-5}$ ) (Bq)	$0.93 \pm 0.07$	$1.06 \pm 0.06$	$1.09 \pm 0.06$	$0.61 \pm 0.04$	$1.06 \pm 0.06$	$1.04 \pm 0.06$	$1.53 \pm 0.09$
Measurement date	January 10, 2020						
$N_{^{27}\text{Al}}$ (atoms)	$(4.52 \pm 0.07) \times 10^{19}$						
$\lambda_{^{26}\text{Al}}$ ( $\text{s}^{-1}$ )	$(3.06 \pm 0.10) \times 10^{-13}$						
Cross-section ( $\mu\text{b}$ )	$160 \pm 13$	$124 \pm 9$	$127 \pm 9$	$69 \pm 5$	$118 \pm 8$	$111 \pm 8$	$2178 \pm 154$
Overall uncertainty (%)	8.2	7.1	7.3	7.5	7.2	7.0	7.1



## 4.4 Half-Life determination of $^{32}\text{Si}$

### 4.4.1 Determination of the activity (concentration): Standardization using LSC

With respect to the half-life determination, the activity will be determined by the “Physikalisch Technische Bundesanstalt” (PTB, Braunschweig, Germany) and the “Institute of Radiophysique” (IRA, Lausanne, Switzerland). During the collaboration, we contributed with stability studies for the LSC samples in order to prove that the chosen matrix is suitable for these. The physical and chemical stability of samples in scintillation cocktail is a major concern. The  $^{32}\text{Si}$  samples used for the half-life determination should be stable over the period several months in order to perform measurements at multiple metrological institutes with good counting statistics. For this reason, preliminary studies were conducted at PSI to assure the stability of the samples. The measurements were carried out on regular schedule between July 10, 2020, and December 10, 2020 (153 days). During that period the decay-corrected count-rate and the quench parameter tSIE were measured. Figure 4.43(a) shows the data for the entire measurement period. During that period the self-adjustment function of the device (“IPA”) was used to monitor the device’s performance. From our preparatory studies, it is apparent, that the different matrices achieve reproducible results within the first ten days of observation (Fig. 4.43(b)) as the measured activity concentration is within the expected value of  $14.40 \pm 0.07$  kBq (reference date: April 15, 2020, 12:00 PM CET). However, some first differences are recognizable, especially for the sample in 0.5M HCl/0.01M HF. Here, a continuous decrease of the activity concentration was observed, while the initial activity concentration also yielded the lowest activity concentration. After 20 days, subsequent measurements show generally an overall decreasing trend of the count-rate, leading to apparent lower activity concentrations. Here, the stability of the samples with “0.5M HCl” and “H<sub>2</sub>O” as aqueous phase show the smallest deviation from the expected mean value.

Upon a recommendation from our colleagues from IRA (Dr Youcef Nadjadi) we were shaking the samples after 120 days. As a result, we were able to obtain for the “H<sub>2</sub>O” and “0.5M HCl” samples the initial activity concentration with only a very slight deviation of 0.05 kBq. We assumed that phase segregation due to micro micellar instabilities causes this effect, while the recovery of the initial activity concentration, due to shaking, restores the initial sample’s homogeneity. After all, as this behavior is not observed for the sample containing 0.5M/0.01M HF, it demonstrates that the addition of HF drastically interferes with the sample’s stability and should be clearly avoided. The need to add HF as a stabilizing agent to maintain the speciation of silicon ( $\text{SiF}_6^{2-}$ ), is therefore not necessary, since the “H<sub>2</sub>O” and “0.5M HCl” yielded the overall best results.

Furthermore, from our results, we can confirm that problems due to adsorption of  $^{32}\text{Si}$  on the walls of the counting vials was not observed (cf. 0.1M HCl: 24h, and 0.1M HCl: 48h, respectively). Although the LSC vials’ pre-saturation with a carrier solution has been reported to be a procedure in liquid scintillation radionuclide standardization (e.g.,  $^{63}\text{Ni}$  (100  $\mu\text{g/g}$   $^{\text{nat}}\text{NiCl}_2$  in 0.1M HCl) , [209]), the  $^{32}\text{Si}$  sample stability was obviously not affected. Apart from the count-rate, a very important parameter to follow is the tSIE. As presented in Fig. 4.44(a), a continuous decrease in the tSIE is

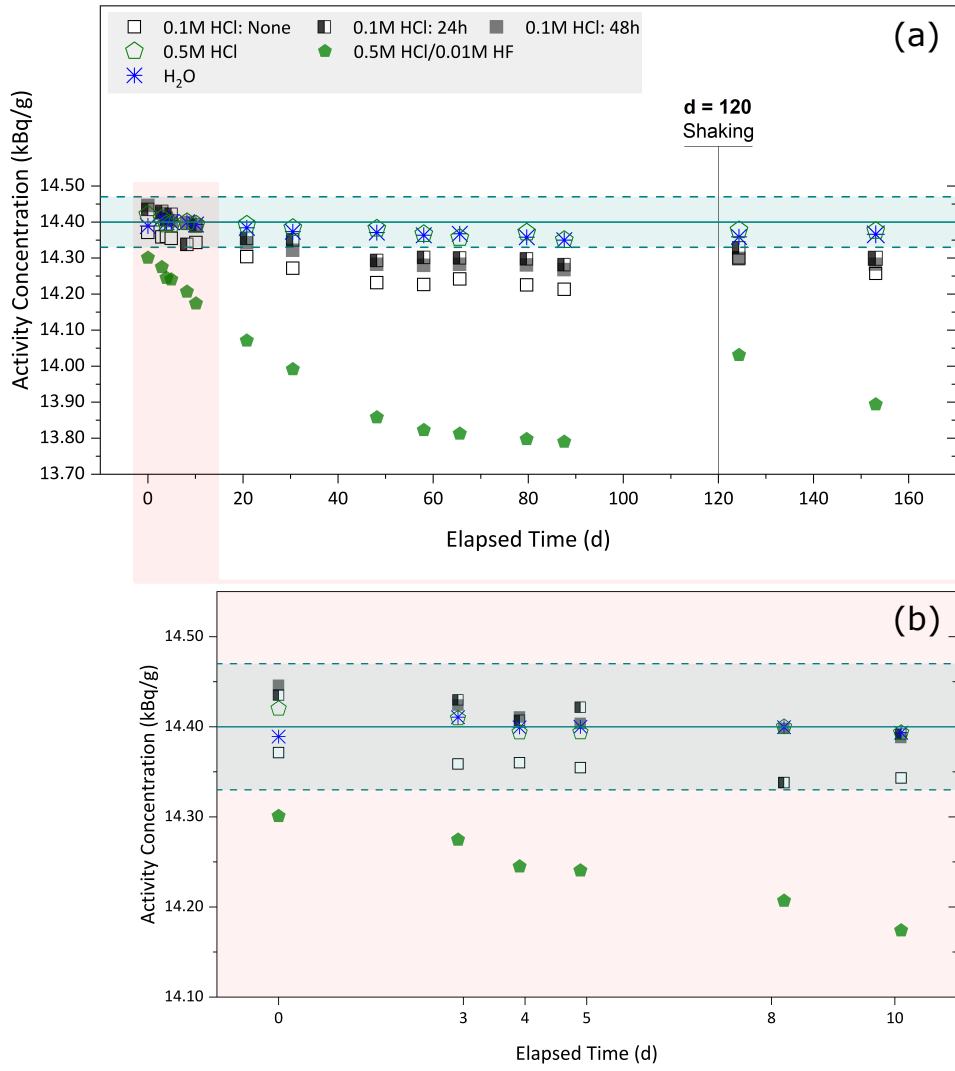


**Fig. 4.43:** (a) Tracing the activity concentration as a function of time, for different sample matrices to study their long-term behavior. (b) Detail of the first ten days of measurement.

visible with the continuation of the experiment which suggests that some degradation of the samples with respect to e.g., destruction of the cocktail or coloring of the solution did occur. But if one focuses, again on the first ten days (Fig. 4.44(b)), the tSIE only slightly changes, which is considered as a sufficient amount of time to perform a reliable standardization of  $^{32}\text{Si}$ , and thus to determine the activity concentration. Consequently, decay-measurements using LSC would be excluded, as this would require a sample stability for several years ( $\approx 4\text{--}5\text{ y}$ ). The results presented in Fig. 4.44(b) are also summarized in Table 4.20, that shows the standard deviation (STD) of the tSIE is only  $\pm 4$  and  $\pm 5$ , respectively. Furthermore, when comparing the counting efficiencies of the counter concerning  $^3\text{H}$  and  $^{14}\text{C}$ , which were automatically determined during the self-adjustment as a quality assurance measure, no similar efficiency decrease was observed for these two nuclides during the time window of the stability study. This suggested that the observed decrease in tSIE is simply caused by the sample's chemical composition, but can be seen as a stable matrix, due to the reliable measurements within the first 10 to 14 days.

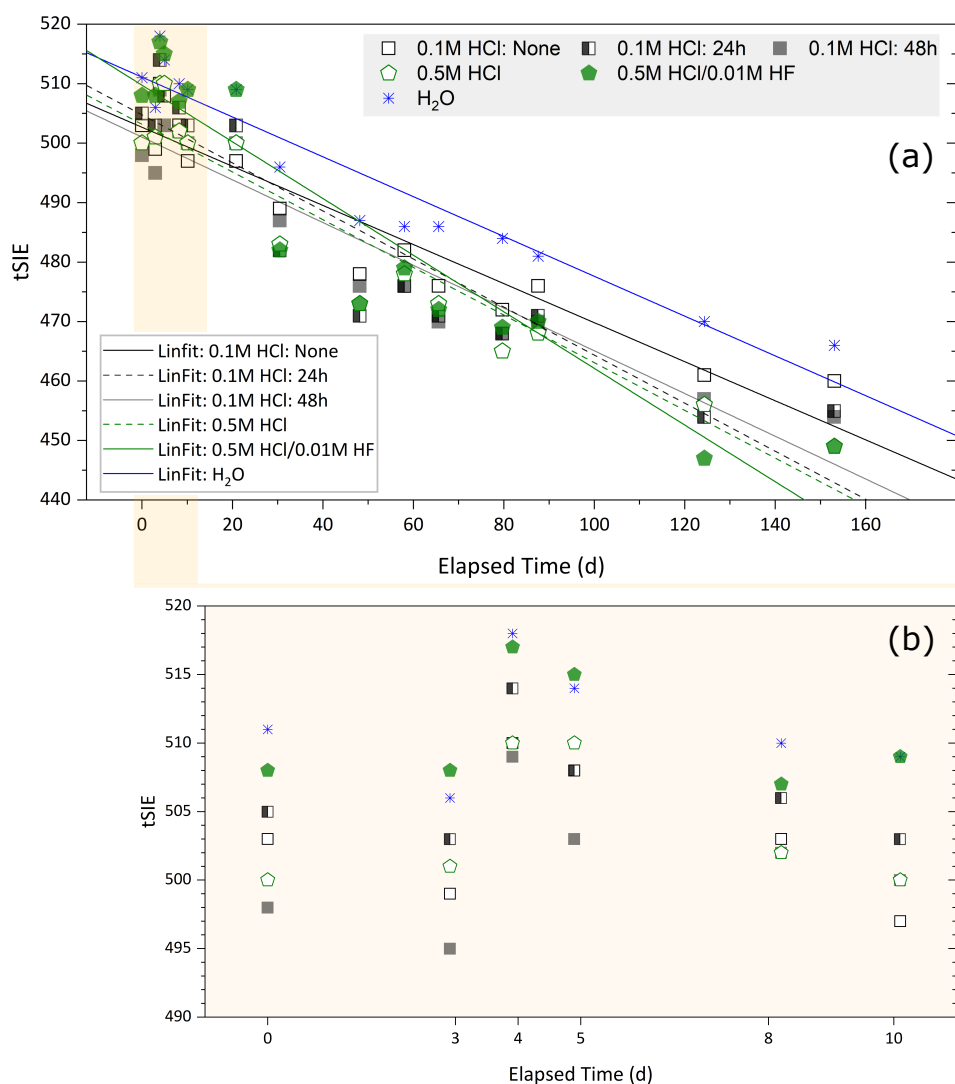


**Fig. 4.44:** (a) Overview of the time-dependent change of the quench indicating parameter (tSIE), and (b) highlighting the first ten days of measurement, which do not show a significant change in the tSIE and confirm the sample's stability.

**Table 4.20:** Overview of the determined tSIE for the different matrices using the Tri-Carb<sup>®</sup> 2250CA.

Day	0.1M HCl: None	0.1M HCl: 24h	0.1M HCl: 48h	H <sub>2</sub> O	0.5M HCl	0.5M HCl/0.01M HF
0	503	505	498	511	500	508
3	499	510	503	495	506	501
4	510	514	309	518	510	517
5	508	508	503	514	510	515
8	503	506	502	510	502	507
10	497	503	500	509	500	509
Average	503	507	501	511	504	511
STD	5	4	4	4	4	4

Finally, as presented in Fig. 4.45 the arithmetic means of the activity concentration for the different samples, observed over the full duration of the measurement period ( $\approx 160$  days), yielded the most reproducible results for the “H<sub>2</sub>O” and “0.5M HCl” samples. This is also expressed by lowest overall standard deviation of only  $\approx 0.14\%$ . In contrast, the standard uncertainty for the sample 0.5M HCl/0.01M HF is about 1.4%, while – more importantly – underestimating the apparent  $^{32}\text{Si}$  activity concentration by  $\approx 2.6\%$ . Furthermore, samples treated with 0.1M HCl also suffer from a sample instability. Here, the pre-treatment of the walls of the LSC vials with saturated Si-solution shows only a slight improvement, but can be ruled out as an important factor, to achieve a long-term stability of the samples. Generally, these experimental observations agree well with previous works (e.g., [169]) in which the practice of using H<sub>2</sub>O top-ups to increase the aqueous fractions of samples show an improved sample stability; even though this results in a loss of detection efficiency. Finally, within the SINCHRON collaboration, PTB has decided to work with H<sub>2</sub>O top-ups, while IRA decided to work with the actual sample matrix (0.5M HCl) to top-up the samples. Nonetheless, with our contribution we could confirm that both methods will yield comparable results which should not be falsified due to sample instabilities.

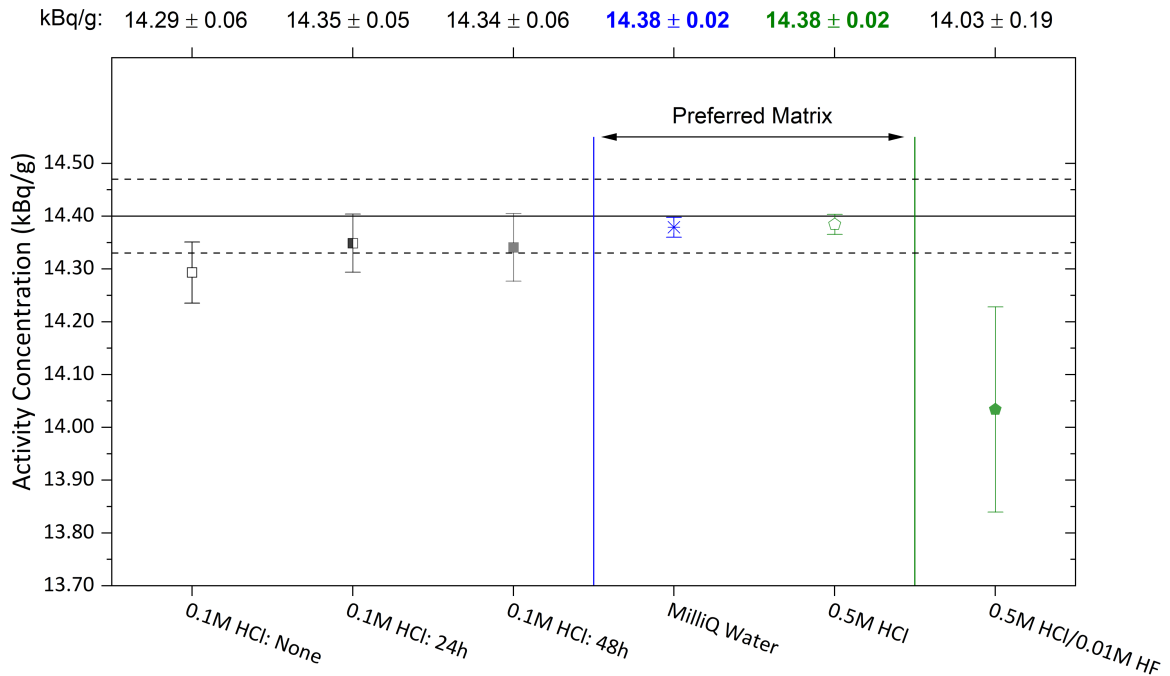


**Fig. 4.45:** Overview of the arithmetic mean for the different matrices. The mean is based on fifteen independent measurements, whereby the results for H<sub>2</sub>O and 0.5M HCl are emphasized.

For the determination of the activity concentration of the prospective  $^{32}\text{Si}$  master solution, we received a preliminary result from PTB which showed a very good agreement with the value, previously determined. The reported activity concentration from PTB was 108.87 kBq/g (TDCR), and 108.89 kBq/g (CNET), respectively, stating an overall uncertainty of  $\approx 0.4\%$ . The measurements were performed, measuring  $^{32}\text{Si}/^{32}\text{P}$  in secular equilibrium and the activity was projected to a reference date (July 20, 2020). Notably, at this stage (August 10, 2022), validated data from IRA were not yet available, but are expected to be communicated in the next few weeks.

#### 4.4.2 Determination of the number of atoms: ICP-MS and AMS measurements

To the time of the thesis submission, only measurements from the Spiez Laboratory were available, allowing to determine the number of  $^{32}\text{Si}$  atoms in the prospective  $^{32}\text{Si}$  master solution. Furthermore, for ICP-MS measurements, model solutions with less activity concentration ( $A(^{32}\text{Si}) = 47.6 \text{ kBq/g}$ ) were sent to the PSI Hot Laboratory and to the National Physics Laboratory (NPL), in order to facilitate the method development. In contrast, for measurements at the Spiez Laboratory (SL), the prospective master solution with an activity concentration of  $108.88 \text{ kBq/g}$  was used. The measurements at the SL were performed with a Thermo Scientific™ Element XR™ SF-ICP-MS (Thermo Fisher Scientific, Waltham, U.S.A.) and two values can be reported here. The sample preparation was directly performed at the SL and included a gravimetric dilution of an aliquot of the  $^{32}\text{Si}$  solution. Here, two dilutions were required, to account for measurements of (i) the isotopic ratio  $^{32}\text{Si}/^{29}\text{Si}$  ( $D_f = 79.20$ ), and (ii) to measure the absolute concentration of  $^{29}\text{Si}$  in the sample ( $D_f = 20.33$ ). Here, using high-quality Ar (5.0) and  $\text{ND}_2$  (6.0), the signal from the resulting mass isobar ( $^{32}\text{S}$ ) was lowered by a factor of  $\approx 10^2$ , compared to former test measurements using Ar (4.8) and  $\text{N}_2$  (4.5). In combination with the sample introduction (Apex combined with an actively cooled membrane (ACM), [210]) the  $^{32}\text{S}$  signal was finally reduced by a factor of  $\approx 10^4$ , which allowed to observe a  $^{32}\text{Si}$  peak (Fig. 4.46). Although it was measured in the “high-resolution” mode, the masses of  $^{32}\text{S}$  (31.9716 amu) and  $^{32}\text{Si}$  (31.9737 amu) are very challenging to resolve since the two peaks cannot be completely separated. Therefore, an integration width of 20% was used (Fig. 4.46). If this width is used for integration, the  $^{32}\text{S}$  interference is negligible for the different dilutions and ranges between  $\approx 0.6\%$  to  $\approx 1.6\%$ .

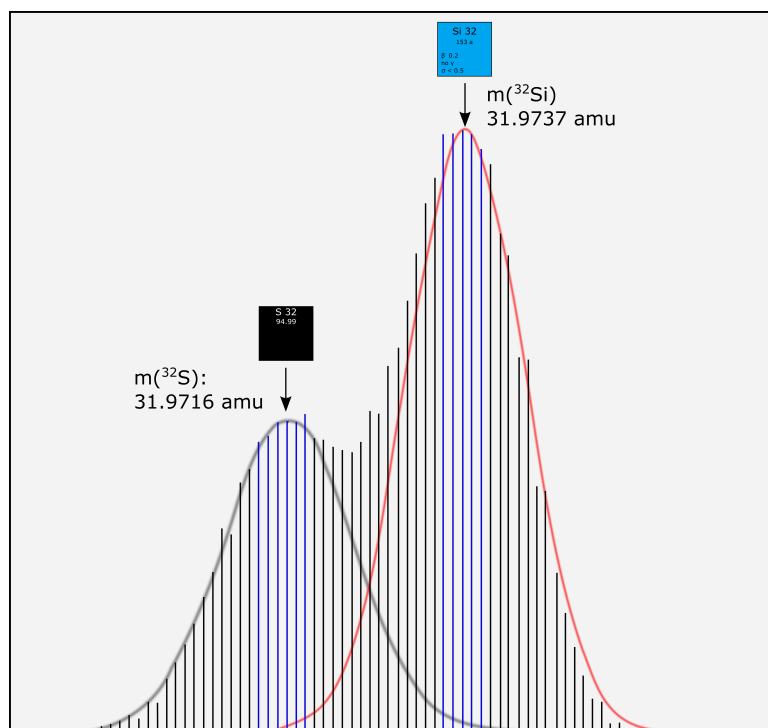


**Fig. 4.46:** Qualitative example of an ICP-MS measurement with the Element XR™ at SL. Two peaks, showing at the lower mass (31.9716) the  $^{32}\text{S}$  signal and at the higher mass (31.9737) the  $^{32}\text{Si}$  signal, respectively. The integration width (=20%) is highlighted in blue. Please note, the graph is a 1:1 reproduction of the software’s output.

Concerning the AMS measurements, three sample sets have been delivered to ETHZ. Two sets (AMS-S1 and AMS-S2;  $^{32}\text{SiO}_2$ ) could be successfully used for the method development. Additionally, we prepared also test samples of  $\text{K}_2^{32}\text{SiF}_6$  (AMS-K1) as such samples have been previously used for  $^{32}\text{Si}$  AMS measurements [211] at the Laboratory of Ion Beam Physics (LIP, ETHZ). Concerning AMS measurements, these measurements are also challenging, as they must remove the mass isobar ( $^{32}\text{S}$ ), too. Within the SINCHRON-collaboration, the development of particular setups (e.g., passive absorber) to effectively separate  $^{32}\text{S}$  from  $^{32}\text{Si}$  is ongoing [212]. As a result of this work, a preliminary identification of  $^{32}\text{Si}$  was achieved, while using Ar as absorber gas (Fig. 4.47). Therefore, the provided dilution series (AMS-S1) could be successfully measured (Fig. 4.48). But, in order to provide an absolute number of  $^{32}\text{Si}$  atoms, the counting efficiency is yet to be determined, which is still the major challenge concerning the AMS measurements and currently in the focus of the ongoing setup optimization.

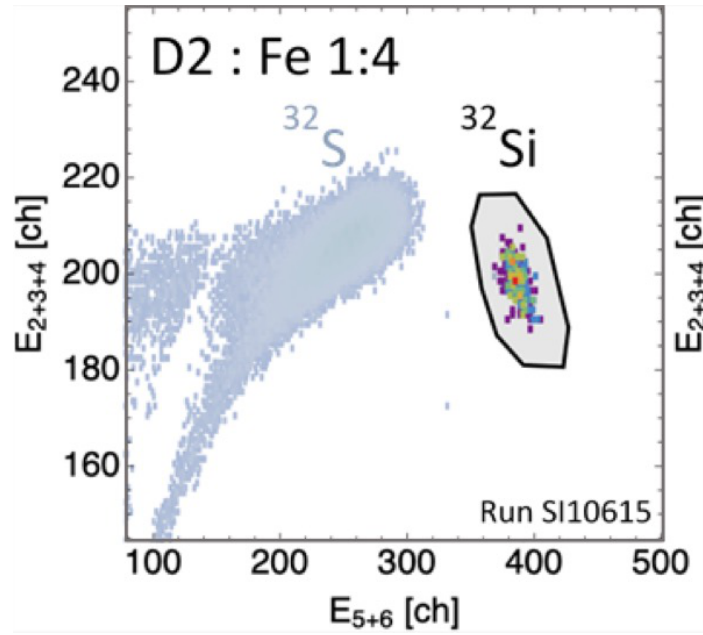


**Fig. 4.47:** Example of the spatial distribution between  $^{32}\text{S}$  and  $^{32}\text{Si}$ , showing the successful separation of the two isotopes (taken from [213]).

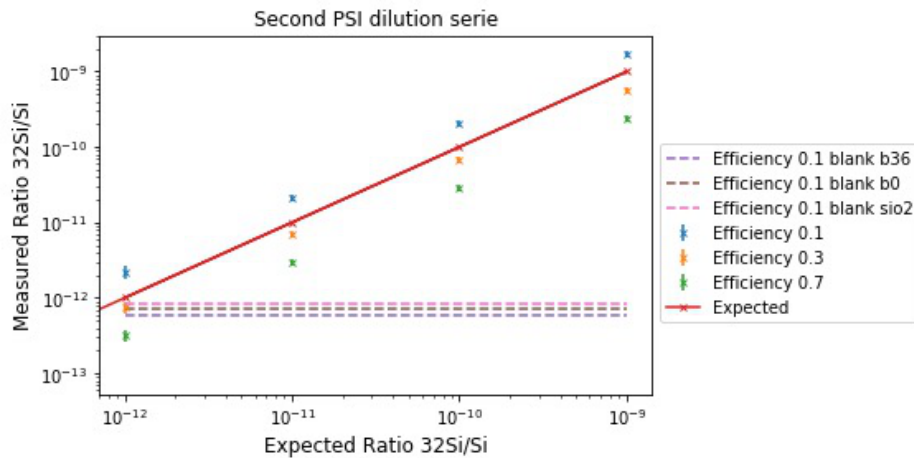


**Fig. 4.48:** Results from AMS-S1 (14.40 kBq  $^{32}\text{Si}$  solution). The figure was kindly provided for use by M. Schlomberg (ETHZ, LIP).

#### 4.4.3 Combining the number of atoms and the activity (concentration)

$$T_{1/2}({}^{32}\text{Si}) = \text{N}({}^{32}\text{Si}) \times \ln(2) / \text{A}({}^{32}\text{Si})$$

Due to the efforts of the SINCHRON collaboration partners, we were able to provide a first, preliminary half-life for  ${}^{32}\text{Si}$ , with a satisfying uncertainty. The value is based on the direct method, thus combining the results of the determination of the number of atoms (Spiez Laboratory, Spiez, Switzerland) with the activity (Physikalisch-Technische Bundesanstalt, Brunswick, Germany). Table 4.21 and Table 4.22 provide the results used for the two calculations, that resulted in two half-life values.

**Table 4.21:** Determined number of atoms of  ${}^{32}\text{Si}$ . The data was kindly provided by Dr Stefan Röllin (Scientist, Spiez Laboratory, Switzerland).

Measurement No.	Measurement date	ppb (ng/g)	Relative Uncertainty (%)	Standard Deviation (ng/g)	$\text{N}({}^{32}\text{Si}) \times 10^{14}$
1	March 04, 2022	33.2	4	1.33	$(6.25 \pm 0.25)$
2	March 04, 2022	32.5	4	1.30	$(6.12 \pm 0.24)$

**Table 4.22:** Determined activity concentration of  ${}^{32}\text{Si}$ . The data was kindly provided by Dr Karsten Kossert (Scientist, PTB, Germany).

Reference date	Method	Activity concentration (kBq/g)	Relative Uncertainty (%)
July 20, 2021; 12:00:00 CET	CIEMAT/NIST	108.87	≈ 0.4
July 20, 2021; 12:00:00 CET	TDCR	108.89	
		108.88 ± 0.44	

According to the equation for the direct method, the half-life was then determined to be  $T_{1/2}({}^{32}\text{Si}) = 126 \pm 5$  y (number of atoms from Measurement No. 1) and  $T_{1/2}({}^{32}\text{Si}) = 123 \pm 5$  y (number of atoms from Measurement No. 2), respectively. Here, we await further data from the collaboration partners, and therefore consider the half-life determination still as ongoing. Thus, to have a sound base enabling us to provide a new recommended half-life for  ${}^{32}\text{Si}$ , further complementary measurements are essential.

#### 4.4.4 Following the decay of $^{32}\text{Si}$

When following the decay of  $^{32}\text{Si}$ , the decrease in the net count rates of the device is followed. Basically, by following the decrease in the net count rates the slope of the fit function is derived, which provides the specific decay constant ( $\lambda$ ) of the nuclide. Finally, the half-life is derived from the following relation (see section 1.1.3, Eq. 1–2):

$$T_{1/2}(^{32}\text{Si}) = \ln(2) / \lambda$$

With respect to the SINCHRON collaboration, both PTB and IRA plan to also measure the decay of  $^{32}\text{Si}$ . However, here via plastic scintillation. For this reason, PTB provided us with four tailor-made vials: two glass, and two plastic scintillation vials. The targeted activity was requested to be about 5 kBq (of  $^{32}\text{Si}$ ). An example of the plastic scintillator vials is shown in Fig. 4.49.



**Fig. 4.49:** Plastic scintillator vials illuminated by UV light to stimulate the emission of scintillation light (taken from [214]).

Using the  $^{32}\text{Si}$  solution with an activity concentration of 108.88 kBq/g to reach 5 kBq, around 50  $\mu\text{L}$  were precisely deposited into the vial. The samples will be then used for continuous measurements using a dedicated TDCR setup. Further, PTB also plans to follow the  $^{32}\text{Si}$  decay using an Ionization Chamber (IC). Herefor,  $\approx 20$  MBq of  $^{32}\text{Si}$  will be needed, while further details (e.g., sample geometry, sample holder) will be finalized during 2022. For measurements at IRA, a dedicated measurement system is under construction. The plastic scintillator is different for this setup (Fig. 4.50). But also here, PSI will provide the activity requested by IRA, which will be then also deposited on the plastic scintillator. Details will be addressed once the IRA-setup is finalized. As reference source, either  $^{36}\text{Cl}$  ( $T_{1/2} = (3.01 \pm 0.02) \times 10^5$  y, [14]) or  $^{87}\text{Rb}$  ( $T_{1/2} = (4.97 \pm 0.03) \times 10^{10}$  y, [14]) are considered, which are quasi-stable and will be used for monitoring the device's stability.

For the sample preparation, IRA will follow the same approach as for the samples prepared for PTB. Here, the  $^{32}\text{Si}$  solution (in 0.5M HCl) was mixed in a ratio (v/v) of 1 : 0.4 : 0.6 with an in-house prepared Ludox<sup>®</sup> and  $\text{La}(\text{NO}_3)_3$  solution, and freshly prepared 1M  $\text{NH}_4\text{OH}$  solution, respectively. This in-house developed procedure avoids activity loss upon the sample's complete evaporation, as dried sources are necessary for the plastic scintillators.

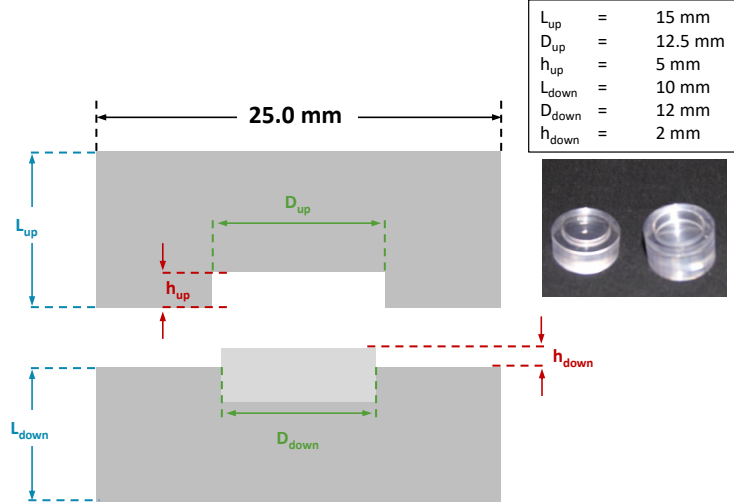


**Fig. 4.50:** Plastic scintillator geometries to be used for the decay measurements performed at IRA. The  $^{32}\text{Si}$  deposition is indicated. The layout and the measures were kindly provided by Dr Teresa Durán (IRA, Switzerland).



## 5 Conclusion and Outlook

The main goal of the thesis to provide ultra-pure  $^{32}\text{Si}$  samples, suitable for different measurements performed at various multinational metrological institutes was achieved. Thus, a  $T_{1/2}$  redetermination of the rare, cosmogenic silicon isotope is possible (within reach). In the frame of the SNSF-funded Sinergia project SINCHRON ( $^{32}\text{Si}$  - a new chronometer), the initially seen major challenge of the separation of radiosilicon was solved and the timely manufacturing of enough sample material of the required quality was achieved. The elaborated wet-chemical separation procedure was continuously optimized since during the separation procedure, other than the expected nuclides have been identified. Here, especially  $^{172}\text{Hf}$ ,  $^{172,173}\text{Lu}$ , and  $^{94}\text{Nb}$  were of concern. Consequently, a purification procedure was successfully developed and applied in which an extraction chromatographic resin ( $\text{LN}^{\text{®}}$ ) is used in combination with a chelating chromatographic resin ( $\text{Monophos}^{\text{®}}$ ). With respect to their high selectivity for Hf, Lu, and Nb, entirely purified  $^{32}\text{Si}$  fractions could be reproducibly obtained. The removal of the volatile radionuclides,  $^3\text{H}$ ,  $^{39,42}\text{Ar}$  by a multi-evaporation to complete dryness procedure was achieved. The final recovery in 0.1M HF turned out to favour a further purification of the  $^{32}\text{Si}$  fractions, by means of anion-exchange chromatography, which in turn allowed to fulfill two additional requirements. Hence, this step enabled us to pre-concentrate various  $^{32}\text{Si}$  fractions to yield activity concentrations of greater than 100 kBq/g. This translates into  $\approx 30$  ng/g (ppb)  $^{32}\text{Si}$  which has proven to be suitable for the ICP-MS measurements. Furthermore, using a combination of different HCl/HF molarities, sulfur was quantitatively removed from the sample solution while – if still detectable in the solution – providing a natural isotopic abundance of the sulfur. The activity concentration of  $^{32}\text{Si}$  during the proof-of-principle separation was rather low with  $14.40 \pm 0.07$  kBq, but sufficiently serving stability studies concerning LSC, and to produce first AMS samples. Finally, on December 23, 2020, a prospective master solution with an activity concentration of  $108.88 \pm 0.44$  kBq/g ( $A(^{32}\text{Si})_{\text{total}} \approx 2.19 \pm 0.09$  MBq) was produced, that has been fully chemically treated regarding the "SINCHRON-Separation" scheme. Based on the first successful ICP-MS measurements, provided by the Spiez Laboratory, the sample's number of atoms was determined, on average, with  $N(^{32}\text{Si}) = 33.2 \pm 1.3$  ng/g (ppb). With respect to the  $^{32}\text{Si}$  activity that was obtained by the presented separation scheme we obtained, up to now (August 10, 2022), around  $22 \pm 2$  MBq. The future work foresees the final purification (on the anion-exchange resin) of further  $^{32}\text{Si}$  fractions, which can be also performed on demand. After the successful preparation of the prospective  $^{32}\text{Si}$  master solution, individually requested aliquots were sent to the partners, and results were constantly reported and discussed during bi-annual meetings, either on- or offline. Therefore, a current overview is provided in Table 5.1.

**Table 5.1:** Overview of the progress on the different measurement techniques.

Measurement	Method	Institution	Result(s) provided	Status	Development
Number of Atoms	ICP-MS	Spiez Laboratory (SL)	✓	■	■
Number of Atoms	ICP-MS	Paul Scherrer Institut (PSI)	✗	■	■
Number of Atoms	ICP-MS	National Physical Laboratory (NPL)	✗	■	■
Number of Atoms	AMS	Australian National University (ANU)	✗	■	■
Number of Atoms	AMS	Laboratory of Ion Beam Physics (LIP)	✓	■	■
Activity Concentration	LSC	Physikalisch-Technische Bundesanstalt (PTB)	✓	■	■
Activity Concentration	LSC	Institute of Radiation Physics (IRA)	✓	■	■
Decay	PS/IC	Physikalisch-Technische Bundesanstalt (PTB)	$\approx$ in 2025	■	■
Decay	PS	Institute of Radiation Physics (IRA)	$\approx$ in 2025	■	■

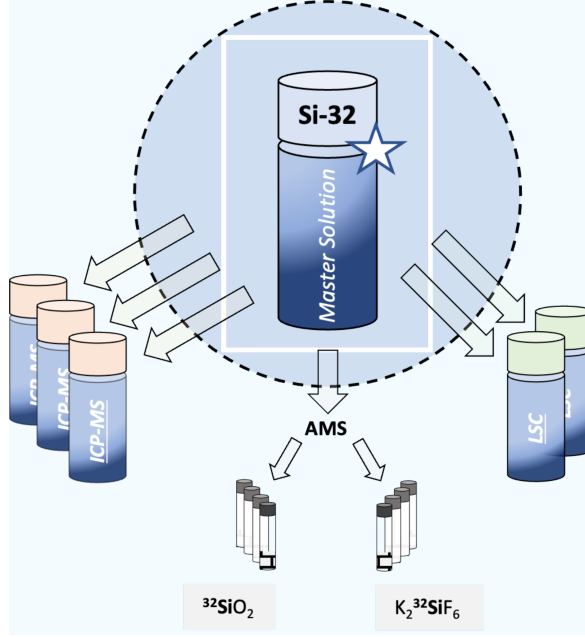


**Fig. 5.1:** Method of distributing aliquots of the "Master Solution" for independent measurements, while PSI ensures careful storage (tracing temperature and tracing mass of the solution).

Owing to the different measurement techniques, individual method developments were performed. Specifically, for, e.g., ICP-MS and AMS, the conditions are challenging. Here, primarily isobaric interference stemming from  $^{32}\text{S}$  must be overcome. In the case of ICP-MS, working with an Apex ACM seemed promising, as it allowed to suppress the  $^{32}\text{S}$  signal by around three orders of magnitude. For AMS, developments are ongoing, aiming for the determination of the absolute efficiency, but also removing the  $^{32}\text{S}$  ions. Here, utilizing a gas-filled magnet causes different mean trajectories due to the different mean charge states and related energy loss of the isobars. Consequently, most  $^{32}\text{S}$  ions are spatially separated and can be blocked, while  $^{32}\text{Si}$  can be measured in a gas ionization chamber.

About LSC measurements, both PTB and IRA presented their progresses, and, e.g., PTB could provide us with a verified ( $1\sigma$ ) activity concentration using both the TDCR and CNET method. Finally, the decay measurements are expected to provide first, reliable results after a measurement period of around three to four years. For these measurements the stability of the device (electronics) is vital and will be traced, using a reference nuclide.

For measurements with the IC, around ten Megabecquerel are requested from PTB which will be provided in due time, once the sample geometry is finalized. The combination of the independent and complementary measurements will finally allow us to provide a recommended half-life value with a relative standard uncertainty of less than five percent. Hence, looking at the history of  $^{32}\text{Si}$  half-life measurements, an urgent need for precise values is obvious.

With the presented work, we contributed to settling the  $^{32}\text{Si}$  half-life, since we were able to provide a first preliminary half-life value for  $^{32}\text{Si}$  (Fig. 5.2) which demonstrates the feasibility of the SINCHRON-project, and proofs the high-quality of the manufactured  $^{32}\text{Si}$ -sample, obtained from the developed separation scheme. Obviously, combining the results from the activity determination (LSC) and the number of atoms (ICP-MS), our value is not within the stated ranges, found in the literature (Fig. 5.2). However, our recommended half-life value is in very good agreement with previous values, from Hofmann et al. [77], and Chen et al. [79], respectively. An overview is presented in Table 5.2: However, the half-life determination in the project is still ongoing.

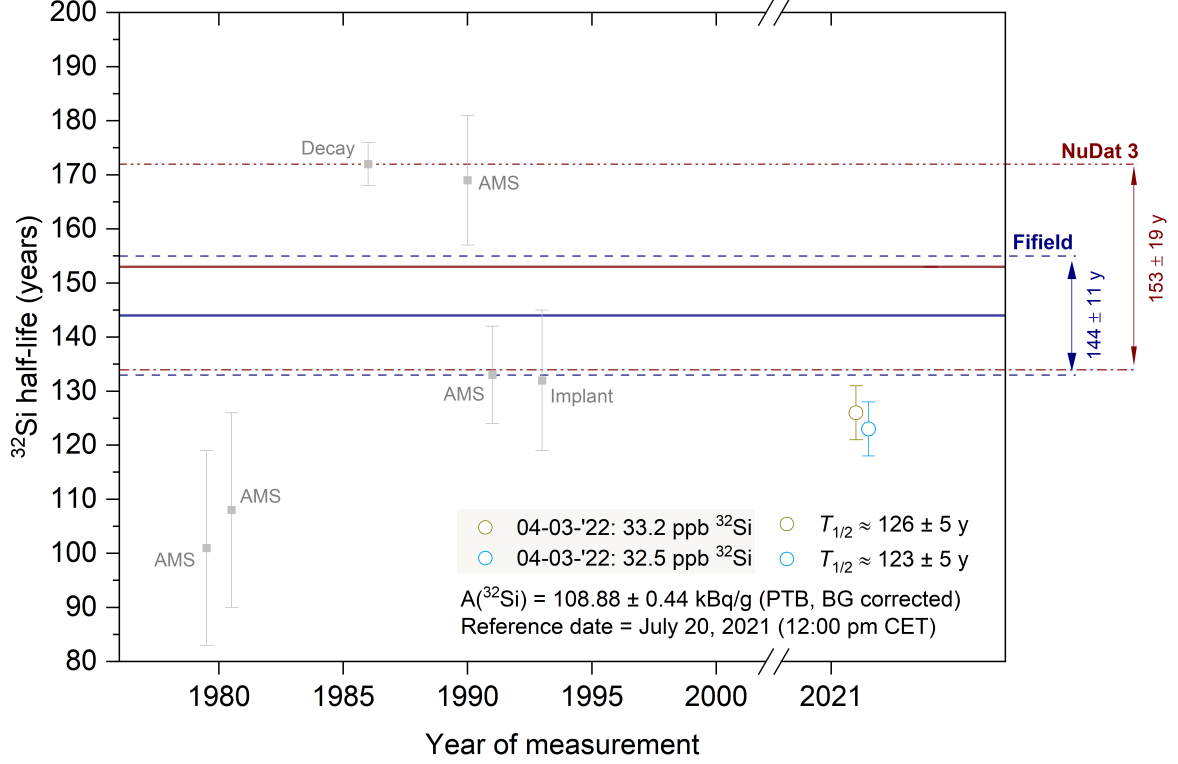


**Fig. 5.2:** Compilation of  $^{32}\text{Si}$  half-life determinations focused on the direct methods (format date: DD-MM-YY). Two references for the mean are shown (from Fifield et al. [12], and from the NuDat 3.0 database, which is based on the careful compilation provided by Quellet & Singh [73]).

**Table 5.2:** Overview of half-life values, similar to the preliminary value determined by the SINCHRON-collaboration.

Work	Year	$T_{1/2}$ (y)	Method	Analysis method	Remark
Hofmann et al.	1990	$133 \pm 9$	Direct	LSC & AMS	Published
Chen et al.	1993	$132 \pm 13$	Direct	Implantation & SSD	Published
SINCHRON-collaboration	2022	$126 \pm 5$	Direct	LSC & ICP-MS	Ongoing Measurements; preliminary value stated
		$123 \pm 5$			

In order to provide a reliable set of independent, complementary measurements, we will evaluate more data which are expected to be obtained during the next year. For the decay measurements, a period of at least four years should be considered, to be able to monitor a decrease in activity. Notably, during the project's period (2018-2022) advancements regarding the Argon Trap Trace Analysis (ArTTA) have been remarkable. Here, Ebser et al. [48] and Tong et al. [46, 49] pioneered to push the limits of the technical boundaries, and improved the  $^{39}\text{Ar}$  atom counts per hour from around 7 of up to 209; a factor of  $\approx 30$ . However, due to questionable half-life of  $^{39}\text{Ar}$  ( $T_{1/2} = 269 \pm 8$  y), achievements such as the first age determination of glacier ice [8] remain arguable. Therefore, with a precise knowledge of the  $^{32}\text{Si}$  half-life a further tool will be available, allowing to finally implement  $^{32}\text{Si}$  as a geochronometer in environmental sciences.

Besides, we demonstrated that vanadium as a target material gives also rise to further carrier-free, scientifically very interesting nuclides, such as  $^{44}\text{Ti}$ ,  $^{41}\text{Ca}$ , and  $^{26}\text{Al}$ . Our results for the experimental-based determination of the cross-sections to produce  $^{44}\text{Ti}$  utilizing the nuclear reaction  $^{nat}\text{V}(\text{p},\text{x})^{44}\text{Ti}$  allowed to provide a consistent data set for the excitation function for proton energies ranging from 111 to 1350 MeV.

Here, the availability of the relatively long-lived parent nuclide  $^{44}\text{Ti}$  enables the realization of a radionuclide generator that can provide  $^{44g}\text{Sc}$  off-site and averts the presence of isomeric  $^{44m}\text{Sc}$ . Considering the long half-life of  $^{44}\text{Ti}$  such a generator will provide  $^{44g}\text{Sc}$  over a long time span, even if the generator has to be renewed after a certain usage time. From a chemical perspective this concerns likely the resin, as long-term exposure to, e.g., high-energy gamma-rays ( $E_\gamma(^{44g}\text{Sc}) = 1157 \text{ keV}$ ) can damage the resin and thus affects its retention ability. Nonetheless, providing a  $^{44}\text{Ti}/^{44g}\text{Sc}$  generator can circumvent costly beamtimes at accelerator facilities and time-consuming target preparations. A further advantage of a generator is, that  $^{44g}\text{Sc}$  can be directly eluted and used, which in addition diminishes activity losses as no further transport, no radiochemical separation or no purification is needed. Therefore, the precise knowledge of the production cross sections to produce the mother nuclide is essential for the successful commercial implementation of a  $^{44}\text{Ti}/^{44g}\text{Sc}$  generator system which could serve as a reliable medical diagnosis tool in the future. As opposed to  $^{44}\text{Ti}$ , the determination of the cross-section for  $^{41}\text{Ca}$  and  $^{26}\text{Al}$  was of special interest, because no data was available for their production based on the nuclear reaction  $^{\text{nat}}\text{V}(\text{p},\text{x})^{41}\text{Ca}$  and  $^{\text{nat}}\text{V}(\text{p},\text{x})^{26}\text{Al}$ , respectively. Therefore, a dedicated radiochemical separation procedure was developed, too, (“DOGADO-Separation” scheme) that allowed to provide purified samples with a recovery yield of  $>99\%$  of the element of interest. Due to their decay mode and relatively long half-lives, both  $^{41}\text{Ca}$  ( $T_{1/2} = (9.94 \pm 0.15) \times 10^5 \text{ y}$ ) and  $^{26}\text{Al}$  ( $T_{1/2} = (7.17 \pm 0.24) \times 10^5 \text{ y}$ ) demand highly sensitive measurement methods. To accurately quantify them as spallation products, accelerator mass spectrometry (AMS) was chosen.

Concerning the results for the nuclear reaction  $^{\text{nat}}\text{V}(\text{p},\text{x})^{41}\text{Ca}$ , the experimental cross-section values show an excellent agreement with the predicted theoretical model. Generally, the shape of the curve is well reproduced, while the experimental values are only slightly lower (factor of  $\approx 1.5$ ). As a result, the data confirm both the accuracy and predictive power of the theoretical models, which means that the various mechanisms involved in the nuclear reactions, are well implemented into INCL++/ABLA07. With respect to  $^{26}\text{Al}$ , comparing the AMS results with the predicted excitation function, the results from the model calculations seem to slightly underestimate the cross-section values for lower proton energies ( $<200 \text{ MeV}$ ) and to overestimate it for higher energies, for which the sample VVSN083 ( $E_{\text{Proton}} = 954 \text{ MeV}$ ) can be compared to. Nonetheless, the experimental data confirm the predicted low reaction probability for  $^{26}\text{Al}$  production, regarding the nuclear reaction  $^{\text{nat}}\text{V}(\text{p},\text{x})$ . Overall, such experimental data are certainly vital in order to validate the theoretical models and to improve the predictions further.

All in all, vanadium as a target material has been studied extensively with a major focus on the isolation of the extremely rare, cosmogenic nuclide  $^{32}\text{Si}$  from the proton-irradiated matrix material. Consequently, the developments performed during this work allow the production of a sufficient amount  $^{32}\text{Si}$  in ultrapure quality in a stable matrix suitable for each of the envisaged measurements. However, the desired goal to establish  $^{32}\text{Si}$  as a nuclear dating tool can only be achieved if all measurement results are consistent and lead to a concordant value. Therefore, the SINCHRON-collaboration will continue their efforts, in order to provide a new, recommended half-life value for  $^{32}\text{Si}$ .

**S I N C H R O N**  
A NEW CHRONOMETER FOR NUCLEAR DATING

**Mario A. Veicht**  
**May 31, 2022**





## 6 Appendices

### 6.1 Liquid scintillation counting (LSC)

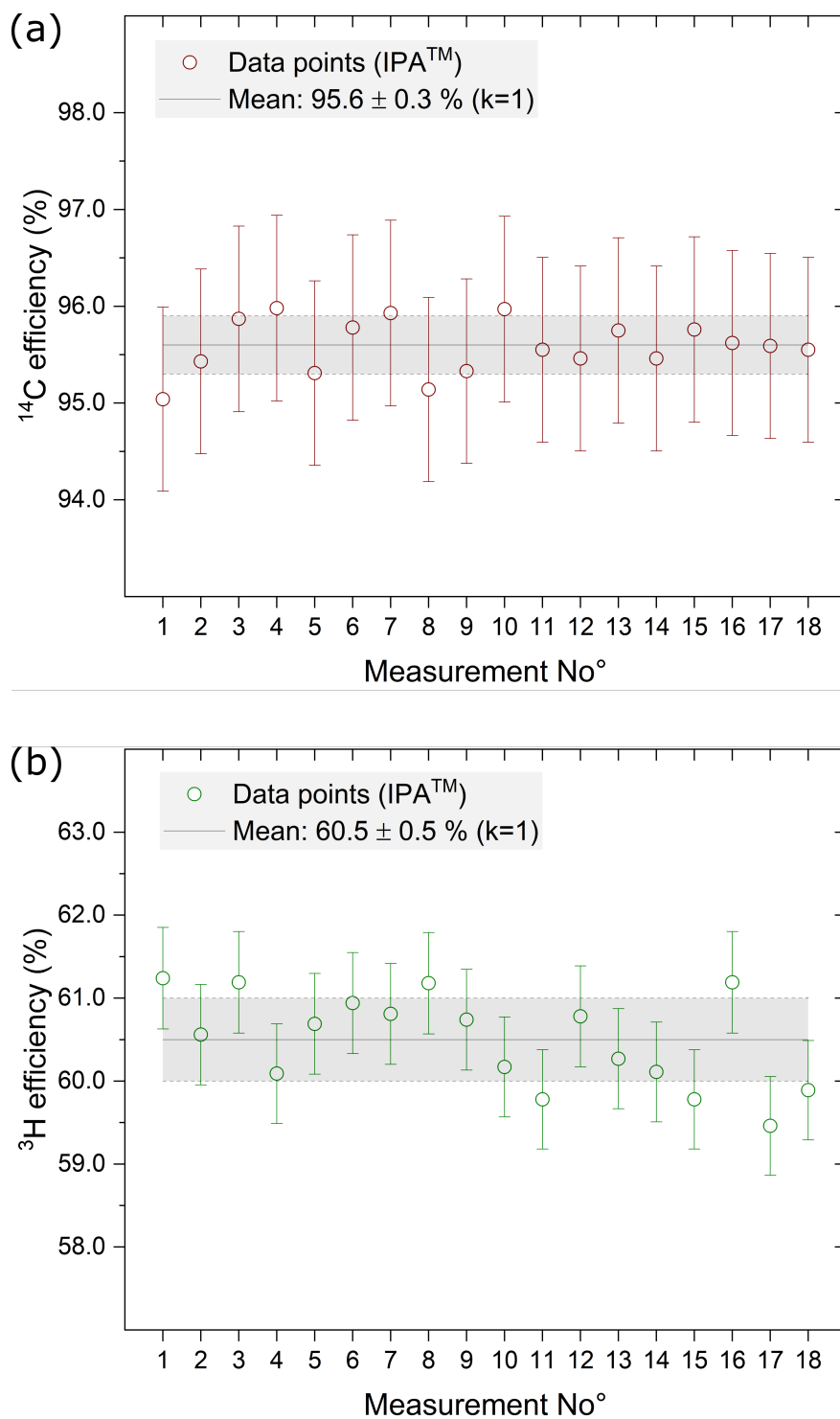


**Fig. 6.1:** Device-specific (a)  $^{14}\text{C}$  and (b)  $^3\text{H}$  efficiency determinations, used for monitoring the performance metrics of the Tri-Carb® 2250CA.

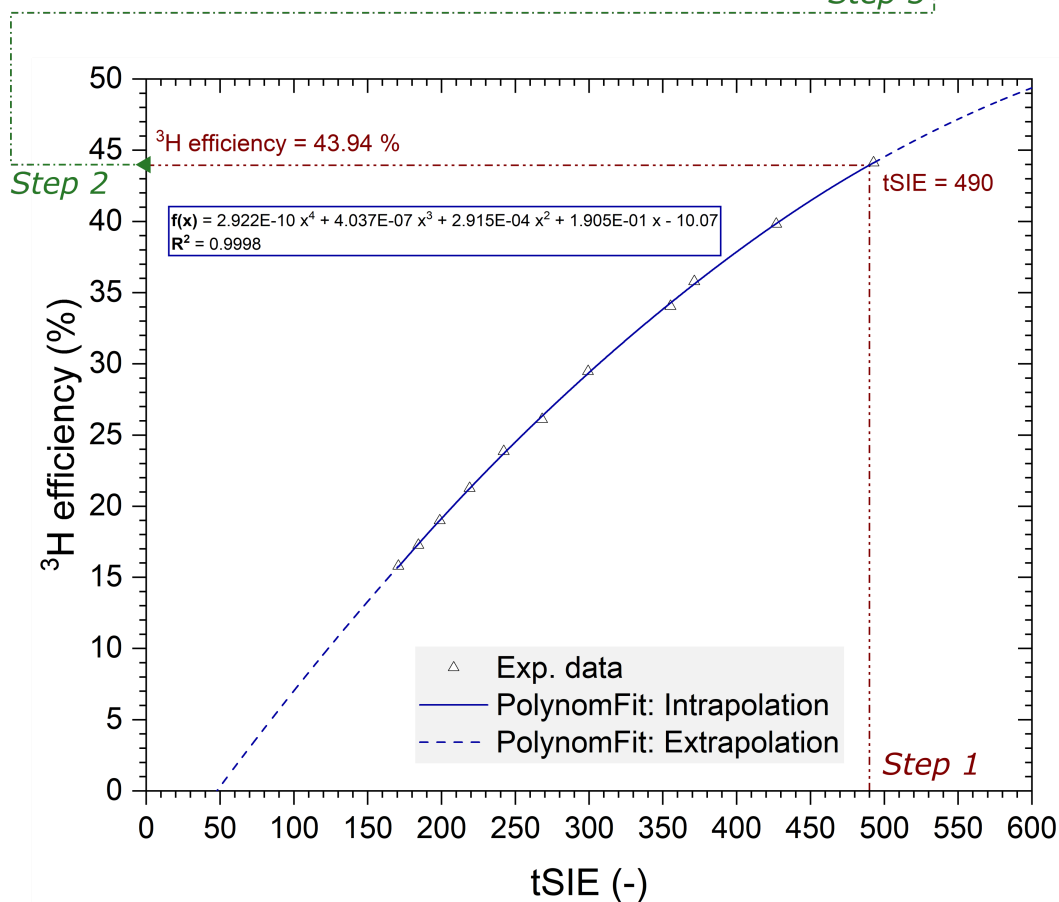
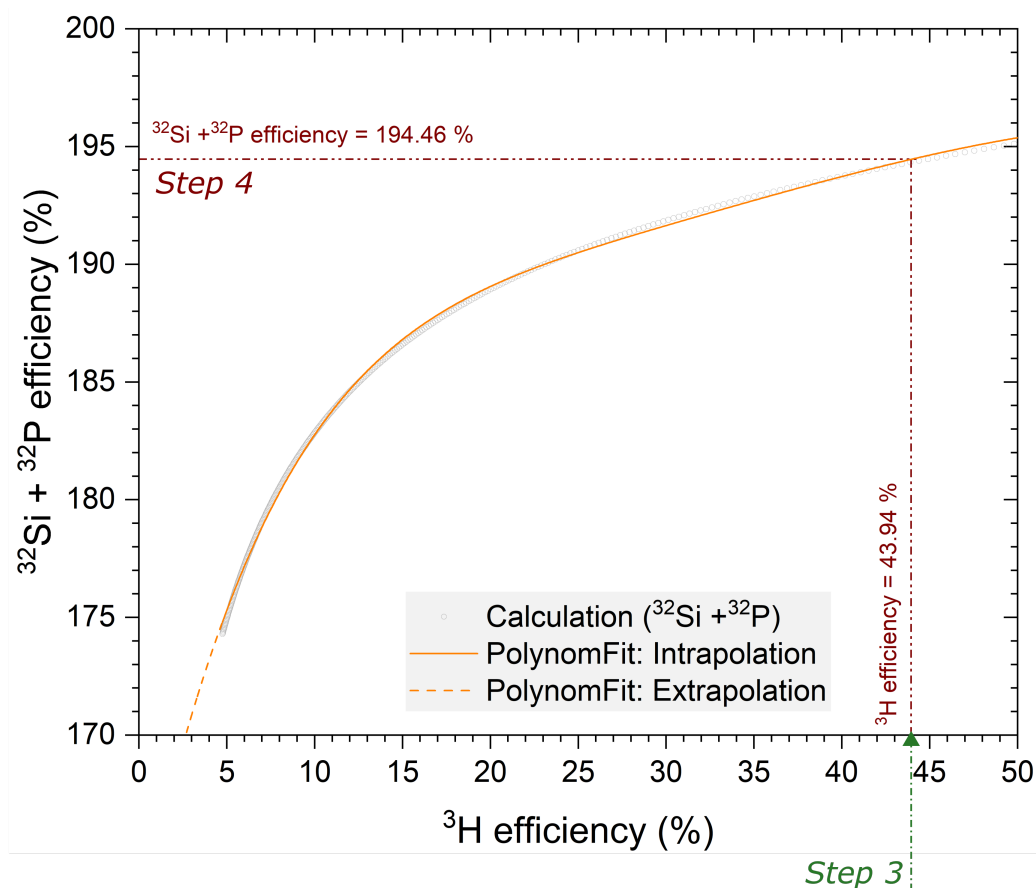


**Fig. 6.2:** Sequence of the in-house determination of the  $^{32}\text{Si}$  activity concentration, using the data thankfully provided by Dr Youcef Nedjadi (Scientist, IRA).

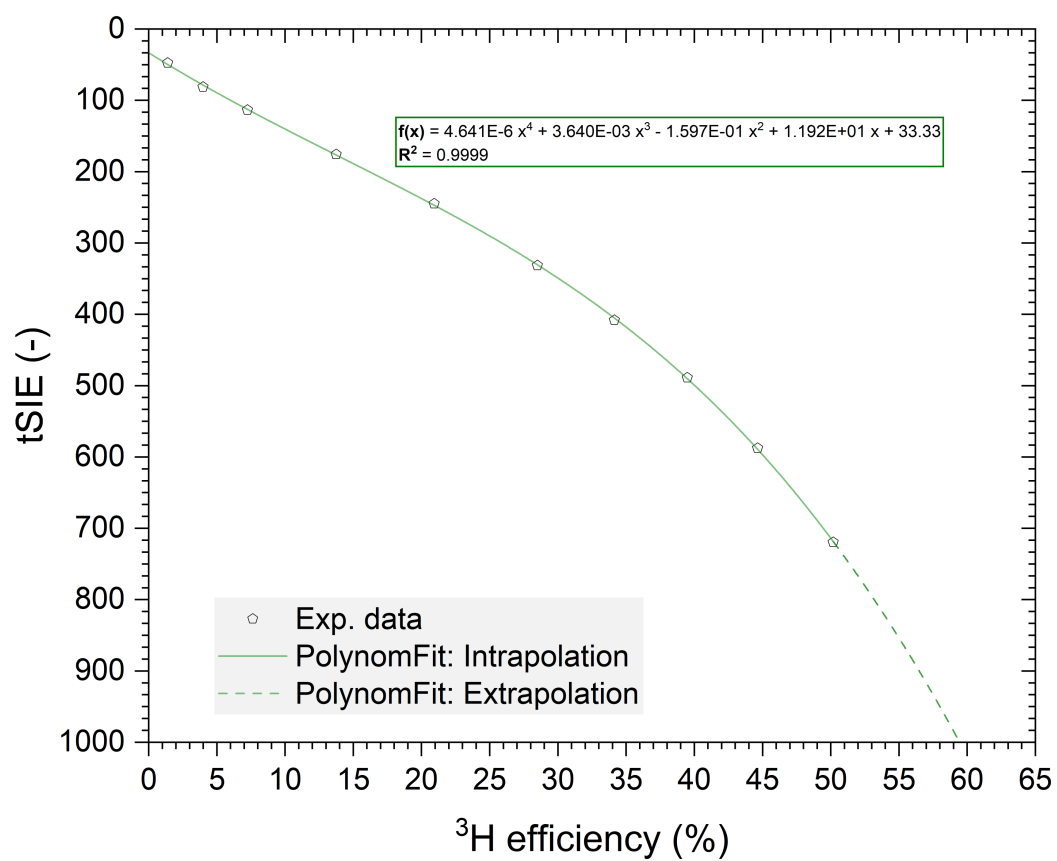


**Fig. 6.3:** Device-specific  $^3\text{H}$  efficiency curve for the Tri-Carb<sup>®</sup> 2250CA.

## 6.2 Uncertainties

**Table 6.2.1:** Compilation of the experimental cross section for the nuclear reaction:  $^{\text{nat}}\text{V}(\text{p}, \text{x})^{44}\text{Ti}$ , used for comparison. Former value ( $\sigma$ ) and adjusted value ( $\sigma^*$ ) are reported. Please note, the reported values were initially stated in mb, while we report them after the adjustment in  $\mu\text{b}$ .

Proton Energy (MeV)	$\sigma_{\text{calc,avg}}(\text{mb})$	$\Delta\sigma_{\text{calc,avg}}(\text{mb})$	$\sigma_{\text{calc,avg}}(\mu\text{b})$	$\Delta\sigma_{\text{calc,avg}}(\mu\text{b})$
Zaitseva et al. (1994); $T_{1/2} = 47.0 \text{ y}$ , $T_{1/2}^* = 59.1 \text{ y}$				
54.6	0.110	0.022	138.3	27.7
56.9	0.130	0.026	163.5	32.7
59.2	0.160	0.032	201.2	40.2
61.3	0.200	0.040	251.5	50.3
63.4	0.270	0.054	339.5	67.9
65.5	0.350	0.070	440.1	88.0
67.5	0.420	0.084	528.1	105.6
69.5	0.500	0.100	628.7	125.7
71.5	0.560	0.112	704.2	140.8
73.4	0.610	0.122	767.0	153.4
75.3	0.630	0.126	792.2	158.4
77.1	0.650	0.130	817.3	163.5
79.0	0.650	0.130	817.3	163.5
80.8	0.660	0.132	829.9	166.0
82.5	0.630	0.126	792.2	158.4
84.3	0.610	0.122	767.0	153.4
86.0	0.600	0.120	754.5	150.9
87.7	0.550	0.110	691.6	138.3
89.3	0.540	0.108	679.0	135.8
90.9	0.540	0.108	679.0	135.8
92.5	0.510	0.102	641.3	128.3
94.1	0.500	0.100	628.7	125.7
95.7	0.470	0.094	591.0	118.2
97.2	0.510	0.102	641.3	128.3
98.7	0.500	0.100	628.7	125.7
Protoschill (1997); $T_{1/2} = 47.9 \text{ y}$ , $T_{1/2}^* = 59.1 \text{ y}$				
119	0.546	0.103	673.7	127.1
129	0.581	0.072	716.8	88.8
134	0.667	0.089	823.0	109.8
139	0.614	0.086	757.6	106.1
154	0.666	0.090	821.7	111.0
159	0.627	0.073	773.6	90.1
164	0.717	0.099	884.6	122.1
171	0.673	0.083	830.4	102.4
277	0.613	0.077	756.3	95.0
1350	0.450	0.116	555.2	143.1

**Table 6.2.2:** Overview of the uncertainty sources in order to calculate the overall uncertainty budget (PLC = Point-Like Source).

		Sample						
		VVUH271	VVUL451	VVUL411	VVUL333	VVUL291	VVUL171	VVSN083
		Relative Uncertainties (%)						
Irradiated V-Samples	Uncertainty Source							
	Target Mass	1						
	<sup>44</sup> Ti Half-Life	0.51						
	Proton Fluence	1.97	1.66	1.64	1.59	1.57	1.52	2.17
	HPGe Measurements (67.9 keV)	0.48	1.68	1.59	1.57	1.56	1.55	14.69
	LEGe Measurements (67.9 keV, 78.3 keV)	0.48	2.22	1.71	2.16	2.21	2.24	4.38
	Standard Deviation	3.89	0.59	2.50	1.29	0.46	5.13	0.04
Counting Statistics		5.31	2.84	3.42	2.97	2.74	5.81	15.33
PLC	FEP Efficiency at 1157 keV	0.96						
	1157 keV $\gamma$ -emission probability	0.40						
	HPGe Measurements (1157 keV)	0.48						
	Balance (2mL, 5mL, PLC)	0.01						
Counting Statistics		1.15						
Overall uncertainty		5.77	3.48	3.95	3.55	3.36	6.11	15.52

**Table 6.2.3:** Specific relative uncertainties ( $\delta$ , in %) and their contribution to the total uncertainty budget ( $\delta_{total}$ , in %) for the  $^{41}\text{Ca}$  samples.

Sample		Activity determination ( <b>AMS</b> )	$\lambda_{^{41}\text{Ca}}$	Number of target atoms	Proton Flux	Final cross-section
<b>VVUH271</b>	$\delta$	5.2	1.5	1.0	2.0	5.8
	$\delta_{total}$	79.8	6.5	2.9	10.9	100
<b>VVUL451</b>	$\delta$	5.0	1.5	1.0	1.7	5.6
	$\delta_{total}$	81.3	7.1	3.1	8.5	100
<b>VVUL411</b>	$\delta$	5.0	1.5	1.0	1.6	5.4
	$\delta_{total}$	46.7	26.3	17.8	9.2	100
<b>VVUL333</b>	$\delta$	5.0	1.5	1.0	1.6	5.6
	$\delta_{total}$	81.8	7.1	3.2	7.9	100
<b>VVUL291</b>	$\delta$	5.0	1.5	1.0	1.6	5.6
	$\delta_{total}$	82.0	7.1	3.2	7.8	100
<b>VVUL171</b>	$\delta$	5.0	1.5	1.0	1.5	5.6
	$\delta_{total}$	82.4	7.2	3.2	7.3	100
<b>VVUL171</b>	$\delta$	8.1	1.5	1.0	2.2	8.6
	$\delta_{total}$	89.4	3.0	1.3	6.2	100

**Table 6.2.4:** Specific relative uncertainties ( $\delta$ , in %) and their contribution to the total uncertainty budget ( $\delta_{total}$ , in %) for the  $^{26}\text{Al}$  samples.

Sample		Activity determination ( <b>AMS</b> )	$\lambda_{^{26}\text{Al}}$	Number of target atoms	Proton Flux	Final cross-section
<b>VVUH271</b>	$\delta$	7.2	3.3	1.0	2.0	8.2
	$\delta_{total}$	77.5	15.5	1.4	5.5	100
<b>VVUL451</b>	$\delta$	6.0	3.3	1.0	1.7	7.1
	$\delta_{total}$	72.1	20.7	1.9	5.3	100
<b>VVUL411</b>	$\delta$	5.8	3.3	1.0	1.6	7.3
	$\delta_{total}$	91.0	7.4	0.1	1.5	100
<b>VVUL333</b>	$\delta$	6.5	3.3	1.0	1.6	7.5
	$\delta_{total}$	75.4	18.5	1.7	4.4	100
<b>VVUL291</b>	$\delta$	6.1	3.3	1.0	1.6	7.2
	$\delta_{total}$	73.1	20.3	1.9	4.7	100
<b>VVUL171</b>	$\delta$	6.0	3.3	1.0	1.5	7.0
	$\delta_{total}$	72.3	21.2	2.0	4.5	100
<b>VVUL171</b>	$\delta$	5.8	3.3	1.0	2.2	7.1
	$\delta_{total}$	67.8	21.1	2.0	9.2	100

# 6.3 Silicon distillation apparatus

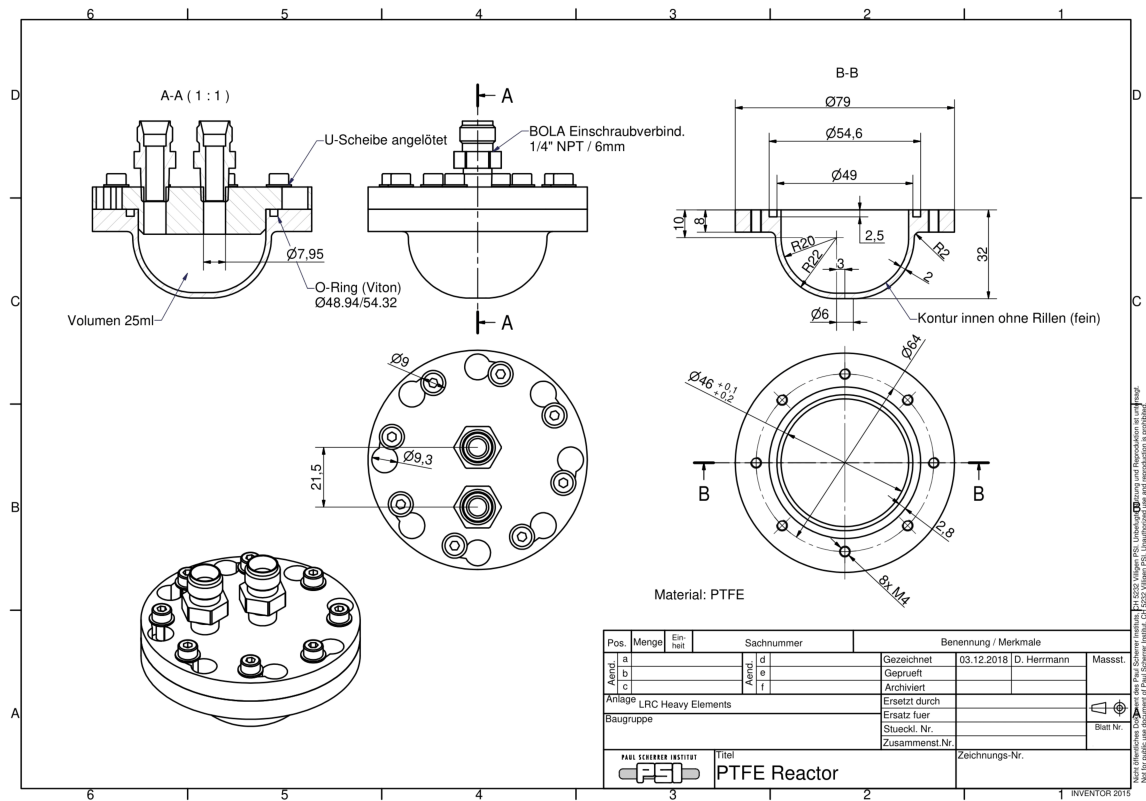


**Fig. 6.4:** Technical drawing of MODUS (Mini silicOn Distillation apparatusUS), thankfully provided by Dominik Herrmann (Technical Assistant, LRC).

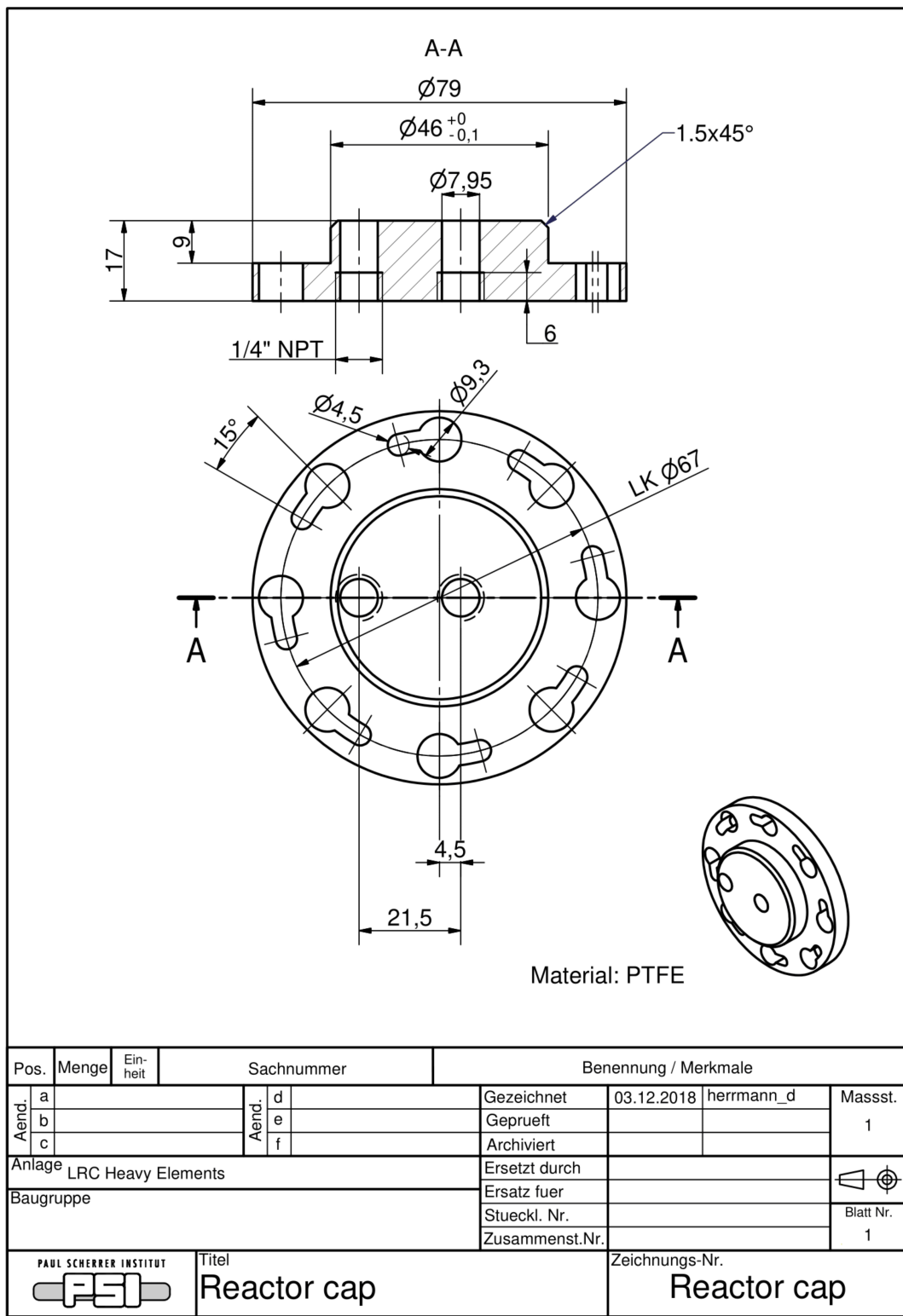


**Fig. 6.5:** Technical drawing of the MODUS' closure, thankfully provided by Dominik Herrmann (Technical Assistant, LRC).



## 7 Bibliography

- [1] Shakun, J. D.; Clark, P. U.; He, F.; Marcott, S. A.; Mix, A. C.; Liu, Z.; Otto-Bliesner, B.; Schmittner, A.; Bard, E. *Nature* **2012**, *484*, 49–54.
- [2] NOAA State of the Climate: Global Climate Report for Annual 2019., <https://www.ncei.noaa.gov/access/monitoring/monthly-report/global/201913>, Accessed: February 21, 2022, (2019).
- [3] Guerreiro, S. B.; Dawson, R. J.; Kilsby, C.; Lewis, E.; Ford, A. *Environmental Research Letters* **2018**, *13*, 034009.
- [4] Outreach, N. P. Press release: The Nobel Prize in Physics 2021., <https://www.nobelprize.org/prizes/physics/2021/press-release/>, Accessed: February 13, 2022, (2021).
- [5] Hegerl, G. C. *Communications Earth & Environment* **2022**, *3*, 1–3.
- [6] Conti, C.; DelRe, E. *Nature Photonics* **2022**, *16*, 6–7.
- [7] Harmon, R. S.; Schwarcz, H. P.; Gascoyne, M.; Hess, J. W.; Ford, D. C. In *Studies of Cave Sediments*; Springer: 2004, pp 199–226.
- [8] Wong, C. I.; Breecker, D. O. *Quaternary Science Reviews* **2015**, *127*, 1–18.
- [9] Scholz, D.; Hoffmann, D. *E&G Quaternary Science Journal* **2008**, *57*, 52–76.
- [10] Edwards, R.; Gallup, C.; Cheng, H. *Reviews in Mineralogy and Geochemistry* **2003**, *52*, 363–405.
- [11] Williams, P.; King, D.; Zhao, J.-X.; Collerson, K. D. *The Holocene* **2004**, *14*, 194–208.
- [12] Fifield, L. K.; Morgenstern, U. *Quaternary Geochronology* **2009**, *4*, 400–405.
- [13] Vimeux, F.; Ginot, P.; Schwikowski, M.; Vuille, M.; Hoffmann, G.; Thompson, L. G.; Schotterer, U. *Palaeogeography, Palaeoclimatology, Palaeoecology* **2009**, *281*, 229–241.
- [14] NNDC Selected Evaluated Nuclear Structure Data., <https://www.nndc.bnl.gov/nudat3/>, Accessed: February 23, 2022, (2022).
- [15] McDougall, I.; Mac Dougall, I.; Harrison, T. M., et al., *Geochronology and Thermochronology by the  $^{40}\text{Ar}/^{39}\text{Ar}$  Method*; Oxford University Press on Demand: 1999.
- [16] Bonani, G.; Ivy, S. D.; Hajdas, I.; Niklaus, T. R.; Suter, M. *Radiocarbon* **1994**, *36*, 247–250.
- [17] Condomines, M.; Allegre, C. J. *Nature* **1980**, *288*, 354–357.
- [18] Wilde, S. A.; Valley, J. W.; Peck, W. H.; Graham, C. M. *Nature* **2001**, *409*, 175–178.
- [19] Appleby, P.; Jones, V.; Ellis-Evans, J. *Journal of Paleolimnology* **1995**, *13*, 179–191.
- [20] Brandenberger, J. M.; Crecelius, E. A.; Louchouart, P. *Environmental Science & Technology* **2008**, *42*, 6786–6790.

- [21] Kretschmer, W.; Anton, G.; Bergmann, M.; Finckh, E.; Kowalzik, B.; Klein, M.; Leigart, M.; Merz, S.; Morgenroth, G.; Piringer, I., et al. *Nuclear Instruments and Methods in Physics Research Section B: Beam Interactions with Materials and Atoms* **1997**, *123*, 455–459.
- [22] Veicht, M.; Mihalcea, I.; Cvjetinovic, Đ.; Schumann, D. *Radiochimica Acta* **2021**, *109*, 735–741.
- [23] Aggarwal, P. K.; Froehlich, K. F.; Gat, J. R., *Isotopes in the water cycle*; Springer: 2005.
- [24] Tykva, R. *Nukleonika* **2004**, *49*, 3–7.
- [25] Saldanha, R.; Back, H. O.; Tsang, R.; Alexander, T.; Elliott, S. R.; Ferrara, S.; Mace, E.; Overman, C.; Zalavadia, M. *Physical Review C* **2019**, *100*, 024608.
- [26] Morgenstern, U.; Fifield, L. K.; Zondervan, A. *Nuclear Instruments and Methods in Physics Research Section B: Beam Interactions with Materials and Atoms* **2000**, *172*, 605–609.
- [27] Lal, D. *Science of the Total Environment* **1999**, *237*, 3–13.
- [28] Lal, D.; Chung, Y.; Platt, T.; Lee, T. *Limnology and Oceanography* **1988**, *33*, 1559–1567.
- [29] Craig, H.; Somayajulu, B.; Turekian, K. *Earth and Planetary Science Letters* **2000**, *175*, 297–308.
- [30] Dansgaard, W.; Clausen, H.; Aarkrog, A. *Journal of Geophysical Research* **1966**, *71*, 5474–5477.
- [31] Collon, P.; Kutschera, W.; Lu, Z.-T. *Annu. Rev. Nucl. Part. Sci.* **2004**, *54*, 39–67.
- [32] Lehmann, B. E.; Davis, S. N.; Fabryka-Martin, J. T. *Water Resources Research* **1993**, *29*, 2027–2040.
- [33] Gu, J.-Q.; Tong, A. L.; Yang, G.-M.; Hu, S.-M.; Jiang, W.; Lu, Z.-T.; Purtschert, R.; Ritterbusch, F. *Chemical Geology* **2021**, *583*, 120480.
- [34] Hua, Q.; Barbetti, M. *Radiocarbon* **2004**, *46*, 1273–1298.
- [35] Loosli, H. H.; Oeschger, H. *Radiocarbon* **1980**, *22*, 863–870.
- [36] Schlitzer, R.; Roether, W.; Weidmann, U.; Kalt, P.; Loosli, H. H. *Journal of Geophysical Research: Oceans* **1985**, *90*, 6945–6952.
- [37] Loosli, H. H.; Heimann, M.; Oeschger, H. *Radiocarbon* **1980**, *22*, 461–469.
- [38] Loosli, H. H.; Möll, M.; Oeschger, H.; Schotterer, U. *Nuclear Instruments and Methods in Physics Research Section B: Beam Interactions with Materials and Atoms* **1986**, *17*, 402–405.

- [39] Benetti, P.; Calaprice, F.; Calligarich, E.; Cambiaghi, M.; Carbonara, F.; Cavanna, F.; Cocco, A.; Di Pompeo, F.; Ferrari, N.; Fiorillo, G., et al. *Nuclear Instruments and Methods in Physics Research Section A: Accelerators, Spectrometers, Detectors and Associated Equipment* **2007**, *574*, 83–88.
- [40] Hall, J.; Aalseth, C. E.; Bonicalzi, R. M.; Brandenberger, J. M.; Day, A. R.; Humble, P. H.; Mace, E. K.; Panisko, M. E.; Seifert, A. *Applied Radiation and Isotopes* **2016**, *107*, 187–190.
- [41] Williams, R. M.; Aalseth, C. E.; Brandenberger, J. M.; Day, A. R.; Finn, E.; Fuller, E. S.; Hoppe, E. W.; Humble, P. H.; Keillor, M. E.; Mace, E. K., et al. *Applied Radiation and Isotopes* **2017**, *126*, 243–248.
- [42] Jiang, W.; Williams, W.; Bailey, K.; Davis, A.; Hu, S.-M.; Lu, Z.-T.; O'Connor, T.; Purtschert, R.; Sturchio, N.; Sun, Y., et al. *Physical Review Letters* **2011**, *106*, 103001.
- [43] Larsson, M. *Mass spectrometry reviews* **2008**, *27*, 397–397.
- [44] Collon, P.; Bowers, M.; Calaprice, F.; Galbiati, C.; Henderson, D.; Hohman, T.; Jiang, C.; Kutschera, W.; Lee, H.; Loer, B., et al. *Nuclear Instruments and Methods in Physics Research Section B: Beam Interactions with Materials and Atoms* **2012**, *283*, 77–83.
- [45] Feng, Z.; Bohleber, P.; Ebser, S.; Ringena, L.; Schmidt, M.; Kersting, A.; Hopkins, P.; Hoffmann, H.; Fischer, A.; Aeschbach, W., et al. *Proceedings of the National Academy of Sciences* **2019**, *116*, 8781–8786.
- [46] Tong, A. L.; Gu, J.-Q.; Yang, G.-M.; Hu, S.-M.; Jiang, W.; Lu, Z.-T.; Ritterbusch, F. *Review of Scientific Instruments* **2021**, *92*, 063204.
- [47] Ritterbusch, F.; Ebser, S.; Welte, J.; Reichel, T.; Kersting, A.; Purtschert, R.; Aeschbach-Hertig, W.; Oberthaler, M. *Geophysical Research Letters* **2014**, *41*, 6758–6764.
- [48] Ebser, S.; Kersting, A.; Stöven, T.; Feng, Z.; Ringena, L.; Schmidt, M.; Tanhua, T.; Aeschbach, W.; Oberthaler, M. K. *Nature Communications* **2018**, *9*, 1–7.
- [49] Tong, A. L.; Gu, J.-Q.; Jia, Z.-H.; Yang, G.-M.; Hu, S.-M.; Jiang, W.; Lu, Z.-T.; Ritterbusch, F.; Sun, L.-T. *Review of Scientific Instruments* **2022**, *93*, 023203.
- [50] Zeldes, H.; Ketelle, B.; Brosi, A.; Fultz, C.; Hibbs, R. *Physical Review* **1952**, *86*, 811.
- [51] Stoenner, R.; Schaeffer, O.; Katcoff, S. *Science* **1965**, *148*, 1325–1328.
- [52] Holden, N. E. *Pure and Applied Chemistry* **1990**, *62*, 941–958.
- [53] Kutschera, W.; Billquist, P. J.; Frekers, D.; Henning, W.; Jensen, K. J.; Xiuzeng, M.; Pardo, R.; Paul, M.; Rehm, K. E.; Smither, R. K., et al. *Nuclear Instruments and Methods in Physics Research Section B: Beam Interactions with Materials and Atoms* **1984**, *5*, 430–435.
- [54] Rugel, G.; Faestermann, T.; Knie, K.; Korschinek, G.; Poutivtsev, M.; Schumann, D.; Kivel, N.; Günther-Leopold, I.; Weinreich, R.; Wohlmuther, M. *Physical Review Letters* **2009**, *103*, 072502.

- [55] Friedman, A.; Milsted, J.; Metta, D.; Henderson, D.; Lerner, J.; Harkness, A.; Op, D. R. *Radiochimica Acta* **1966**, *5*, 192–194.
- [56] Meissner, F.; Schmidt-Ott, W.-D.; Ziegeler, L. *Zeitschrift für Physik A Atomic Nuclei* **1987**, *327*, 171–174.
- [57] Kinoshita, N.; Paul, M.; Kashiv, Y.; Collon, P.; Deibel, C.; DiGiovine, B.; Greene, J.; Henderson, D.; Jiang, C.; Marley, S., et al. *Science* **2012**, *335*, 1614–1617.
- [58] McKeague, J.; Cline, M. *Canadian Journal of Soil Science* **1963**, *43*, 83–96.
- [59] Lal, D.; Goldberg, E. D.; Koide, M. *Physical Review Letters* **1959**, *3*, 380.
- [60] Lindner, M. *Physical Review* **1953**, *91*, 642.
- [61] Orrell, J. L.; Arnquist, I. J.; Bliss, M.; Bunker, R.; Finch, Z. S. *Astroparticle Physics* **2018**, *99*, 9–20.
- [62] Lal, D.; Schink, D. R. *Review of Scientific Instruments* **1960**, *31*, 395–398.
- [63] Brzezinski, M. A.; Phillips, D. R. *Limnology and Oceanography* **1997**, *42*, 856–865.
- [64] Tréuer, P.; Lindner, L.; van Bennekom, A. J.; Leynaert, A.; Panouse, M.; Jacques, G. *Limnology and Oceanography* **1991**, *36*, 1217–1227.
- [65] Nijampurkar, V.; Somayajulu, B. In *Proceedings of the Indian Academy of Sciences-Section A*, 1974; Vol. 80, pp 289–298.
- [66] Lai, D.; Nijampurkar, V.; Somayajulu, B.; Koide, M.; Goldberg, E. *Limnology and Oceanography* **1976**, *21*, 285–293.
- [67] Morgenstern, U.; Geyh, M.; Kudrass, H. R.; Ditchburn, R.; Graham, I. *Radiocarbon* **2001**, *43*, 909–916.
- [68] Morgenstern, U.; Ditchburn, R.; Vologina, E.; Sturm, M. *Journal of Paleolimnology* **2013**, *50*, 345–352.
- [69] Nijampurkar, V.; Amin, B.; Kharkar, D.; Lal, D. *Nature* **1966**, *210*, 478–480.
- [70] Thomsen, M.; Heinemeier, J.; Hornshøj, P.; Nielsen, H.; Rud, N. *Nuclear Instruments and Methods in Physics Research Section B: Beam Interactions with Materials and Atoms* **1988**, *31*, 425–432.
- [71] Gong, J.; Li, C.; Wang, W.; Zheng, G.; Hu, H.; He, M.; Jiang, S. *Nuclear Instruments and Methods in Physics Research Section B: Beam Interactions with Materials and Atoms* **2011**, *269*, 2745–2749.
- [72] He, M.; Wang, X.; Zhen, G.; Gong, J.; Ruan, X.; Li, C.; Dong, K.; Li, Z.; Hu, H.; Jiang, S. *Nuclear Instruments and Methods in Physics Research Section B: Beam Interactions with Materials and Atoms* **2013**, *294*, 104–106.
- [73] Ouellet, C.; Singh, B. *Nuclear Data Sheets* **2011**, *112*, 2199–2355.
- [74] Kutschera, W.; Henning, W.; Paul, M.; Smither, R.; Stephenson, E.; Yntema, J.; Alburger, D.; Cumming, J.; Harbottle, G. *Physical Review Letters* **1980**, *45*, 592.

- [75] Elmore, D.; Anantaraman, N.; Fulbright, H.; Gove, H.; Hans, H.; Nishiizumi, K.; Murrell, M.; Honda, M. *Physical Review Letters* **1980**, *45*, 589.
- [76] Alburger, D.; Harbottle, G.; Norton, E. *Earth and Planetary Science Letters* **1986**, *78*, 168–176.
- [77] Hofmann, H.; Bonani, G.; Suter, M.; Wölfl, W.; Zimmermann, D.; Von Gunten, H. *Nuclear Instruments and Methods in Physics Research Section B: Beam Interactions with Materials and Atoms* **1990**, *52*, 544–551.
- [78] Thomsen, M.; Heinemeier, J.; Hornshøj, P.; Nielsen, H.; Rud, N. *Nuclear Physics A* **1991**, *534*, 327–338.
- [79] Chen, Y.; Kashy, E.; Bazin, D.; Benenson, W.; Morrissey, D.; Orr, N.; Sherrill, B.; Winger, J.; Young, B.; Yurkon, J. *Physical Review C* **1993**, *47*, 1462–1465.
- [80] Brodzinski, R.; Finkel, J.; Conway, D. *Journal of Inorganic and Nuclear Chemistry* **1964**, *26*, 677–681.
- [81] Sakamoto, K.; Kaga, K.; Komura, K. *Journal of Inorganic and Nuclear Chemistry* **1978**, *40*, 1183–1184.
- [82] Forberg, S. *Radiochimica Acta* **1972**, *18*, 194–197.
- [83] Sato, T. *Journal of Radioanalytical and Nuclear Chemistry* **1977**, *40*, 75–83.
- [84] Dai, Y.; Brun, R.; Gao, W.; Geissmann, K.; Hahl, S.; Hou, H.; Huang, Y.; Linder, H.; Long, B.; Spahr, A., et al. *Journal of Nuclear Materials* **2012**, *431*, 2–9.
- [85] Endo, H. **2021**.
- [86] Chen, J.; Singh, B.; Cameron, J. A. *Nuclear Data Sheets* **2011**, *112*, 2357–2495.
- [87] Mullins, W. T.; Leddicotte, G. W. *The Radiochemistry of Silicon*; tech. rep.; Oak Ridge National Lab., 1961.
- [88] Polak, P.; Garcia, S.; Taylor, W.; Barnes, J.; Lindner, L.; O'BRIEN, H.; Thomas, K. *Radiochimica Acta* **1985**, *38*, 73–78.
- [89] Phillips, D.; Hamilton, V.; Jamriska, D.; Brzezinski, M. *Journal of Radioanalytical and Nuclear Chemistry* **1995**, *195*, 251–261.
- [90] NIDC National Isotope Development Center., <https://www.isotopes.gov/production-network>, Accessed: February 24, 2022, (2022).
- [91] NIDC National Isotope Development Center., <https://www.isotopes.gov/sites/default/files/2021-02/Si-32.pdf>, Accessed: February 25, 2022, (2022).
- [92] Huclier-Markai, S.; Alliot, C.; Kerdjoudj, R.; Mougin-Degraef, M.; Chouin, N.; Haddad, F. *Cancer Biotherapy & Radiopharmaceuticals* **2018**, *33*, 316–329.
- [93] Dressler, R.; Ayranov, M.; Bemmerer, D.; Bunka, M.; Dai, Y.; Lederer, C.; Fallis, J.; Murphy, A. S.; Pignatari, M.; Schumann, D., et al. *Journal of Physics G: Nuclear and Particle Physics* **2012**, *39*, 105201.

- [94] LNHB Laboratoire National Henri Becquerel., <http://www.lnhb.fr/nuclear-data/module-lara/>, Accessed: March 7, 2022, (2022).
- [95] Besmehn, A.; Hoppe, P.; Ott, U. *Meteoritics & Planetary Science* **2011**, *46*, 1265–1275.
- [96] Roesch, F. *Current Radiopharmaceuticals* **2012**, *5*, 187–201.
- [97] Pruszyński, M.; Loktionova, N.; Filosofov, D.; Rösch, F. *Applied Radiation and Isotopes* **2010**, *68*, 1636–1641.
- [98] Radchenko, V.; Meyer, C. A. L.; Engle, J. W.; Naranjo, C. M.; Unc, G. A.; Mastren, T.; Brugh, M.; Birnbaum, E. R.; John, K. D.; Nortier, F. M., et al. *Journal of Chromatography A* **2016**, *1477*, 39–46.
- [99] Radchenko, V.; Engle, J. W.; Medvedev, D. G.; Maassen, J. M.; Naranjo, C. M.; Unc, G. A.; Meyer, C. A.; Mastren, T.; Brugh, M.; Mausner, L., et al. *Nuclear Medicine and Biology* **2017**, *50*, 25–32.
- [100] Larenkov, A. A.; Makichyan, A. G.; Iatsenko, V. N. *Molecules* **2021**, *26*, 6371.
- [101] Severin, G.; Engle, J.; Valdovinos, H.; Barnhart, T.; Nickles, R. *Applied Radiation and Isotopes* **2012**, *70*, 1526–1530.
- [102] Sitarz, M.; Szkliniarz, K.; Jastrzębski, J.; Choiński, J.; Guertin, A.; Haddad, F.; Jakubowski, A.; Kapinos, K.; Kisieliński, M.; Majkowska, A., et al. *Applied Radiation and Isotopes* **2018**, *142*, 104–112.
- [103] Sharp, R.; Diamond, R. *Physical Review* **1954**, *93*, 358.
- [104] Nesaraja, C.; McCutchan, E. *Nuclear Data Sheets* **2016**, *133*, 1–220.
- [105] Basunia, M.; Hurst, A. *Nuclear Data Sheets* **2016**, *134*, 1–148.
- [106] Elmore, D.; Bhattacharyya, M. H.; Sacco-Gibson, N.; Peterson, D. P. *Nuclear Instruments and Methods in Physics Research Section B: Beam Interactions with Materials and Atoms* **1990**, *52*, 531–535.
- [107] Freeman, S.; Serfass, R.; King, J.; Southon, J.; Fang, Y.; Woodhouse, L.; Bench, G.; McAninch, J. *Nuclear Instruments and Methods in Physics Research Section B: Beam Interactions with Materials and Atoms* **1995**, *99*, 557–561.
- [108] Klein, J.; Fink, D.; Middleton, R.; Nishiizumi, K.; Arnold, J. *Earth and Planetary Science Letters* **1991**, *103*, 79–83.
- [109] Mahoney, W.; Ling, J.; Jacobson, A.; Lingenfelter, R. *The Astrophysical Journal* **1982**, *262*, 742.
- [110] Zerkov, V.; Pritychenko, B.; Totans, J.; Vrapcenjak, L.; Rodionov, A.; Shulyak, G. *Journal of Instrumentation* **2022**, *17*, P03012.
- [111] Christl, M.; Vockenhuber, C.; Kubik, P. W.; Wacker, L.; Lachner, J.; Alifimov, V.; Synal, H.-A. *Nuclear Instruments and Methods in Physics Research Section B: Beam Interactions with Materials and Atoms* **2013**, *294*, 29–38.

- [112] Lachner, J.; Christl, M.; Alifimov, V.; Hajdas, I.; Kubik, P. W.; Schulze-König, T.; Wacker, L.; Synal, H.-A. *Journal of Environmental Radioactivity* **2014**, *129*, 68–72.
- [113] Miltenberger, K.-U.; Müller, A. M.; Suter, M.; Synal, H.-A.; Vockenhuber, C. *Nuclear Instruments and Methods in Physics Research Section B: Beam Interactions with Materials and Atoms* **2017**, *406*, 272–277.
- [114] Fenclová, K.; Prášek, T.; Němec, M.; Christl, M.; Gautschi, P.; Vockenhuber, C.; Tecl, J. *Nuclear Instruments and Methods in Physics Research Section B: Beam Interactions with Materials and Atoms* **2021**, *503*, 45–52.
- [115] Vivo-Vilches, C.; López-Gutiérrez, J. M.; García-León, M.; Vockenhuber, C. *Nuclear Instruments and Methods in Physics Research Section B: Beam Interactions with Materials and Atoms* **2019**, *438*, 193–197.
- [116] Zagorodni, A. A., *Ion Exchange Materials: Properties and Applications*; Elsevier: 2006.
- [117] L’Annunziata, M. F., *Handbook of Radioactivity Analysis*; Academic press: 2012.
- [118] Marhol, M. *Wilson and Wilson’s comprehensive analytical chemistry* **1982**, 34.
- [119] Braun, T.; Ghersini, G., *Extraction Chromatography*; Elsevier: 1975.
- [120] Korkisch, J., *Handbook of ion exchange resins: their application to inorganic analytical chemistry*; Routledge: 2017.
- [121] Schönbächler, M.; Fehr, M. In *Treatise on Geochemistry. Vol. 15: Analytical Geochemistry/Inorganic Instrument Analysis*; Elsevier: 2013, pp 124–146.
- [122] International, T. Product Sheet: Analytical Grade Ion Exchange Resins., [https://www.triskem-international.com/scripts/files/61fac5780a76a3.80254384/PS\\_IX-resins\\_EN\\_220201.pdf](https://www.triskem-international.com/scripts/files/61fac5780a76a3.80254384/PS_IX-resins_EN_220201.pdf), Accessed: May 17, 2022, (2022).
- [123] Ltd., S. B. R. T. C. Chelating resin., [http://www.bojieresin.com/product\\_Chelating\\_resin.html](http://www.bojieresin.com/product_Chelating_resin.html), Accessed: May 13, 2022, (2022).
- [124] Holdings, M. C. Chelating resins., [https://www.m-chemical.co.jp/en/products/departments/mcc/ion/product/1201069\\_8072.html](https://www.m-chemical.co.jp/en/products/departments/mcc/ion/product/1201069_8072.html), Accessed: May 13, 2022, (2022).
- [125] Page, M. J.; Solden hoff, K.; Ogden, M. D. *Hydrometallurgy* **2017**, *169*, 275–281.
- [126] Wang, G.; Zhao, Y.; Yang, B.; Song, Y. *Hydrometallurgy* **2018**, *176*, 69–72.
- [127] International, T. Product Sheet: Monophos resin., [https://www.triskem-international.com/scripts/files/5f46343b046794.47250034/PS\\_Monophos-Resin\\_EN\\_151210.pdf](https://www.triskem-international.com/scripts/files/5f46343b046794.47250034/PS_Monophos-Resin_EN_151210.pdf), Accessed: May 16, 2022, (2015).
- [128] Ostapenko, V.; Vasiliev, A.; Lapshina, E.; Ermolaev, S.; Aliev, R.; Totskiy, Y.; Zhuikov, B.; Kalmykov, S. *Journal of Radioanalytical and Nuclear Chemistry* **2015**, *306*, 707–711.
- [129] Gharibyan, N.; Dailey, A.; McLain, D. R.; Bond, E. M.; Moody, W. A.; Happel, S.; Sudowe, R. *Solvent Extraction and Ion Exchange* **2014**, *32*, 391–407.

- [130] International, T. Product Sheet: LN/LN2/LN3 resins., [https://www.triskem-international.com/scripts/files/5f46343a7c97d9.45835022/PS\\_LN-Resin\\_EN\\_200603.pdf](https://www.triskem-international.com/scripts/files/5f46343a7c97d9.45835022/PS_LN-Resin_EN_200603.pdf), Accessed: May 13, 2022, (2020).
- [131] International, T. Product Sheet: DGA resin., [https://www.triskem-international.com/scripts/files/60afaeab517ce4.59925166/PS\\_DN-Resin\\_EN\\_151210.pdf](https://www.triskem-international.com/scripts/files/60afaeab517ce4.59925166/PS_DN-Resin_EN_151210.pdf), Accessed: May 13, 2022, (2015).
- [132] Khan, H. U. *Ion Exchange Technologies* **2012**, 331–342.
- [133] Heinitz, S.; Maugeri, E. A.; Schumann, D.; Dressler, R.; Kivel, N.; Guerrero, C.; Köster, U.; Tessler, M.; Paul, M.; Halfon, S., et al. *Radiochimica Acta* **2017**, *105*, 801–811.
- [134] Purolite Ion Exchange Resin Characteristics., <https://www.purolite.com/index/core-technologies/industry/food-and-beverage/sweetener-applications/corn-sweetener-refining-with-ion-exchange-resins/ion-exchange-resin-characteristics>, Accessed: June 04, 2022, (2022).
- [135] Lenntech Ion Exchange Resins: Practical Guidelines., <https://www.lenntech.com/Data-sheets/Dowex-practical-guidelines-L.pdf>, Accessed: June 04, 2022, (2003).
- [136] Happel, S., Personal Communication, 2019.
- [137] Malmbeck, R.; Banik, N. L. *Radiochimica Acta* **2022**.
- [138] Sóti, Z.; Magill, J.; Dreher, R. *EPJ Nuclear Sciences & Technologies* **2019**, *5*, 6.
- [139] Kossert, K.; Broda, R.; Cassette, P.; Ratel, G.; Zimmerman, B. *Metrologia* **2015**, *52*, S172.
- [140] Nedjadi, Y.; Bailat, C.; Caffari, Y.; Froidevaux, P.; Wastiel, C.; Kivel, N.; Guenther-Leopold, I.; Triscone, G.; Jaquenod, F.; Bochud, F. *Applied Radiation and Isotopes* **2012**, *70*, 1990–1996.
- [141] Kivel, N.; Schumann, D.; Günther-Leopold, I. *Analytical and Bioanalytical Chemistry* **2013**, *405*, 2965–2972.
- [142] May, T. W.; Wiedmeyer, R. H. *Atomic Spectroscopy-Norwalk Connecticut* **1998**, *19*, 150–155.
- [143] Pommé, S. *Metrologia* **2015**, *52*, S51.
- [144] Kajan, I.; Heinitz, S.; Kossert, K.; Sprung, P.; Dressler, R.; Schumann, D. *Scientific Reports* **2021**, *11*, 1–9.
- [145] Pommé, S.; Camps, J.; Van Ammel, R.; Paepen, J. *Journal of Radioanalytical and Nuclear Chemistry* **2008**, *276*, 335–339.
- [146] Da Silva, M. A.; de Almeida, M. C.; da Silva, C. J.; Delgado, J. U. *Applied Radiation and Isotopes* **2004**, *60*, 301–305.
- [147] Van Ammel, R.; Pommé, S.; Sibbens, G. *Applied radiation and isotopes* **2004**, *60*, 337–339.

- [148] Collins, S.; Gilligan, C.; Pierson, B.; Ramirez, N.; Goodwin, M.; Pearce, A.; Archambault, B.; Haney, M.; Regan, P. *Applied Radiation and Isotopes* **2022**, *182*, 110140.
- [149] Inc., A. T. ICP-OES Frequently Asked Questions., <http://www.agilent.com/en/support/atomic-spectroscopy/inductively-coupled-plasma-optical-emission-spectroscopy-icp-oes/icp-oes-instruments/icp-oes-faq>, Accessed: May 13, 2022, (2022).
- [150] Leskinen, A.; Salminen-Paatero, S. *Journal of Radioanalytical and Nuclear Chemistry* **2022**.
- [151] Günther, E. *Applied Radiation and Isotopes* **2002**, *56*, 357–360.
- [152] Armbruster, D. A.; Pry, T. *The Clinical Biochemist Reviews* **2008**, *29*, S49.
- [153] Eurachem The Fitness for Purpose of Analytical Methods: A Laboratory Guide to Method Validation and Related Topics: Second edition., [https://www.eurachem.org/images/stories/Guides/pdf/MV\\_guide\\_2nd\\_ed\\_EN.pdf](https://www.eurachem.org/images/stories/Guides/pdf/MV_guide_2nd_ed_EN.pdf), Accessed: May 13, 2022, (2014).
- [154] Thompson, M.; Ellison, S. L.; Wood, R. *Pure and Applied Chemistry* **2002**, *74*, 835–855.
- [155] International des poids et mesures, B. Evaluation of measurement data — An introduction to the “Guide to the expression of uncertainty in measurement”., <https://www.bipm.org/en/search:>, Accessed: May 23, 2022, (2009).
- [156] Eurachem Quantifying Uncertainty in Analytical Measurement., [https://www.eurachem.org/images/stories/Guides/pdf/QUAM2012\\_P1.pdf](https://www.eurachem.org/images/stories/Guides/pdf/QUAM2012_P1.pdf), Accessed: May 23, 2022, (2012).
- [157] Kragten, J. *Analyst* **1994**, *119*, 2161–2165.
- [158] Cremona, P.; Rogaume, T.; Richard, F.; Batiot, B. In *Journal of Physics: Conference Series*, 2018; Vol. 1107, p 032019.
- [159] PSI The PSI proton accelerator., <https://www.psi.ch/en/media/the-psi-proton-accelerator>, Accessed: May 23, 2022, (2022).
- [160] D, G.; Filges, F. Handbook of Spallation Research., 2009.
- [161] Kopecký, P. *The International Journal of Applied Radiation and Isotopes* **1985**, *36*, 657–661.
- [162] Hermanne, A.; Adam-Rebeles, R.; Tárkányi, F.; Takacs, S.; Ditroi, F. *Nuclear Instruments and Methods in Physics Research Section B: Beam Interactions with Materials and Atoms* **2015**, *359*, 145–154.
- [163] Gloris, M.; Michel, R.; Sudbrock, F.; Herpers, U.; Malmborg, P.; Holmqvist, B. *Nuclear Instruments and Methods in Physics Research Section A: Accelerators, Spectrometers, Detectors and Associated Equipment* **2001**, *463*, 593–633.
- [164] Mancusi, D.; Boudard, A.; Cugnon, J.; David, J.-C.; Kaitaniemi, P.; Leray, S. *Physical Review C* **2014**, *90*, 054602.

- [165] Boudard, A.; Cugnon, J.; David, J.-C.; Leray, S.; Mancusi, D. *Physical Review C* **2013**, *87*, 014606.
- [166] Kelic, A.; Ricciardi, M. V.; Schmidt, K.-H. *arXiv preprint arXiv:0906.4193* **2009**.
- [167] David, J.-C. *The European Physical Journal A* **2015**, *51*, 1–57.
- [168] Titarenko, Y. E.; Shvedov, O.; Batyaev, V.; Karpikhin, E.; Zhivun, V.; Koldobsky, A.; Mulambetov, R.; Kvasova, S.; Sosnin, A.; Mashnik, S., et al. *Physical Review C* **2002**, *65*, 064610.
- [169] Nedjadi, Y.; Duc, P.-F.; Bochud, F.; Bailat, C. *Applied Radiation and Isotopes* **2016**, *118*, 25–31.
- [170] Smith, S.; Pruszkowski, E. Benefits of NexION 300/350 Introduction ICP-MS Technology for the Analysis of Power Plant Flue Gas Desulfurization Wastewaters., [https://resources.perkinelmer.com/corporate/cmsresources/images/44-136964app\\_nexion300d-fluegasdesulfurizationwastewaters.pdf](https://resources.perkinelmer.com/corporate/cmsresources/images/44-136964app_nexion300d-fluegasdesulfurizationwastewaters.pdf), Accessed: May 07, 2022, (2014).
- [171] plc, L. Produktdatenblatt, Argon 5.0., [https://produkte.linde-gase.de/db\\_neu/argon\\_5.0.pdf](https://produkte.linde-gase.de/db_neu/argon_5.0.pdf), Accessed: March 07, 2022, (2022).
- [172] Gasilova, N., Personal Communication, 2019.
- [173] Lindner, L.; Polak, P. *Radiochimica Acta* **1982**, *31*, 23–26.
- [174] Dirks-Fandrei, C. Entwicklung von Methoden zur selektiven Trennung von Scandium, Zirkonium und Zinn für radiopharmazeutische Anwendungen., Ph.D. Thesis, Philipps-Universität Marburg, Germany, 2014.
- [175] (LNS), L. N. S. Plus d’anneaux autour de Saturne., <https://cds.cern.ch/record/1740121/files/vol39-issue2-p033-f.pdf>, Accessed: May 07, 2022, (1999).
- [176] Svedberg-laboratoriet, T. Slutstrålat för Forskning, Medicin och Industri., [https://www.tsl.uu.se/digitalAssets/625/c\\_625036-1\\_3-k\\_imagepuff.jpg](https://www.tsl.uu.se/digitalAssets/625/c_625036-1_3-k_imagepuff.jpg), Accessed: May 07, 2022, (2022).
- [177] Veicht, M.; Kajan, I.; David, J.-C.; Chen, S.; Strub, E.; Mihalcea, I.; Schumann, D. *Physical Review C* **2021**, *104*, 014615.
- [178] Protoschill, J. Untersuchung der Restkernproduktion durch Protoneninduzierte Reaktionen an Schweren Targetelementen., Ph.D. Thesis, Gottfried Wilhelm Leibniz Universität Hannover, Germany, 1997.
- [179] Sajjad, M.; Lambrecht, R. M. *Analytical Chemistry* **1986**, *58*, 667–668.
- [180] Maxeiner, S.; Synal, H.-A.; Christl, M.; Suter, M.; Müller, A.; Vockenhuber, C. *Nuclear Instruments and Methods in Physics Research Section B: Beam Interactions with Materials and Atoms* **2019**, *439*, 84–89.
- [181] Taylor, P.; Maeck, R.; De Bièvre, P. *International Journal of Mass Spectrometry and Ion Processes* **1992**, *121*, 111–125.

- [182] Gourgiotis, A.; Ducasse, T.; Barker, E.; Jollivet, P.; Gin, S.; Bassot, S.; Cazala, C. *Analytica Chimica Acta* **2017**, *954*, 68–76.
- [183] Gunnarsson, I.; Arnórsson, S. *Geochimica et Cosmochimica Acta* **2000**, *64*, 2295–2307.
- [184] Ichikawa, F.; Sato, T. *Radiochimica Acta* **1970**, *13*, 69–71.
- [185] Martell, A. E.; Smith, R. M., *Critical Stability Constants: Second Supplement*; Springer Science & Business Media: 2013; Vol. 6.
- [186] Ciavatta, L.; Iuliano, M.; Porto, R. *Polyhedron* **1988**, *7*, 1773–1779.
- [187] Sudakova, T.; Krasnoshchekov, V. *Zh. Neorg. Khim* **1978**, *23*, 1506–1508.
- [188] Mizuhata, M.; Saito, Y.; Takee, M.; Deki, S. *Journal of the Ceramic Society of Japan* **2009**, *117*, 335–339.
- [189] Holt, B. *Analytical Chemistry* **1960**, *32*, 124–128.
- [190] Ferrer, E.; Baran, E. *Biological Trace Element Research* **2001**, *83*, 111–119.
- [191] Kustin, K.; Toppen, D. L. *Inorganic Chemistry* **1973**, *12*, 1404–1407.
- [192] Buettner, K. M.; Collins, J. M.; Valentine, A. M. *Inorganic Chemistry* **2012**, *51*, 11030–11039.
- [193] Gaonkar, A. G.; McPherson, A., *Ingredient interactions: effects on food quality*; CRC press: 2016.
- [194] Dong, L.; Yang, N.; Yang, Y.; Li, W.; Quan, Y.; Deng, B.; Meng, D.; Du, Y.; Li, S.; Tan, Z. *RSC Advances* **2017**, *7*, 890–896.
- [195] Engström, E.; Rodushkin, I.; Baxter, D. C.; Öhlander, B. *Analytical Chemistry* **2006**, *78*, 250–257.
- [196] Bossew, P. *Applied Radiation and Isotopes* **2005**, *62*, 635–644.
- [197] Zaitseva, N.; Rurarz, E.; Tchikalov, M.; Vobecky, M.; Khalkin, V.; Popinenkova, L. *Radiochimica Acta* **1994**, *65*, 157–160.
- [198] Ziegler, E. IGG100 68Ge/68Ga Generator (Chemical Grade), Cyclotron-independent production of the positron emitter 68Gallium., <https://radiopharma.com/product/igg100/>, Accessed: March 04, 2022, (2022).
- [199] Laboratory, O. R. N. Spallation Neutron Source., <https://neutrons.ornl.gov/sns>, Accessed: March 04, 2022, (2022).
- [200] Center, J.-P. Facilities at J-PARC., <https://j-parc.jp/c/en/facilities/index.html>, Accessed: March 04, 2022, (2022).
- [201] TRIUMF Proton Irradiation Facility & Neutron Irradiation Facility., <https://www.triumf.ca/pif-nif>, Accessed: March 04, 2022, (2022).
- [202] (ESS), E. S. S. ESS Accelerator Division., <https://europeanspallationsource.se/accelerator>, Accessed: March 04, 2022, (2022).

- [203] Veicht, M.; Mihalcea, I.; Gautschi, P.; Vockenhuber, C.; Maxeiner, S.; David, J.-C.; Chen, S.; Schumann, D. *Radiochimica Acta* **2022**.
- [204] Pourmand, A.; Dauphas, N. *Talanta* **2010**, *81*, 741–753.
- [205] Müller, C.; Bunka, M.; Haller, S.; Köster, U.; Groehn, V.; Bernhardt, P.; van der Meulen, N.; Türlér, A.; Schibli, R. *Journal of Nuclear Medicine* **2014**, *55*, 1658–1664.
- [206] Butler, A.; Clague, M. J.; Meister, G. E. *Chemical Reviews* **1994**, *94*, 625–638.
- [207] Nishiizumi, K. *Nuclear Instruments and Methods in Physics Research Section B: Beam Interactions with Materials and Atoms* **2004**, *223*, 388–392.
- [208] Schumann, D.; David, J.-C. *Nuclear Data Sheets* **2014**, *119*, 288–291.
- [209] Terlikowska, T.; Cassette, P.; Péron, M.; Broda, R.; Hainos, D.; Tartes, I.; Kempisty, T. *Applied Radiation and Isotopes* **1998**, *49*, 1041–1047.
- [210] (ESI), E. S. ACM module., <http://www.icpms.de/pdf/ACM-membrane.pdf>, Accessed: May 23, 2022, (2022).
- [211] Zimmermann, D.; von Gunten, H. R. *Radiochimica Acta* **1996**, *72*, 97–100.
- [212] Schlomberg, M.; Vockenhuber, C.; Synal, H.-A. Isobar Separation Of  $^{32}\text{Si}$  From  $^{32}\text{S}$ . Investigation of a passive absorber., [https://ethz.ch/content/dam/ethz/special-interest/phys/particle-physics/ion-beam-physics-dam/documents/LIP\\_annual\\_report\\_2021pdfX4\\_corrected.pdf](https://ethz.ch/content/dam/ethz/special-interest/phys/particle-physics/ion-beam-physics-dam/documents/LIP_annual_report_2021pdfX4_corrected.pdf), Accessed: May 19, 2022, (2021).
- [213] Schlomberg, M.; Mihalcea, I.; Schumann, D.; Synal, H.-A.; Veicht, M.; Vockenhuber, C.; Wallner, A. Isobar Separation Of  $^{32}\text{Si}$  From  $^{32}\text{S}$ . Investigation of passive absorber and gas-filled magnet., [https://ethz.ch/content/dam/ethz/special-interest/phys/particle-physics/ion-beam-physics-dam/documents/AR\\_2020\\_Inhalt\\_06042021.pdf](https://ethz.ch/content/dam/ethz/special-interest/phys/particle-physics/ion-beam-physics-dam/documents/AR_2020_Inhalt_06042021.pdf), Accessed: May 19, 2022, (2020).
- [214] PSI Annual Report 2020 (Laboratory of Radiochemistry)., <https://www.psi.ch/en/lrc/annual-reports>, Accessed: June 04, 2022, (2022).



## List of Publications as of August 01, 2022: Mario A. Veicht

### First-Author Publications (Peer-Reviewed Journals)

06|2022 **Radiochim. Acta, (Published online)**

■ Radiochemical separation of  $^{26}\text{Al}$  and  $^{41}\text{Ca}$  from proton-irradiated vanadium targets for cross-section determination by means of AMS

Mario Veicht, I. Mihalcea, P. Gautschi, C. Vockenhuber, S. Maxeiner, J.-C. David, S. Chen and D. Schumann

08|2021 **Radiochim. Acta, (Published)**

■ Radiochemical separation and purification of non-carrier-added silicon-32

Mario Veicht, I. Mihalcea, D. Cvjetinovic and D. Schumann

07|2021 **Phys. Rev. C, (Published)**

■ Experiment-based determination of the excitation function for the production of  $^{44}\text{Ti}$  in proton-irradiated vanadium samples

Mario Veicht, I. Kajan, J.-C. David, S. Chen, E. Strub, I. Mihalcea and D. Schumann

### Co-Author Publications (Peer-Reviewed Journals)

05|2022 **Nucl. Instrum. Methods Phys. Res., Sect. B (Under Review)**

■ Isobar Separation of  $^{32}\text{Si}$  from  $^{32}\text{S}$  in AMS using a Passive Absorber

M. Schlomberg, C. Vockenhuber, H.-A. Synal, Mario Veicht, I. Mihalcea, D. Schumann

04|2022 **Nucl. Instrum. Methods Phys. Res., Sect. A, (Published)**

■ Preparation of PbSe targets for  $^{79}\text{Se}$  neutron capture cross section studies

N. M. Chiera, E. A. Maugeri, I. Danilov, J. Balibrea-Correa, C. Domingo-Pardo, U. Köster, J. Lerendegui-Marco, Mario Veicht, I. Zivadinovic, D. Schumann, and nTOF collaboration

### In preparation

06|2022 **Radiochim. Acta, (Submission upcoming)**

■ No-carrier-added recovery of  $^{41}\text{Ca}$ ,  $^{44}\text{Ti}$ , and  $^{26}\text{Al}$  from high-energy proton-irradiated vanadium Targets

End of 2022 **To be submitted: e.g., Sci. Rep. (Nature)**

■ Direct determination of the  $^{32}\text{Si}$  half-life: solving a long-lasting scientific issue

End of 2022 **To be submitted: e.g., J. Chromatogr. Sep. Tech. or J. Chromatogr. A**

■ Separation of Ti, Zr, Nb, Mo, Hf, Ta, and W in HCl-HF, HNO<sub>3</sub>-HF system employing TEVA and TBP resin

End of 2022 **To be submitted: e.g., Appl. Radiat. Isot.**

■ Half-life determination of  $^{179}\text{Ta}$  by means of high-resolution gamma-ray spectrometry

## Summary

Highly motivated, 4<sup>th</sup> year Ph.D. candidate working at the Paul Scherrer Institut and EPFL with a passion for data analysis, quantitative problem solving, and chemistry. Accustomed to work in an international environment with the innate ability to perform and deliver against ambitious deadlines and team goals. Consistently ranked among the best performing students with various best in class feedbacks. Won PSI's Best 1<sup>st</sup> and 4<sup>th</sup> year Ph.D. Student Award and EPFL's Teaching Excellence Award, and finished 3<sup>rd</sup> at the European Rover Challenge (Poland) while winning the Best Science Team Award. Fluent in German and English, intermediate French, and avid traveler who has visited 10+ countries on three continents.

## Education

- 10|18 – Today **Ph.D. Candidate**, *École Polytechnique Fédérale de Lausanne (EPFL)*, Lausanne, Switzerland  
Department: Chemistry and Chemical Engineering (EDCH), Academic Supervision: Prof. Dr. Andreas Pautz  
12 (+2\*) of 12 ECTS Credits | 820 of 580 Teaching Hours
- 07|18 – Today **Ph.D. Candidate**, *Paul Scherrer Institut (PSI)*, Villigen, Switzerland  
Laboratory of Radiochemistry, Isotope and Target Chemistry Group | PhD thesis in Radiochemistry:  
«Towards Implementing New Isotopes for Environmental Research: Re-determination of the <sup>32</sup>Si Half-Life»
- 11|15 – 02|18 **Master of Science (M.Sc.)**, *Ruprecht-Karls-University (RKU)*, Heidelberg, Germany  
**Grade average: 1.1 (GER)** | Equivalent to 5.9/6.0 (CH) or GPA: 3.95/4.00 (USA)  
120 (+21\*) of 120 ECTS Credits | Master's thesis in Radiochemistry: Final Grade: 1.0 (GER)  
«Influence of Cement Pore Water on the Sorption of Actinides on Natural Argillaceous Rocks»
- 04|12 – 11|15 **Bachelor of Science (B.Sc.)**, *Johannes Gutenberg University (JGU)*, Mainz, Germany  
**Grade average: 2.1 (GER)** | Equivalent to 4.9/6.0 (CH) or GPA: 3.40/4.00 (USA)  
180 (+60\*) of 180 ECTS Credits | Bachelor's thesis in Numerical Modeling:  
«Estimate Lithospheric Rheologies of the Andes that Preserve the Present-Day Topography»

\*Additional ECTS Credit Points related to extracurricular courses.

## Job Experience

### 🏛 Academic

- 07|18 – Today **Graduate Research Assistant**, *Paul Scherrer Institut, Villigen*  
Planning and Performing of Experiments, Responsible for Project-Meetings (in-situ and online), Supervising Undergraduate Students (B.Sc, M.Sc.), Teaching Practical Laboratory Classes at EPFL
- 05|15 – 03|18 **Student Research Assistant**, *Johannes Gutenberg University, Mainz*  
Close Cooperation with Scientists, Practical Laboratory Work, Running Analyses, Processing and Storage of Acquired Data, Supervising Undergraduate Students (B.Sc.), Creating Illustrations for Scientific Publications

### 🍷 Hospitality

- 11|12 – 05|18 **Assistant Manager**, *Gaul's Catering GmbH & Co. KG, Opel-Arena, Mainz*  
Responsible for efficient day to day operations on Match Days
- 01|10 – 12|14 **Barista and Waiter**, *Rüd's Coffeebar, Singen (Hohentwiel)*  
Preparation of Food/Drinks/Coffee Specialties, and daily financial closing

## Volunteering Activities

- 11|19 – 09|21 **Student Representative in Introducing PSI to the Public**, *Visitor Centre psi forum, Villigen*
- 05|16 – 06|17 **Elected Student Representative**, *RKU Heidelberg*
- 10|14 – 10|15 **Elected Student Representative and Member of the Faculty Council**, *JGU Mainz*
- 04|14 – 10|15 **Elected Student Representative**, *JGU Mainz*
- 10|12 – 03|15 **Study Mentor**, *JGU Mainz*

## Computer Skills

- **Office:** Microsoft Excel, Outlook, PowerPoint and Word
- **Specific Software:** Inkscape, LaTeX, Origin, Python
- **Operating Systems:** Linux, Mac OS, Windows

## Language Skills and Interests

- **German:** Native Speaker
- **English:** Fluent in written and spoken English (C1/C2)
- **French:** Intermediate level of written and spoken French (A2/B1)
- **Business Economics and Sciences:** Technology and semi-conductor industry; chemistry-related fields
- **Travelling:** Backpacking in Australia, Cambodia, France, Ireland, Laos, New Zealand, Oman, Spain and Thailand

## Awards and Honors

- 2022 **Best Contribution (Poster & Presentation): 4<sup>th</sup> Year Ph.D. Student (Research Division: NES)**, *PSI and Nuklearforum Schweiz*
- 2021 **European Rover Challenge (ERC), Kielce (Poland), 3<sup>rd</sup> Place**, *EPFL*  
Participation with EPFL Xplore. Member of the Xplore's Science Delegation and awarded the Best Science Team-Award.
- 2020 **Teaching Excellence Award**, *EPFL*  
Elected by both Students and Professors among the ten best PhD Students for outstanding contributions in their teaching, practical work, courses, exercises and project supervision.
- 2019 **Best Contribution (Poster & Presentation): 1<sup>st</sup> Year Ph.D. Student (Research Division: NES)**, *PSI and Nuklearforum Schweiz*